

VNIVERSITAT (ò) VALÈNCIA (ò) Facultat de Física

Departament de Física de la Terra i Termodinàmica
Programa de Doctorado en Teledetección



Calibration and Validation of Thermal Infrared Remote Sensing Sensors and Land/Sea Surface Temperature algorithms over the Iberian Peninsula

Mayo de 2017

Tesis doctoral presentada por:
Dražen Skoković Jovanović

Director: José Antonio Sobrino Rodríguez
Codirector: Juan Carlos Jiménez Muñoz

«Pobladores del mundo, salvaguardemos esta belleza, no la destruyamos»

Yuri Alekseyevich Gagarin, 12 de abril de 1961, primer ser humano en viajar al espacio

«Folk of the world, protect this beauty, do not destroy it»

Yuri Alekseyevich Gagarin, April 12, 1961, first human to travel into outer space

«Stanovnici svijeta, sačuvajmo ovu ljepotu, nemoj da je uništimo»

Yuri Alekseyevich Gagarin, 12 April 1961, prvi čovek koji je putovao u svemir

José A. Sobrino Rodríguez, Catedràtic de Física de la Terra, adscrit al Departament de Física de la Terra i Termodinàmica de la Facultat de Física de la Universitat de València,

y

Juan Carlos Jiménez Muñoz, Profesor titular de Física de la Terra, adscrit al Departament de Física de la Terra i Termodinàmica de la Facultat de Física de la Universitat de València,

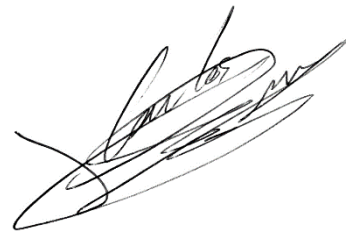
CERTIFICAN:

Que la presente Memoria “**Calibration and Validation of Thermal Infrared Remote Sensing Sensors and Land/Sea Surface Temperature algorithms over the Iberian Peninsula**”, presentada por Dražen Skoković Jovanović ha sido realizada bajo su dirección y que constituye su Trabajo de Tesis Doctoral para optar al Grado de Doctor en Física.

Y para que así conste, en cumplimiento de la legislación vigente, firmamos el siguiente certificado en Burjasot, 26 de Mayo de 2017:



Fdo. J. A. Sobrino Rodríguez



Fdo. J. C. Jiménez Muñoz

AGRADECIMIENTOS

Deseo expresar en estas líneas mi agradecimiento a las personas e instituciones que han hecho posible la realización de este trabajo:

A mi tutor y director, el Dr. José Antonio Sobrino, por sus continuas orientaciones y consejos dentro del mundo de la Teledetección.

A mi codirector, el Dr. Juan Carlos Jiménez-Muñoz, por la ayuda prestada cuando más se necesitaba.

A la Doctora Soledad Gandía, decana de la facultad de Física, y al Doctor José Antonio Martínez Lozano, actual director del Departament de Física de la Terra i Termodinàmica, por su buena acogida dentro del departamento.

Al Profesor Víctor Reglero, director del Laboratorio de Procesamiento de Imágenes por facilitarme el uso de las instalaciones del centro que dirige.

A todos mis compañeros de la UCG: Juan Carlos, Guillem, Yves y José, por haber estado ahí siempre que lo he necesitado, por todos los buenos momentos pasados y por el gran ambiente y buen rollo que siempre ha habido en el trabajo. A Rosa, Belén y Cristian que han formado parte del grupo y han dejado una huella imborrable.

A la gente que ha pasado por estos despachos: Javier, JJ, Marko, Carlos pero, en especial, a Marek y Mario, con los que he compartido un montón de experiencias dentro y fuera de estos despachos, aunque sólo fuera por un par de meses (se os echa de menos).

A mis compañeros de comidas: Julián, por conseguir siempre hacerme desconectar del trabajo con sus absurdos y por las experiencias compartidas; Chiara, por tus limoncellos y porque se te echa en falta; Benja, por ser la persona más galante que hay y, por supuesto, a Annamaria, que me ha aportado siempre un aura positiva en el despacho y con la que he aprendido muchísimo.

A mis compañeros de doctorado: Carolina, Sergio, Roberto, Niobe y Amparo con los que he forjado una gran amistad y con los que he pasado ratos estupendos.

A mis amigos de Físicas: Elena, Jorge, Víctor, Isa, Dani y a toda la gente que he conocido con vosotros. A pesar de la distancia, sé que siempre estáis ahí y que puedo contar con vosotros.

A mis amigos de siempre, Jolu, Chust, Nico, Santi y otros tantos que han estado ahí cuando se les necesitaba.

A mi familia, tata, mama y Vanja, por haberme dado siempre su apoyo, en todos los momentos fáciles y difíciles de mi vida. *Zahvaljujuci Vama, i Vasim savjetima, postigao sam da budem to što jesam. Volim vas! sto tako, zahvaljujem se cijeloj mojoj familiji (Dedi, Baki, "Kekarama" Ujki i Ujini, Tetkovima i svim mojim rođacima) oja se me cesto sjeca, iako smo daleko.* También a Raúl, al que ya aprecio como a un hermano.

A la meua xiqueta, por todo el tiempo que hemos pasado juntos, por lo que hemos compartido, por creer siempre en mí y por estar siempre que se te necesita. Un beset!

La realización de esta tesis doctoral ha sido posible gracias al programa de becas FPI subvencionado por el Ministerio de Economía y Competitividad, además de otros proyectos que se enumeran a continuación:

- Calibration of Earth Observation Satellites in SPAIN (CEOS-SPAIN)
Ministerio de Economía y Competitividad.
- Calibration of Earth Observation Satellites in Spain 2 (CEOS-SPAIN 2)
Ministerio de Economía y Competitividad.
- Smart Irrigation From Soil Moisture Forecast Using Satellite And Hydro
Meteorological Modelling (SIM).
Ministerio de Economía y Competitividad.
- Metodologías avanzadas en observación de la Tierra: calibración de datos
ópticos y extracción de la información (EODIX).
Ministerio de Educación y Ciencia.

RESUMEN

El inicio de la teledetección como una ciencia global que integrara datos de satélite de toda la superficie terrestre, se inició con el lanzamiento del Landsat-1 en el año 1972. La misión Landsat, fue la primera en obtener datos de la superficie terrestre con una resolución adecuada para la detección de los detalles superficiales de La Tierra. Desde ese momento, más de 197 misiones han sido enviadas al espacio, de las cuales, en la actualidad, más de 150 Sensores de Observación de La Tierra (EOS, por sus siglas en inglés) están suministrando datos en tiempo real de la superficie terrestre (Tatem et al. 2013). Debido a este incremento masivo de los datos, en la actualidad, más de 1 terabyte

RESUMEN

de información está listo para utilizarse en estudios terrestres de todo tipo (Maa et al. 2015), que incluyen análisis de series temporales de variables biofísicas o la obtención de parámetros puntuales requeridos para la gestión del entorno.

Por todo ello, el comité de observación de La Tierra a través de satélites (CEOS por sus siglas en inglés) y en concreto el grupo de trabajo de calibración y validación (WGCV por sus siglas en inglés) que está integrado en CEOS, han establecido en consenso con la comunidad internacional la necesidad de incorporar un programa de control de calidad de los datos, que incluye la calibración (cal), validación (val) e inter-comparación de todos los datos registrados por los actuales y futuros satélites de observación de La Tierra.

La calibración es un procedimiento clave de cualquier sistema electrónico, ya que nos permite saber la calidad de los datos brutos registrados o, dicho de otra manera, la respuesta del sistema a una señal dada, controlada por el usuario. La importancia de la calibración es obvia, ya que si los datos brutos registrados por satélite no son precisos, todos los productos obtenidos a partir de ellos tampoco lo serán. Por otra parte, la validación, se refiere a la detección de errores a un nivel de procesado de datos más alto, que incluye los productos derivados de satélite, que son los que representan las variables biofísicas que al final se utilizan para los estudios científicos.

Entre estas variables, el subgrupo de validación de productos de tierra (LPV por sus siglas en inglés) incluyó en el año 2015 a la Temperatura de la Superficie Terrestre (TST) como una de las variables esenciales que intervenían en los procesos terrestres, ya que interviene de forma directa en el intercambio de energía a escala local y global (Kustas et al. 2009). Como la TST, la Temperatura de la Superficie de la Mar (TSM) es otra variable fundamental en la teledetección, ya que juega un papel importantísimo en la estabilidad de todos los procesos terrestres y atmosféricos. La TST/TSM está íntimamente ligada con el espectro Infrarrojo Térmico (TIR, por sus siglas en inglés) que abarca el espectro desde los 8 μm hasta los 14 μm y que es usado por los sensores como fuente de información de la energía emitida que proviene de La Tierra (a través de la atmosfera, que juega un papel importante en la distorsión de los datos registrados por satélite). Por ello, el adecuado conocimiento de la emisividad terrestre y los efectos atmosféricos es fundamental para la precisa obtención de la TST y la TSM.

Hoy en día, la técnica de calibración utilizada para la mayoría de los EOS térmicos, una vez estos se encuentran en órbita terrestre, es la Calibración Vicaria (VC por sus siglas en inglés) que consiste en la obtención de los valores de radiancias a nivel de satélite, mediante la simulación de las medidas registradas in-situ. Para la VC (y la validación), es necesaria la obtención de datos in-situ representativos de la resolución espacial del sensor, por lo que la homogeneidad del terreno donde está situado el radiómetro que mide

la temperatura, en términos de TST, juega un papel clave en las medidas de suelo. Los lugares en los que se implementan las medidas in-situ, además de ser lo más homogéneos posibles, tienen que cumplir otras características, como ser totalmente accesibles, tener la mínima perturbación atmosférica posible (como pueden ser lugares que estén situados a más de 1 km de altura) o que tengan pocos días nublados. Ya que encontrar un lugar lo más adecuado posible para las actividades de cal/val es difícil, un estudio lo más completo posible del terreno sobre el cual se desarrollarán estas actividades es necesario (para el control de los errores que se pueden introducir en nuestras medidas). Las campañas de medidas con sensores aerotransportados son una herramienta útil para este propósito, ya que aportan información útil del terreno estudiado y permiten la inter-comparación de los datos con otros EOS a una escala más amplia de la que se obtendría con una sola medida.

Dependiendo del EOS considerado, la TST o TSM se puede obtener mediante variadas técnicas que dependen de las bandas TIR integradas en los sensores y de los datos atmosféricos disponibles. Entre estas técnicas destacan: la Ecuación de Transferencia Radiativa (ETR) y la ecuación Monocanal (SC), que sólo necesitan una banda en el espectro TIR; la ecuación Split-Window (SW) que se basa en la diferencia de absorción entre dos bandas TIR y, finalmente, el método Temperature Emissivity Separation (TES), que requiere más de 2 bandas. Todas estas técnicas estiman la TST con un error entre 1.0-2.0 K y la TSM con errores inferiores a 1.0 K.

Para contribuir al control de calidad de los datos obtenidos mediante los EOS, en este trabajo se presentan las actividades realizadas en el marco del proyecto Calibration of Earth Observation Satellites in SPAIN (CEOS-SPAIN), que han consistido en la puesta en marcha de estaciones automáticas para la toma continua de datos de la TST (junto a un análisis de idoneidad de las estaciones), la cal/val de EOS y la propuesta de nuevos algoritmos para la estimación de la TST y la TSM, así como un método para la mejora de la resolución espacial de la TST.

Para llevar a cabo estos objetivos, esta tesis se ha dividido en cinco capítulos que se resumen de forma breve en las siguientes páginas:

CAPÍTULO 1: SENSORES Y ALGORITMOS

En este capítulo se realiza una descripción de los sensores utilizados que han servido para llevar a cabo las actividades de cal/val, así como los algoritmos utilizados para la obtención de la TST y la SST.

RESUMEN

Los sensores se pueden dividir en dos tipos: Unos con una resolución espacial, en el espectro térmico, moderada (≤ 100 m) que son el Thermal InfraRed Sensor (TIRS) y el Enhanced Thematic Mapper Plus (ETM+), ambos a bordo de la serie de satélites Landsat – concretamente el Landsat-7 (ETM+) y el Landsat-8 (TIRS). Los otros dos, MODerate resolution Imaging Spectroradiometer (MODIS) y el Spinning Enhanced Visible and Infrared Imager (SEVIRI), son sensores de baja resolución espacial con un tamaño de pixel de 1 km para MODIS y 3 km para SEVIRI (en nadir). MODIS y SEVIRI son sensores con un amplio ángulo de visión por lo que a mayor ángulo de visión, mayor será el tamaño del pixel medido.

Entre los algoritmos, se hace una referencia más amplia a los propuestos en esta tesis y entre los que destacan el algoritmo Monocanal y Split-Window propuestos para el TIRS y el Water vapor Path length SST (WPSST) propuesto para el MODIS (algoritmo de tipo SW). Los coeficientes de estos algoritmos se han extraído a partir de bases de datos atmosféricas (Global Atmospheric Profiles from Reanalysis Information para el sensor TIRS) y de valores de boyas de la red de puertos del estado para el WPSST. Además, en este trabajo, se describen brevemente otros algoritmos que son validados en este trabajo, como son los productos MODIS de TST (MOD11) y de TSM (el Non-Linear Sea Surface Temperature, NLSST) propuestos por la NASA, o los algoritmos SW de MODIS y Monocanal del sensor ETM+ propuestos en los trabajos de Jiménez-Muñoz et al. (2008) y Jiménez-Muñoz et al. (2009a) respectivamente.

Para finalizar, se presenta también un análisis de sensibilidad de los algoritmos propuestos en este trabajo, para tener una idea de su posible precisión a la hora de aplicarlos a los datos de satélite. Además de los errores proporcionados por los nuevos algoritmos propuestos, que no superan los 2.0 K para la TST ni los 0.70 K para la TSM, también se ofrece un resumen de los errores detectados en todos los algoritmos descritos (tanto teóricos como obtenidos en validaciones).

CAPÍTULO 2: PROCESADO DE LOS DATOS

Este capítulo hace énfasis en el proceso seguido para el tratamiento de los datos necesarios para la realización de la VC y de la validación, tanto directa (con datos medidos in-situ) como indirecta (o cruzada, con comparaciones de datos entre sensores mediante el procedimiento de up-scaling, que consiste en la degradación de una imagen de mayor resolución a una resolución igual a la del sensor que se pretende validar).

Entre los datos más importantes hay que destacar los perfiles atmosféricos utilizados provenientes de datos de reanálisis, concretamente del National Center for Environmental Prediction (NCEP), o del producto atmosférico MOD07 ofrecido por MODIS. Estos

datos son utilizados para la obtención de los parámetros atmosféricos que son necesarios como entrada a los algoritmos de estimación de la TST. Entre los parámetros obtenidos se extrae la transmisividad atmosférica, la emisión atmosférica en dirección ascendente y descendente y, por último, el vapor de agua en todo el perfil atmosférico.

Además se ofrece una descripción detallada de los datos in-situ de las boyas de la red de Puertos del Estado, que cuenta con una larga serie de valores de temperatura del mar Mediterráneo y del Océano Atlántico. Estas boyas, miden la temperatura del mar a 3 metros por debajo de su superficie, lo que no equivale a la TSM. Sólo en ciertas condiciones, estas dos temperaturas (la de la superficie y a mínimas profundidades) se llegan a igual: con velocidades de viento entre los 3-10 m/s y con un mínimo impacto de la radiación solar. Estas son las condiciones más idóneas para la validación de la TSM con boyas.

En el trabajo también se detalla la aplicación del método de down-scaling propuesto para el sensor TIRS y MODIS que consiste en la mejora de la resolución espacial de la TST basada en el uso de bandas del espectro visible e infrarrojo. El método denominado Nearest Neighbor Temperature Sharpening (NNTS) se ha propuesto en esta tesis como alternativa al Temperature Sharpening (TsHARP) descrito en Jeganathan et al. (2011). El proceso además de basarse en la relación de la TST con el NDVI, incorpora las bandas situadas entre los 1.5-2.5 μm para mejorar la relación de los suelos desnudos y semi-desnudos con la TST. Además, como el nombre del método indica, incorpora la relación por cercanía entre los píxeles similares, confiriéndole la posibilidad de mejorar la resolución espacial incluso con presencia de nubes y masas de agua (lo que no es posible con el método TsHARP y la relación con el NDVI).

Finalmente, se detalla (mediante esquemas) el proceso seguido por los datos descritos para la obtención final de los productos de la TST y la TSM que serán testeados.

CAPÍTULO 3: ESTACIONES AUTOMÁTICAS DE MEDIDA Y CAMPAÑAS DE CAMPO

Una descripción completa y detallada de la toma de datos in-situ de la TST y de todo el proceso de gestión y tratamiento de datos se puede encontrar en este capítulo.

La instalación de estaciones automáticas permanentes para el registro y control de la TST fue el primer paso para el desarrollo de actividades de cal/val. Las zonas de medida elegidas para la instalación de las estaciones fueron, por sus facilidades de acceso:

RESUMEN

- Barrax, con un área netamente agrícola en la que se han instalado dos estaciones (Las Tiesas, localizada en 39.059° N, 2.099° W y El Cruce, localizada en 39.061° N, 2.099° W)
- El parque nacional de Doñana que dispone de áreas muy extensas en las que existe una marisma que se inunda cada año cíclicamente. Tres estaciones han sido puestas en marcha en Doñana: Fuente Duque: 36.998° N, 6.434° W, Juncabalejo: 36.946° N, 6.389° W y Cortes: 36.996° N, 6.513° W
- Por último, el parque natural del Cabo de Gata, que ofrece un área con muy pocos cambios a lo largo del año y en la que se instaló una estación recientemente, en diciembre del 2015 (Balsa Blanca: 36.939° N, 2.034° W).

Cada estación dispone de instrumental para la medida de la TST u otras variables que puedan ayudar a su estimación.

El procesado de los datos de las estaciones, así como el control de calidad, se gestionan mediante programas generados en la Unidad de Cambio Global (UCG) que, finalmente, nos ofrecen valores de la TST pasando el máximo control de calidad posible.

Además de los datos obtenidos por las estaciones permanentes, en el capítulo se describen las campañas de campo que han hecho posible el control de la emisividad de las zonas de medida, realizadas con el radiómetro CIMEL, así como las campañas realizadas con el sensor aerotransportado Airborne Hyperespectral Sensor (AHS) que han servido para la realización de la validación indirecta de los EOS y para los estudios de homogeneidad del terreno de nuestras zonas de medida.

CAPÍTULO 4: ERRORES DE LA TST EN LAS MEDIDAS IN-SITU

Una vez los datos in-situ han pasado el control de calidad necesario que garantiza la máxima precisión de los valores registrados, en este capítulo se hace referencia a la cuantificación de la precisión de esos datos.

Para ello, en primer lugar se localizaron las principales fuentes de error, gran parte de ellas localizadas como valores de entrada de la ecuación de transferencia Radiativa (ETR), para, a continuación, detallarlas y cuantificarlas mediante estudios.

Entre las fuentes de error para la obtención de la TST podemos destacar:

- El efecto pass-band, que introduce un error en la TST al utilizar el valor efectivo de la longitud de onda de un filtro en vez de ecuación de transformación, específica para cada filtro.

- La radiación descendente procedente de la atmosfera, que si no se mide de forma directa, se puede obtener mediante otros métodos que, finalmente, introducen un error en su estimación.
- La imprecisión en la estimación de la emisividad, que no se puede obtener de una forma totalmente precisa, debido a todos los cambios que se producen en la cobertura o composición de las superficies medidas.
- La imprecisión del mismo radiómetro, que con el paso del tiempo se vuelve más impreciso en la medida de la TST.
- Y, finalmente, la homogeneidad del terreno, que no es un error directo en la estimación de la TST, pero sí un error importante en las actividades de cal/val. El error se produce cuando se comparan valores in-situ registrados con una alta resolución espacial de sólo unos pocos metros, con un valor que representa áreas grandes de cientos o incluso miles de metros. Este error ha sido ampliamente estudiado para los sensores de moderada y baja resolución espacial utilizados en esta tesis, mediante los datos de las campañas del sensor AHS y las imágenes TIRS del Landsat-8.

Como parte final del capítulo, mediante la teoría clásica de errores – que consiste en la raíz de la suma de los cuadrados de cada error – se obtuvo el error final esperado de las medidas de la TST para cada estación del año y para cada estación automática de medidas. A pesar de no disponer siempre de datos directos de todos los errores para cada momento del año, mediante información complementaria (ya sea de fotografías, información de satélite, comparación de los sensores de medida de la TST o transectos) se pudo estimar el error de la TST para cada uno de los sensores a bordo de satélite utilizados en esta tesis.

CAPÍTULO 5: CALIBRACIÓN VICARIA Y VALIDACIÓN DE LA TST/TSM

En este capítulo se han resumido los resultados más importantes extraídos de este trabajo entre los que destacan la validación de los algoritmos propuestos para la estimación de la TST y TSM, la calibración vicaria de las bandas del Infrarrojo Térmico de los sensores y la obtención de los errores de cal/val esperados para cada sensor y estación.

Para acabar con el análisis de errores iniciado en el capítulo anterior, el error debido a la perturbación de la señal que le llega al sensor a través de la atmosfera fue calculado mediante la comparación de una base de datos de radiosondeos con perfiles atmosféricos derivados del producto atmosférico MOD07. Mediante la comparación de los perfiles y su influencia en la determinación de la TST, se pudo obtener el error inducido por la atmosfera que, añadido a los errores de la medida in-situ de la TST, posibilitaron la

RESUMEN

estimación de los errores esperados para la calibración vicaria (VC) y la validación de cada algoritmo.

La VC realizada en las bandas del Infrarrojo Térmico nos mostró que la desviación de las bandas de los sensores con respecto de los valores in-situ simulados a la altura del sensor era mínima, con valores muy cercanos al cero. La banda 11 del sensor TIRS a bordo del Landsat-8 fue la única que mostró una desviación más grande (entre -0.9 K y 0.8 K, dependiendo de la temperatura registrada por el sensor) pero dentro de los límites de precisión de nuestra calibración. Además se pudo observar que el efecto stray-light detectado en las bandas del sensor TIRS era menor que el predicho por Barsi et al. (2015).

La validación directa de los algoritmos de estimación de la TST mostró en general valores de Error Cuadrático Medio (ECM) inferiores a los 2.0 K, pero muy dependientes de las condiciones atmosféricas imperantes del momento. El algoritmo SW fue el que más estabilidad mostró, tanto en el sensor TIRS como en el MODIS con diferencias de valores de 0.3-0.6 K entre condiciones de alto y bajo contenido de vapor de agua en la atmósfera. A pesar de que la ETR y el algoritmo TES implementado en MODIS mostraron los valores más bajos de ECM, no mostraron tanta estabilidad entre las dos condiciones atmosféricas de alto y bajo contenido de vapor de agua, mostrando diferencias entre atmósferas con alto y bajo contenido de vapor de agua de 0.5-1.0 K. Finalmente los algoritmos tipo Monocanal de los sensores a bordo de la serie Landsat mostraron una gran variabilidad de resultados, con diferencias de hasta 2.0 K entre condiciones atmosféricas de alto (con precisiones de la TST de 2.0-3.5 K) y bajo (1.0-1.5 K) contenido de vapor de agua, por lo que su uso queda muy restringido a atmósferas con niveles bajos de vapor de agua. A nivel global, y debido a la estabilidad mostrada en diferentes condiciones de medida, el algoritmo SW es el más recomendado para estudios de variaciones temporales de la TST. Para valores puntuales, la ETR es la que ha mostrado mayor precisión aunque, para valores de vapor de agua bajos, la ecuación Monocanal también obtiene buenos resultados.

Con la validación indirecta (mediante el procedimiento de up-scaling) se pudieron contrastar los resultados obtenidos de la validación directa, pero con una gran cantidad de datos. Valores muy similares a los obtenidos por la validación directa fueron obtenidos, con valores de ECM para la TST del sensor TIRS de entre 1.9-2.3 K (dependiendo del algoritmo) y valores de 1.3 K para MODIS. Para grandes ángulos de medida del sensor MODIS los valores fueron superiores a los esperados, con ECM superiores a 3.0 K en las campañas de Doñana, lo que contrasta con los valores de la validación directa (1.5 K aproximadamente). Estas diferencias son debidas al proceso de up-scaling, que se vuelve menos preciso en zonas de costa y gran variedad de superficies,

lo que lleva a grandes contrastes de la TST que inducen un error extra al proceso de up-scaling. Análogos resultados a MODIS se obtuvieron para el sensor SEVIRI, pero con un ECM más alto para la campaña realizada en la zona de Miajadas (Cáceres) de 2.5 K y valores similares a MODIS en las campañas de Doñana (2.6 K y 4.4 K).

Mediante la misma fórmula de validación indirecta se validaron las imágenes generadas por down-scaling. En comparación con la imagen original, las imágenes con mayor resolución espacial (a las que se les aplicaron los métodos de mejora de la resolución espacial) obtuvieron valores de ECM algo más grandes que las imágenes originales (entre 0.5-1.0 K de más) lo cual se esperaba, ya que las imágenes que se generan mediante down-scaling no mantienen la radiometría (o valor) del píxel original. Comparando el método NNTS con el TsHARP y con la imagen Landsat proporcionada por la United States Geological Survey (USGS) a 30 m (cuando la resolución espacial del sensor TIRS Landsat-8 es de 100 m), el NNTS obtiene los valores más bajos de ECM, con diferencias de 0.2-0.5 K.

Para finalizar con el análisis de los algoritmos, los SW descritos para la obtención de la TSM (el WPSST y el NLSST) fueron validados tanto en el mar Mediterráneo como en el océano Atlántico con resultados muy similares (diferencias de 0.03 K). Cabe destacar que, en las mejores condiciones de validación con boyas, ambos algoritmos alcanzaron precisiones de 0.50 K, lo que nos indica que, con la validación mediante boyas que miden a una profundidad de 3 m por debajo de la superficie del mar, no se puede obtener una precisión mejor que medio Kelvin.

Finalmente, un pack de productos de TST y TSM, para su inclusión en la cadena de procesado que mantiene la UCG a cargo del proyecto CEOS-SPAIN, han sido propuestos. Para el sensor MODIS, un producto de TST mediante el algoritmo TES a 500 m y un producto de la TSM que cubre el Atlántico y el Mediterráneo. Para el sensor TIRS a bordo del Landsat-8, un producto de TST a 30 m de resolución espacial que cubra toda la superficie de la Península Ibérica.

CONCLUSIONES:

En esta tesis, una pequeña (pero importante) contribución a la calidad de los datos derivados del Infrarrojo Térmico se ha realizado en el marco de las necesidades del WGCV. Tres importantes actividades se desarrollaron para ello: la instalación de estaciones automáticas y permanentes para el desarrollo de la cal/val, la VC de los datos TIR obtenidos a través de los EOS y la validación de los algoritmos para la estimación de la Temperatura de la Superficie Terrestre y del Mar. El establecimiento de las estaciones fue el primer paso para el desarrollo de la cal/val que, desde que comenzó con

RESUMEN

la instalación de la primera estación en Enero del 2011 en Doñana, ya dispone de 6 puntos con los que controlar los datos obtenidos por las bandas del espectro Infrarrojo Térmico. Todas las estaciones tienen la capacidad de calibrar y validar los datos procedentes de los sensores a bordo de satélites con un error aproximado de ± 1.0 K.

Con la calibración de los sensores se ha comprobado el adecuado funcionamiento de sus bandas mientras que, con la validación, se ha comprobado la validez de los algoritmos propuestos en este trabajo y su posible implementación en la cadena de procesado para estudios que necesiten la temperatura como valor de entrada. Entre estos estudios podemos destacar los temporales, como es el análisis de las variaciones de la TSM a lo largo de los años o los instantáneos, que necesitan un valor para obtener una magnitud física como puede ser la evapotranspiración.

Hay que tener en cuenta que los resultados obtenidos en esta tesis se refieren a nuestras zonas de calibración y validación, aunque los resultados obtenidos se pueden extrapolar a otras regiones con condiciones de suelo, emisividad o atmosféricas similares a las nuestras. Aun así, para tener una idea más global del funcionamiento de los algoritmos, habría que validarlos en condiciones más extremas, como pueden ser atmósferas con alto contenido de vapor de agua o suelos con emisividades bajas.

Para el futuro se espera seguir ampliando las zonas de cal/val, con las que tener más puntos de muestreo. De esta forma, se puede incrementar la calidad de los datos obtenidos y se puede dar más validez a los resultados extraídos mediante la VC y la validación directa de los algoritmos.

TABLE OF CONTENTS

ACRONYMS	I
LIST OF FIGURES	III
LIST OF TABLES	IX
ABSTRACT	XV
INTRODUCTION	1
1 SENSOR AND ALGORITHMS	7
1.1 SENSOR DATA	8
1.1.1 The Airborne Hyperspectral Scanner (AHS)	8
1.1.2 Enhanced Thematic Mapper Plus (ETM+) and Thermal InfraRed Sensor (TIRS)	9
1.1.3 MODerate resolution Imaging Spectroradiometer (MODIS)	10
1.1.4 Spinning Enhanced Visible and Infrared Imager (SEVIRI)	11
1.2 RADIATIVE TRANSFER EQUATION	12
1.3 LAND AND SEA SURFACE TEMPERATURE ALGORITHMS	14
1.3.1 Single-Channel	14
1.3.2 Split-Window	15
1.3.3 TES algorithm	17
1.4 SIMULATED DATA	18
1.5 ALGORITHM COEFFICIENTS AND SENSITIVE ANALYSIS	20
1.5.1 Landsat 8 TIRS	21
1.5.2 Landsat 7 ETM+	23
1.5.3 Terra/Aqua MODIS Land Surface Temperature	24
1.5.4 Terra/Aqua MODIS Sea Surface Temperature	25
1.5.5 SEVIRI	28
1.5.6 AHS	29
1.6 LAND SURFACE EMISSIVITY	29
1.7 ALGORITHMS SUMMARY	30
2 DATA PROCESSING	33
2.1 ATMOSPHERIC DATA	34
2.1.1 Local Soundings	34
2.1.2 MODIS atmospheric profiles product (MOD07)	34
2.1.3 National Center for Environmental Prediction (NCEP)	35
2.2 IN-SITU DATA	36
2.2.1 Sea temperature measurements	36
2.3 SENSOR IMAGERY AND PROCESSING	38

2.4	RESAMPLING METHODS	40
2.4.1	Nearest Neighbor Temperature Sharpening method	41
2.4.2	Temperature Sharpening local variant method	44
2.5	CALIBRATION AND VALIDATION PROCEDURE	44
2.5.1	Vicarious Calibration (VC)	44
2.5.2	Temperature Validation	45
3	PERMANENT STATIONS AND FIELD CAMPAIGNS	49
3.1	TEST SITES	50
3.1.1	Barrax	51
3.1.2	Doñana	51
3.1.3	Cabo de Gata	52
3.1.4	Miajadas	52
3.2	INSTRUMENT SET UP AND FIXED STATIONS	52
3.3	PERMANENT STATIONS SET UP AND DATA	55
3.3.1	Stations characteristics	55
3.3.2	Data quality control	58
3.4	FIELD CAMPAIGNS	60
3.4.1	Airborne campaigns	60
3.4.2	LSE and LST homogeneity campaigns	61
4	UNCERTAINTY OF IN-SITU MEASUREMENTS	65
4.1	LST RETRIEVAL FOR IN-SITU MEASUREMENTS	66
4.2	PASS BAND EFFECT	67
4.3	LAND SURFACE EMISSIVITY	70
4.4	DOWN-WELLING RADIANCE	72
4.5	RADIOMETERS CALIBRATION	74
4.6	LST HOMOGENEITY	78
4.6.1	INH for moderate spatial resolution (< 100 m)	80
4.6.2	INH for low spatial resolution (< 2 Km)	81
4.6.3	INH over fixed stations	83
4.6.4	INH with transects	85
4.7	TOTAL IN-SITU UNCERTAINTY	86
5	VICARIOUS CALIBRATION AND LST/SST VALIDATION	89
5.1	ATMOSPHERIC INFLUENCE ON CAL/VAL ACTIVITIES	90
5.2	VICARIOUS CALIBRATION	95
5.2.1	ETM+ and TIRS	95
5.2.2	MODIS	98
5.3	DIRECT VALIDATION	101
5.3.1	ETM+ LST algorithms	101
5.3.2	TIRS LST algorithms	106

5.3.3 MODIS LST algorithms	108
5.3.4 MODIS SST algorithms	111
5.4 DOWN-SCALING RESULTS VALIDITY	115
5.5 INDIRECT VALIDATION	118
5.5.1 TIRS	118
5.5.2 MODIS	120
5.5.3 SEVIRI	123
5.6 LST VALIDATION SUMMARY	125
5.7 LST/SST PRODUCTS	126
5.5.1 MODIS	127
5.5.2 Landsat-8 TIRS	127
CONCLUSIONS	131
APPENDIX A	137
APPENDIX B	143
APPENDIX C	147
APPENDIX D	153
REFERENCES	155

LIST OF ACRONYMS

AHS	Airborne Hyperspectral Scanner
ASTER	Advanced Spaceborne Thermal Emission Reflection Radiometer
ASTERlib	ASTER emissivity spectra library
BB	Black Body
Cal/Val	Calibration and Validation
CEOS	The Committee on Earth Observation Satellites
CEOS-SPAIN	Calibration of Earth Observation Satellites in SPAIN
ECV	Essential Climate Variable
EO	Earth Observation
EOS	Earth Observation Sensor
ETM+	Enhanced Thematic Mapper Plus
FOV	Field Of View
FWHM	Full Width at Half Maximum
GAPRI	Global Atmospheric Profiles from Reanalysis Information
GCU	Global Change Unit
L7	Landsat-7
L8	Landsat-8
LPV	The Land Product Validation subgroup, included in the WGCV
LSE	Land Surface Emissivity
LST	Land Surface Temperature
M-AERI	Atmosphere Emitted Radiance Interferometer
MIR	Middle-Infrared
MMD	Spectral contrast Maximum–Minimum Difference
MOD11	MODIS Land Surface Temperature product
MODIS	MODerate-resolution Imaging Spectroradiometer
MWIR	Middle Wavelength Infrared
NE Δ T	Noise Equivalent Delta Temperature
NLSST	Nonlinear SST algorithm
OISST	Optimum Interpolation SST variable used un the NLSST algorithm
OLI	Operational Land Imager

LIST OF ACRONYMS

RMSE	Root Mean Square Error
SC	Single-Chanel
SC _w	Single-Channel water vapor approximation algorithm
SC _ψ	Single-Channel general algorithm
SEVIRI	Spinning Enhanced Visible and Infrared Imager
SST	Sea Surface Temperature
StaDa QC	Station Data Quality and Control
STD	STanDard atmospheric database
SW	Split Window
SWIR	Short-Wave Infrared
TES	Temperature and Emissivity Separation
TIGR	Thermodynamic Initial Guess Retrieval database
TIR	Thermal Infrared spectra
TIRS	Thermal Infrared Sensor
TOA	Top Of Atmosphere
USGS	U.S. Geological Survey
VC	Vicarious Calibration
VNIR	Visible and Near-Infrared
<i>w</i>	Total atmospheric water vapor column
WGCV	The CEOS Working Group on Calibration and Validation
WPSST	Water vapor Path length SST algorithm

LIST OF FIGURES

Figure 1.1. Spectral response functions normalized for the thermal bands of the different sensors described in this work in the 8-14 μm window.

Figure 1.2. MODIS Terra comparison for WPSST algorithm coefficients extraction.

Figure 1.3. MODIS Aqua comparison for WPSST algorithm coefficients extraction.

Figure 2.1. Buoys location over the surrounding seas of Iberian Peninsula.

Figure 2.2. (a) Anchored buoy scheme and (b) buoy picture.

Figure 2.3. Summary scheme of the Nearest Neighbor Temperature Sharpening method.

Figure 2.4. Scheme of the VC procedure over ground test sites.

Figure 2.5. Steps followed for the VC (left) and the LST-SST (right) validation.

Figure 2.6. Scheme of cross-validation process which includes description of up-scaling process.

Figure 3.1. Test site location over Landsat images and Iberian Peninsula map.

Figure 3.2. Images of the instruments described above: (a) Flux Radiometers NR01, (b) IR120 broadband radiometer, (c) CIMEL CE312-2 multiband radiometer, (d) Apogee handheld broadband radiometer, (e) HMP45C temperature and humidity cover and (f) datalogger.

Figure 3.3. Normalized spectral response functions for the thermal bands of the IR120, CIMEL CE312-2 and Apogee handheld radiometers.

Figure 3.4. (a) Las Tiesas, (b) El Cruce, (c) Balsa Blanca, (d) Fuente Duque, (e) Juncabalejo and (f) Cortes stations.

LIST OF FIGURES

Figure 3.5. Timeline of LST measurements on Balsa Blanca, Cortes, Juncabalejo, Fuente Duque, Las Tiasas and El Cruce stations.

Figure 3.6. Screenshot of the: (a) StaDa QC software and (b) annual txt file generated for Las Tiasas station (2015).

Figure 3.7. Screenshot of the graphic interface included in the StaDa QC software where graphic black points symbolizes data selected for its deletion.

Figure 3.8. Example of flight lines over (a) Doñana on May 7, 2013 and (b) Barrax on June 12, 2011 field campaigns.

Figure 3.9. Emissivities evolution of our fixed stations during year 2014. Values were obtained with the CIMEL broadband radiometer.

Figure 3.10. Evolution of the fallow-crop land during year 2015: (a) February, (b) May, (c) August and (d) December.

Figure 3.11. Evolution of the marshland during year 2014: (a) February, (b) March, (c) April (d) May, (e) Jun, (f) August and (g) November.

Figure 3.12. Grass plot evolution during the year: (a) April-December, (b) January-March.

Figure 3.13. (a) Image of transect performed on February, 2016 and (b) the results obtained.

Figure 4.1. Graphic description of sources that influence the radiance measurements performed by radiometer at surface level.

Figure 4.2. Temperature – Radiance conversion for (a) MODIS bands and (b) broadband radiometers.

Figure 4.3. LST differences on conversion process from brightness temperature to LST.

Figure 4.4. (a) Direct broadband emissivity comparison between CIMEL CE 312-2 and IR120 radiometer. (b) Emissivity differences (CIMEL CE 312-2 minus IR120) versus CIMEL CE 312-2 emissivities.

Figure 4.5. (a) In-situ down-welling radiance measured at El Cruce station; (b) Down-welling radiance differences ΔL_{down} (In-situ minus predicted MOD07 – nadir and multi-angle – and Prata’s model) versus the day of year.

Figure 4.6. Sources (black body) of calibration used for: (a) direct indoor calibration – LAND P80P – and (b) direct outdoor calibration performed with platinum thermometer.

Figure 4.7. Direct outdoor calibration of IR120 radiometer against Black Body temperature – (a), (c) and (e) – and Black Body-IR120 difference – (b), (d) and (f).

Figure 4.8. Direct indoor calibration against LAND P80P BB temperature of: (a)-(b) CIMEL CE 312-2 and (c)-(d) IR120 and Optris radiometers.

Figure 4.9. Graphic procedure to compute the INH index. The window (in green over the main image) slides across every pixel of the LST image.

Figure 4.10. INH index retrieved from AHS sensor for moderate spatial resolution sensors.

Figure 4.11. Temporal evolution of the INH index at three Spanish test sites: Cabo de Gata: images (a), (b), (c) and (d); Doñana: images (e), (f), (g) and (h); Barrax: images (i), (j), (k) and (l).

Figure 4.12. Temporal evolution of the INH index in four fixed locations: Fuente Duque, Juncabalejo, Balsa Blanca and Las Tiesas.

Figure 5.1. SC_w differences (in Kelvin) between real sounding and MOD07 atmospheric product (ΔT), in function of the sounding atmospheric water vapor content.

Figure 5.2. RTE differences (ΔL) – sounding minus MOD07 product – (in $W \cdot m^{-2} \cdot sr^{-1} \cdot \mu m^{-1}$) versus the sounding atmospheric water vapor content (w) for: MODIS (b29, b31 and b32), TIRS (b10 and b11) and ETM+ (b6) into two locations: (a) Madrid and (b) Murcia.

Figure 5.3. Diagrams of the water vapor difference – Sounding minus MOD07 product – versus the atmospheric water vapor registered by the soundings.

Figure 5.4. VC results for L7 ETM+ sensor: (a) is the sensor radiance versus the VC-based (TOA predicted) radiance, (b) is the plot of residual bias error through three years.

LIST OF FIGURES

Figure 5.5. VC results for L8 TIRS sensor: (a) sensor radiance versus the VC-based (TOA predicted) radiance and (b) plot of residual bias error through three years.

Figure 5.6. Comparison of MODIS Terra (left side) and Aqua (right side) radiances versus the VC-based (TOA predicted) radiances.

Figure 5.7. Plots of in-situ LST minus algorithm LST versus: (s) in-situ LST measurements and (b) MOD07 v6 atmospheric w content.

Figure 5.8. Diagrams of in-situ LST measurements minus LST retrieved by the algorithms – in blue, SC algorithm; in green SW algorithm; in red RTE – are shown in function of (a) in-situ LST and (b) atmospheric w content.

Figure 5.9. Comparison of MODIS Terra (left) and Aqua (right) LST retrievals – in blue, TES algorithm.

Figure 5.10. In-situ measurements minus MODIS Terra (a) and Aqua (b) LST algorithms – in blue, TES algorithm; in green MOD11 product; in red SW algorithm – versus MODIS zenith angle.

Figure 5.11. Buoy minus SST algorithm – in blue NLSST and in orange WPSST – in the Mediterranean Sea versus zenith angle (a)-(c) and wind velocity (b)-(d).

Figure 5.12. Buoy minus WPSST algorithm in the Atlantic Ocean versus (a) the zenith angle and (b) the wind velocity.

Figure 5.13. Buoy bulk temperature minus NLSST (in blue) and WPSST (in orange) SST algorithms as a function of buoy bulk temperature.

Figure 5.14. Plots of standard deviation (crosses) and percentage of values below 0.5 K (squares) between the coarse images versus the NNTS (in blue) and TsHARP (in green) sharpened images.

Figure 5.15. LST validation of TIRS algorithms versus AHS data.

Figure 5.16. Validation of resampled LST obtained with inverse RTE versus AHS data.

Figure 5.17. Down-scaled LST image obtained with the inverse RTE in Doñana test site: (a) is the LST obtained with NNTS method; (b) is the original USGS LST.

Figure 5.18. LST validation of MODIS algorithms versus AHS data. Colors represent field campaigns: Blue, Doñana 2015; Red, Doñana 2013 and purple Miajadas 2012.

Figure 5.19. LST validation of SEVIRI SW algorithm versus (a) AHS TES product and (b) TIRS algorithms.

Figure 5.20. MODIS LST image of the Iberian Peninsula for August 13, 2014 at 11 o'clock provided by Terra platform with spatial resolution at (a) 500 m (b) 1000 m.

Figure 5.21. MODIS SST retrieved by the WPSST algorithm for Atlantic Ocean and Mediterranean Sea.

Figure 5.22. LST product estimated with RTE at 30 m over Barrax test site. The amplified images show the results of NNTS and USGS sharpening methods.

Figure 5.23. LST product estimated with RTE at 30 m over Doñana test site.

LIST OF TABLES

Table 1.1. ETM+ and TIRS bandwidth of VNIR and SWIR spectra (given in μm).

Table 1.2. SC_w coefficients retrieved by applying GAPRI database on TIRS.

Table 1.3. SW coefficients retrieved by applying GAPRI database on TIRS.

Table 1.4. Test of the Single-Channel (SC) and Split-Window (SW) algorithms using independent simulated data.

Table 1.5. SC_w coefficients extracted with four different databases on ETM+ sensor.

Table 1.6. SW coefficients (a_0 – a_6) obtained for MODIS Terra (TE) – Aqua (AQ).

Table 1.7. MMD coefficients (m_1 – m_3) retrieved in the TES algorithm.

Table 1.8. WPSST algorithm coefficients (c_0 – c_4), number of points (n), Pearson's correlation coefficient (r), the total error of the different terms (δ_{alg} , δ_{NEAT} and δ_θ) as well as the total error of T_{SST} (σ_{sens}) through sensitive analysis for each zenith view angle (θ) range.

Table 1.9. SEVIRI SW coefficients (a_0 – a_6), Pearson's correlation coefficient (r) and error contributions (δ) to the total LST error.

Table 1.10. Emissivity estimation with NDVI Thresholds Method (NDVI-THM).

Table 1.11. Summary of algorithms, databases (used for coefficients retrieval), emissivity inputs for the errors analysis, sensor bands and the different errors expected for each sensor algorithm.

Table 2.1. Buoys location in the Atlantic Ocean and Mediterranean Sea.

Table 2.2. Sensors characteristics summary including the amount of images provided over the Iberian Peninsula, the atmospheric correction applied for VC and direct-indirect validation (DIR) as well as the sensor pixel area chosen for radiance/LST extraction.

LIST OF TABLES

Table 3.1. Summary of the instruments installed in our test sites.

Table 3.2. Sensor characteristics summary including the amount of images provided over the Iberian Peninsula and the atmospheric correction applied for cal/val.

Table 4.1. Specific constants (k_1 and k_2) retrieved for Planck's law to avoid the pass-band effect. Landsat constants have been extracted from Landsat handbook.

Table 4.2. Pass band effect for broadband radiometers and some TIR sensor bands. Results are expressed in radiances (temperatures in brackets).

Table 4.3. Differences in the conversion process of brightness temperature to LST (in Kelvin) due to use of effective wavelength in Planck's law instead of the own filter function constants (see Figure 4.1).

Table 4.4. Bias, standard deviation, RMSE, slope, offset and correlation coefficient obtained from CIMEL CE 312-2 vs IR120 emissivity comparison.

Table 4.5. Average and standard deviation value of LSE measured by CIMEL CE 312-2 over four surface covers.

Table 4.6. Statistics of predicted down-welling radiances, where bias is the In-situ data minus model data.

Table 4.7. Summary of radiometers calibration results shown in this section which include indoor and outdoor calibrations.

Table 4.8. Acquisition date of L8 images used to retrieve INH index for our test sites.

Table 4.9. Summary of the INH index obtained in Barrax, Doñana and Cabo de Gata in the black rectangle of Figure 4.11.

Table 4.10. Summary of the INH results obtained at four fixed stations for three spatial resolutions: 100 m (high-medium EOS), 2 km (low EOS) and 4 km (approximately SEVIRI spatial resolution).

Table 4.11. Transects performed for inhomogeneity (INH) retrievals. The number of measurements (n) and date is also shown.

Table 4.12. Summary of main fixed stations characteristics managed in Doñana, Barrax and Cabo de Gata test sites.

Table 4.13. Summary of suitable periods for cal/val activities for ETM+, TIRS (moderate spatial resolution) and MODIS, SEVIRI (low spatial resolution).

Table 5.1. RTE uncertainty due to MOD07 version 6 inaccuracy in comparison to sounding values at Murcia and Madrid test sites (in brackets is included the number of data analyzed).

Table 5.2. SC_w uncertainty results (Figure 5.2b) given for ETM+ band 6 (b6) and TIRS bands 10 and 11 (b10, b11).

Table 5.3. Expected uncertainty associated to TIR bands and fixed stations. The values are given in Kelvin.

Table 5.4. Expected uncertainty associated to LST algorithms for atmospheric w below 1.6 g/cm^2 and, in brackets, for w above 1.6 g/cm^2 .

Table 5.5. Results of VC for three atmospheric profiles between L7 ETM+ versus TOA predicted radiance data.

Table 5.6. Results of VC between L8 TIRS versus in situ predicted radiance data for four Spanish test sites.

Table 5.7. VC summary of the L7 ETM+ sensor (see Table 5.5) and L8 TIRS (see Table 5.6).

Table 5.8. Bias (TIRS minus VC) values for three different brightness temperature measured in Kelvin.

Table 5.9. Results of the MODIS VC – Terra and Aqua platforms – at four Spanish test sites and for the three TIR bands (29, 31 and 32) considered in this work.

Table 5.10. VC summary of Table 5.9. Bias, standard deviation and RMSE are given in radiances ($\text{W}\cdot\text{m}^{-2}\cdot\text{sr}^{-1}\cdot\mu\text{m}^{-1}$) and, in brackets, the equivalency in temperatures at 300 K is also given.

Table 5.11. Comparison between Land Surface Temperatures measured in situ (LST_{SITU}) and LST obtained with different algorithms (LST_{ALG}).

Table 5.12. LST differences obtained by applying different atmospheric profiles to RTE and SC_w algorithm.

LIST OF TABLES

Table 5.13. Atmospheric parameters (transmissivity; up-welling radiance, given in $W \cdot \mu m^{-1} \cdot m^{-2} \cdot sr^{-1}$; total water vapor, given in g/cm^2) and LST validation of the RTE ($\Delta_{SITU-RTE}$) and the SC TIGR2311 dataset ($\Delta_{SITU-SC}$) for each Atmospheric profile (MOD07 v5, MOD07 v6 and NCEP) in Doñana test site.

Table 5.14. Expected and statistical uncertainties for LST algorithms of ETM+ sensor for high and low atmospheric w content. In brackets, the statistical uncertainties without the three extreme values included in the Table 5.13 are also shown.

Table 5.15. Validation of TIRS LST algorithms for each station (in brackets the number of LST values analyzed for low, high atmospheric w content).

Table 5.16. Validation of TIRS LST algorithms in each station (in brackets the number of LST values analyzed).

Table 5.17. Validation of TIRS LST algorithms for three w ranges.

Table 5.18. MODIS LST algorithms versus in-situ values retrieved at our test sites. Validation was performed for three conditions and for both platforms.

Table 5.19. Results of SST validation versus MODIS zenith angle.

Table 5.20. Results of SST validation versus wind velocity.

Table 5.21. Results of SST algorithms validation with anchor buoys in the Mediterranean Sea.

Table 5.22. Results of Water vapor Path length SST algorithm validation with anchor buoys in the Atlantic Ocean.

Table 5.23. Minimal, maximal and average (σ) values obtained in the comparison of down-scaled and coarse L8/TIRS and MODIS images.

Table 5.24. Average percentage of pixels that show radiometry changes below 0.5 K ($T_{0.5}$) and 1.5 K ($T_{1.5}$).

Table 5.25. Main statistics of the up-scaling AHS process on TIRS coarse image and on sharpened images.

Table 5.26. Bias, standard deviation and RMSE (given in kelvin) between LST retrieved by MODIS algorithms and LST obtained with AHS.

Table 5.27. Bias and standard deviation values (in Kelvin) in addition to the correlation coefficient and clouds percentage obtained in the comparison of down-scaled and coarse MODIS images for the three field campaigns.

Table 5.28. Bias, standard deviation and RMSE (given in kelvin), of the cross-validation performed on SEVIRI SW algorithm with the AHS sensor and TIRS.

Table 5.29. Summary of direct (in-situ) and indirect (cross) validation results of ETM+, TIRS, MODIS and SEVIRI sensors given in Kelvin. The validation of the NNTS method was also included.

Table 5.30. SST and bulk temperature differences between years 2011 and 2012 (2012 minus 2011).

ABSTRACT

Land Surface Temperature (LST) and Sea Surface Temperature (SST) are a key parameters in physical processes of surface energy at local and global scales. LST/SST are directly related to Thermal Infrared (TIR) spectra, which constitute the main source of Earth emission. Control of satellite TIR data can be performed through Vicarious Calibration (VC), which is the more common way to guaranty data quality once sensor is on orbit. Usually, direct validation of LST algorithms and VC of TIR data is performed through in-situ measurements of LST while SST is controlled through anchor buoys or ship transect data. In the framework of CEOS-SPAIN project, Global Unit Change (GCU) group has installed six fixed and automatic stations in three test sites over the Iberian Peninsula (Barrax, Doñana and Cabo de Gata), which provides suitable data for calibration and validation (cal/val) activities of middle and low spatial resolution Earth Observation Sensors (EOS). Validation of SST has been performed with buoys web data available in the database of Puertos del Estado webpage.

Before sensors cal/val, complete suitability study of land test sites was performed in order to obtain the maximal precision given by our fixed stations (in Kelvin). Uncertainties sources linked to in-situ LST retrievals were analyzed such as area inhomogeneity, emissivity or down-welling radiance among others. Finally, with each uncertainty source contribution it was possible to establish the precision of our in-situ measurements regarding the sensor's spatial resolution. For our test sites, LST precision was set below 1 K.

Keeping in mind the values of in-situ LST precision, VC was performed on Landsat TIR sensor (TIRS) and Enhanced Thematic Mapper Plus (ETM+) as well as Terra/Aqua MODerate-resolution Imaging Spectroradiometer (MODIS), showing no displacement in raw TIR data. Test of LST algorithms was also performed with direct and indirect (through airborne sensor data) validations. Results showed Root Mean Square Errors (RMSE) in LST estimations below 2 K and, in the best cases (with the most favorable external conditions), values of 1 K. SST algorithms (Split-Window type) demonstrated precisions below 0.8 K and, in the best case (no solar radiation and high wind velocity), values of 0.5 K.

ABSTRACT

Finally, two LST algorithms (for TIRS and MODIS) and one SST algorithm (MODIS) have been proposed for its inclusion in the sensor images process chain managed by the GCU group.

INTRODUCTION

The launch on 1972 of the Landsat-1 was the start of the Earth Observation (EO) satellite era focused on the global data collection of the Earth land cover (Belward and Skøien 2015). Before, some geostationary satellites as Television Infrared Observation Satellite (TIROS-1) or Metor also collected global images of the Earth but with a low spatial and spectral resolution mainly focused on the land/water/cloud boundaries and meteorological uses. After that, 197 land cover missions and, currently, more than 150 EO sensors were launched providing remote sensing data from ultra violet to microwave spectra (Tatem et al. 2013, Belward and Skøien 2015).

INTRODUCTION

In comparison to previous years, the sheer volume of data acquired by EO satellites have increased at an exponential rate - following Maa et al. (2015), it is expected that the global archived observation data would probably exceed one Exabyte - and have provided unprecedented local and global views of our planet and useful data for environmental management. Because the satellites often use different methodologies, the efficient exploitation of the data for trend analysis and environmental monitoring can be very difficult. Thus, it is essential to establish globally recognized guidelines for calibration and validation (cal/val) processes, as well as for improving available mechanisms for efficient data (and product) management, distribution and processing. The Committee on Earth Observation Satellites (CEOS), the space contribution to Global Earth Observation System of Systems (GEOSS), identified the need to pursue a more active role in tackling these specific issues. The CEOS Working Group on Calibration and Validation (WGCV) established consensus within the international community that cal/val and quality assurance processes should be incorporated into satellite programs in a harmonized way. The intergovernmental Group on Earth Observations stressed that in order for GEOSS to be fully successful, there must be cal/val and inter-calibration mechanisms in place between all available and new instruments.

Validation is the process of assessing by independent means the accuracy of the data products derived from the system outputs, whereas calibration is the process of quantitatively defining the system response to known, controlled signal inputs. Calibration is a key procedure because determines the quality of raw data, which is the background of the offered satellite products. If raw data is inaccurate, all the products will also be incorrect. Moreover, in general, validation refers to assessing the uncertainty of high level satellite sensor derived products by analytical comparison to reference data, which is presumed to represent the target value. Inter-comparison of data products or model outputs provides an initial indication of gross differences and possibly insights into the reasons for the differences, however independent validation data are needed to determine product accuracy (Justice et al. 2000).

The Land Product Validation (LPV) subgroup, included in the WGCV, focuses on standardizing inter-comparison and validation across products from different satellite, algorithms, and agency sources. These products include essential climate and biodiversity variables, such as Leaf Area Index, Soil moisture or Albedo. Recently, in the year 2015, Land Surface Temperature (LST) and Land Surface Emissivity (LSE) variables, which were excluded in the 2010 implementation plan, have been incorporated to LPV subgroup as a new Essential Climate Variable (ECV).

LST is a key parameter in the physical processes of surface energy at local and global scales (Kustas et al. 2009, Karnieli et al. 2010). Knowledge of LST provides direct or indirect information in other study fields, such as evapotranspiration (Kalma et al. 2008; Sanchez et al. 2008), climate change (Julien et al. 1999) or urban heat island effects (Lehoczky et al. 2017). Through the Radiative Transfer Equation, LST is directly related to Thermal Infrared (TIR) spectra, which constitute the main source of Earth emission (supposing average Earth temperature around 290 K). TIR spectra goes from 8 μm to 14 μm and is used by satellite sensors to retrieve information of surface emissions. TIR data is not only dependent on surface emitted radiation (linked with emissivity and temperature), but also on atmospheric absorption effects. The accuracy of TIR data and the knowledge of emissivity and atmospheric effects is fundamental in the precision of LST retrievals and in the target accuracy requirements for LST (Li et al. 2013). See https://lpvs.gsfc.nasa.gov/LSTE/LST_home.html for more information about LST/LSE as ECV.

As LST, Sea Surface Temperature (SST) is another ECV that plays important roles in the exchanges of energy, momentum, moisture and gases between the ocean and atmosphere. Because water represents more than 70% of Earth surface, it is a key study factor in climate studies. Small variations in SST (less than 1 K) as described in Rayner et al. (2003) were observed during the last century, which means that a high precision is necessary in SST estimations to retrieve reliable time series. As suggested in Reynolds et al. (2005) or Merchant et al. (2012) an objective of 0.1 – 0.5 K is required. SST is also obtained from TIR data, although some algorithms include Middle Wavelength Infrared (MWIR) spectra – centered in 4 μm – as additional data (only at nighttime, since at daytime there is solar “contamination” of the observed radiances). More information about SST as ECV can be found at <http://database.eohandbook.com/climate/gcosecv.aspx?gcospECVID=14>.

Radiometric calibration of EO sensors (EOSs) is a critical component to provide accurate global measurements of environmental variables at useful spatial and temporal resolutions. The calibration techniques used for most TIR sensors (TIRSSs) includes a pre-launch calibration, performed in a similar fashion as it would be performed for any instrument; on-board calibration, using a blackbody source; and, finally, in-flight calibration methods, referred to as Vicarious Calibration (VC), that are essential for ensuring highly consistent and accurate radiometric calibration of EOS (Slater et al., 1996). Usually, for VC, in-situ measurements from ground (Thome et al. 1997) or water test sites (Tonooka et al. 2005) are needed. This part is the most problematic, since the measurements performed in-situ have higher spatial resolution than the EOS measurements. For this reason, the knowledge of what test sites are the most suitable

INTRODUCTION

for the infrared radiometers installation is critical, as these should be representative of sensor pixel size. An ideal test site for development of cal/val activities should comply with several critical characteristics that are essential for the simplification of cal/val tasks. As suggested in Thome, (2001) or Schneider et al. (2012) these characteristics can be summarized as follows:

- High spatial uniformity (homogeneity) over large areas minimizes the errors of in situ measurements.
- Knowledge of temporal variations of test sites implies the knowledge of the changes in the emissivity and, consequently, the correct retrieval of the LST.
- An elevation of at least 1 km reduces calibration atmospheric-associated errors.
- High probability of cloud-free days.
- Easy accessibility to the test site is also an important factor.

Of course, it is not always possible to find a test site that verifies all these conditions. For example, desert test sites or lake test sites do not have an easy accessibility, however the high homogeneity and the year surface invariability make them ideal for cal/val.

One way to find possible test sites candidates is by performing an inhomogeneity analysis, which is one of the most important contributions to the uncertainty of in-situ measurements. Test sites should be as homogeneous as possible, so that they can be represented by a single or only a few measurements in comparison to the pixel size of the EOS. But, usually, it is not possible to have the equipment and personnel needed to cover the measured area due to high costs. Furthermore, it is not always clear how to combine the different in situ measurements (if one measurement is more representative than other or not) to represent the EOS data (especially for sensors with low spatial resolution). To solve these difficulties, a detailed knowledge of the selected area is recommended in terms of homogeneity variation over time.

Field campaigns and airborne campaigns are a necessary and useful complement of remote sensing science. Usually, the goal of the field campaigns is to support geo/biophysical algorithm development, to perform cal/val activities, to obtain a detailed knowledge of the area and to simulate future spaceborne Earth Observation missions (Sobrino et al. 2008). The Airborne Hyperspectral Scanner (AHS) is one of these airborne sensors, developed by SensyTech Inc., currently ArgonST, and operated by the Spanish Institute of Aeronautics. With it, many campaigns were performed over Barrax area for cal/val of remote sensing observations (Sobrino et al. 2009), for land-atmosphere exchanges (Su et al. 2008) or for surface energy fluxes derivation (Andreu

et al. 2015). From 2012 to 2015 many additional campaigns were carried out for the purpose of this work allowing multiple studies referred to LST. These included:

- A detailed homogeneity analysis in order to find the best site location for the installation of permanent fixed stations for cal/val activities.
- An indirect validation (or cross validation) of a great number of EOS pixels per image, instead of a few pixels allowed by in-situ measurements. This validation process, called up-scaling because airborne image simulates the pixel size of an EOS by pixel aggregation, has the advantage that atmospheric correction is only needed below the flight height line so that the radiometric measures performed by the airborne sensor are less atmospheric disturbed than the spaceborne sensors. The use of airborne-spaceborne data allows accurate (in atmospheric terms) cross validation in comparison to satellite-satellite cross validation.
- A validation of down-scaling procedures for the improvement of LST spatial resolution.

Depending of sensors considered, LST and SST can be estimated using methods that depend of the available TIR number bands in the sensor. The common LST retrievals include the Radiative Transfer Equation (RTE), the Single-Chanel (SC) and Split-Window (SW) algorithm and the Temperature Emissivity Separation (TES) algorithm that provide, typically, 1.0-2.0 K of LST uncertainty. For SST, the SW algorithm is usually applied, providing an estimated precision of 0.5 K. Currently, 3 moderate spatial resolution sensors - Enhanced Thematic Mapper Plus (ETM+), Thermal Infra-Red Sensor (TIRS) and Advanced Spaceborne Thermal Emission Reflection Radiometer (ASTER) - 4 low spatial resolution polar orbiting sensors - Advanced Very High Resolution Radiometer, MODerate-resolution Imaging Spectroradiometer (MODIS), Visible Infrared Imaging Radiometer Suite (VIIRS) and Sea and Land Surface Temperature Radiometer (SLSTR) – and one geostationary sensor - Spinning Enhanced Visible and Infrared Imager (SEVIRI) – are taking TIR images over the Iberian Peninsula. From those sensors, only ETM+, TIRS, MODIS and SEVIRI were taken in account for cal/val activities because of the data availability (MODIS and SEVIRI data are received and archived in the installations of our group) or data amount (ETM+ and TIRS have taken data in each satellite pass unlike ASTER, which data must to be ordered).

In response to the aforementioned needs, this work has tried to contribute to WGCV on the improvement of quality TIR data with the establishment of permanent stations for LST measurements over Spain - which allows for a continuous monitoring of TIR data

INTRODUCTION

- and with the development of new methodologies for LST and SST retrievals. In order to achieve these objectives, the thesis is divided into five chapters:

The **first chapter** presents the specific equations for SST/LST estimation as well as the procedure followed to retrieve them with a particular focus on the temperature retrievals proposed in this work. Furthermore, specific coefficients for each retrieval, uncertainty associated to each algorithm and LSE retrievals for each sensor are shown. Finally, in order to better understand the algorithms, a description of the EOS in which algorithms are applied is also performed.

The **second chapter** on the one hand, describes the data used in this work which includes atmospheric profiles, satellite data and in-situ data. On the other hand, the methodology followed for sensors calibration and LST and SST validation, including the down-scaling process, is explained.

The **third chapter** describes the in-situ data measured by the permanent stations located at our test sites. This chapter includes a description of test sites – including its temporal (year) evolution –, the in-situ data validation procedure and the instrumental installed in each test site.

The **fourth chapter** is focused in the analysis of the uncertainties sources of the LST measurements. These include emissivity, atmospheric and radiometer calibration sources plus an analysis of the test sites inhomogeneity which is EOS dependent.

The **fifth chapter** presents the results of the cal/val activities. This chapter is divided in six sections which show the cal/val expected uncertainty for each station and sensor, the VC and direct validation results, the validity of down-scaling procedure, the cross-validation of LST products and, finally, the presentation of possible temperature products that can be introduced in the process chain of the Global Change Unit (GCU) group.

Finally, the **conclusion chapter** summarizes the main results obtained in the thesis.

CHAPTER 1:

SENSORS AND ALGORITHMS

This chapter is focused on the description of the LST and SST algorithms analyzed in this work. A brief resume of the coefficients retrieval procedure, database used and expected errors is included. Furthermore, two new algorithms for LST and SST estimation are presented here. In order to better understand the relation between sensors bands and algorithms, a section of satellite and airborne sensors characteristics is introduced in the beginning of the chapter (including the technical problems detected in the TIR bands).

1.1. SENSOR DATA

In this section, characteristics of high (AHS), moderate (ETM+ and TIRS) and low (MODIS, SEVIRI) spatial resolution sensors are described as well as the calibration problems detected.

1.1.1. The Airborne Hyperspectral Scanner (AHS)

AHS is carried onboard the aircraft CASA 212-200 Paternina and incorporates advanced components to ensure high performance while maintaining the ruggedness to provide operational reliability in a survey aircraft. The main AHS technical specifications following Sobrino et al. (2008) are:

- Optical design: scan mirror plus Cassegrain-type afocal telescope with a single IFOV determining field stop (Pfund assembly).
- FOV (Field Of View)/IFOV (Instantaneous Field Of View): 90/2.5 mrad.
- GSD (Ground Sampling Distance): Flight high dependence, but usually 2-8 m.
- Scan rates: 12.5, 18.75, 25, 35 Hz, with corresponding ground sampling distances from 7 m to 2 m.
- Digitization precision: 12 bits to sample the analog signal, with gain level from $\times 0.25$ to $\times 10$.
- Samples per scan line: 750 pixels/line,
- Reference sources: two controllable thermal black bodies (“cold” and “hot”) placed at the edges of the field of view for each acquired scanline,
- Spectrometer: four dichroic filters to split radiation in four optical ports - Visible and Near-Infrared (VNIR), Short-Wave Infrared (SWIR), Middle-Infrared (MIR) and TIR - and diffraction gratings within each port, plus lens assemblies for re-focusing light onto the detectors.
- Spectral bands: 80 bands, with continuous coverage in four spectral regions (VNIR, SWIR, MIR and TIR) + single band at 1.5 μm .

- 10 TIR thermal bands, from 71 to 80, with effective wavelengths of 8.18, 8.66, 9.15, 9.60, 10.07, 10.59, 11.18, 11.78, 12.35 and 12.93 μm and a Full Width at Half Maximum (FWHM) of approximately 0.4-0.5 μm .
- Mean Noise Equivalent Delta Temperature (NE Δ T) for TIR bands of \sim 0.25 K, depending on the considered band.

Only once, during SPARC 2004 campaign, technical problems have been found for the AHS sensor (Sobrino et al. 2006). Since then, TIR bands have shown accurate values as it is indicated in Sobrino et al. (2008) and as it was obtained during internal calibration operations performed in our group for each campaign.

1.1.2. Enhanced Thematic Mapper Plus (ETM+) and Thermal InfraRed Sensor (TIRS)

Landsat series are the only EO platforms which have been providing long-term high spatial resolution TIR data since the 1980s (even though Landsat-3 was the first with a thermal band, it failed shortly after launch). Today, two Landsat platforms remain operational: Landsat-7 (L7), launched in 1999 and Landsat-8 (L8), launched in 2013. Both have a revisiting time of 16 days with a gap between them of 8 days. More information is available on <https://landsat.gsfc.nasa.gov/>.

The ETM+ instrument carried by L7, collects data at 60 m (resampled to 30 m) in the TIR band region (band 6) in a window of 10.3-12.3 μm (see Figure 1.1) and with NE Δ T around 0.2-0.3 K (Barsi et al. 2003). Band 6 has been continuously monitored by the NASA/Jet Propulsion Laboratory (JPL) and the Rochester Institute of Technology (RIT) since 1999. Data obtained during these years allowed the identification of three calibration problems. The first problem was a detection of constant bias in the data of $0.31 \text{ W}\cdot\text{m}^{-2}\cdot\text{sr}^{-1}\cdot\mu\text{m}^{-1}$ at the end of the year 2000 with the ETM+ sensor estimating about 3 K too high for typical LST. The second one was a small gain correction identified in the year 2010 with ETM+ estimating too hot for cold targets and too cold for hot targets. The associated bias at 273 K, 285 K and 300 K was reported to be 0.8 K, 0 K and -0.7 K, respectively (Schott et al. 2012). Finally, was relayed an update in the year 2013, with a bias correction of 0.4 K at 300 K. These corrections, which can be found in the Landsat web site (http://landsat.usgs.gov/science_L7_Cal_Notices.php) have aided in increasing the quality of L7 ETM+ TIR data.

The most recent Landsat platform carries on board the Operational Land Imager (OLI), and the TIRS. OLI sensor collects data at 30 m spatial resolution with 8 bands located in the VNIR and in SWIR regions of the electromagnetic spectrum, plus an additional

CHAPTER 1: SENSORS AND ALGORITHMS

panchromatic band at 15 m spatial resolution (see table 1.1). TIRS measures the TIR radiance at 100 m spatial resolution (resampled to 30 m in order to match with OLI) using two bands located in the atmospheric window between 10-12 μm (see Figure 1.1). NE Δ T for TIRS bands is estimated at 0.4 K (pre-launch values), but later revision showed a NE Δ T below 0.1 K (Ren et al. 2014). Calibration problems of TIRS bands have been reported by the U.S. Geological Survey (USGS) with bias error of 0.29 and 0.51 $\text{W}\cdot\text{m}^{-2}\cdot\text{sr}^{-1}\cdot\mu\text{m}^{-1}$ or -2.1 K and -4.4 K at 300 K in Band 10 and 11 respectively, where TIRS data was too hot (Barsi et al. 2015). On February 2014, all the L8 archive was reprocessed but the residual variability was still larger showing out-of-field stray light - stray light is unwanted light entering into the sensor by ghosting or scattering and depends on scene or pixel location (Tonooka et al. 2005) - which has not yet been corrected. For this reason, band 11, which has the largest variability with 1.67 K at 300 K, is not recommended for temperature retrievals.

Table 1.1. ETM+ and TIRS bandwidth of VNIR and SWIR spectra (given in μm).

Sesnor	b1	b2	b3	b4	b5	b6	b7	b9
ETM+	0.45-0.52	0.52-0.60	0.63-0.69	0.77-0.90	1.55-1.75	-	2.09-2.35	-
TIRS	0.43-0.45	0.45-0.51	0.53-0.59	0.64-0.67	0.85-0.88	1.57-1.65	2.11-2.29	1.36-1.38

1.1.3. MODerate resolution Imaging Spectroradiometer (MODIS)

Terra and Aqua missions are a key component of NASA's EO System that were launched on December 18, 1999 and on May 4, 2002, respectively. Terra and Aqua satellites carry on board the MODIS instrument, among others, and are operated in a near sun-synchronous polar orbit at a nominal altitude of 705 km, with Terra's equatorial crossing time of 10:30 AM (descending southward) and Aqua's equatorial crossing time of 1:30 PM (ascending northward). MODIS provides high radiometric sensitivity (12 bits) in 36 spectral bands ranging in wavelength from 0.4 μm to 14.4 μm in three different spatial resolutions:

- 250 m: Band 1 and 2, with a central wavelength at 0.645 μm and 0.859 μm , respectively.
- 500 m: Band 3 to 7, with a central wavelength at 0.469, 0.550, 1.24, 1.64 and 2.13 μm , respectively.

– 1000 m: Reflective bands from 8 to 20, with a central wavelength at 0.422, 0.443, 0.488, 0.531, 0.551, 0.667, 0.678, 0.748, 0.870, 0.905, 0.936 and 0.940 μm , respectively.

– 1000 m: Emissive bands from 21 to 36, with a central wavelength at 3.75, 3.96, 3.96, 4.05, 4.47, 4.52, 1.38, 6.72, 7.33, 8.55, 9.73, 11.03, 12.02, 13.34, 13.94 and 14.24 μm , respectively.

A $\pm 65^\circ$ scanning pattern achieves a 2,330 km swath and provides global coverage every one to two days providing spatial resolution TIR images of 1 km at nadir and of 4 km at the edge of the image. Of thermal emissive bands, band 29, 31 and 32 were taken in account for calibration and temperature retrieval purposes. Spectral functions for each band are shown in Figure 1.1 with a NE Δ T of 0.05 K. More information can be found on <https://modis.gsfc.nasa.gov/>.

Calibration of MODIS instrument is performed with on-board calibrators that include a blackbody or a space view port among others (Xiong et al. 2015). Although there is a slow but continuing increase in noisy detectors (uncertainty increase around 1%), MODIS instruments continue to provide valuable Earth imagery. Regarding the bands 29, 31 and 32, radiance uncertainties below 0.3% are reported, which is lower than the required specification of 0.5% for bands 30 and 31 and 1% for band 29. More information of calibration issues and performance can be found at <http://mcst.gsfc.nasa.gov/calibration/information> and (Xiong et al. 2015). As an additional problem, it has been reported that thermal emissive band 29 has been significantly affected by electronic crosstalk, which impacts directly in instrument response and induces striping, which in last years has become very pronounced (Sun et al. 2016a, 2016b). In spite of this problem, band 29 has been used in TES algorithm though LST product shows striping effects.

1.1.4. Spinning Enhanced Visible and Infrared Imager (SEVIRI)

SEVIRI is a line by line scanning radiometer, which provides image data in four VNIR channels from 0.4 to 1.6 μm and eight InfraRed (IR) channels from 3.9 to 13.4 μm . VNIR and IR channels take images at spatial resolution of 1 km and 3 km, respectively. SEVIRI, which is carried by Meteosat Second Generation (MSG) series, spin of 100 rpm allows to complete (east – west direction) a full image in about 12.5 min. A flip-flop mechanism is activated to put the on-board black body in the optical path for the instrument calibration. The black body is removed after about 2 seconds from the calibration position. After that, the scan mirror moves back to its initial position. The Earth observation is resumed (after a stop of ~ 2 min) leading to an overall repeat cycle

of maximum 15 minutes. In our case, images over Iberian Peninsula are taken 8 min after the start of the measurement with an average spatial resolution of 3.5×4.5 km for IR channels. IR10.8 and IR12.0 channels, which spectral response function can be found in Figure 1.1, were used in this work for LST validation purposes.

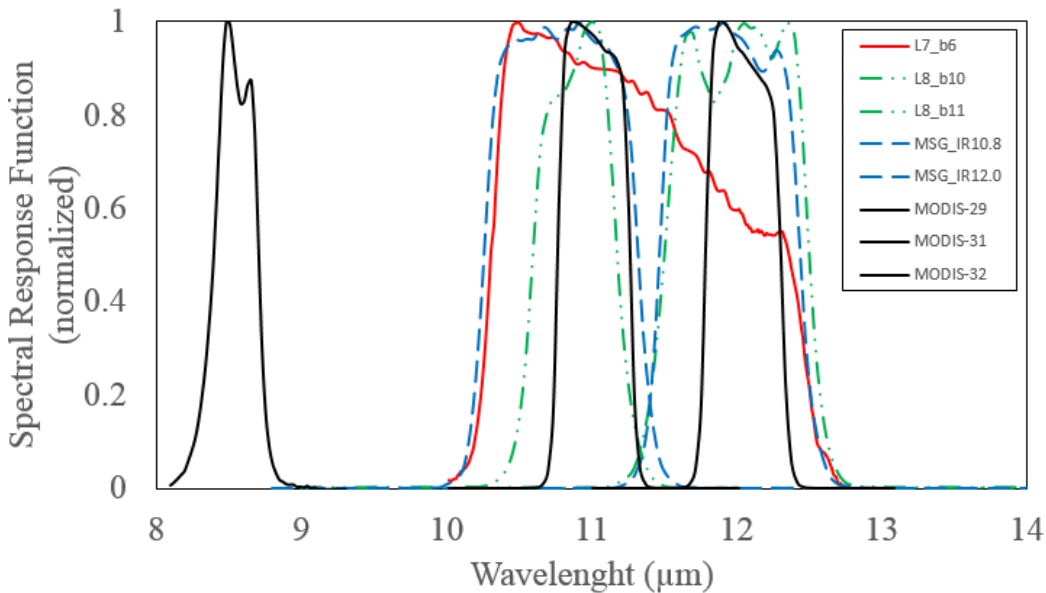


Figure 1.1. Spectral response functions normalized for the thermal bands of the different sensors described in this work in the 8-14 μm window.

1.2. RADIATIVE TRANSFER EQUATION

All objects with temperatures greater than absolute zero emit radiation, and the amount of radiation from a black body in thermal equilibrium at wavelength λ and temperature T is described by Planck's law:

$$B_{\lambda}(T_s) = \frac{c_1}{\lambda^5} \left(\exp \left[\frac{c_2}{\lambda T_s} \right] - 1 \right) \quad (1.1)$$

where $B_{\lambda}(T_s)$ is the spectral radiance ($\text{W} \cdot \mu\text{m}^{-1} \cdot \text{m}^{-2} \cdot \text{sr}^{-1}$) of a black body at temperature T_s (K) and wavelength λ (μm). Because most natural objects are non-black bodies, the emissivity ε , which is defined as the ratio between the radiance of an object and that of

a black body at the same temperature, must be taken into account. The spectral radiance of a non-black body is given by the spectral emissivity multiplied by Planck's law as shown in Eq. (1.1). Obviously, if the atmosphere exerts no influence on the measured radiance, LST or SST (i.e. T_s) can be retrieved by making temperature as the subject of Eq. (1) once the emitted radiance and emissivity are known. It is interesting to keep in mind that the surface temperature obtained by remote sensing methods is only representative of a few surface thickness (approximately $\sim 1 \mu\text{m}$) which is important for SST studies.

When atmosphere exists, thermal radiance measured at-sensor level (L_{sen}) is given by the emission from the ground at a certain temperature T_s (B_{T_s} , where B is the radiance referred to the Planck's law), emission of the atmosphere in the upward direction (L_u), and the emission of the atmosphere in the downward direction reflected by the surface – $(1-\varepsilon) \times L_d$. The radiation terms leaving the ground are also subject to the atmospheric absorption. All these terms are related through the Radiative Transfer Equation (RTE):

$$L_{\lambda}^{\text{sen}} = [\varepsilon_{\lambda} B_{\lambda}(T_s) + (1 - \varepsilon_{\lambda}) L_{d,\lambda}] \tau + L_{u,\lambda} \quad (1.2)$$

where ε is the Land Surface Emissivity (LSE), T_s is the Land Surface Temperature (LST) and τ , L_u , L_d are the atmospheric parameters, namely, the atmospheric transmissivity, the up-welling atmospheric radiance (or path radiance) and the down-welling atmospheric radiance, respectively. Except for T_s , all the magnitudes involved in Eq. (1.2) are spectral magnitudes. By solving for B_{T_s} , and applying the inverse of the Planck's law, LST is finally obtained as

$$T_s = \frac{c_2}{\lambda \ln \left[\frac{c_1}{\lambda^5 B_{\lambda}(T_s)} + 1 \right]} \quad (1.3)$$

where λ is the band wavelength (e.g. effective wavelength, averaged from the spectral response function), and c_1 and c_2 are the Planck's radiation constants, with values of $1.19104 \cdot 10^8 \text{ W} \cdot \mu\text{m}^4 \cdot \text{m}^{-2} \cdot \text{sr}^{-1}$ and $14387.7 \mu\text{m} \cdot \text{K}$, respectively and T_s and $B_{\lambda}(T_s)$ were defined above. Note that retrieving LST from the RTE (Eq. 1.2) requires the knowledge of the atmospheric parameters τ , L_u , L_d . Surface emissivity ε must also be known. More information about RTE can be found in Jimenez-Muñoz and Sobrino (2003) and Li et al. (2013).

1.3. LAND AND SEA SURFACE TEMPERATURE ALGORITHMS

In the past years, many algorithms have been proposed for LST estimation onboard different satellites and using different assumptions and approximations for the RTE and LSEs. In our case, for the purpose of this work, only three algorithms will be considered: the Single Channel (SC) and Split Window (SW) methods and the Temperature and Emissivity Separation (TES) method. Furthermore, a new LST retrieval for L8/TIRS and SW method for SST estimation will be presented.

1.3.1. Single Channel

The Single-Channel general algorithm (SC_ψ) retrieves LST using the following general equation:

$$T_s = \frac{T_{sen}^2}{b_\gamma L_{sen}} \left[\frac{1}{\epsilon} (\Psi_1 L_{sen} + \Psi_2) + \Psi_3 \right] + T_{sen} - \frac{T_{sen}^2}{b_\gamma} \quad (1.4)$$

where T_{sen} is the at-sensor brightness temperature, T_s is the LST, $b_\gamma = c_2/\lambda$, and Ψ_1 , Ψ_2 and Ψ_3 are the so-called atmospheric functions, given by

$$\Psi_1 = \frac{1}{\tau}; \quad \Psi_2 = -L_d - \frac{L_u}{\tau}; \quad \Psi_3 = L_d \quad (1.5)$$

If atmospheric parameters τ , L_u , L_d are known, the atmospheric functions can be calculated from Eq. (1.5) and then the LST. The Eq. (1.4) referred to SC_ψ algorithm is similar to Eq. (1.2) referred to RTE, but with different mathematical structure.

The atmospheric functions defined in Eq. (1.5) can be approached with a polynomial second order relation versus the atmospheric water vapor content (w) in order to obtain the Single-Channel water vapor approximation algorithm (SC_w). The polynomial relation can be expressed as:

$$\begin{bmatrix} \Psi_1 \\ \Psi_2 \\ \Psi_3 \end{bmatrix} = \begin{bmatrix} c_{11} & c_{12} & c_{13} \\ c_{21} & c_{22} & c_{23} \\ c_{31} & c_{32} & c_{33} \end{bmatrix} \begin{bmatrix} w^2 \\ w \\ 1 \end{bmatrix} \quad (1.6)$$

where coefficients c_{ij} are retrieved with a direct relation between Ψ parameters against w .

The τ , L_u , L_d spectral parameters, which are related with Ψ parameters through Eq. (1.5), are retrieved with the introduction of atmospheric database profiles in MODTRAN-5 radiative transfer code (Beck et al. 1999). Fitting these parameters against w , c_{ij} in Eq. (1.6) can be extracted and, then, the LST by applying Eq. (1.4). To estimate the LST with SC_w , the only atmospheric input required is the w . More information about SC algorithm can be found in Jiménez-Muñoz et al. (2009a).

1.3.2. Split-Window

The Split-Window (SW) technique uses two TIR bands typically located in the atmospheric window between 10 and 12 μm . The basis of the technique is that the radiance attenuation for atmospheric absorption is proportional to the radiance difference of simultaneous measurements at two different wavelengths, each subject to different amounts of atmospheric absorption (McMillin, 1975). SW was used for LST retrievals as well as for SST retrievals. Below are shown the SW used in this work:

- The land SW algorithms tested and proposed in this work are based on the mathematical structure proposed by Sobrino et al. (1996), and applied to different Earth Observation sensors in Jiménez-Muñoz and Sobrino (2008):

$$T_S = T_i + a_0 + a_1(T_i - T_j) + a_2(T_i - T_j)^2 + (a_3 + a_4w)(1 - \varepsilon) + (a_5 + a_6w)\Delta\varepsilon \quad (1.7)$$

where T_S is the LST, T_i and T_j are the at-sensor brightness temperatures at the SW bands i and j (in K), ε is the mean LSE, $\varepsilon = 0.5 (\varepsilon_i + \varepsilon_j)$, $\Delta\varepsilon$ is the LSE difference, $\Delta\varepsilon = \varepsilon_i - \varepsilon_j$, w is the total atmospheric water vapor content (in $\text{g}\cdot\text{cm}^{-2}$), and a_0 to a_6 the SW coefficients to be determined from simulated data. Similar to the SC algorithm, the SW algorithm only requires the knowledge of w .

- MOD11_L2 LST product is retrieved using the generalized split-window algorithm (Wan & Dozier, 1996):

$$T_S = a_0 + \left[a_1 + a_2 \frac{(1 - \varepsilon)}{\varepsilon} + a_3 \frac{\Delta\varepsilon}{\varepsilon^2} \right] (T_i + T_j)/2 + \left[a_4 + a_5 \frac{(1 - \varepsilon)}{\varepsilon} + a_6 \frac{\Delta\varepsilon}{\varepsilon^2} \right] (T_i - T_j)/2 \quad (1.8)$$

where T_i , T_j , ε and $\Delta\varepsilon$ have equal mean as the previous equation. As was said, a_i coefficients are also obtained with regression for a large range of surface and atmospheric conditions.

Regarding the SST retrievals, McClain et al. (1985) introduced the linear algorithm Multi-Channel SST (MCSST) that is based on a formula of the following form:

$$T_{SST} = T_i + c_0 + c_1(T_{ij}) + c_2(\sec \theta_z - 1) \quad (1.9)$$

where θ_z represents the sensor scan angle and was introduced to minimize the error due to the increase (with the angle) of the atmospheric path length, T_{ij} represent the difference between T_i and T_j and, finally, T_{SST} represents the SST. Because of the non-linear relationship in the effect of water vapor (Minnett, 1990), other algorithms were introduced following the structure of Eq. (1.9) as a Quadratic (QDSST) algorithm introduced by Emery et al. (1994), and a Nonlinear SST (NLSST) method used currently for the MODIS SST product introduced by Walton et al., (1988,1998). Below, a SST algorithm proposed in this work and the NASA algorithm are presented:

- A variant of the QDSST algorithm named Water vapor Path length (WPSST) algorithm is proposed here and is based on the nonlinear relationship of total atmospheric w content and zenith angle (or path length):

$$T_{SST} = T_i + c_0 + c_1(T_{ij}) + c_2(T_{ij})(1 - \sec \theta_z) + c_3(T_{ij})^2 + c_4(T_{ij})^2(1 - \sec \theta_z)^2 \quad (1.10)$$

where c_0 to c_4 are the WPSST coefficients to be determined empirically from buoys data versus the satellite observations.

- The NLSST method tested here is formulated as follows:

$$T_{SST} = T_i + c_0 + c_1(T_{ij})T_{sfc} + c_2(T_{ij})(\sec \theta_z - 1) \begin{cases} dT_{ij} \leq 0.5 \\ dT_{ij} \geq 0.9 \end{cases}$$

$$T_{SST} = T_{SST}(dT_{ij} \leq 0.5) + \frac{T_{ij}-0.5}{0.9-0.5}(T_{SST}[dT_{ij} \geq 0.9] - T_{SST}[dT_{ij} \leq 0.5]) \quad (1.11)$$

where T_{sfc} is a ‘climatological’ estimate of the SST in the area produced by National Oceanic and Atmospheric Administration (NOAA) and called Optimum Interpolation SST (OISST) (Reynolds et al., 2002). The coefficients are derived and continuously verified based on match-ups between the satellite retrievals of brightness temperature and moored buoys and the Atmosphere Emitted Radiance Interferometer (M-AERI). More information can be found on Liang et al., (2013) and Minnett et al., (2004).

1.3.3. TES algorithm

The TES method estimates LSE and LST from land-leaving thermal data and downwelling atmospheric irradiances (Gillespie et al., 1998). It is based on the radiative transfer equation applied to thermal data, in which the land-leaving radiance (L_{LLR}^i) for band i is given by:

$$L_{LLR}^i = \varepsilon^i B_{T_s} + \pi^{-1}(1 - \varepsilon^i)L_d^i \quad (1.12)$$

In order to completely determine Eq. (1.12) it is necessary to supply one independent measurement. This is provided by a semi-empirical relation determined from laboratory spectra, between the minimum emissivity and spectral contrast Maximum–Minimum Difference (MMD).

Taking into account that L_{LLR}^i and L_d^i are the input data, from an initial value of emissivity it is possible to obtain a first value for land surface temperature. In fact, five different values will be obtained for T_s using Eq. (1.12) by inversion of Planck's law for each involved thermal band. The final value for T_s is chosen as the maximum value between the five different values. Then, T_s can be introduced again in Eq. (1.12) and obtain the emissivity values for thermal bands. This methodology can be repeated again in order to obtain another value for T_s and other emissivity values. The described iterative procedure is called as NEM (Normalized Emissivity Method) module, and constitutes itself a method for retrieving surface emissivities and temperature (Gillespie, 1985). In order to obtain more accurate emissivity values, another two modules are applied: the RATIO and the MMD modules. The RATIO module obtains relative emissivities (β_i) by rationing the NEM emissivities to their average value, whereas in the MMD module final emissivity values are obtained according to the following expression:

$$\varepsilon_i = \beta_i \left(\varepsilon_{min} / \min(\beta_i) \right) \quad (1.13)$$

where ε_i is the minimum emissivity obtained from the following empirical relationship:

$$\varepsilon_{min} = m_1 + m_2 MMD^{m_3} \quad (1.14)$$

with MMD the spectral contrast calculated as:

$$MMD = \max(\beta_i) - \min(\beta_i) \quad (1.15)$$

The TES method is capable of recovering surface emissivities within about 0.015 and surface temperatures within about 1.5 K. A detailed description of the algorithm is given in Gillespie et al. (1998).

1.4. SIMULATED DATA

Both the SC and the SW algorithms require the retrieval of several coefficients; in the case of the SC, the coefficients appear in the relationship between atmospheric functions and water vapor (Eq. 1.6), and in the case of the SW algorithm the coefficients appear in the SW algorithm itself (Eq. 1.7 to 1.11). These coefficients are retrieved from statistical fits performed over a simulated database. Simulated data are obtained from atmospheric profiles datasets used as input to the MODTRAN radiative transfer code (Beck et al. 1999). MODTRAN spectral outputs are averaged using the spectral response functions to finally obtain the band-averaged values of the atmospheric parameters τ , L_u , L_d . In the case of SW algorithms, where at-sensor brightness temperatures need to be simulated, different emissivity spectra (108 samples) extracted from ASTER library (Baldrige et al. 2009) are used. For the TES algorithm, ASTER emissivity spectra library (ASTERlib) was also used for coefficients retrieval of the empirical relationship showed in Eq. (1.14). Additional details on the simulation procedure for SW, SC and TES algorithms can be found in Jiménez-Muñoz and Sobrino (2008), Jiménez-Muñoz et al. (2009a) and Sobrino et al. (2008) respectively.

Different atmospheric profiles databases were used to derive the atmospheric functions:

a) STanDard (STD), extracted from the atmospheres included in MODTRAN code, with 66 atmospheres and with mean w of 1.96 g/cm²;

b) Thermodynamic Initial Guess Retrieval (TIGR) sounding database which includes three datasets: 1) reduced TIGR₆₁ with 61 atmospheres (28 atmospheres assigned to the tropical model, 12 to midlatitude summer model, 12 to subarctic winter, and 9 to U.S. Standard) compiled by Sobrino et al., (1993), with mean w of 2.94 g/cm²; 2) TIGR₁₇₆₁, 1761 atmospheres composed by 322 tropical, 388 midlatitude summer, 354 midlatitude winter, 104 subarctic summer, and 593 subarctic winter (Escobar, 1993), with mean w of 1.03 g/cm²; 3) TIGR₂₃₁₁, 2311 atmospheres that includes TIGR₁₇₆₁ atmospheres plus 550 atmospheres assigned to the tropical model (Chevallier et al., 1998), with mean w of 1.82 g/cm².

c) Global Atmospheric Profiles from Reanalysis Information (GAPRI) that was recently created. GAPRI database is a comprehensive compilation of selected atmospheric profiles at global scale derived from ERA-Interim reanalysis data (Dee et al., 2011) during 2011. Atmospheric profiles were extracted from a global spatial grid of about 0.75°×0.75° latitude-longitude, and they include 29 vertical levels. The GAPRI database used in this study contains 4,838 atmospheric profiles selected over land (GAPRI₄₈₃₈), covering tropical, mid-latitude, sub-arctic and arctic weather conditions. A detailed description of the GAPRI database is provided in Mattar et al. (2015).

For simplicity, the databases will be denoted as STD₆₁, TIGR₆₁, TIGR₁₇₆₁, TIGR₂₃₁₁ and GAPRI₄₈₃₈ where the number refers to the number of atmospheric profiles included in each database.

To account for differences between LST and air temperature (temperature at the first layer in the atmospheric profile), the following variations were considered for LST: T_0-5 , T_0 , T_0+5 , T_0+10 and T_0+20 , where T_0 is the temperature at the first layer. These temperature steps were used in other studies (e.g. Jiménez-Muñoz and Sobrino, 2008), though the highest temperature step (T_0+20) could be too low for desert regions. Therefore, the number of atmospheric profiles included in each database must be multiplied by 5 when these variations are considered. In the case of the SW algorithm, where 108 surface emissivities are also used in the simulation, the number of atmospheric profiles must be multiplied by 108 to obtain the total amount of simulated cases.

In the case of WPSST (see Eq. 1.10), retrieval of the coefficients is performed with the buoys values acquired during the year 2014. Because buoys measurements are taken at a depth of 3 meters, this temperature is not representative of the surface or skin temperature of the sea. This difference of temperatures, known as bulk-skin effect, has

been studied in many works as e.g. Hook et al. (2003) or Ghanea et al. (2016) and shows differences of 0.5 K over Lake Tahoe or 0.1 – 0.4 K over open sea. Some authors demonstrated that the relationship between bulk-skin temperatures depends on two forcing factors: wind and net air-sea heat flux (North et al. 2002). When heat flux is near to zero (at night) and the wind speed is above 5-6 m/s (Donlon et al. 2002; Gentemann et al. 2003), the layers of ocean are less stratified and the value of skin temperature is closer to bulk temperature. Following this, a database of buoys (always with coincident MODIS pass) was compiled with only at night and wind speed ≥ 5 m/s values.

1.5. ALGORITHM COEFFICIENTS AND SENSITIVE ANALYSIS

In this section, coefficients for each algorithm and sensor described in Section 1.1 and 1.2 (copied from the original works or retrieved in this work) are showed. In our case, SC_w algorithm was tested on L7/ETM+ and L8/TIRS; SW algorithm on L8/TIRS, MODIS and SEVIRI and TES algorithm on MODIS. The uncertainty of the LST algorithms proposed in this work (errors of the other algorithms were extracted from the original works), has been obtained in three different manners:

a) Sensitive analysis: solving Eq. 1.5, 1.7 and 1.10 with the assumption of different uncertainties for the input data (θ , w and ϵ) and a certain value of NEAT.

$$\sigma_{SENS} = \sqrt{\delta_{alg} + \delta_{NEAT} + \delta_{\theta} + \delta_w + \delta_{\epsilon}} \quad (1.16)$$

where δ_{alg} is the standard deviation of the algorithm obtained in the minimization (standard error of estimation), δ_{NEAT} is the contribution of the noise equivalent delta temperature (NEAT), δ_{ϵ} is the error due to the uncertainty of the surface emissivity, δ_w is the error due to the uncertainty of the atmospheric water vapor content and σ_{SENS} is the total sensitivity analysis error of the algorithm. These contributions are given by:

$$\delta_{NEAT} = \sqrt{\left(\frac{\partial Ts}{\partial T_i}\right)^2 e(T_i)^2 + \left(\frac{\partial Ts}{\partial T_j}\right)^2 e(T_j)^2} \quad (1.17)$$

$$\delta_{\theta} = \left(\frac{\partial Ts}{\partial \theta}\right)e(\theta) \quad (1.18)$$

$$\delta_w = \left(\frac{\partial T_s}{\partial w} \right) e(w) \quad (1.19)$$

$$\delta_\varepsilon = \sqrt{\left(\frac{\partial T_s}{\partial \varepsilon_i} \right)^2 e(\varepsilon_i)^2 + \left(\frac{\partial T_s}{\partial \varepsilon_j} \right)^2 e(\varepsilon_j)^2} \quad (1.20)$$

where e refers to the error of the parameter considered in brackets. The different derivatives of the T_s given by Eq. (1.16) can be easily calculated. Values of $e(T_i) = e(T_j) = 0.07-0.40$ K (depends of $NE\Delta T$ of considered sensor), $e(\varepsilon_i) = 0.01$ and $e(w) = 0.5$ g/cm² have been considered for MODIS, SEVIRI and TIRS. In the case of WPSST, Eq. (1.10), where there is a dependence of zenith angle, an error of $e(\theta) = 0.08^\circ$ for $\theta > 45^\circ$ and $e(\theta) = 0.03^\circ$ for $\theta \leq 45^\circ$ has been considered, based on the gap of two consecutive MODIS angles.

b) From Independent Simulated Data: the databases presented above were applied to SC and SW algorithms (including 108 emissivity spectra) to retrieve the LST and compare it with the LST database values. This procedure provides an idea of algorithm temperature precision value (σ_{SIM})

c) Direct validation from in-situ data: this is the last step in order to test the algorithm with direct ground LST data comparison. The sensitivity with direct validation (σ_{VAL}) was included for the algorithms that have been tested in previous works.

1.5.1. Landsat 8 TIRS

The coefficients showed in Table 1.2 and 1.3 were obtained in this work and published in Jiménez-Muñoz et al. (2014). The SC algorithm was obtained for band 10 (because of the lower atmospheric absorption of this band than the band 11) for the atmospheric functions (Eq. 1.5 and Eq. 1.6) using GAPRI database. Because $b_\gamma = c_2/\lambda$ parameter has a λ dependence it was calculated for TIRS to be 1324 K. SW algorithm was also developed using GAPRI database.

SC Pearson's linear correlation coefficient is higher than 0.98 for the three atmospheric functions (Eq. 1.6). Since total atmospheric water vapor column (w) is the main input to the algorithm (except for surface emissivity), we tested the sensitivity of the algorithm to variations in w of ± 0.5 g·cm⁻² for all the simulated data obtained from the GAPRI database. Bias (LST for a given variation of w minus LST when nominal w_0 value is considered) values are of (0.2 ± 0.7) K for $w_0 - 0.5$, and of (-0.5 ± 1.0) K for $w_0 + 0.5$,

CHAPTER 1: SENSORS AND ALGORITHMS

with respective root mean square errors (RMSEs) of 0.8 and 1.1 K. For SW algorithm, the standard error of estimation in the statistical fit (δ_{alg}) was 0.6 K, with a Pearson's linear correlation coefficient of 0.98. The RMSE of sensitivity analysis (σ_{SENS}) is of 2.1 K, with $\delta_{\text{alg}} = 0.6$ K, $\delta_{\text{NEAT}} = 1.5$ K (considering $\text{NEAT}=0.4$ K), $\delta_{\epsilon} = 1.4$ K and $\delta_w = 0.1$ K. Major contributions to this error are due to the NEAT and the uncertainty of the surface emissivity). If the sensor's NEAT is assumed to be only 0.1 K (as it was reported in the Section 1.1) the contribution of the NEAT to the total LST error is significantly reduced (from 1.5 to 0.4 K), and total LST error is then 1.5 K.

Furthermore, SC and SW algorithms were applied to simulated data obtained from the TIGR and STD databases. Bias (LST retrieved from the algorithm minus the reference LST), standard deviation, and RMSE values are provided in Table 1.4, including also the linear correlation coefficient.

Table 1.2. SC_w coefficients retrieved by applying GAPRI database on TIRS.

c_{11}	c_{21}	c_{31}	c_{12}	c_{22}	c_{32}	c_{13}	c_{23}	c_{33}
0.0402	0.0292	1.0152	-0.3833	-1.5029	0.203	0.0092	1.3607	-0.2751

Table 1.3. SW coefficients retrieved by applying GAPRI database on TIRS.

a_1	a_2 (K ⁻¹)	a_3 (K)	a_4 (K · cm ² g ⁻¹)	a_5 (K)	a_6 (K · cm ² g ⁻¹)	a_0 (K)
-0.268	1.378	0.183	54.30	-2.238	-129.20	16.40

RMSEs for the SW algorithm over the whole range of water vapor values are around 1.0 K, with almost no bias. As commented in Jiménez-Muñoz et al. (2009a), the SC_w algorithm estimated from the w approach fails for moderate to high w values (e.g., $w > 3$ g · cm⁻²). Therefore, RMSEs for the SC algorithm over the whole range of w values increase to 3–4 K, except for the TIGR1711 database, with an RMSE of 2 K. This last result is explained by the w distribution, which is biased toward low values of w in this database. When only atmospheric profiles with w values lower than 3 g · cm⁻² are selected, the SC algorithm provides RMSEs around 1.5 K, with almost equal values of bias and standard deviation, around 1.0 K in both cases (with a negative bias, thus the SC underestimates the LST). In contrast, when only w values higher than 3 g · cm⁻² are considered, the SC algorithm provides RMSEs higher than 5 K. In these cases, it is preferable to calculate the atmospheric functions of the SC algorithm directly from Eq. (1.5) rather than approximating them by a polynomial fit approach as given by Eq. (1.6).

Table 1.4. Test of the Single-Channel (SC) and Split-Window (SW) algorithms using independent simulated data.

Database	Algorithm	W range (g·cm ⁻²)	n data	Bias (K)	St. Dev. (K)	RMSE (K)	r
TIGR ₆₁	SW	0-6	32940	-0.1	1.2	1.2	0.997
	SC	0-6	32940	-2.7	3.0	4.0	0.982
	SC	0-3	17820	-1.2	1.5	1.9	0.996
	SC	3-6	15120	-4.5	3.2	5.6	0.954
TIGR ₁₇₆₁	SW	0-6	950940	0.0	0.6	0.6	0.999
	SC	0-6	950940	-1.1	1.7	2.0	0.996
	SC	0-3	886680	-0.8	0.9	1.2	0.999
	SC	3-6	58860	-4.0	3.5	5.4	0.957
TIGR ₂₃₁₁	SW	0-6	249588	0.4	1.0	1.1	0.999
	SC	0-6	249588	-2.2	3.7	4.3	0.981
	SC	0-3	186732	-1.0	1.1	1.5	0.998
	SC	3-6	54216	-4.5	4.6	6.5	0.936
STD ₆₆	SW	0-6	35640	-0.2	0.9	0.9	0.998
	SC	0-6	35640	-2.1	2.6	3.3	0.989
	SC	0-3	28080	-1.2	1.2	1.7	0.997
	SC	3-6	7020	-4.7	2.3	5.4	0.961

1.5.2. Landsat 7 ETM+

The coefficients showed in Table 1.5 were extracted from Jiménez-Muñoz et al. (2009a) for band 6 L7/ETM+ for the atmospheric functions (Eq. 1.5 and Eq. 1.6) of the SC algorithm using the databases presented in Section 2.3. Because $b_\gamma = c_2/\lambda$ parameter has a λ dependence, for ETM+ b_γ is equal to 1277 K.

Table 1.5. SC_w coefficients extracted with four different databases on ETM+ sensor.

database	c ₁₁	c ₂₁	c ₃₁	c ₁₂	c ₂₂	c ₃₂	c ₁₃	c ₂₃	c ₃₃
STD ₆₁	0.0917	-0.0989	1.0966	-0.7166	-0.6422	-0.1718	-0.0350	1.5406	-0.4643
TIGR ₆₁	0.0759	-0.0713	1.0857	-0.6144	-0.7092	-0.1938	-0.0289	1.4605	-0.4320
TIGR ₁₇₆₁	0.0652	0.0068	1.0272	-0.5300	-1.2587	0.1049	-0.0197	1.3695	-0.2431
TIGR ₂₃₁₁	0.0698	-0.0337	1.0490	-0.5104	-1.2003	0.0630	-0.0546	1.5263	-0.3214

CHAPTER 1: SENSORS AND ALGORITHMS

Correlation coefficients (r^2) obtained for the three atmospheric functions (Eq. 1.6) are above 0.96 and the RMSE of the algorithms using STD and TIGR independent simulated data is around 2–4 K for a whole w range. Taking in account only the results obtained for w values between 0.5 and 2 $\text{g}\cdot\text{cm}^{-2}$, which can be considered the range of good performance for the algorithm (Jiménez-Muñoz et al. 2009a), RMSE < 1.0 K are obtained for all the databases.

1.5.3. Terra/Aqua MODIS Land Surface Temperature

Coefficients and errors of SW and MMD of TES algorithms are presented in Table 1.6 and 1.7 respectively for Terra and Aqua platforms. SW coefficients have been extracted from Jiménez-Muñoz et al. (2008) using TIGR₆₁ database with the minimization of 164,700 data points for MODIS bands 31 and 32. The uncertainty obtained with the sensibility analysis (σ_{SENS}) was of 2.1 K, assuming a NE Δ T=0.1 K, with major contributions due to emissivity error ($\delta_\epsilon=1.8$ K).

In the case of TES algorithm (where band 29, 31 and 32 are involved), the semi empirical relation between ϵ_{min} and MMD (see Eq. 1.14) has been extracted from Jiménez-Muñoz et al. (2014) with a standard error of determination (1-sigma) of 0.006 and a correlation coefficient of 0.990.

Table 1.6. SW coefficients (a_0 – a_6) obtained for MODIS Terra (TE) – Aqua (AQ). SW errors contributions are given by (δ) and the total sensitivity error of algorithm is given by σ_{SENS} .

SW	a_1	a_2 (K ⁻¹)	a_3 (K)	a_4 (K·cm ² g ⁻¹)	a_5 (K)	a_6 (K·cm ² g ⁻¹)	a_0 (K)	δ_{alg} (K)	δ_{NEAT} (K)	δ_ϵ (K)	δ_w (K)	σ_{SENS} (K)
TE	2.625	0.424	41.4	0.04	-201	26.6	0.004					
AQ	2.601	0.424	41.3	0.14	-199	26.3	0.012	0.9	0.6	1.8	0.1	2.1

Table 1.7. MMD coefficients (m_1 – m_3) retrieved in the TES algorithm. Standard error of determination (σ) and correlation coefficient (r^2) for MMD fit are also shown.

	m_1	m_2	m_3	σ (K)	r^2
TES	0.998	0.654	0.736	0.006	0.990

MOD11 products were also validated in this work, however, since fixed coefficients are not used to obtain the product and depend on zenith angle, atmospheric water vapor content and emissivity values (condition dependence), the coefficients are extracted from a LookUp Table (LUT) and are not shown here. More information about MOD11 and MYD11 product can be found in Wan and Dozier (1996), Wan (2014) and MOD11 Algorithm Theoretical Basis Document (ATBD) at website https://modis.gsfc.nasa.gov/data/atbd/atbd_mod11.pdf.

The uncertainty of TES algorithm through direct validation (based on MOD21 ATBD at https://modis.gsfc.nasa.gov/data/atbd/atbd_mod21.pdf) is below 1.5 K in all test sites. Although MMD coefficients analyzed here are not the same as MOD21 product, the low σ (or ε uncertainty) in the MMD relationship presents minimal differences with TES algorithms (0.005 in ε uncertainty leads 0.3 K in LST). For MOD11, reported RMSE with simulated data is approximately 1.0 K and 0.8 K for daytime and nighttime data, respectively (see MOD11 ATBD) while direct validation shows values of 1.0 K to 2.0 K for both daytime and nighttime data (Wan, 2014).

1.5.4. Terra/Aqua MODIS Sea Surface Temperature

Results obtained for QDSST algorithm proposed in this work (see Eq. 1.10) are summarized in Figure 1.2 and 1.3 – showing relationship between T_{SST} , direct measurement, versus T_{31} and T_{32} band difference (T_{312}) and zenith angle (θ) – and Table 1.8, which includes the SW coefficients (c_0 – c_4), number of data used in the relationship, the Pearson's correlation coefficient (r) and the contribution to the total sensitivity error of the different terms (δ_{alg} , δ_{NEAT} and δ_{θ}). Algorithm has been divided in four ranges in order to be more sensitive to the atmospheric path length.

In terms of the different contributions to σ_{SENS} , it is clearly shown that the main contributions is angle dependent. For θ below 40° , the main contribution is due to algorithm adjustment but, for θ above 40° , the contribution due to NEAT and θ increases reaching similar values to algorithm contribution. These differences between angles are due to different values assumed in the T_{312} and θ that were taken as the average value of all the data used for each range algorithm. The values used for each range, from lower to higher θ , were: 0.55 K, 0.60 K, 0.75 K and 0.90 K for T_{312} and 15° , 30° , 45° and 60° for θ . In terms of total error on SST, values below 0.5 K and 1.0 K were obtained for low and high zenith angles, respectively, showing clearly that there is a quick decrease in precision for large angles.

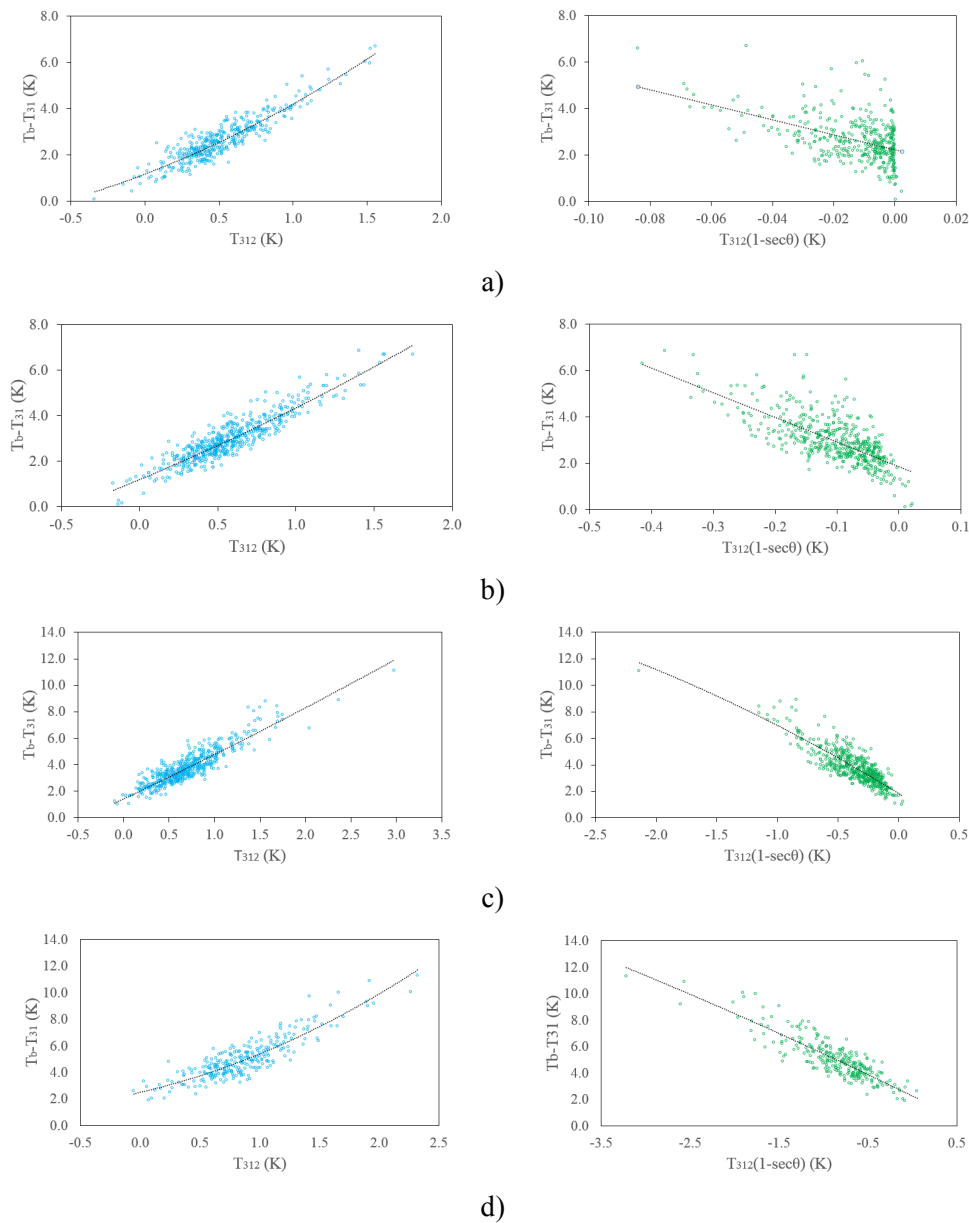


Figure 1.2. MODIS Terra comparison between buoy temperature minus band 31 brightness temperature ($T_b - T_{31}$) versus band 31 minus band 32 brightness temperature (T_{312}) for left plots, and with a zenith view angle dependence ($1 - \sec\theta$) in the right plots. Comparison was separated for four zenith view angle ranges: a) $\theta < 20^\circ$; b) $20 \leq \theta < 40^\circ$; c) $40 \leq \theta < 55^\circ$; d) $\theta \geq 55^\circ$.

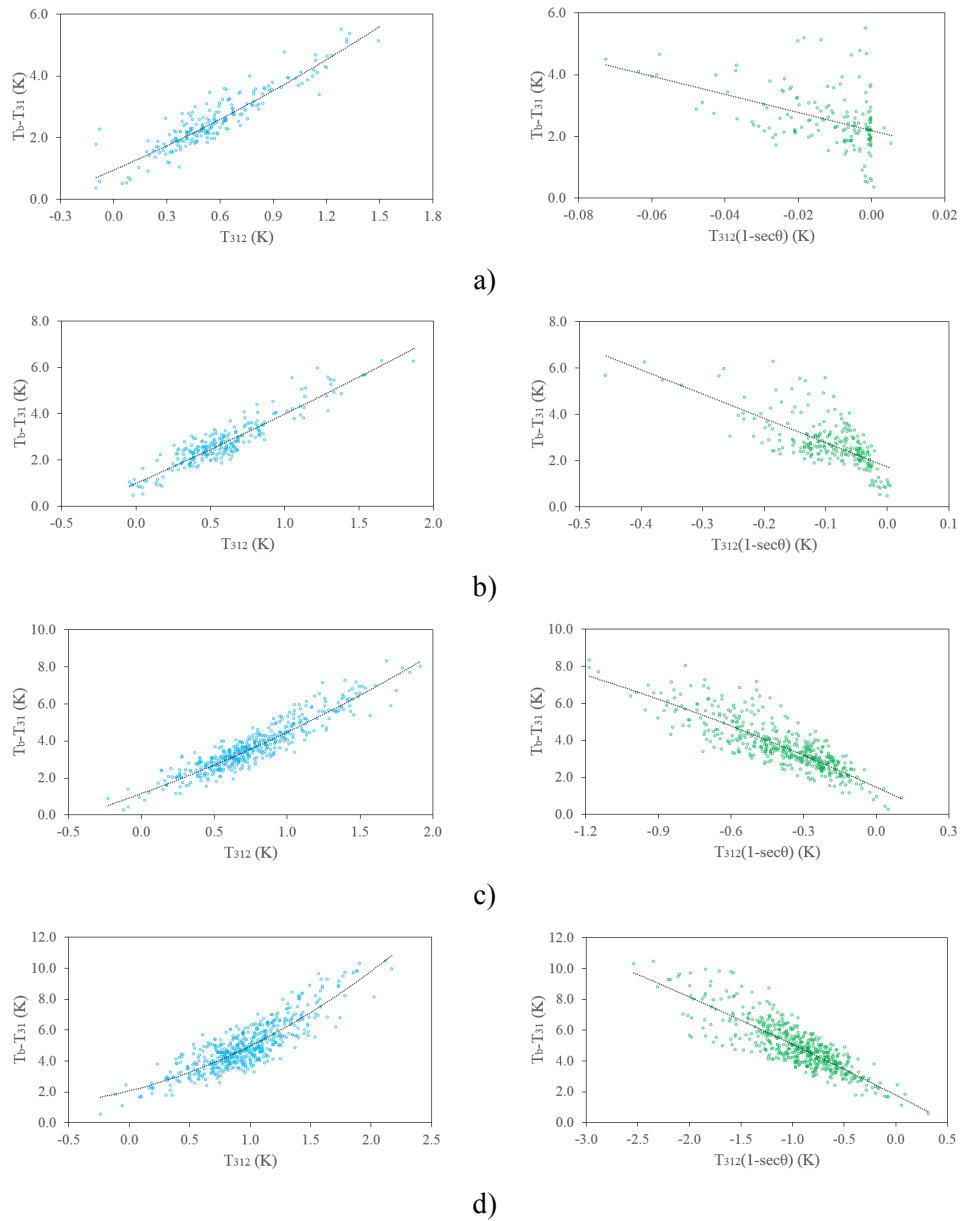


Figure 1.3. MODIS Aqua comparison between buoy temperature minus band 31 brightness temperature ($T_b - T_{31}$) versus band 31 minus band 32 brightness temperature (T_{312}) for left plots, and with a zenith view angle dependence ($1 - \sec\theta$) in the right plots. Comparison was separated for four zenith view angle ranges: a) $\theta < 20^\circ$; b) $20 \leq \theta < 40^\circ$; c) $40 \leq \theta < 55^\circ$; d) $\theta \geq 55^\circ$.

CHAPTER 1: SENSORS AND ALGORITHMS

Table 1.8. WPSST algorithm coefficients (c_0 – c_4), number of points (n), Pearson’s correlation coefficient (r), the total error of the different terms (δ_{alg} , δ_{NEAT} and δ_{θ}) as well as the total sensitivity error of algorithm (σ_{sens}) through sensitive analysis for each zenith view angle (θ) range. See also Figure 1.1 and 1.2.

Platform	θ°	c_1	c_2	c_3 (K ⁻¹)	c_4 (K ⁻¹)	c_0 (K)	n	r	δ_{alg} (K)	δ_{NEAT} (K)	δ_{θ} (K)	σ_{SENS} (K)
Terra	< 20	2.44	-0.85	0.56	-	1.18	393	0.917	0.38	0.09	0.01	0.39
	[20, 40]	2.61	-1.14	0.33	-	1.21	489	0.918	0.41	0.09	0.03	0.42
]40, 55]	2.52	-1.41	0.12	-0.19	1.45	498	0.906	0.57	0.46	0.04	0.73
	> 55	-0.43	-2.54	1.24	-0.46	2.54	363	0.894	0.63	0.66	0.36	0.98
Aqua	< 20	2.51	0.49	0.40	-	0.95	203	0.922	0.37	0.25	0.01	0.45
	[20, 40]	2.72	-0.97	0.14	-	0.99	282	0.916	0.41	0.09	0.05	0.42
]40, 55]	2.36	-0.87	0.49	-0.06	1.19	432	0.933	0.49	0.47	0.03	0.68
	> 55	-0.97	-2.90	1.53	-0.58	2.12	515	0.889	0.68	0.66	0.38	1.01

The NLSST algorithm presented in Eq. (1.11) and processed by Ocean Biology Processing Group uses month dependent coefficients that can be downloaded at <https://oceancolor.gsfc.nasa.gov/atbd/sst/>. The errors provided by the sensibility analysis and extracted from the ATBD (https://modis.gsfc.nasa.gov/data/atbd/atbd_mod25.pdf) were retrieved as 0.337 K at nadir and 0.48 K at $\theta=45^\circ$. Direct validation of SST product was also performed in other works as, for example, Minnett et al. (2004), Qin et al. (2014) or Ghanea et al. (2016) with biases and 1-sigma results ranging from -0.3 K to 0.1 K and 0.45 K to 0.68 K, respectively. More information can be found on Kilpatrick et al. (2015).

1.5.5. SEVIRI

SEVIRI SW coefficients presented in Eq. (1.7), were obtained with zenith angle dependence form Atitar and Sobrino, (2009) with simulations performed on TIGR₆₁ database (see Table 1.9). SW algorithm was applied to IR10.8 and IR12.0 channels. Errors of different contributions were also included in the Table 1.9 (except δ_w which in all cases is below 0.1 K) for a simulation performed at $\theta=30^\circ$. The total sensitivity error (σ_{SENS}) showed by the algorithm is 1.13 K.

Furthermore, uncertainties from direct validation were found in the work, with nighttime RMSE values of 1.0 K to 1.9 K.

Table 1.9. SEVIRI SW coefficients (a_0 – a_6), Pearson’s correlation coefficient (r) and error contributions (δ) to the total LST error. μ is equal to $1/\cos^2(\theta)$.

a_1	a_2 (K ⁻¹)	a_3 (K)	a_4 (K · cm ² · g ⁻¹)	a_5 (K)	a_6 (K · cm ² · g ⁻¹)	a_0 (K)	r	δ_{alg} (K)	δ_{NEAT} (K)	δ_ϵ (K)
1.34-	0.29+	60.67-	-6.71+	-125.91+	19.44-	-0.44+	0.98	0.42	0.40	0.97
0.11 μ	0.08 μ	10.01 μ	2.47 μ	15.09 μ	4.27 μ	0.57 μ				

1.5.6. AHS

TES algorithm was used in AHS for LST retrieval because of its 10 thermal channels. Following the work of Sobrino et al. (2008), a configuration of 7 channels (less affected by atmospheric absorption) was considered as optimal to retrieve LST. AHS bands considered are 72, 73, 75, 76, 77, 78 and 79.

$$\epsilon_{min} = 0.999 - 0.777MMD^{0.815} \rightarrow r = 0.996, \sigma = 0.005$$

Applying the MMD relation (Eq. 1.14) to TES algorithm, a RMSE below 1.6 K was obtained in a direct validation of LST.

1.6. LAND SURFACE EMISSIVITY

Because of the coupling between LST and LSE, all the algorithms for LST retrieval require the knowledge of LSE (except the TES algorithm). In this work, we used the NDVI Thresholds Method (NDVI-THM), originally presented by Sobrino et al. (2001) and revised by Sobrino et al. (2008). LSE is estimated from information collected in VNIR bands (reflectance or vegetation index) depending on the Fractional Vegetation Cover (FVC) for a given pixel. Different approaches have been proposed to retrieve FVC from vegetation indices (e.g. NDVI) or other techniques. A review can be found in Jiménez-Muñoz et al. (2009b). Equations for LSE are given as:

$$\begin{aligned} \epsilon &= a + b\rho_{red} \quad (FVC = 0) \\ \epsilon &= \epsilon_s(1 - FVC) + \epsilon_v FVC + C \quad (0 < FVC < 1) \\ \epsilon &= 0.99 \quad (FVC = 1) \end{aligned} \tag{1.21}$$

CHAPTER 1: SENSORS AND ALGORITHMS

where ρ_{red} is the reflectance in the red band, the term C accounts for the cavity effect (multiple scattering), and ε_s and ε_v are reference soil and vegetation emissivity values. The empirical linear relationship between ε and ρ_{red} for the case $FVC=0$ was introduced to avoid an a priori knowledge of the soil emissivity, and also to account for the variation in emissivity over different soil types. When working over a particular area with only one type of soil with known emissivity, and neglecting the cavity term because of practical considerations, Eq. (1.21) can be simplified to $\varepsilon = \varepsilon_s(1 - FVC) + \varepsilon_v FVC$. ε_s and ε_v values have been obtained using laboratory measurements of emissivity spectra included in the ASTER spectral library (Baldrige et al., 2009). In Table 1.10, the final expressions for emissivity retrievals are shown.

Table 1.10. Emissivity estimation with NDVI Thresholds Method (NDVI-THM). The different conditions (land cover) are expressed in terms of Fractional Vegetation Cover instead of NDVI values.

Sensor	Band	Land Cover	Expression
L8	10	FVC=0	$0.979-0.046\rho_{\text{OLI},B4}$
		$0 < FVC \leq 1$	$0.971+0.0167FVC$
	11	FVC=0	$0.982-0.027\rho_{\text{OLI},B4}$
		$0 < FVC \leq 1$	$0.977+0.011FVC$
MODIS	31	FVC=0	$0.984-0.088\rho_1$
		$0 < FVC \leq 1$	$0.974+0.015FVC$
	32	FVC=0	$0.982-0.028\rho_1$
		$0 < FVC \leq 1$	$0.968+0.021FVC$
SEVIRI	10.8	FVC=0	$0.977-0.048\rho_{\text{VIS}0.6}$
		$0 < FVC \leq 1$	$0.968+0.021FVC$
	12.0	FVC=0	$0.981-0.026\rho_{\text{VIS}0.6}$
		$0 < FVC \leq 1$	$0.976+0.015FVC$

1.7. ALGORITHMS SUMMARY

A summary of the algorithms, databases for coefficients retrieval, bands and the different errors (σ_{SENS} , σ_{SIM} and σ_{VAL}) expected for each sensor are shown in Table 1.11 (no data is symbolized with a line). These errors will be taken in account for the validation analysis performed in Chapter 4.

Table 1.11. Summary of algorithms, databases (used for coefficients retrieval), emissivity inputs for the errors analysis, sensor bands and the different errors expected for each sensor algorithm: σ_{SENS} is the error obtained with the sensitive analysis, σ_{SIM} is the RMSE obtained with the simulation of the algorithm in an independent database and σ_{VAL} is the RMSE obtained with a direct validation. Values shown in brackets represent the uncertainty for low atmospheric w range conditions.

Sensor	Algorithm	Bands	Data base	Emissivity input	σ_{SENS} (K)	σ_{SIM} (K)	σ_{VAL} (K)
SEVIRI	SW	10.8, 12.0	TIGR ₆₁	NDVI-THM	1.1	-	1.0 - 1.9
	SW	31, 32	TIGR ₆₁	NDVI-THM	2.1	-	-
	TES	29, 31 and 32	ASTERlib	MMD	-	-	< 1.5
MODIS	MOD11	31, 32	MOD07	MMD	-	0.8 - 1.0	1.0 - 2.0
	QDSST	31, 32	Buoys	-	0.42 at 40°	-	-
	NLSST	31, 32	Buoys/ M-AERI	-	0.48 at 45°	-	0.45 - 0.68
TIRS	SW	10, 11	GAPRI	NDVI-THM	1.5	1.1	-
	SC	10	GAPRI	NDVI-THM	1.1	3.8 (1.7)	-
ETM+	SC	6	STD ₆₁	NDVI-THM	< 2.0 (< 0.7)	4.0 (0.8)	-
			TIGR ₆₁	NDVI-THM	~3.0 (< 0.7)	3.0 (0.8)	-
			TIGR ₁₇₆₁	NDVI-THM	< 2.0 (< 0.7)	2.6 (0.9)	-
			TIGR ₂₃₁₁	NDVI-THM	~3.0 (< 0.7)	2.5 (0.9)	-
AHS	TES	72,73,75, 76,77,78 and 79.	ASTERlib	MMD	-	-	1.6

In general, all algorithms obtain RMSE values below 2 K, except SC algorithms if all w range is considered. TES algorithm has the advantage that it only needs as input the atmospheric functions, while SC and SW algorithms need, additionally, an emissivity input value. As TES algorithm, SW SST algorithms do not need emissivity input because the high emissivity in the infrared spectral intervals of concern are relatively invariant under the usual range of environmental conditions. As a result, variability in surface processes is not a major source of uncertainty and then, the accuracy of SST algorithms is higher than LST algorithms.

CHAPTER 2:

DATA PROCESSING

In this chapter we described the in-situ, satellite, airborne and atmospheric data used for cal/val activities in addition to process of these data. Furthermore, a new methodology for LST sharpening developed in this work and the VC and algorithm validation process are presented.

2.1. ATMOSPHERIC DATA

Atmospheric corrections are difficult to implement. The presence of the atmosphere between surface and sensors affects the radiances measured by a radiometer at the TOA. These radiances result primarily from emission/reflection at the surface modulated by the effects of the attenuation, and emission of the atmosphere. Atmospheric corrections thus consist in correcting the radiance measured by sensors for the effects of atmospheric attenuation (or transmissivity), emission (up-welling atmospheric radiance) and emission-reflection (the down-welling atmospheric radiance). Correcting for the atmospheric effects requires accurate knowledge of the vertical profiles of atmospheric water vapor and temperature both highly variable spatially and temporally (Perry & Moran, 1994).

Local soundings are a useful and most precise tool for atmospheric vertical profile knowledge. The problem is that soundings do not cover all regions of the world but only specific local areas. For this reason, alternative atmospheric profile sources covering our test sites were used in this study. These atmospheric profiles are MODIS MOD07 atmospheric product and the reanalysis data extracted from the National Center for Environmental Prediction (NCEP).

2.1.1. Local Soundings

In the web page <http://weather.uwyo.edu/upperair/sounding.html> of the University of Wyoming, soundings of Madrid (40.50N, 3.48W) and Murcia (38.00N, 1.16W) airports were downloaded for years 2013, 2014 and 2015. Soundings are launched two times per day, at 00:00 and 12:00 with measurements of pressure, temperature, relative humidity, wind speed and direction. Altitude of the soundings was computed using the hydrostatic equation, which is a function of pressure.

These soundings were not used for the cal/val activities because of their distant location, but were used for error estimations of alternative atmospheric profile sources. Madrid location was tested as a representative profile of inland atmospheres (such as Barrax location) and Murcia was tested as a representative of coastal of south Iberian Peninsula locations (Doñana and Cabo de Gata).

2.1.2. MODIS atmospheric profiles product (MOD07)

MODIS project provides the scientific community with many Standard Products, among them include the atmospheric profile product, denoted as MOD07 or MYD07 for Terra or Aqua platform, respectively. In general, we use the term MOD07 to refer both Terra and Aqua derived products. MOD07 consists of several parameters, such as total-ozone

burden, atmospheric stability, temperature and moisture profiles, and atmospheric water vapor. All of these parameters are produced day and night at 5×5 1-km pixel resolution when at least 9 observations are cloud free. It provides a total amount of 20 atmospheric levels. In particular, the pressure levels of profiles are 5, 10, 20, 30, 50, 70, 100, 150, 200, 250, 300, 400, 500, 620, 700, 780, 850, 920, 950 and 1000 hPa. The algorithm uses 11 infrared MODIS bands (bands 25, and from 27 to 36) to extract the vertical profiles with a statistical regression. Profiles include temperature, moisture as well as total column estimates of precipitable water vapor, ozone, and atmospheric stability. Two latest versions, version 5 (v5) and version 6 (v6) were considered in this work. The differences between v5 and v6 (processing data differences) can be found in Borbas et al. (2011) and Seemann et al. (2006) and MODIS Atmosphere Web site at <http://modis-atmos.gsfc.nasa.gov/>.

For cal/val purposes, MOD07 v6 and v5 profiles were extracted for one single pixel centered in our desired area. Furthermore, MOD07 v6 was used for indirect validation or cross-validation of LST products proposed in this work and derived from L8/TIRS or MODIS. In this last case, for the retrieval of LST maps, a huge number of profiles is required which needs large computing time using normal computers. For this reason, in order to reduce computing time, the profiles were averaged to 20×20 km. As an example, to compute all the pixels over Iberian Peninsula (10 million pixels) it is necessary 50 hours approximately. Averaging the pixels, the time is reduced to 3 hours approximately.

2.1.3. National Center for Environmental Prediction (NCEP)

An Atmospheric Correction Parameter Calculation (ACPC) web tool was proposed by Barsi et al. (2005) in order to provide atmospheric parameters particularized to the Landsat series TIR bands as well as vertical atmospheric profiles. Data included in the ACPC is generated by NCEP, and they incorporate satellite and surface data to predict a global atmosphere at 28 altitudes, plus one extra altitude at the TOA (at 0 hPa). These modelled profiles are sampled on a $1^\circ \times 1^\circ$ grid and generated every 6 h, 00:00, 06:00, 12:00, and 18:00 UTC. Vertical atmospheric information includes the most important variables such as pressure, geopotential height, air temperature and relative humidity, among others. In the web-tool (<http://atmcorr.gsfc.nasa.gov>), the user needs to enter the latitude and longitude coordinates to obtain the vertical atmospheric profile that are sent by e-mail.

Because each profile must to be obtained manually and through web site, the usefulness of this tool is focused only for a small areas or few satellite pixels. For this reason, NCEP profiles were used only on AHS sensor and Landsat series for cal/val purposes.

2.2. IN-SITU DATA

In-situ data is the key of cal/val activities because it estimates our ground or sea true temperature values. Mostly of in-situ data is measured by radiometers or pyrgeometers (taking in account only the TIR region) that provide radiance values in a spectral range of 8–14 μm and 4.5–50 μm respectively, from which it is possible to extract LST or SST. Contact thermometers are not used for temperature estimations (except for SST) because of the difficulty to take measurements for surfaces thickness of only 1 μm (which is the width representative of remote sensing methods). In this section, in-situ sea temperatures are presented. Because of the time and work dedicated to the establishment of the ground fixed stations and the viability studies performed, ground data will be developed in the next chapter.

2.2.1. Sea temperature measurements

The Iberian Peninsula is surrounded by the Atlantic Ocean and the Mediterranean Sea which are located north-eastward and westward, respectively. Atlantic Ocean is the second largest of the world's oceans with a total area of about 106,460,000 km^2 . The Mediterranean Sea is located between latitudes 30–46° N and longitudes from 6° W to 36° E (see Figure 2.1). In this study, only a little fraction of the sea area were used. Concretely, the area delimited by the coastal shape of the Iberian Peninsula. In this area, the State-owned Spanish Port System includes anchored buoys (SeaWatch type) network data that provide real time data of the state of the sea. Data include sea temperature, speed and direction of stream and air, air temperature and atmospheric pressure. Sea parameters are taken at a depth of 3 m, while atmospheric parameters are taken at 3 m above the surface (see Figure 2.2).

Because the goal of this work is the validation of SST retrievals, only the buoys with sea temperature, wind speed measurements (because wind speed is the key parameter to relate buoy temperature and SST) and located at least 5 km from the coast (in order to avoid mixed pixels sea-ground) were taken in account. Following this, six Atlantic and five Mediterranean buoys were used. Locations of the buoys are shown in Figure 2.1 and in Table 2.1.

Sea temperature is retrieved with a contact thermometer with a precision of ± 0.03 K which register data every hour with an instantaneous measurement. The wind speed is measured every 10 min and averaged and registered every hour with a precision of ± 0.3 m/s. As posted in Embury et al. (2012), hourly depth temperature variations are lower than 0.1 K (registered below 1 m), therefore hourly temporal resolution is enough for validation activities.

Table 2.1. Buoys location in the Atlantic Ocean and Mediterranean Sea.

Atlantic Buoy	Location	Mediterranean Buoy	Location
Golfo de Cádiz	36.48° N, 6.96° W	Tarragona	40.68° N, 1.47° E
Cabo Silleiro	42.12° N, 9.43° W	Dragonera	39.56° N, 2.10° E
Villano-Sisargas	43.50° N, 9.21° W	València	39.52° N, 0.21° E
Estaca de Bares	44.12° N, 7.67° W	Cabo de Palos	37.65° N, 0.33° W
Cabo de Peñas	43.75° N, 6.16° W	Cabo de Gata	36.57° N, 2.32° W
Bilbao-Vizcaya	43.64° N, 3.05° W		



Figure 2.1. Buoys location over the surrounding seas of Iberian Peninsula.

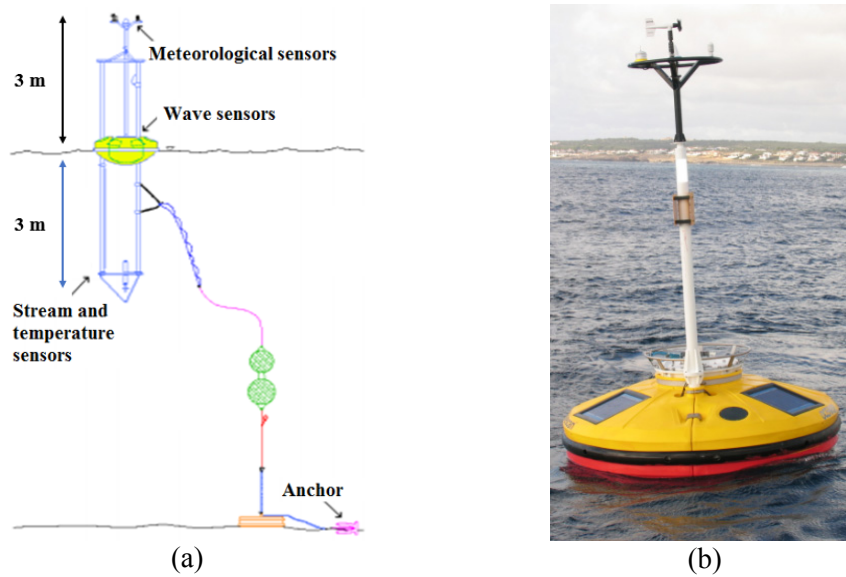


Figure 2.2. (a) Anchored buoy scheme and (b) buoy picture.

The buoys showed in Table 2.1 cover more than ten years of data, even twenty at Cádiz buoy, which is shown in real time in the web page <http://www.puertos.es/es-es/oceanografia/Paginas/portus.aspx> and can be obtained via email. In our case, only three years of data were selected, from 2012 to 2014.

2.3. SENSOR IMAGERY AND PROCESSING

Forty-four and forty-seven daytime L7 and L8 scenes, respectively, were acquired in the period between April 2013 and June 2016, around 10:45 and 11:00 UTC for Barrax and Doñana, respectively. Images were downloaded from the web page <https://earthexplorer.usgs.gov/>. MODIS data were obtained from NASA web page <https://reverb.echo.nasa.gov/reverb/>. Data used goes from January 2013 to January 2016 with more than 2,000 scenes over the Iberian Peninsula. Downloaded MODIS products include MOD02 (raw data for each band at 500 m and 1000 m), MOD03 (ancillary data), MOD07 (atmospheric data), MOD11. Finally, for SST validation, NASA product was downloaded although for years 2012 to 2014. SEVIRI data were obtained directly from the web page managed by our team (<http://ceosspain.lpi.uv.es/>), in which the LST product and ancillary data were downloaded.

For Vicarious Calibration and direct validation of temperature, Digital Count (DC) values and LST/SST product values were extracted over the pixel location of our fixed stations. For Landsat series, average values for an array of 3×3 pixels centered on the site and, for MODIS and SEVIRI, the pixel value over the site were taken in account. Moreover, SEVIRI, MODIS and L8/TIRS LST were validated in an indirect way (called cross-validation) with the AHS images or between them. In these cases, a complete LST image was produced for the validation of a large amount of pixels.

To obtain the radiance value of the raw images, Digital Counts of the ETM+ band 6, TIRS band 10 and 11 and MODIS band 29, 31 and 32 were converted to radiance units ($W \cdot \mu m^4 \cdot m^{-2} \cdot sr^{-1}$) using image metadata (gain and offset values). These radiances were used for sensors band calibration and for the estimation of LST through RTE and TES algorithm. For the other LST retrievals (SC and SW methods), and SW SST retrieval, at-sensor brightness temperatures were calculated with Planck's law although with specific band constants (k_1 and k_2) in order to avoid the error introduced by using Eq. (1.3), known as the band-pass effect (Richter and Coll, 2002, Jimenez-Muñoz and Sobrino, 2006) which will be developed in the Chapter 4. From brightness temperatures and atmospheric parameters, LST and SST can be estimated. For SEVIRI LST product, MOD11 and SST NASA product, values are extracted directly from the image, using metadata gain and offset constants. All images were visually inspected to rule out cloud contamination. Table 2.2 shows a summary of sensor characteristics and cal/val procedure.

In the case of the OLI and MODIS VNIR bands, Digital Counts were converted to Top Of Atmosphere (TOA) reflectance using image metadata (gain and offset). In the case of OLI image, a simple atmospheric correction based on the Dark Object Subtract (DOS) was performed to obtain at-surface reflectance (Chavez, 1996). For MODIS data, SMART software (Seidel et al. 2010) was used for atmospheric correction. From NDVI values, Fractional Vegetation Cover (FVC) was estimated according to Gutman and Ignatov (1998):

$$FVC = \frac{NDVI - NDVI_s}{NDVI_v - NDVI_s} \quad (2.1)$$

where $NDVI_s$ and $NDVI_v$ are representative NDVI values for bare areas and green vegetation, respectively. These values were estimated as 0.15 and 0.9, respectively. FVC values were used to obtain the surface emissivity as presented in Section 1.6. For L7, emissivity values were obtained from in-situ measurements and not from VNIR data.

Atmospheric profiles required for computation of τ , L_u , and L_d parameters (as required in the inversion of the RTE and TES algorithm) and w values (as required to apply the SC

CHAPTER 2: DATA PROCESSING

and SW algorithms) were extracted from the atmospheric data of Section 2.1 and were introduced into the MODTRAN-5 radiative transfer code (Beck et al. 1999) to obtain spectral outputs, which are finally convoluted with the spectral response function of the sensor or in-situ radiometer desired thermal band.

Table 2.2. Sensors characteristics summary including the amount of images provided over the Iberian Peninsula, the atmospheric correction applied for VC and direct-indirect validation (DIR) as well as the sensor pixel area chosen for radiance/LST extraction. M7v5 refers to MOD07 version 5, M7v6 refers to MOD07 version 6 and NCEP to reanalysis data.

Sensor	N. Images	Spatial Resolution (m)	IFOV	NE Δ T (K)	Calibration control	Atmosphere product	Pixels
SEVIRI	72 per day	3500×4500	45°	0.13 0.21	On-board	-	1×1
MODIS	5-6 per day	1000 – 4000	63°	0.05	On-board	VC – M7v6 DIR – M7v6	1×1
TIRS	1-2 per 16 days	100	7°	0.10	Vicarious On-board	VC – NCEP DIR – M7v6	3×3
ETM+	1-2 per 16 days	60	7°	0.20	Vicarious On-board	VC and DIR M7 v5, M7v6 NCEP	3×3
AHS	Campaign dependent	3–8	45°	0.25	Vicarious	DIR – M7v6 DIR – NCEP	-

2.4. RESAMPLING METHODS

Usually, TIR bands of sensors onboard satellite have spatial resolution data lower than other spectra data such as visible or near-Infrared bands. Therefore for studies with high spatial resolution requirements it is not always possible to estimate LST precisely. In the case of MODIS the spatial resolution is two or even four (for red and infrared bands) times lower than for VNIR and SWIR channels and, for L8/TIRS, it is three times lower. Therefore, it is very necessary to increase the spatial resolution of LST images in order to meet the needs of many studies (Clinton et al. 2014; Nichol et al. 2009) requiring pixel scale to identify the LST variation in agricultural or rural environments.

Downscaling refers to the process of deriving local to regional-scale information from disaggregation of a coarse spatial resolution (thermal) data to finer spatial resolution (sub-pixel temperatures) through sharpening or unmixing algorithms by using an empirical relationship between the two resolutions (Mechri et al. 2016). Different methods exist for sharpening of coarse spatial resolution data which include those based on statistical regression schemes (Kustas et al. 2003, Agam et al. 2007), data assimilation based approaches (Kallel et al. 2013), principal components analysis (Wang et al. 2015) or data fusion using multi sensor data (Zhu et al. 2010), among others. Between many statistical regression models, the NDVI-LST relationship has been commonly used for downscaling cokriging methods (Rodriguez-Galiano et al. 2012) or empirical fits (Jeganathan et al. 2011) over agricultural or urban areas.

The main advantage of statistical regression models is that it can be automatized (i.e. a classification process is not necessary), obtaining synthetic images without human interaction and based only on the image data. On the other hand, the main disadvantage of pixel decomposition with statistical regression methods is that they are not able to maintain the pixel TIR radiance unchanged (to maintain radiometry) after decomposition. Differences between coarse image and disaggregated image are always generated due to local influences and differences in soil and vegetation types, soil moisture or emissivity as well as the precision of the model used.

Between statistical regression methods, local models use relationships reduced to a local neighborhood area (size of $n \times n$ pixels) instead of global models that use the relation for the complete image and generate unique relationship between LST and other variable. The advantage of local models are that local changes have less influence in the regression and then radiometry is well maintained (Mukherjee et al. 2014). Furthermore, NDVI or other vegetation index are not completely sensible to soils, and thus to emissivity differences. For this reason, the introduction of SWIR spectra is needed for soil discrimination (Vaughan et al. 2003) and accurate LST disaggregation.

2.4.1. Nearest Neighbor Temperature Sharpening method

Here is proposed a new sharpening method called Nearest Neighbor Temperature Sharpening (NNTS) and based on the local variant model proposed by Jeganathan et al. (2011) called Temperature Sharpening (TsHARP) local variant. The difference between models lies on the relationship between NDVI and LST: while in TsHARP model the LST is estimated by ordinary least square regression, the NNTS method is based on similar pixel properties and its distance, both over an $n \times n$ area. This procedure was chosen because, sometimes, the relationship between the NDVI and LST is poor and then the LST estimation is not accurate. In this way, it is possible to apply disaggregation in

CHAPTER 2: DATA PROCESSING

presence of water body, river bed or even clouds. For more accurate predictions, SWIR spectra relation with LST was also included in the model.

In the scheme of Figure 2.3, the NNTS method procedure is explained as follows: NDVI and SWIR thin image were up-scaled to the coarse spatial resolution image, obtaining at the same time the standard deviation of each coarse pixel (and therefore assessing the purity of each coarse pixel) and the average NDVI and SWIR value of coarse pixels. Then, with LST, NDVI and SWIR images at coarse resolution, a sliding window of $N \times N$ pixels is applied to all the coarse image pixels (in our case, a window of 5×5 pixels was used). The method, from here is divided in two steps:

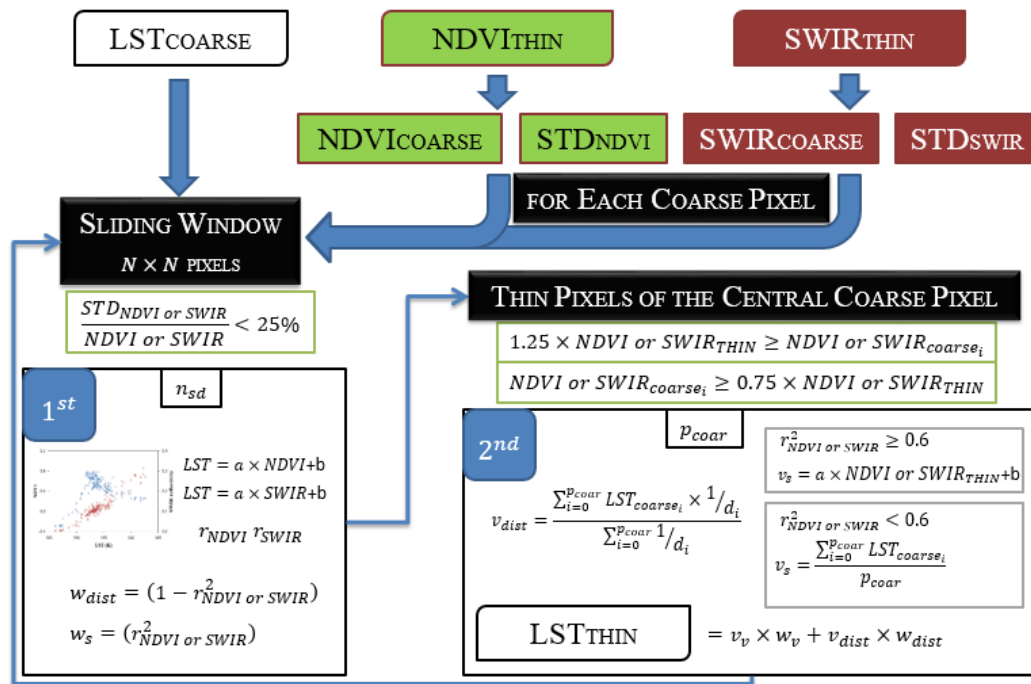


Figure 2.3. Summary scheme of the Nearest Neighbor Temperature Sharpening method. STD refers to standard deviation (σ), Thin refers to sharpened image, w_s is the similarity weight coefficient, w_{dist} is the distance weight coefficient, n_{sd} is the number of pixels taken in account for the least square regression and p_{coar} is the number of coarse pixels used for v_{dist} (LST dependent of distance) and v_s (LST dependent of pixel similitude) computation.

In the first step, only the coarse pixels in the sliding window with less than 25% of standard deviation in comparison to average value (Kustas et al. 2003) were considered (n_{sd}) for the regression, in which the correlation coefficient (r^2) for both fits (NDVI and SWIR) were obtained, selecting the highest one. Slope and intercept parameters (a and b) were also obtained for LST computation. If r^2 is high, it means that the similitude or relation between pixels is more important than the distance between them giving to similarity weight coefficient (w_s) high values ($w_s = r^2$) and to distance weight coefficient (w_{dist}) low values ($w_{dist} = 1 - r^2$). On the contrary, if r^2 is low, it means that the distance, pixel closeness, is more important than the properties similitude, giving low values for w_s and high for w_{dist} .

Once the first step is over, with the distance and similitude weight distribution, the second step consist into fill with LST values the thin pixels contained in the central coarse pixel (sub-pixels of the coarse pixel) of the $N \times N$ window. Eq. 2.2 shows how is computed the final LST for thin pixels.

$$LST_{THIN} = w_{dist} \times v_{dist} + w_s \times v_s \quad (2.2)$$

where v_{dist} is the LST value retrieved with inverse distance average values (Eq. 2.3) and v_s is LST retrieved with: a) the least square regression (Eq. 2.4.1) obtained in step one – if r^2 is higher than 0.6 – or b) simply averaging coarse values (Eq. 2.4.2). Both average equation (Eq. 2.3 and Eq. 2.4.1) are applied only for coarse pixels included in the $N \times N$ window that meet NDVI o SWIR coarse values of $\pm 25\%$ of NDVI o SWIR thin pixel value considered (p_{coar}) – the most similar coarse pixels to thin pixel.

$$v_{dist} = \frac{\sum_{i=0}^{p_{coar}} LST_{coarse_i} \times 1/d_i}{\sum_{i=0}^{p_{coar}} 1/d_i} \quad (2.3)$$

$$v_s = \begin{cases} 1. \frac{\sum_{i=0}^{p_{coar}} LST_{coarse_i}}{p_{coar}} & r_{NDVI \text{ or } SWIR}^2 < 0.6 \\ 2. a \times NDVI \text{ or } SWIR_{THIN} + b & r_{NDVI \text{ or } SWIR}^2 \geq 0.6 \end{cases} \quad (2.4)$$

Depending of r^2 results, v_s is retrieved with Eq. 2.4.1 or 2.4.2. Applying these two steps for the whole coarse image, thin LST (LST_{THIN}) can be obtained. Finally, if gaps are leaved in LST_{THIN} image when the process is over, repetition of all the method is performed increasing window size to 7×7 , 9×9 , etc. until all the gaps were filled.

2.4.2. Temperature Sharpening local variant method

The procedure of the TsHARP local variant method is similar to the NNTS method although step two is avoided and LST_{THIN} image is directly obtained from slope and intercept parameters estimated for $N \times N$ pixels window. In order to improve the method, a SWIR spectra was added additionally to NDVI and the fit with better r^2 in each window was used for the LST_{THIN} estimation. The local method can be expressed as:

$$LST_{THIN} = a \times NDVI/SWIR_{THIN} + b \quad (2.5)$$

where a and b are the slope and intercept parameters of the coarse fit window.

The mean advantage of this method is that is computationally faster than the NNTS, as it is only based on the Eq 2.5, but is less accurate on water or cloud pixels (because of the poor relationship of NDVI and SWIR parameters to LST)

2.5. CALIBRATION AND VALIDATION PROCEDURE

As was said, the goal of this thesis is to contribute to quality data control of the EOS with the cal/val activities. In this section, a summary of the process followed for VC and algorithms validation was explained.

2.5.1. Vicarious Calibration (VC)

Over the last 10-20 years VC has become widely adopted as the means to provide independent assurance of the quality of remotely sensed data from space-borne sensors. VC refers to methods that make use of natural or artificial targets of the Earth for the post-launch calibration of sensors. In TIR spectra, VC makes use of RTE to simulate the radiance of the ground/water targets on the TOA. By comparing sensor radiance and simulated radiance from VC it is possible to establish a relation between the sensor data and the simulated data that sensor should measure. The process shown in Figure 2.4 and Figure 2.5 is repeated for each sensor band, simulating in each case the radiance by the application of the band spectral response function. VC was performed over TIR bands used for temperature retrievals on ETM+, TIRS and MODIS sensors.

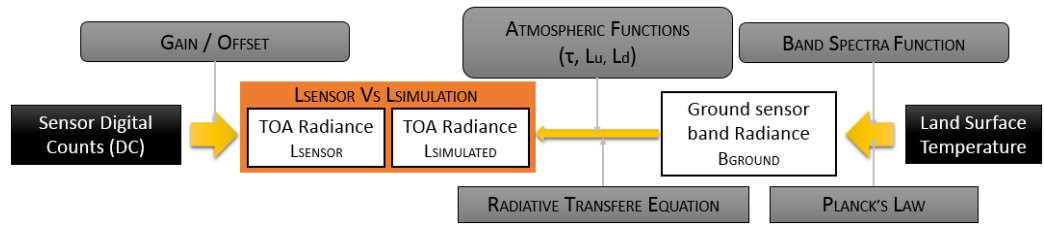


Figure 2.4. Scheme of the VC procedure over ground test sites.

2.5.2. Temperature Validation

Unlike the VC which is focused on the raw data provided by sensors, validation is a main way to prove algorithm usefulness for the retrieval of bio-physical parameters. In our case, the algorithm analysis was focused on the temperature retrievals which were tested in two ways: direct validation and indirect validation.

- Direct Validation is the comparison of satellite LST or SST products with ground or sea true temperature values. Combination of atmospheres, algorithms and sensors for satellite LST retrieval is shown in Figure 2.5.
- Indirect Validation (or cross-validation) is the comparison of satellite LST products with ground temperature values measured with airborne or satelliteborne sensors. Cross-validation was performed mainly with the AHS sensor over TIRS, MODIS and SEVIRI sensors. The Figure 2.8 shows the procedure for cross-validation, which includes algorithms, sensors and sharpening procedures used in this work.

The main advantage of indirect validation is that it is possible to validate the algorithm over a large amount of different kind of pixels in the same image which is not always possible for the in-situ validation. Another advantage is that the atmospheric effect is reduced by the use of the same atmospheric profile - totally in the case of satelliteborne-satelliteborne validation or partially in the case of airborne-satelliteborne validation) for the sensors considered in the cross-validation. In the case of AHS, the sensor takes measurements at 3 km a.s.l. approximately which implies the share of this atmospheric path.

The mean disadvantages of the indirect validation are the up-scaling process and the geo-reference between the sensors.

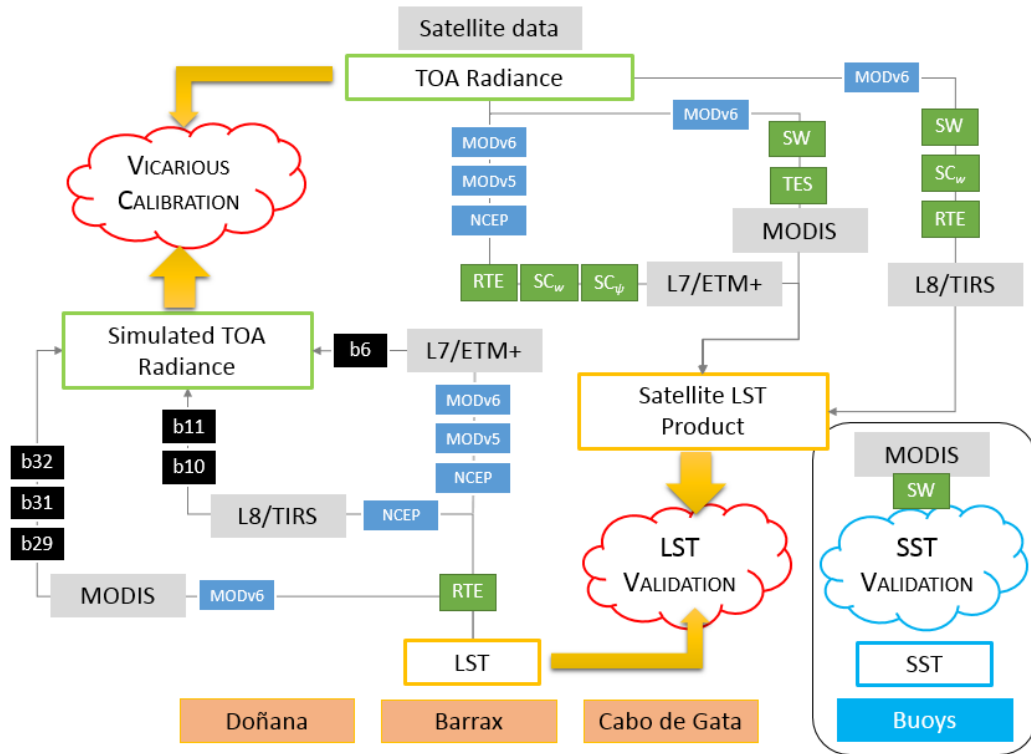


Figure 2.5. Steps followed for the VC (left) and the LST-SST (right) validation. Colors are referred to a combination of atmospheric profile (blue), algorithm (green) and sensor (grey) used for the LST estimation. In the case of VC, the black boxes symbolizes sensor bands.

In the up-scaling process, it is not always clear how to combine the different pixels in order to obtain a coarse pixel. Usually a Gaussian function or a simple average are used for this purpose. Another problem is that the high spatial resolution pixels not always fit with the size of coarse pixel so that the final values are disturbed by outside pixels. In our case, to partially avoid this problems, for high amount of thin pixels the Gaussian function was used for coarse pixel simulation (see Figure 2.6).

Sensor geo-location are designed to enable pixel position with a certain accuracy. In the case of MODIS, the geo-location accuracy is approximately 50 m at nadir (Wolfe et al. 2002) and on L8/TIRS is about 10 m (Storey et al. 2014). This leads to an uncertainty in the up-scaling process because the retrieved coarse pixel is contaminated with stray pixels or some ‘good pixels’ are not included in the simulated pixel.

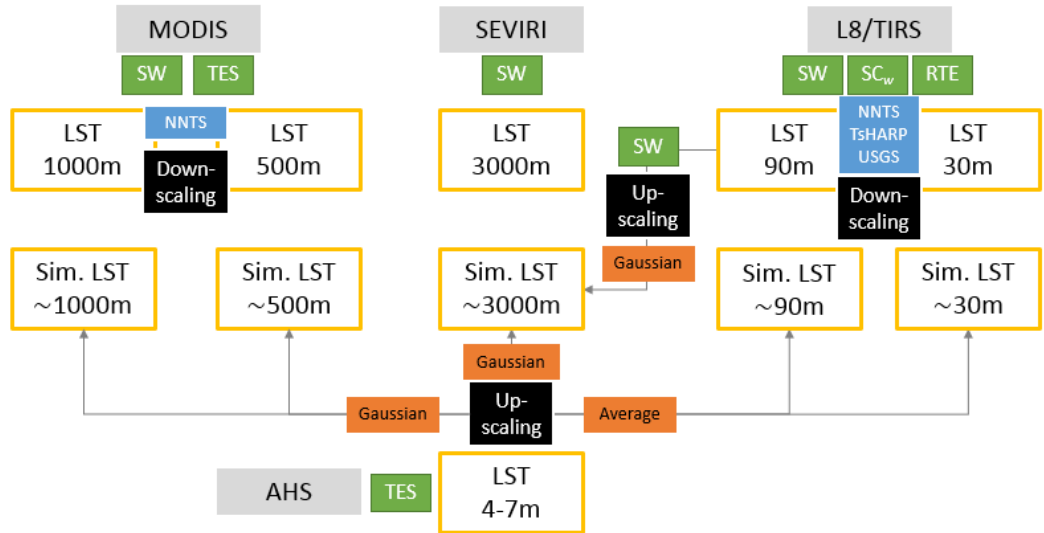


Figure 2.6. Scheme of cross-validation process which includes description of up-scaling process (in orange the function used for simulation of coarse pixel), and of down-scaling procedure (in blue). In yellow boxes, sensor spatial resolution and simulated spatial resolution are shown.

CHAPTER 3:

PERMANENT STATIONS AND FIELD CAMPAIGNS

In-situ data measurements are a key procedure for the development of cal/val activities. The accuracy of VC and validation process is strongly related to the validity of the in-situ data. For this reason, in this Chapter a wide description of the permanent stations for in-situ measurements as well as data processing, are described. Field campaigns – in the framework of Calibration of Earth Observation Satellites in SPAIN (CEOS-SPAIN) project – are also described as part of indirect validation and complementary and necessary information for LST estimation.

CHAPTER 3: PERMANENT STATIONS AND FIELD CAMPAIGNS

3.1. TEST SITES

Three test sites were considered for permanent cal/val activities plus one for indirect validation. All of them are situated in the Iberian Peninsula and have different characteristics in terms of surface covers and sizes of the samples which make them useful for the cal/val of a wide range of sensors. The sites considered are: i) the agricultural area of Barrax (Albacete; 39°N, 2°W, 700 m a.s.l.), ii) the Doñana National Park (Huelva; 37° N, 6°25' W, sea level), iii) Cabo de Gata National Park (Almería, 37° N, 2° W, 100 m a.s.l.) and the Miajadas area in Extremadura (Caceres, 40° N, 5°46' W, 250 m a.s.l.). The location and the plots of the permanent areas for cal/val are shown in the Figure 3.1.

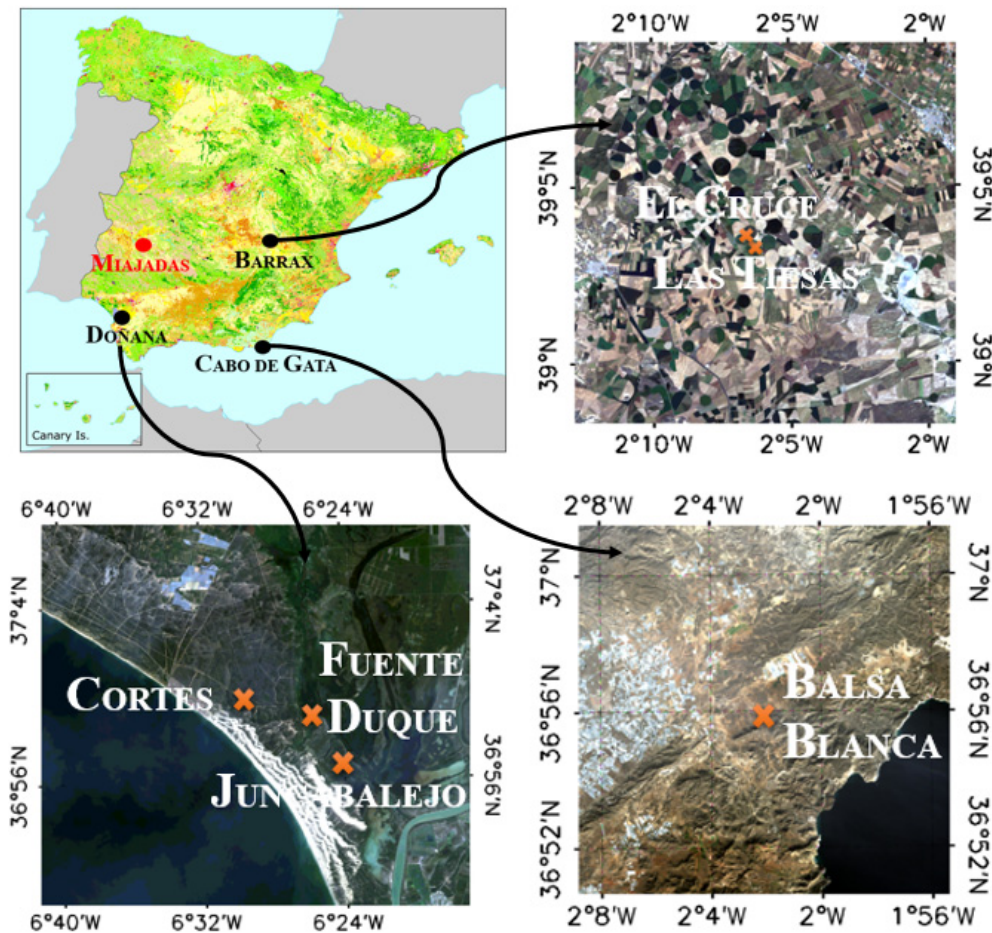


Figure 3.1. Test site location over Landsat images and Iberian Peninsula map.

3.1.1. Barrax

Barrax area has been selected in many field campaigns since year 2002 for cal/val activities because of its flat terrain and the presence of large, uniform land-use units (approximately 100 ha), suitable for validating moderate resolution satellite image products. Most of the area is cultivated and includes dry land (e.g. winter cereals, fallow) and irrigated land (e.g. corn, alfalfa, vegetables). In winter, the major part of the surface is not cultivated and a wide extension of bare soil (Inceptisols in terms of soil taxonomy) are available for cal/val of low spatial resolution sensors. Barrax has a Mediterranean-type climate, with heavy rainfall in spring and autumn and lighter rainfall in summer. It presents a continental climate, with sudden changes from cold months to warm months and high thermal oscillations in all seasons between maximum and minimum daily temperatures.

Specifically, two plots were considered for the installation of the fixed stations: a green grass terrain (in which El Cruce station lays) that covers an area of 120 m × 200 m and is located at 39.061° N, 2.099° W; and a bare soil or crop cover (depending on season and in which Las Tiasas station lays) which is located at 39.059° N, 2.099° W and covers a circular area of 1 km of diameter. On both sites, fixed station have been installed for continuous LST measurements and other variables as air temperature, energy fluxes or soil moisture.

3.1.2. Doñana

Doñana National Park is located in South Western Spain near the Atlantic Ocean coast. The Doñana Biological Reserve is a scientific and technological infrastructure located inside Doñana National Park, and it operates different meteorological stations and scientific instrumentation for the long-term monitoring of different geo-biophysical parameters. Approximately half of its area is marshland and it includes also areas covered by bushes, pine forest and sand dunes, in addition to small lagoons. The marshes undergo a yearly cycle of inundation in autumn and drying out during the spring season and its flood extension varies considerably between years depending on the precipitation. The topography of the marshes is extremely flat, with a maximum elevation difference of 2.5 m.

Three plots were considered in Doñana National Park for the installation of fixed stations: two marshland areas (Fuente Duque: 36.998° N, 6.434° W and Juncabalejo: 36.946° N, 6.389° W), with a huge and uniform extension covered with senescent or green

CHAPTER 3: PERMANENT STATIONS AND FIELD CAMPAIGNS

vegetation, bare soil or water (depending of season); and a pine forest area (Cortes: 36.996° N, 6.513° W) that covers an extension of 2.5 km × 3 km. In all of them continuous LST measurements were taken with one or more radiometers.

3.1.3. Cabo de Gata

Cabo de Gata National Park is located in Southern Spain near the Mediterranean Sea. Of volcanic origin and an extension of 38,000 ha, the park is characterized by a semi-arid climate with low rainfall (approximately 400 mm year⁻¹). Balsa Blanca field is located 6 km from the coast with surface cover characterized by perennial vegetation (green in rainfall periods and senescent in summer) and bare soil which covers approximately 40% of the field extension (Morillas et al. 2013).

A plot that covers approximately 4 km × 4 km has been considered for the installation of a fixed station (Balsa Blanca: 36.939° N, 2.034° W).

3.1.4. Miajadas

The test site is located in La dehesa Extremeña. La dehesa is a clear forest of holm oak, cork oak and other species, with a grassland and bush soil cover. The forest is an ecosystem derived of the human activity which is destined to pastureland. Because of its heterogeneity characteristics (lack of wide clears and tree random distribution), the site has not been taken in account for the installation of permanent stations. However, it was included in the work because of the airborne data obtained during a field campaign.

3.2. INSTRUMENT SET UP AND FIXED STATIONS

Many instruments have been used for the in-situ measurements as part of the fixed stations or as a complement for field campaigns measurements. Only the instruments used for the aim of this thesis are described although additional instruments have been installed on the test sites. Figure 3.2 show these instruments which are listed as:

- Datalogger: It is a kind of multiplexor that measures electrical signals and converts the measurements to engineering units, performs calculations and reduces acquired data to statistical values. This data acquisition system provides data files easier to ingest in a PC.

- Thermal Radiometers: The thermal radiometers were used for the brightness temperature measurements at ground level. These are a single-band radiometers with spectral range from 8 μm to 14 μm (see Figure 3.3). The IR120 and the Apogee SI100 radiometer have a wider field of view (20° half-angle) with an operative range of temperatures from -25°C to $+60^\circ\text{C}$. Some of these instruments – as the Apogee handheld radiometer (see Figure 3.2d) – can display and save the temperature measurements so that they can be used for field campaigns.
- Flux Radiometers: The NR01 measures the 4 separate components of the surface radiation balance. It uses pyranometers to measure the solar radiation (global and reflected radiation) and pyrgeometers to measure the infrared radiation (emitted by the sky and emitted by the ground). The pyranometers measures the solar radiation flux from a field of view of 180° and has a spectral response from 0.3 μm to 2.8 μm . The pyrgeometers measure the far infra-red radiation flux from a field of view of 180° and has a spectral response from 4.5 μm to 50 μm . The upper pyrgeometer was used for L_d estimations.
- Temperature and Humidity: the HMP45C sound contains a platinum resistance temperature detector and a capacitive relative humidity sensor. The temperature sensor has a measurement range (-40° to $+60^\circ$) with a max accuracy of $+0.4^\circ\text{C}$. The relative humidity sensor has an accuracy of $+3\%$. Downward radiance can be estimated with the temperature and humidity data using the down-welling equation proposed by Prata (1996).
- GPS: The GPS16-HVS sensor, manufactured by Garmin, consisted of a receiver and an integrated GPS antenna. It receives signals from Global Positioning System (GPS) satellites, and then uses the signals to calculate its position and velocity.
- Multiband Radiometer: The CIMEL model CE312-2 ASTER is a radiance-based thermal-infrared radiometer composed of an optical head and a data storage unit. The CE312-2 detector includes 6 bands, a wide one, and five narrower filters, (see Figure 3.3). Temperature and emissivity values can be estimated from this instrument.

Many of those instruments were installed in the fixed stations as part of the Calibration of Earth Observation Satellites in SPAIN project, funded by the Spanish economy and competitiveness department. To ensure their correct performance, the instruments are calibrated every two years (as manufacturer recommends) in the Global Unit Change (GCU) laboratory.

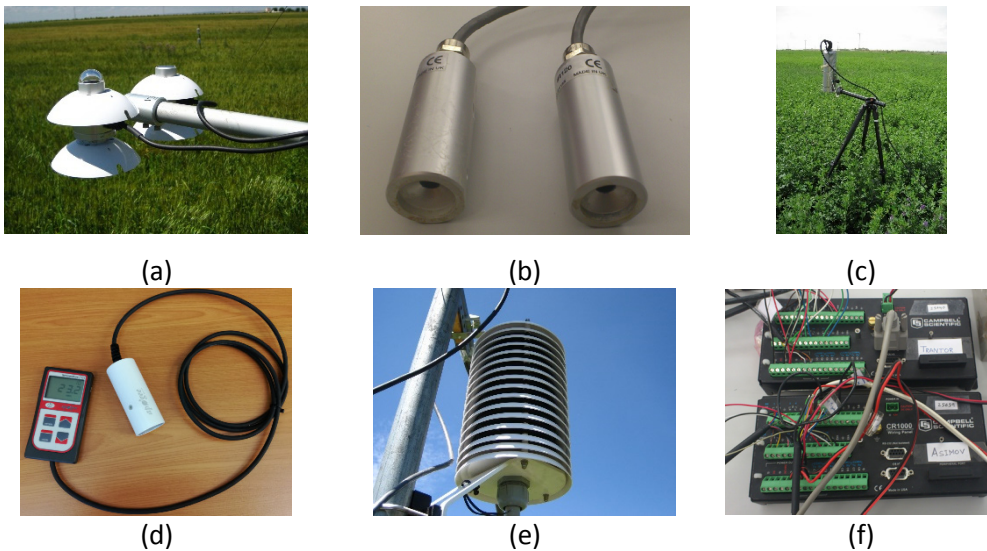


Figure 3.2. Images of the instruments described above: (a) Flux Radiometers NR01, (b) IR120 broadband radiometer, (c) CIMEL CE312-2 multiband radiometer, (d) Apogee handheld broadband radiometer, (e) HMP45C temperature and humidity cover and (f) datalogger.

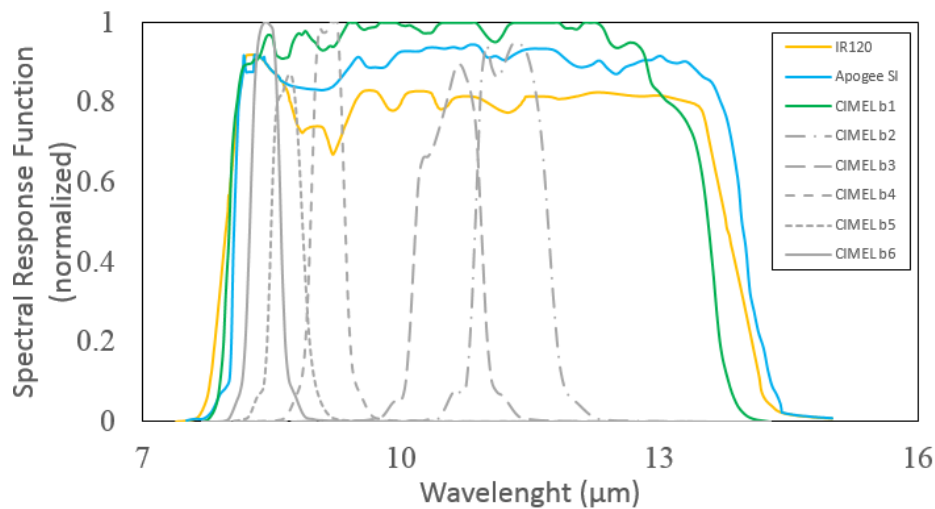


Figure 3.3. Normalized spectral response functions for the thermal bands of the IR120, CIMEL CE312-2 and Apogee handheld radiometers. In color, broadband spectral response functions are plotted.

3.3. PERMANENT STATIONS SET UP AND DATA

From year 2011 to current date, six fixed stations have been set up in order to provide continuous LST measurements for cal/val purposes. The stations, introduced in the Section 3.1, obtain data over different plots trying to encompass as many ground surfaces as possible and to be representative of as many spatial resolutions as possible. Each station has its particularities: changes in the land cover (and then in emissivity), atmospheric conditions, or more or less instruments for LST retrieval. These influences are important in quality of the obtained data and in data uncertainties which will be analyzed in the next chapter. Images of the fixed stations can be found in Figure 3.4.

3.3.1. Stations characteristics

The instruments installed at the fixed stations and the LST measurements timeline of each station are resumed in the Table 3.1 and Figure 3.5, respectively. A brief description of the stations is provided:

- Fuente Duque station (Doñana) was the first one to be installed at the beginning of year 2011 (January 10). Initially, the station included one radiometer for LST measurements, although in the next years the number of radiometers was extended to four and a NDVI sensor was added. Currently the sensors cover is about 5 m² and data are obtained through the mobile web.
- Juncabalejo station (Doñana) was set up on September 10 of year 2014. The station has one radiometer (covering an area of 2 m²) that provides data through the mobile web.
- Three radiometers were installed at Cortes station (Doñana) on April 8, 2014. The station, which takes additional measurements as NDVI, solar radiation and air humidity and temperature, provides LST values covering an area of 5 m². As the above stations, data are received directly through the mobile web.
- El Cruce station (Barrax) is a mobile mast which was installed on June 30, 2011 over the grass field but, during the next two years, the mast was moved to Las Tias location during crop harvesting period (from April to July). From year 2014, the station remains fixed over grass field. This station provides LST with one radiometer among other variables as wind direction and speed, soil flux, moisture and temperature, air humidity, air temperature as well as net radiation. LST measurement footprint is around 1 m² and the data are obtained from direct download to a dedicated computer.

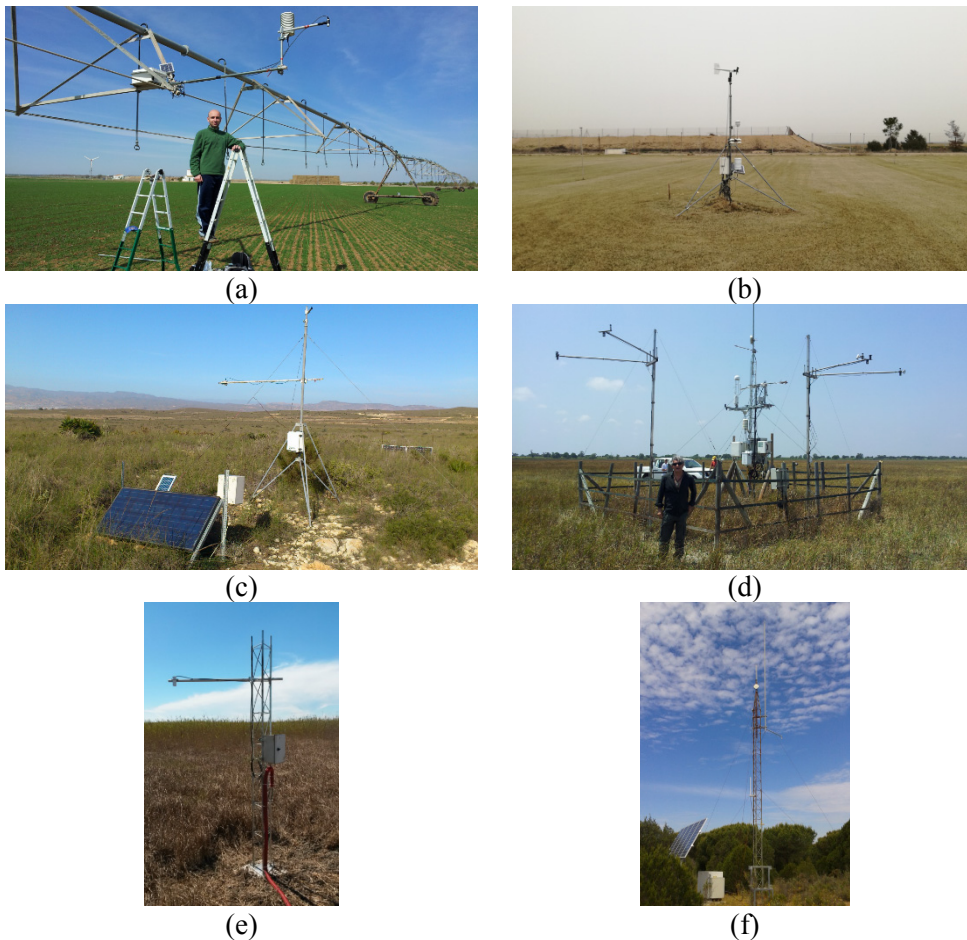


Figure 3.4. (a) Las Tiasas, (b) El Cruce, (c) Balsa Blanca, (d) Fuente Duque, (e) Juncabalejo and (f) Cortes stations.

- Las Tiasas station (Barrax) was installed permanently on April 2, 2014 over the arm of an irrigation pivot. Because the pivot spins for irrigation purposes, the station is continuously changing its location. For this reason, additionally to the air temperature and humidity sensor, a GPS was installed to track the location of the station. One radiometer with a footprint of 3 m^2 is measuring the LST. As in El Cruce station, data are downloaded to a computer.
- Balsa Blanca station (Cabo de Gata) was the last one installed on December 16, 2015. Taking advantage of the bare mast available in the area, a radiometer with a footprint of 2 m^2 was installed for LST purposes. Additionally to the radiometer, air temperature, air humidity sensor as well as soil temperature and

CHAPTER 3: PERMANENT STATIONS AND FIELD CAMPAIGNS

humidity instrumental are available. Data are received via email through Almería University personal.

In all the stations, the measurements of the radiometers are performed every 10 seconds, storing mean measured data in the datalogger every 5 min.

Table 3.1. Summary of the instruments installed in our test sites.

Station	n° Radio meters	Flux	Temp & humidity	Others
El Cruce	1	Yes	Yes	Wind direction and speed Soil flux, moisture and temperature
Las Tiasas	1	No	Yes	GPS
Fuente Duque	4	No	No	NDVI
Juncabalejo	1	No	No	
Cortes	2	No	Yes	NDVI
Balsa Blanca	1	No	Yes	Soil temperature and moisture

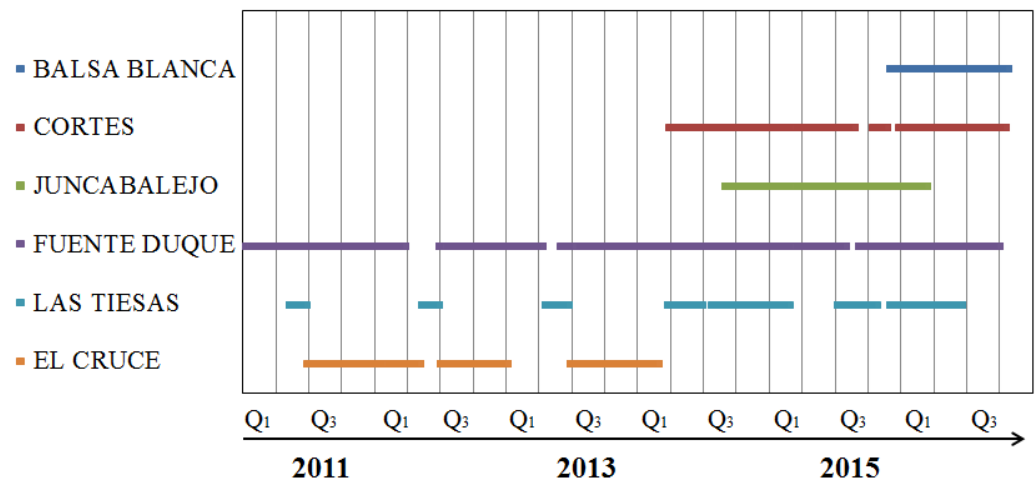


Figure 3.5. Timeline of LST measurements on Balsa Blanca, Cortes, Juncabalejo, Fuente Duque, Las Tiasas and El Cruce stations.

3.3.2. Data quality control

Data obtained through datalogger are stored in a raw database sorted by years and stations. To transform this data from engineering units to physical variables and in order to control the quality of data, a specific program made in C++ programming environment by our team is used for these purposes. The program, called Station Data Quality and Control (StaDa QC) is divided in two parts, and is able to validate and generate a processed station database.

The first program is designed to sort variables and dates, to include LSE values (which are not included into the datalogger file) to perform a preliminary data check. The program store data in text files with physical variables and units, and an alphabetic code describing its quality. It can detect and solve possible problems with repetition or date gap ensuring in this way the uniformity of the text file. Values are labeled with specific letters that have different meanings; letter 'a' means that the measurement is correct; 'b' means that the measurement is correct but that the standard deviation of the averaged five minutes is higher than 2 K; 'c' means that the measurement is correct but it was performed in a low battery condition. Finally, the program can calculate hourly and daily averages for each station (see Figure 3.6).

The second part is a graphic interface that allows plotting and visualizing all station data. The program shows the five minute data for visual validation. The wrong or suspected to be wrong values can be 'erased' with the program by the direct selection of given values. The 'erase' procedure means that the alphabetic code of the selected value is changed for new letters; 'o', 'p' and 'q' are the opposite letters of 'a', 'b' and 'c' code, respectively. Once the code is changed (it can be undone if necessary), the values marked as 'erase' data are not used for cal/val activities and for average computation. This graphic interface allows an easy, quick and secure way for data validation (see Figure 3.7). If necessary, it is possible to activate the automatic detection tool for abnormal data which can control as an example very high values, inconsistency between data obtained from past periods or changes from standard behavior. After this process control, data are finally ready to use.

CHAPTER 3: PERMANENT STATIONS AND FIELD CAMPAIGNS

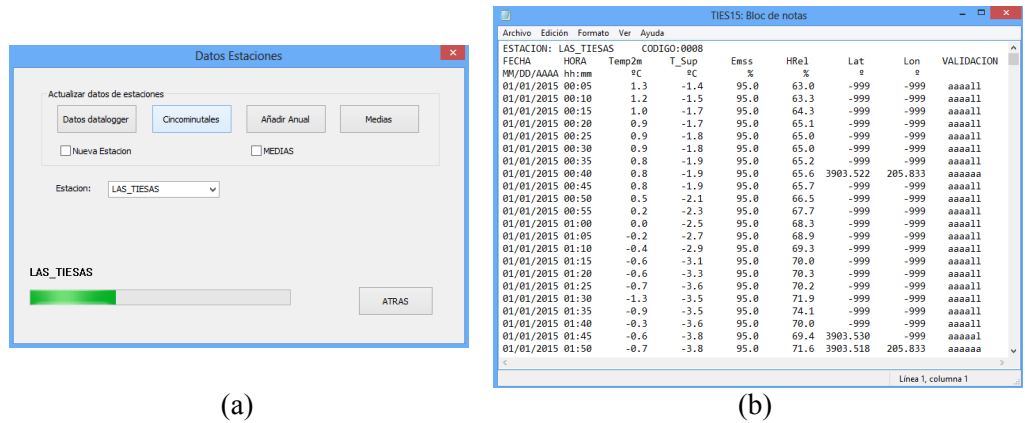


Figure 3.6. Screenshot of the: (a) StaDa QC software and (b) annual txt file generated for Las Tiesas station (2015).

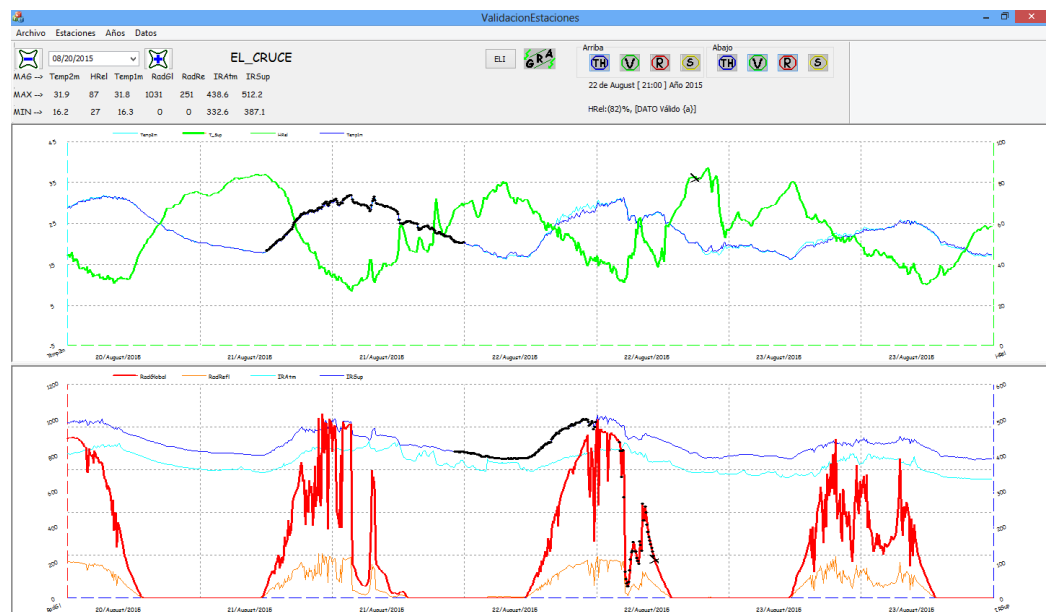


Figure 3.7. Screenshot of the graphic interface included in the StaDa QC software where graphic black points symbolizes data selected for its deletion.

3.4. FIELD CAMPAIGNS

3.4.1. Airborne campaigns

During the CEOS-SPAIN project, five field campaigns with different purposes were performed with the AHS sensor in our test sites (except for Cabo de Gata because of technical problems in the aircraft). The campaigns were designed for cross-validation and ground homogeneity LST purposes – among others that are not taken in account in this work – in which the flight lines (see Figure 3.8) tried to encompass as much test site area as possible. For these reasons, the spatial resolution of the AHS images has a test site dependence. In Table 3.2 information about the field campaigns can be found (only the days used in this thesis). Barrax, Miajadas, Almeria and Doñana – only the year 2013 – campaigns were used for homogeneity LST analysis while Doñana and Miajadas campaigns were used for indirect validation of LST.

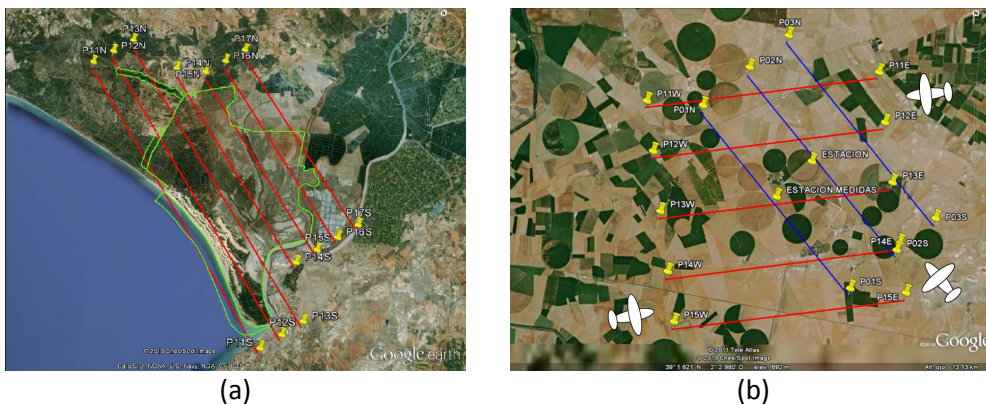


Figure 3.8. Example of flight lines over (a) Doñana on May 7, 2013 and (b) Barrax on June 12, 2011 field campaigns.

Additionally to AHS data, ground measurements were taken simultaneously to airborne pass in order to validate the LST product retrieved from the AHS sensor, to characterize the emissivity of the ground covers. Instruments described above, especially the CIMEL radiometer and the Apogee handheld radiometer, were used for these purposes because of its practicality and mobility. With the CIMEL radiometer, it was possible to retrieve the emissivity with the use of the TES algorithm while the handheld radiometers were used for transects.

Table 3.2. Sensor characteristics summary including the amount of images provided over the Iberian Peninsula and the atmospheric correction applied for cal/val.

Test site	Year	Date	UTC Time	Images Number	Spatial Resolution	Max image size (Km)
Barrax	2011	June 12	09:00-10:20	8	4 m	8.0 × 2.8
		June 13	01:00-02:00	6		
Barrax	2012	July 25	08:40-09:40	8	4 m	16.0 × 2.8
			21:30-22:40	6		
Miajadas	2012	October 04	11:00-13:00	12	4 m	16.0 × 2.8
Almeria	2013	May 28	11:00-12:00	7	4 m	16.0 × 2.8
Doñana	2013	May 07	10:40-12:10	9	7 m	52.0 × 7.0
Doñana	2015	May 11	10:10-12:10	8	7 m	70.0 × 7.0

3.4.2. LSE and LST homogeneity campaigns

Because emissivity is a key factor for LST retrieval, dedicated field campaigns have been performed during these years in order to characterize land surface emissivity. For this purpose, regular measurements with CIMEL radiometer and photos with the land cover evolution have been realized in our test sites. Figure 3.9 shows the evolution of the LSE during the year 2014 for our stations. While in some stations – Cortes and Balsa Blanca – the LSE is quasi-constant, in others it depends of the period considered and it can change dramatically, such as at Las Tiesas during harvest (in July).

To see more clearly this land cover evolution and the importance of the need of the field campaigns for LSE evolution, Figures 3.10, 3.11 and 3.12 show the evolution (through images) of the fallow-crop land, marshland and grass land covers, respectively.

The cover and Land Surface Emissivity of Las Tiesas station changes along with agricultural needs. Half of the year the cover remains fallow and the access to the station is easy. The other half, when crops covers station area, the emissivity increases with green cover (NDVI). At El Cruce, the emissivity remains constant while the grass cover remains green. When cold temperatures come, the grass turns senescent and LSE decreases to values of 0.96.

CHAPTER 3: PERMANENT STATIONS AND FIELD CAMPAIGNS

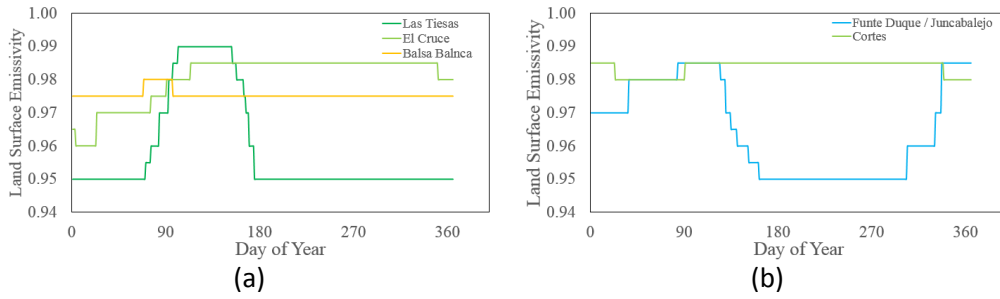


Figure 3.9. LSE evolution of our fixed stations during year 2014. Values were obtained with the CIMEL broadband radiometer.

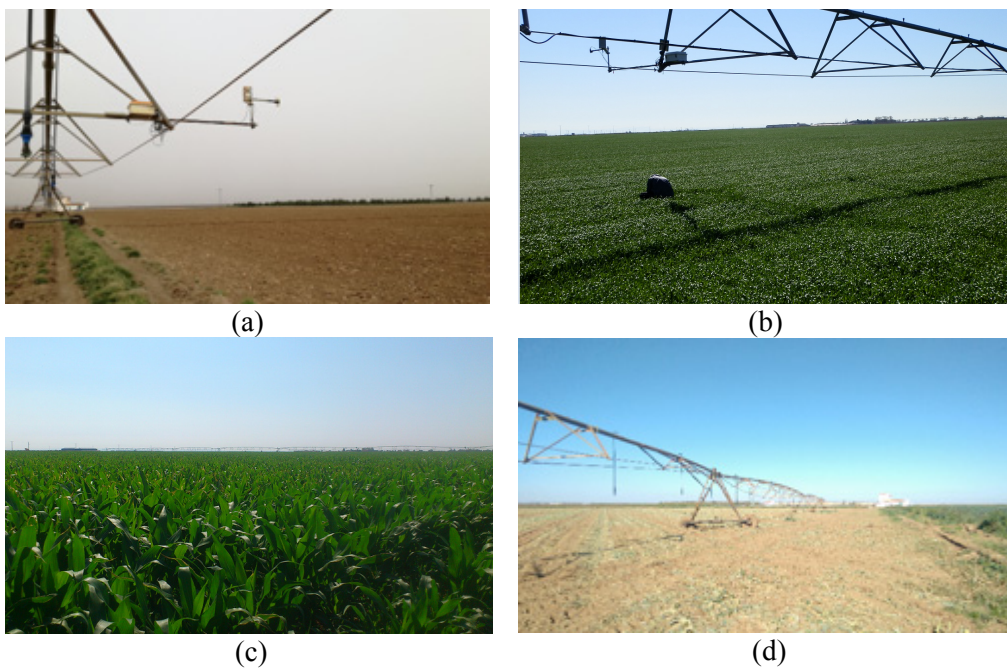


Figure 3.10. Evolution of the fallow-crop land during year 2015: (a) February, (b) May, (c) August and (d) December.

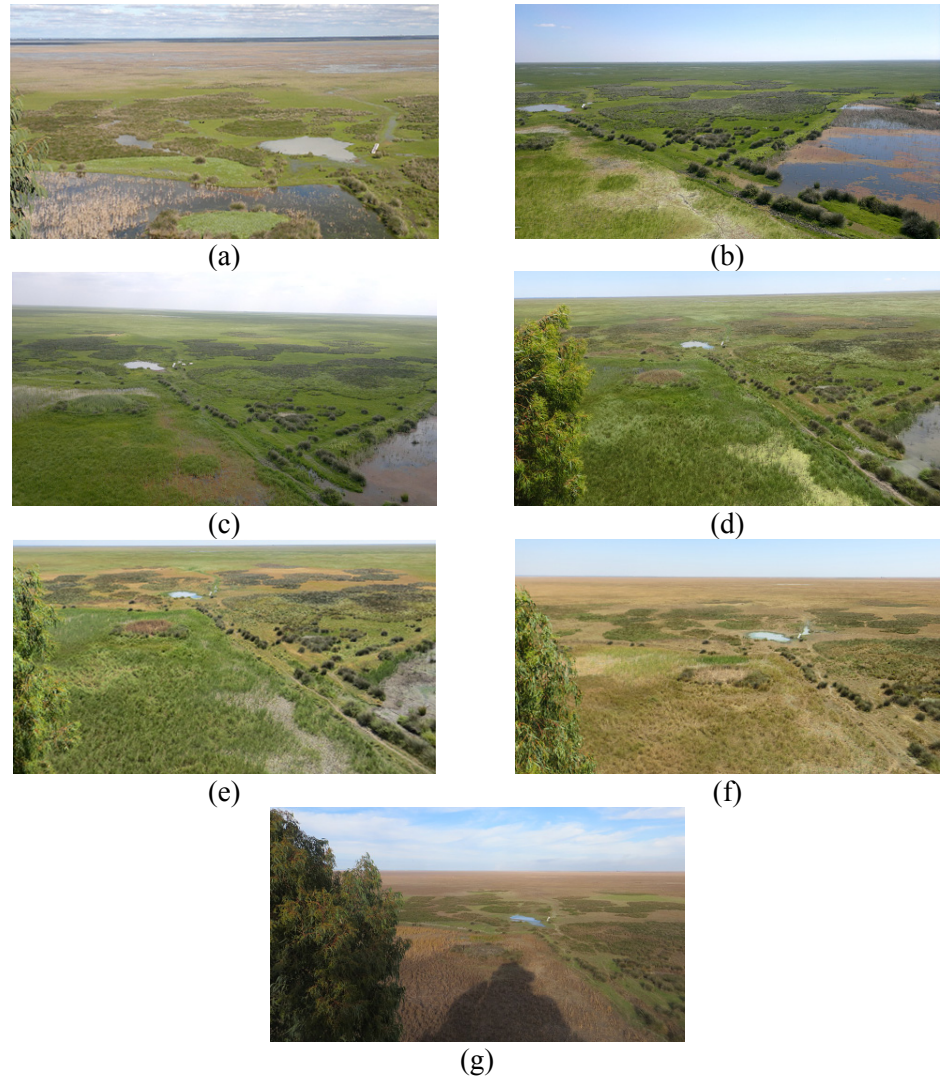


Figure 3.11. Evolution of the marshland during year 2014: (a) February, (b) March, (c) April (d) May, (e) Jun, (f) August and (g) November.

The marshland evolution highly depends of the flood periods and in the case of Figure 3.11, this period starts before February flooding the senescent vegetation that lives in the area. As time goes, the water cover diminishes and the vegetation turns green. Finally, in the beginning of summer, the senescent vegetation starts to cover once again the marshland. Only in this summer-autumn periods it is possible to access the marshland stations.



Figure 3.12. Grass plot evolution during the year: (a) April-December, (b) January-March.

Additionally to the LSE, LST homogeneity was monitored for each campaign. With the Apogee handheld radiometer – which can store one hundred measurements – transects around the station were performed covering an area no superior to $100 \times 100 \text{ m}^2$. With these measurements, it was possible to retrieve the inhomogeneity (INH) index of the area near the station that, in most of the cases, represents the pixel size of a high-medium spatial resolution sensor. Temperature measurements were realized in different seasons in order to check the representativeness of the area for cal/val activities. Figure 3.13 shows, as an example, transect performed around El Cruce station on Barrax.

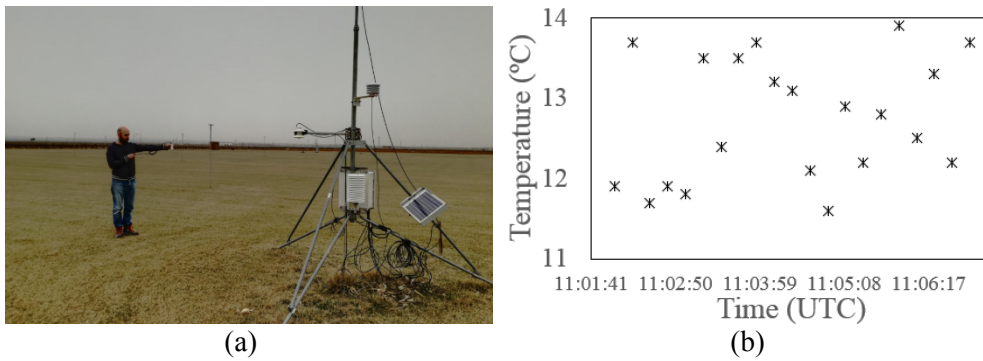


Figure 3.13. (a) Image of transect performed on February, 2016 and (b) the results obtained.

CHAPTER 4: UNCERTAINTY OF IN-SITU MEASUREMENTS

In-situ LST cannot be measured directly with radiometers because complementary information and data processing are required. In this chapter, the influence of each component for LST retrieval process was analyzed. Pass band effect, uncertainty of emissivity, down-welling radiance retrieval and additional influences from radiometer calibration or LST heterogeneity have been studied. Finally, LST measurements uncertainty is provided for each station.

4.1. LST RETRIEVAL FOR IN-SITU MEASUREMENTS

In Chapter one, RTE was introduced as a way to estimate TIR radiance coming from the ground at the TOA level. At few meters above ground level, RTE can be used for radiance estimation although with the inclusion of one assumption: the atmosphere between ground and radiometer is negligible. This is true for our fix measurements in which the radiance path to the radiometer is less than a few meters. This ‘null’ atmosphere implies two approximations of RTE: atmospheric emission in the upward direction (L_u) is zero and atmospheric transmissivity (τ) is set to one. Therefore, with these assumptions, for radiometers that take measurements at ground level, the RTE can be expressed as:

$$L_{RAD,\lambda} = [\varepsilon_\lambda B_{LST,\lambda} + (1 - \varepsilon_\lambda)L_{d,\lambda}] \quad (4.1)$$

where L_{RAD} is the TIR radiance registered by the radiometer, B_{LST} is the black body radiance emitted by the surface and $(1 - \varepsilon)L_d$ is the reflected down-welling radiance emitted by the atmosphere. Retrieving B_{LST} and, by Planck’s law, LST is obtained. Scheme describing the different contributions of radiometer measurements are shown in the Figure 4.1.

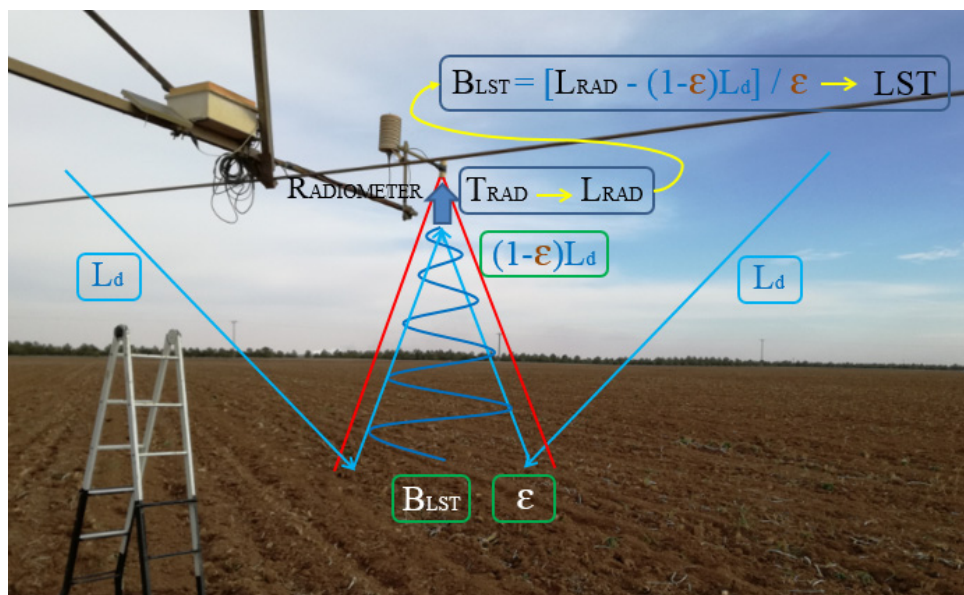


Figure 4.1. Graphic description of sources that influence radiance measurements performed by radiometer at surface level.

4.2. PASS BAND EFFECT

LST is obtained from B_{LST} by inversion of Planck’s law (see Eq. 1.1) using the effective wavelength calculated with the following expression:

$$\lambda_{eff} = \frac{\int \lambda f(\lambda) d\lambda}{\int f(\lambda) d\lambda} \quad (4.2)$$

where λ are the wavelengths included in the filter function and $f(\lambda)$ is the response of the filter to a given λ . The use of the effective wavelength in order to simplify the calculus instead of the sensor filter function generates an error in LST estimation. This error increases when the Full Width Half-Maximum (FWHM) value of the filter function is wider (Jimenez-Muñoz and Sobrino, 2006). It should be noted that this error can be avoided if the filter functions of the sensor are known, however, in some cases (as broadband radiometers) the filter functions are not available.

In order to convert temperature to radiance and vice versa avoiding the use of Eq. 4.2, radiance values were simulated for each temperature with steps of 0.1 K in a range of 260 – 330 K for filter function of in-situ radiometers and for MODIS bands 29, 31 and 32 (see Figure 4.2). Fitting those simulations to Planck’s law structure, specific constants have been retrieved for Temperature-Radiance conversion. Table 4.1 shows k_1 and k_2 constants retrieved for each filter function. Landsat ETM+ and TIRS thermal bands functions were directly copied from the Landsat handbook. For even more precise conversion, values retrieved in Figure 4.2 can be directly used.

Table 4.1. Specific constants (k_1 and k_2) retrieved for Planck’s law to avoid the pass-band effect. Landsat constants have been extracted from Landsat handbook.

Sensor	Band	k_1	k_2	Planck’s law
L8 TIRS	b10	774.89	1321.08	$T_B = \frac{k_2}{\ln(k_1/L_{sen} + 1)}$
	b11	480.89	1201.14	
L7 ETM+	b6	666.09	1282.71	
MODIS	b29	2699.35	1692.65	$T_B = \frac{k_2}{\ln(k_1/L_{sen})}$
MODIS	b31	789.37	1323.71	
MODIS	b32	518.15	1217.83	
IR120 Campbell	broadband	1169.58	1448.68	
SI100 Apogee	broadband	1080.69	1425.32	

CHAPTER 4: UNCERTAINTY OF IN-SITU MEASUREMENTS

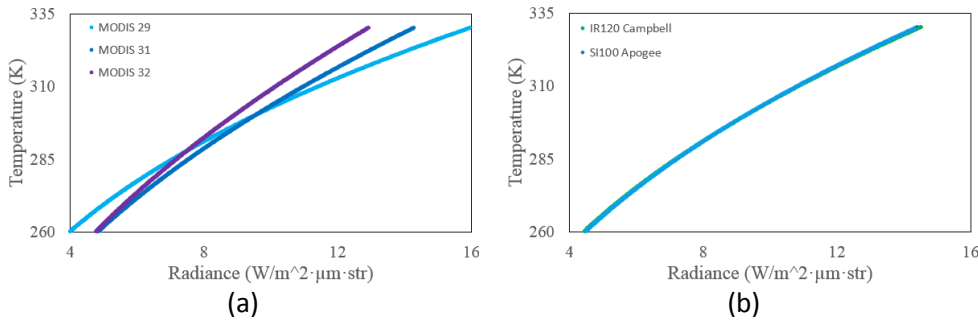


Figure 4.2. Temperature – Radiance conversion for (a) MODIS bands and (b) broadband radiometers.

By not using k_1 and k_2 constants, we introduces an inaccuracy in Temperature-Radiance conversion of -0.2 K to -3.0 K, depending of the FWHM width (if we compare the temperature obtained of Planck’s law with specific constants minus Planck’s law with effective wavelength). Table 4.2 shows the uncertainty associated to the pass band effect for a broadband (8-14 μm) and some narrow function filters (sensor filters). Note that the uncertainty associated is an accuracy problem that leads always to an overestimation of temperature. Broadband radiometers are the most affected by pass band effect as it is shown in Table 4.2.

Table 4.2. Pass band effect for broadband radiometers and some TIR sensor bands. Results are expressed in radiances (temperatures in brackets).

LST	Pass band effect $\text{W/m}^2 \cdot \text{str} \cdot \mu\text{m}$ (K)				
	8-14 μm	b6 ETM+	b10 TIRS	b11 TIRS	b29 MODIS
280	-0.386 (-3.14)	-0.037 (-0.33)	-0.020 (-0.17)	-0.021 (-0.20)	-0.021 (-0.15)
300	-0.287 (-1.89)	-0.038 (-0.28)	-0.024 (-0.17)	-0.023 (-0.19)	-0.021 (-0.15)
320	-0.067 (-0.37)	-0.036 (-0.23)	-0.028 (-0.17)	-0.025 (-0.18)	-0.021 (-0.15)

However, in the process of conversion from radiometer temperature (T_{RAD}) to radiometer radiance (L_{RAD}) and vice versa (B_{LST} to LST) – once the Eq. 4.1 is applied to correct emissivity and atmospheric effects (see Figure 4.1) – it may seem that the pass band effect is annulled and no uncertainty is associated to LST (because of the double conversion). In spite of this double radiance-temperature conversion, the use of the

CHAPTER 4: UNCERTAINTY OF IN-SITU MEASUREMENTS

effective wavelength leads to an inaccuracy – overestimation of LST – of -0.1 to -0.4 K as is shown in Table 4.3 and Figure 4.3.

Table 4.3. Differences in the conversion process of brightness temperature to LST (in Kelvin) due to use of effective wavelength in Planck’s law instead of the own filter function constants (see Figure 4.1). The inaccuracy is given for three down-welling radiances and five Land Surface Emissivity (LSE) values. See also Figure 4.3.

LST (K)	L_d ($W/m^2 \cdot str \cdot \mu m$)	LSE				
		0.95	0.96	0.97	0.98	0.99
275	0.5	-0.22	-0.18	-0.13	-0.09	-0.05
	2.0	-0.21	-0.17	-0.13	-0.09	-0.05
	4.5	-0.21	-0.17	-0.13	-0.09	-0.05
285	0.5	-0.22	-0.17	-0.12	-0.08	-0.03
	2.0	-0.20	-0.16	-0.11	-0.07	-0.03
	4.5	-0.18	-0.14	-0.10	-0.06	-0.02
295	0.5	-0.25	-0.20	-0.15	-0.09	-0.04
	2.0	-0.23	-0.18	-0.13	-0.08	-0.03
	4.5	-0.19	-0.15	-0.11	-0.07	-0.03
305	0.5	-0.30	-0.24	-0.18	-0.12	-0.07
	2.0	-0.27	-0.21	-0.16	-0.11	-0.06
	4.5	-0.23	-0.18	-0.14	-0.09	-0.05
315	0.5	-0.31	-0.25	-0.18	-0.12	-0.06
	2.0	-0.28	-0.22	-0.16	-0.11	-0.06
	4.5	-0.23	-0.18	-0.14	-0.09	-0.05
325	0.5	-0.37	-0.29	-0.21	-0.13	-0.06
	2.0	-0.32	-0.25	-0.18	-0.12	-0.05
	4.5	-0.26	-0.21	-0.15	-0.09	-0.04

Because there is a relation between LST, LSE and down-welling radiance, inaccuracy is dependent on these values as is shown in Table 4.3. The lower the LSE – down-welling radiance and higher the LST, the higher the inaccuracy due to pass band effect, reaching values of -0.4 K for a LST of 325 K, L_d of $0.5 W/m^2 \cdot str \cdot \mu m$ and LSE of 0.95. For high LSE surfaces, the inaccuracy is minimal but it should be accounted as LST value is biased.

For our stations, even if the pass-band effect is avoided, an uncertainty due to not knowing filter function remains, which implies uncertainties on k_1 and k_2 and then on LST. This uncertainty was calculated and computed as 0.1 K for our broadband radiometers.

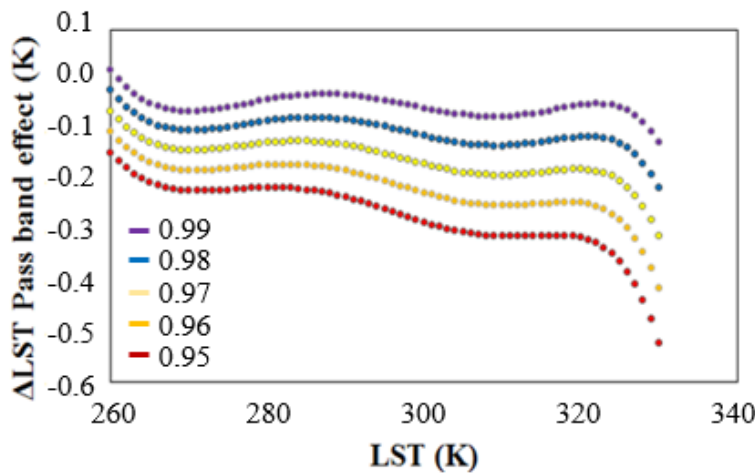


Figure 4.3. LST differences on conversion process from brightness temperature to LST. Δ LST symbolizes the difference between the specific and effective wavelength Planck's law equation for a fixed down-welling radiance ($L_d = 1.5 \text{ W/m}^2 \cdot \text{str} \cdot \mu\text{m}$). Violet, blue, yellow, orange and red colors symbolize LSE values.

4.3. LAND SURFACE EMISSIVITY

Emissivity values were characterized for our test sites as a part of LST estimation process. CIMEL CE 312-2 multiband radiometer is used for this purpose however it is not used for continuous measurements in our fixed stations. As was presented in the previous chapter, CIMEL radiometer and other broadband radiometers – used for in-situ measurements – present slight broadband filter function differences and therefore, different values of LSE for the same surface – as LSE values are wavelength dependent. For this reason, CIMEL emissivity is not totally representative of the other radiometers.

In order to retrieve these differences, a relation – using the ASTER spectral library as a database – between CIMEL and IR120 and SI100 broadband radiometers was retrieved for accurate emissivity conversion (see Figure 4.4). Computing soils, vegetation and water database, more than 85% of the values present absolute differences below 0.005 and mean absolute difference of 0.003 (see Table 4.4). Because there are higher differences in soils and not in vegetation and water, a regression fit for soils was performed in order to reduce this difference. Applying the fit results, mean differences are reduced to 0.0008 in comparison to 0.0038. This means that the uncertainty associated to LSE values due to measuring it with a CIMEL radiometer is reduced to

0.003. Because the IS100 and IR120 radiometers present similar results, only IR120 comparison is shown in Figure 4.4 and Table 4.4.

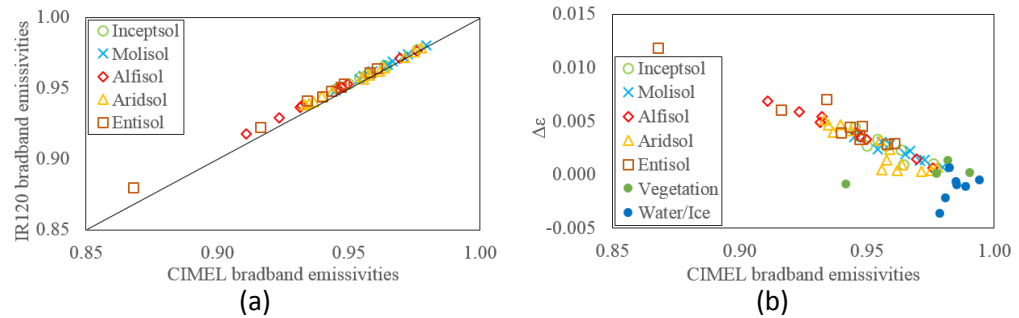


Figure 4.4. (a) Direct broadband emissivity comparison between CIMEL CE 312-2 and IR120 radiometer. (b) Emissivity differences (CIMEL CE 312-2 minus IR120) versus CIMEL CE 312-2 emissivities. Values have been extracted from ASTER spectral library and filtered for each radiometer.

Table 4.4. Bias, standard deviation, RMSE, slope, offset and correlation coefficient obtained from CIMEL CE 312-2 vs IR120 emissivity comparison. In brackets, new bias, standard deviation and RMSE, applying the correction terms between emissivities (slope and offset) to CIMEL CE 312-2 values are also shown (see Figure 4.4).

	bias	sigma	RMSE	slope	offset	R ²
Soils	0.0032 (0.0004)	0.0022 (0.0007)	0.0038 (0.0008)	0.0090	0.0981	0.99
Water/Vegetation	0.0007	0.0012	0.0014	-	-	-

Additionally to conversion, the measurement uncertainty was also computed. With CIMEL values obtained in field campaigns – time measurements within 30 min in the same point – the standard deviation has been calculated in order to check radiometer stability, over four different surfaces: Green grass, bare soil (Barrax), senescent vegetation and mixed vegetation-soil (Cabo de Gata). Results obtained in the Table 4.5, show us a standard deviation values of 0.005, which is considered as the uncertainty of emissivity measurements. Adding the conversion uncertainty (0.008 or 0.0014 – see Table 4.4 – depending of the surface type) to IR120 and IS100 stability values, the total LSE uncertainty associated to our test sites can be calculated as a sum of Root Mean

CHAPTER 4: UNCERTAINTY OF IN-SITU MEASUREMENTS

Square Errors (RMSE). In our case, the average uncertainty obtained for LSE is $\delta_\varepsilon = 0.006$ that in terms of temperature is associated to an uncertainty of 0.4-0.5 K for an LSE value of 0.97. It should be noted that the measurement uncertainty was obtained in periods (spring and summer) of high atmospheric contribution, increasing, in this way, the uncertainty of our measurements, which are probably a little bit lower in other seasons of the year.

Table 4.5. Average and standard deviation value of LSE measured by CIMEL CE 312-2 over four surface covers.

	Green grass Jul 25, 2012	Bare soil Jun 13, 2011	Senescent vegetation May 07, 2013	Mixed May 28, 2013
$\varepsilon_{\text{mean}}$	0.981	0.965	0.965	0.974
δ_ε	0.005	0.005	0.005	0.006

4.4. DOWN-WELLING RADIANCE

In addition to LSE, L_d is the other factor that can influence LST estimation. L_d can be measured directly by the pyrgeometer pointing to the sky. Values retrieved in W/m^2 must to be transformed to $\text{W}\cdot\text{m}^{-2}\cdot\text{sr}^{-1}\cdot\mu\text{m}^{-1}$ by applying the spectrum response function of desired radiometer and integrating hemispherically this value. In this way, it is easy to retrieve L_d with high precision.

Because the pyrgeometer is not available in all of our test sites (only in Barrax), alternative procedures have been tested for accurate L_d estimation. Of these procedures, the model proposed by Prata (1996) – which basically follows Brutsaert (1975) derivation using adjusted slab emissivity – was selected because of the performance obtained in Carmona et al. (2014). The model proposed is given by the following expression:

$$LW_d = [1 - (1 + w)\exp(-[a + bw]^{1/2})]\sigma T^4 \quad (4.3)$$

where $a=1.2$, $b=3 \text{ cm}^2\cdot\text{g}^{-1}$, and w is the precipitable water content calculated as $46.5\cdot(\varepsilon_{\text{air}}/T_{\text{air}}) \text{ g}\cdot\text{cm}^{-2}$ and where ε_{air} is the air emissivity and T_{air} is the air temperature. LW_d is the down-welling radiance given in W/m^2 . The constants in the Eq. 4.3 are

location dependent and it should be readjusted for high precision estimations (not performed in this work).

In Doñana marshland stations, there is not availability of air temperature and humidity and L_d measurements must to be obtained by alternative means. One of them is through the use of atmospheric profiles which can be processed with MODTRAN-5 to extract L_d . In this way the location dependence of Prata (1996) model is avoided. In our case, the values are extracted from the MOD07 product. Because L_d is an hemisphere-integrated down-welling radiance, it should be estimated for multiple angles – 11.6°, 26.1°, 40.3° and 53.7° (Gaussian angles) plus 0°, 65°, 70°, 80°, 85°, and 89° for a better description at larger angles – which implies multiple simulations (Galve et al. 2008). Typically, a unique simulation of L_d (in the MODTRAN-5 code) is performed assuming only λ dependence.

To compute the uncertainties on the down-welling radiance estimations for cloudless days, a comparison between in-situ measurements performed at El Cruce station with the pyrgeometer versus Prata (1996) model and MOD07 estimations (multi-angle and nadir) was carried out from 2013 to 2015. Figure 4.5 shows these differences as a function of the day of year. It is appreciated that the Prata's model is very stable during the year while MOD07 profiles have two differenced periods: one for summer time, and another one for the rest of the year. From days 150 to 300, bias (in-situ minus model) decreases, showing multi-angle values overestimating in-situ L_d and, in the case of nadir approximation, underestimating the in-situ L_d values. To show better the models results, in Table 4.6 statics of the L_d comparison are shown. Prata model and multi-angle computation (for no summer period) show a negligible bias and a standard deviation below $0.7 \text{ W}\cdot\text{m}^{-2}\cdot\text{sr}^{-1}\cdot\mu\text{m}^{-1}$ while for summer period shows absolute biases above $0.7 \text{ W}\cdot\text{m}^{-2}\cdot\text{sr}^{-1}\cdot\mu\text{m}^{-1}$. This means that the nadir computation always underestimate the down-welling radiance which implies an overestimation of LST. At the contrary, in the summer period, the multi-angle computation of MOD07 product overestimates L_d and, then underestimates LST.

Finally, setting the LSE at 0.97, it is possible to obtain the influence of L_d uncertainty on LST estimation (see Table 4.6). All the models retrieve RMSE values below 0.3 K with a bias of 0.2 K for nadir approximation. Taking in account the results obtained in the study, Prata model (when it is possible) and a combination of multi-angle (no summer period) and nadir (summer period) model can be used for L_d retrievals in our stations, assuming an uncertainty (δL_d) below 0.2 K.

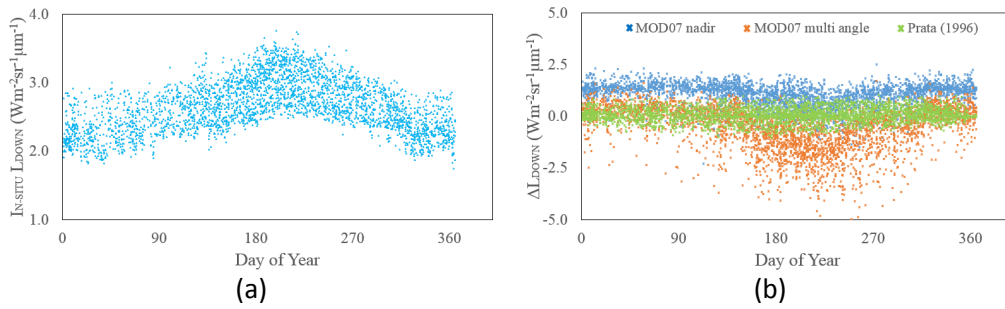


Figure 4.5. (a) In-situ down-welling radiance measured at El Cruce station; (b) Down-welling radiance differences ΔL_{down} (In-situ minus predicted MOD07 – nadir and multi-angle – and Prata’s model) versus the day of year. Three years were considered for the study: 2013, 2014 and 2015.

Table 4.6. Statistics of predicted down-welling radiances, where bias is the In-situ data minus model data. Winter encompasses the first 150 and the last 60 days of year while summer is referred to the rest of days. The influence on LST (supposing a LSE value of 0.97) is also shown.

	Model/ Profile computation	L_d (W·m ⁻² ·sr ⁻¹ ·μm ⁻¹)			ΔLST (K)		
		bias	sigma	RMSE	bias	sigma	δL_d
Barrax (El Cruce)	MOD07 nadir winter	0.739	0.568	0.933	0.2	0.1	0.2
	MOD07 nadir summer	1.284	0.407	1.346	0.2	0.1	0.2
	MOD07 multi-angle winter	-1.221	0.975	1.562	-0.2	0.2	0.3
	MOD07 multi-angle summer	0.027	0.688	0.689	0.0	0.2	0.2
	Prata et al. (1996)	0.073	0.354	0.362	0.0	0.1	0.1

4.5. RADIOMETERS CALIBRATION

Additionally to the estimation of variables involved in Eq 4.1 and Planck’s law approximation, LST uncertainty is also influenced by accuracy and precision of measurements performed with the radiometers. Continuous measurements require a stable uncertainty with little changes through the radiometers life. To ensure and control these changes, the radiometers should be calibrated in the laboratory as often as possible but it is not always possible due to the location of the test sites and the availability of substitution radiometers. For these reason, two types of calibrations are performed to guaranty radiometer’s good quality data:

- Direct calibration: Performed with a Black Body (BB) source in indoor or outdoor conditions where indoor is referred to controlled temperature conditions that can be set on BB source (see Figure 4.6a) and outdoor refers to simultaneous measurements performed on BB source with radiometer and contact thermometer in which temperature is determined by external factors, as temperature or solar radiance (see Figure 4.6b). Advantage of the outdoor calibration is that it simulates better the field conditions than the indoor calibration and that it provides more calibration points. The negative point is that the value range is determined by external factors.
- Indirect calibration: Consists on a direct comparison between radiometers of which one is calibrated. In this way, accuracy can be tested. The great disadvantage is that only a few points can be extracted for calibration.

Indirect calibration is performed in each field campaign and is the first test of the correct radiometer function. Meanwhile the direct calibration is carried out every one-two years – as manufacturer recommends or when malfunction is detected – and it is used to set the accuracy to zero and to obtain the new precision of the radiometer.



Figure 4.6. Sources (black body) of calibration used for: (a) direct indoor calibration – LAND P80P – and (b) direct outdoor calibration performed with platinum thermometer.

The precision of a new radiometer is specified by manufacturer – below 0.2 K – but, the precision decreases with time due to its use. For this reason, Table 4.7 shows precision of IR120 radiometer for gaps of two years and calibration of CIMEL and Optris (simple broadband radiometer). To complement the information, Figures 4.7 and 4.8 show plots of direct calibrations performed for indoor and outdoor conditions for IR120, CIMEL and Optris radiometers.

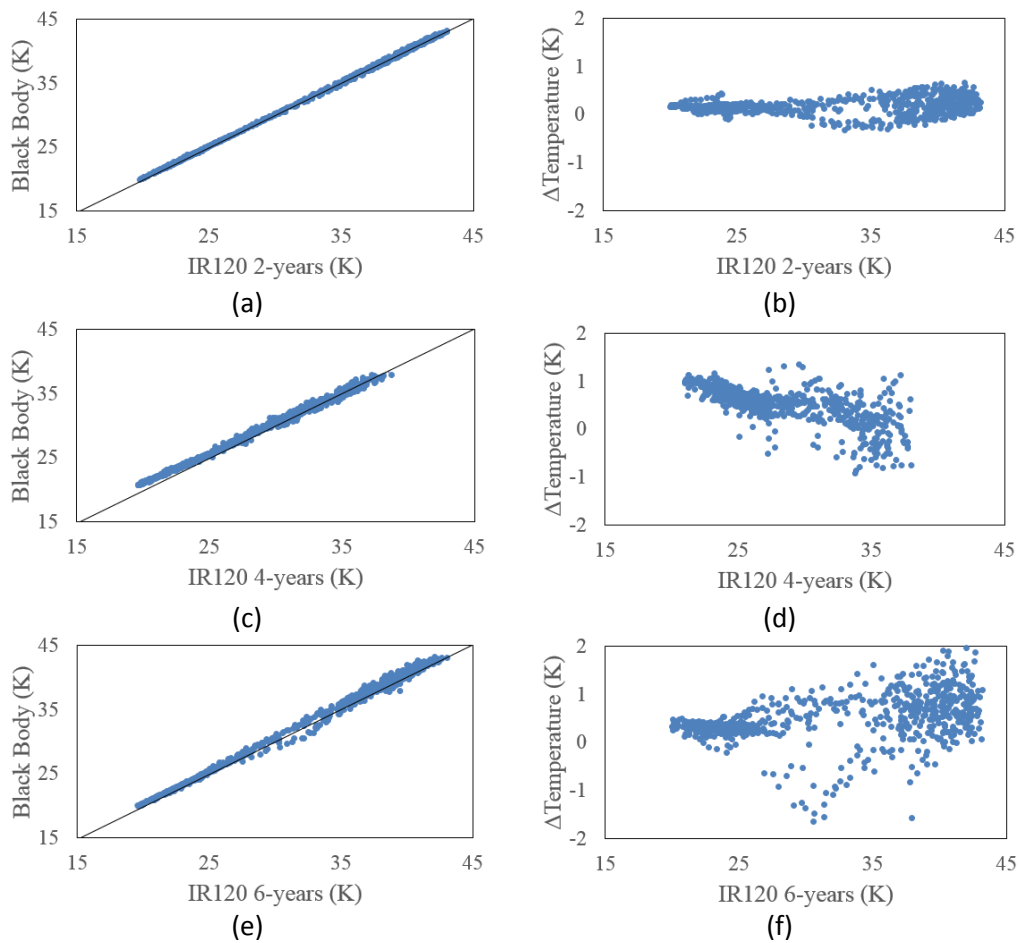


Figure 4.7. Direct outdoor calibration of IR120 radiometer against Black Body temperature – (a), (c) and (e) – and Black Body-IR120 difference – (b), (d) and (f).

Figure 4.7 and Table 4.7 show that the precision of IR120 radiometer increases with its use, reaching values of 0.4 K in the sixth year of use (from the previous 0.2 K). Comparing with Optris radiometer – which does not have surrounding temperature influence correction – the IR120 is twice as precise. It is also observed that the indoor calibration shows better precision than the outdoor. This is probably due to a precision of the BB temperature estimation (LAND P80P has precision of ± 0.01 K while platinum thermometer retrieves precision of ± 0.03 K) and because of the laboratory conditions which are more stable in terms of air temperature and zero solar radiation.

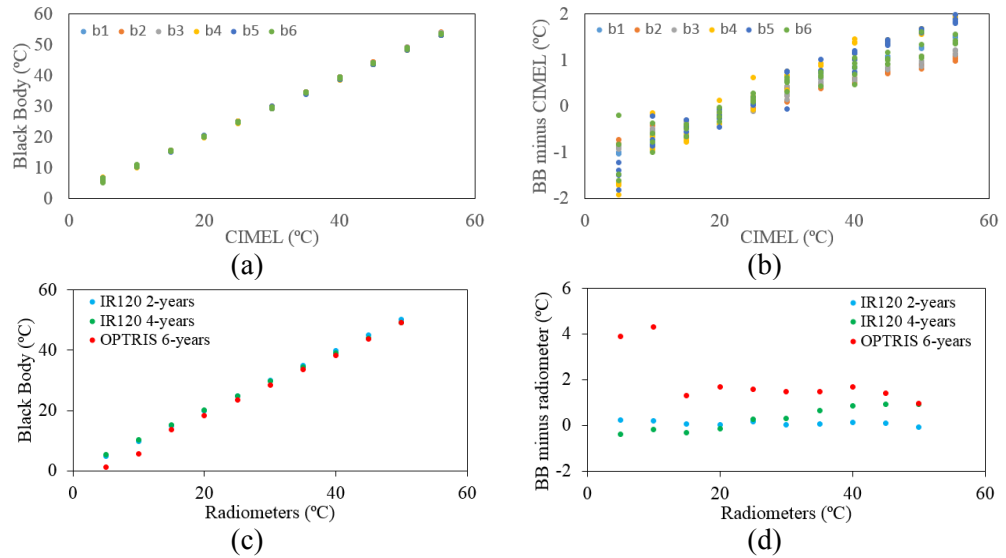


Figure 4.8. Direct indoor calibration against LAND P80P BB temperature of: (a)-(b) CIMEL CE 312-2 and (c)-(d) IR120 and Optris radiometers.

Table 4.7. Summary of radiometers calibration results shown in this section which include indoor and outdoor calibrations. Slope, offset and correlation coefficient of the calibration fit as well as radiometers precision (δT_{CAL}) are shown.

Calibration type	Radiometer	Band	slope	offset	δT_{CAL} (K)	r^2	
Outdoor	IR120 2-years		1.004	0.043	0.15	0.999	
	IR120 4-years	broadband	0.971	-1.181	0.26	0.997	
	IR120 6-years		1.022	-0.203	0.39	0.997	
Indoor (Laboratory)	IR120 2-years		0.996	0.211	0.07	0.999	
	IR120 4-years	broadband	1.035	-0.665	0.15	0.999	
	Optris 6-years		0.945	3.371	0.78	0.997	
	CIMEL CE312-2	band 1		1.052	0.043	0.05	0.999
		band 2		1.038	-2.181	0.12	0.999
		band 3		1.041	-0.203	0.11	0.999
		band 4		1.073	-1.732	0.28	0.999
		band 5		1.068	-1.589	0.22	0.999
		band 6		1.051	-1.209	0.25	0.999

4.6. LST HOMOGENEITY

As was indicated in the Introduction, field homogeneity in terms of LST is the most important factor of uncertainty for cal/val activities. It is not strictly associated to in-situ measurements because it depends of the selected area that, at the same time, is related to the considered spatial resolution of Earth Observation Sensor (EOS). The inhomogeneity (INH) of an area is directly related to the situation of sensor on the field and the surroundings. Usually, most common statistics as minimum, maximum, standard deviation or bias have been used to determinate the INH. Some authors as Coll et al. (2005) or Hale et al. (2011) used these statistics with high spatial resolution EOS to determinate the homogeneity. In these studies, L7 ETM+ or ASTER sensor had been used to analyze the variation of the LST within a low spatial resolution pixel such as MODIS or SEVIRI. Other authors as Göttsche et al. (2013) used multiple in-situ measurements (transects) across a site to determine spatial LST homogeneity.

In our case, the INH index for moderate spatial resolutions (≤ 100 m) was obtained through transects and AHS images. L8 TIRS was used for retrieving low spatial resolution data. To obtain the INH of our test sites through sensor images in terms of LST, bias and standard deviation have been computed to obtain the INH index over a window of n pixels. This window slides across every pixel of the image as is showed in Figure 4.9. Bias, standard deviation and INH index of the area shown in Figure 4.9 are expressed as follows:

$$bias = 1/n \sum_{i=1}^n T_c - T_i \quad (4.4)$$

$$\sigma = \sqrt{\frac{1}{n-1} \sum_{i=1}^n |T_i - \bar{T}|} \quad (4.5)$$

$$INH = \sqrt{bias^2 + \sigma^2} \quad (4.6)$$

where T_c is the LST of central pixel of the window, T_i is the LST of the window pixels, \bar{T} is the mean LST over the window and n is the number of pixels of the window, which depends of the sensor image used. Eq. 4.4 is the mean difference between the chosen pixel and the neighbor pixels, Eq. 4.5 is the variability in the window and, finally, Eq. 4.6 is the INH index of the central pixel respect to the considered window area. In other

words, INH is the uncertainty due to heterogeneity at a given spatial resolution, when measurements are performed for the central pixel.

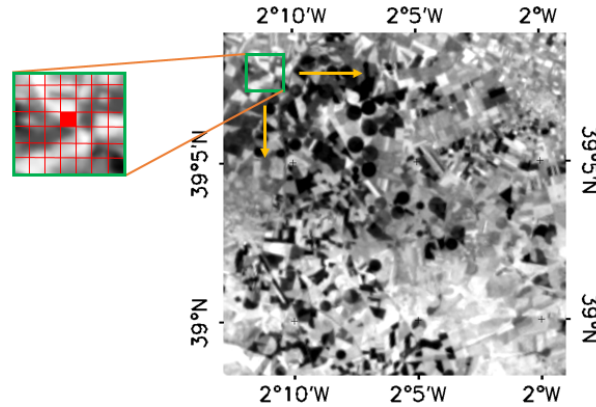


Figure 4.9. Graphic procedure to compute the INH index. The window (in green over the main image) slides across every pixel of the LST image.

To consider one pixel as a candidate for carrying out cal/val activities, the INH index should be lower than a certain value that depends of the LST uncertainty. For example, for moderate resolution sensors (< 100 m), the uncertainties for LST estimation range between 0.5 K-1.5 K as described in Hook et al. (2007) or Coll et al. (2010) and for low resolution sensors, the uncertainties are about 2 K (Wan 2014, Coll et al. 2009) for MODIS sensor. Based on these values, the INH index obtained in AHS image and TIRS image should be lower than 1.5 K and 2 K respectively to consider the pixel suitable for cal/val activities.

The AHS spatial resolution covers approximately the same footprint as the in situ measurements. For this reason, in this study it is assumed that the LST values obtained with the AHS sensor are representative of ground measurements. In contrast, the spatial resolution of the TIRS is lower than the AHS sensor and covers a considerably larger area than the in-situ measurements. For this reason, only the areas that allow the cal/val of moderate spatial resolution sensors are suitable for low spatial resolution sensors.

4.6.1. INH for moderate spatial resolution (< 100 m)

Figure 4.10 shows the INH values derived from the AHS images for a spatial resolution of 100 meters. Depending of the image pixel size, a window of 14×14 pixels – Doñana – or 25×25 pixels – Barrax and Cabo de Gata – was used for INH index. Because initially the Balsa Blanca station was not foreseen as a test site, Cabo de Gata field campaign was performed in the west part of the National Park, leaving out the Balsa Blanca area. In that case, a similar zone was chosen as representative of the Balsa Blanca area.

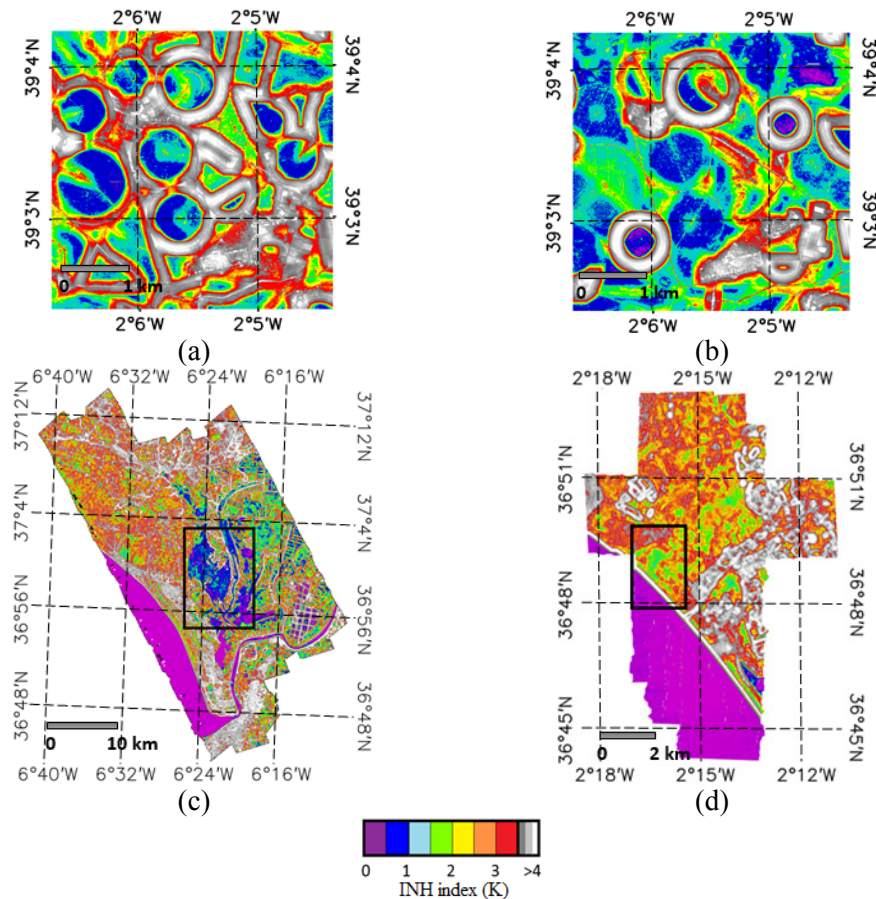


Figure 4.10. INH index retrieved from AHS sensor for moderate spatial resolution sensors. Images (a) and (b) represents Barrax test site on 12 June 2011 and on 25 July 2012, respectively. The (c) and (d) images are referred to Doñana on 9 May 2013 and Cabo de Gata on 28 May 2013 respectively. Black rectangles in figure (c) and (d) show the marshland and an area similar to Balsa Blanca test site, respectively.

The images were analyzed over two periods for Barrax area – crop growth period and after crop harvest – and only in one period for Doñana – with partial flood of the marshland – and Cabo de Gata – where the land cover conditions change little throughout the year. Due to narrow images width for each flight, a composite image of all the images obtained in each field campaign was built in order to calculate the INH index of the whole area and to better present the final results. Errors associated with differences of flight times can be neglected because the INH index was calculated over individual AHS images.

Looking at Figure 4.10, three zones can be considered for the cal/val activities due to its high homogeneity: marshland, in Doñana, with an INH index below 1.5 K; Some parts of Cabo de Gata, where values range between 1 K and 2 K and some fields of Barrax where the INH index is below 1 K.

4.6.2. INH for low spatial resolution (< 2 Km)

As the pixel size of low resolution sensors have zenith view angle dependence – from 1 km (zenith angle of 0°) to 3 km (zenith angle of 60°) as reported in Wolfe et al., (2002) –and the location of the pixels change in every new image acquired through the day, a sliding window of 66×66 pixels of TIRS was chosen as representative of low spatial resolution sensors. The limit of 2×2 km was chosen because it is more precise to perform cal/val activities with low zenith angles (Wang et al, 2008). Table 4.8 lists the number and dates of the L8 images acquired for the temporal analysis of the homogeneity. Only clear sky images over our test sites were used for this purpose.

Table 4.8. Acquisition date of L8 images used to retrieve INH index for our test sites.

Test Site	n° L8 images	Acquisition date			
		2013		2014	
Barrax	14	14, 30 April	10 July	5 Sep	19 Feb
		23 May	4, 11 August	24 Nov	7, 23 March
		1, 24 Jun		12 Dec	
Doñana	12	19 April	9 August	29 Nov	
		5 May	28 Oct	15, 31 Dec	21 March
		22 Jun	13 Nov		
		8, 24 July			
Cabo de Gata	12	1 Jun	4, 20 August	11 Nov	27 Jan
		3, 19 July	7 Oct	26 Dec	12 Feb
					16 March
					17 April

CHAPTER 4: UNCERTAINTY OF IN-SITU MEASUREMENTS

Figure 4.11 shows the evolution of the INH for different astronomical seasons at Cabo de Gata, Doñana and Barrax. The seasonal images were retrieved as a seasonal average value of the images presented in Table 4.8.

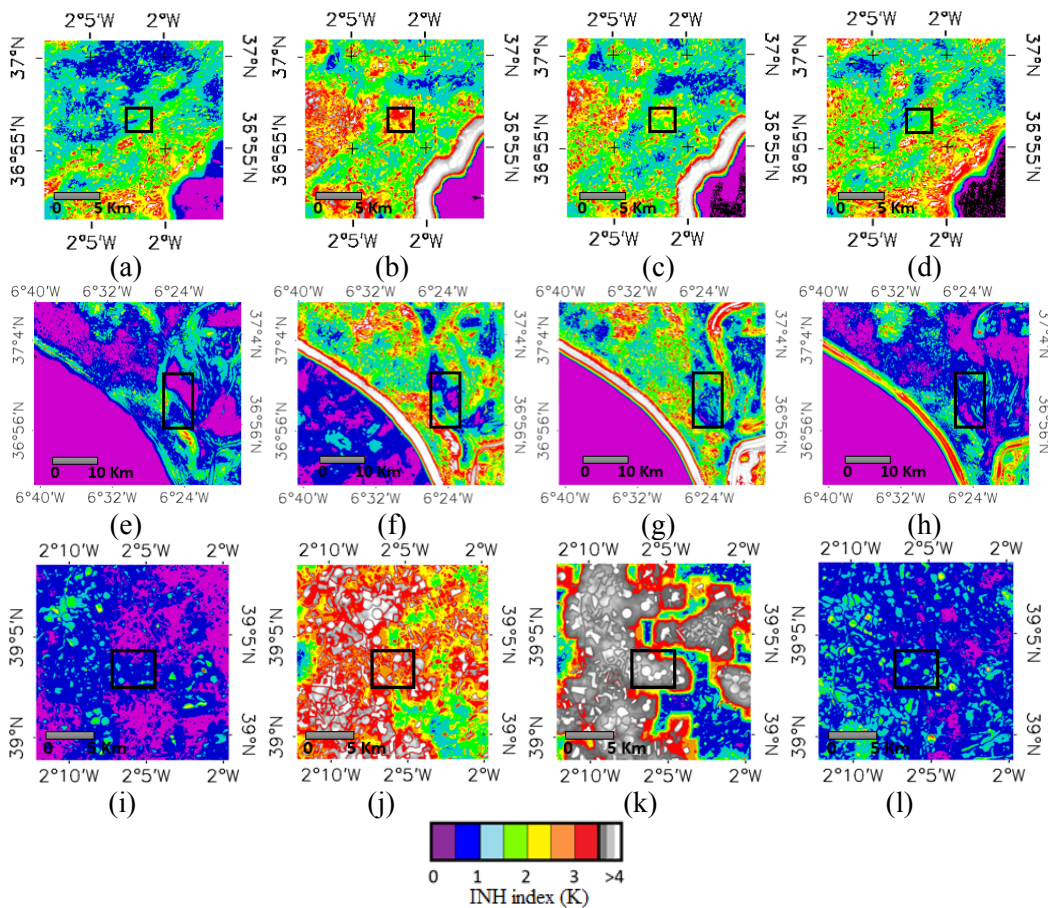


Figure 4.11. Temporal evolution of the INH index at three Spanish test sites: Cabo de Gata: images (a), (b), (c) and (d); Doñana: images (e), (f), (g) and (h); Barrax: images (i), (j), (k) and (l). From left to right, the images are sorted by astronomical seasons: winter, spring, summer and autumn. Black rectangles mark the considered areas for the temporal analysis.

Figure 4.11 shows that in summer and spring there are more inhomogeneity than in winter and autumn. Analyzing only the zones selected within the black rectangle, it is observed that the seasonal variability is higher in Doñana and Barrax than Cabo de Gata (see Table 4.9). Particularly, Doñana’s marshland presents the maximal homogeneity in autumn and winter with some values of INH below 0.5 K. When the rainfall period starts, in late autumn, the INH increases and reaches its maximum in the early summer, with values near to 2 K. Barrax presents the maximal homogeneity in autumn and early winter when fallow lands cover the area. In late winter, when the crops start to grow, the INH increases reaching maximal values in summer. Barrax is only recommendable for cal/val activities in autumn and early winter. Finally, as Cabo de Gata has minimal seasonal variations in the ground cover, the INH index hardly changes, with range values of 0.5–2 K (except in spring, when INH index show values above 2.0 K). Table 4.9 shows the INH index summary for low spatial resolution sensors.

Table 4.9. Summary of the INH index obtained in Barrax, Doñana and Cabo de Gata in the black rectangle of Figure 4.11. Annual range is the maximal and minimal INH index and the last column is the number – in percentage – of INH values below 2 K when considering all acquired images for each test site.

Zone	Seasonal average (K)				Annual range (K)	INH below 2 K
	Winter	Spring	Summer	Autumn	min-max	(%)
Barrax	1.2	2.8	3.9	0.9	0.5 – 7.0	30-50
Doñana	0.8	1.6	1.8	0.5	0.5 – 3.0	> 90
Cabo de Gata	1.1	2.4	1.7	1.0	0.5 – 3.5	> 90

4.6.3. INH over fixed stations

To conclude the study, INH index at the location of our fixed stations has been retrieved for moderate and low spatial resolution sensors. Additionally, the INH index of SEVIRI pixel was also retrieved. As the SEVIRI pixel does not change – the location of the pixel is always the same – the INH of the nearest SEVIRI pixel to the fixed stations was simulated with TIRS data. The area simulated was of 132×132 pixels – little more than the SEVIRI real pixel – centered in the nearest SEVIRI pixel.

CHAPTER 4: UNCERTAINTY OF IN-SITU MEASUREMENTS

The INH retrieved with AHS images for the coordinates of fixed stations (see Figure 4.10) shows values below 1.5 K at Las Tiesas, Fuente Duque, Juncabalejo and at the black rectangle of Cabo de Gata (with the same characteristics as Balsa Blanca). The stations can be considered suitable for cal/val activities for high-medium sensors when INH index is below 1.5 K. These values of INH index were obtained in spring and summer, so, considering the results of temporal analysis retrieved with Landsat data, the INH index in other seasons will be lower, especially in winter and autumn. Consequently, the INH index for moderate resolution sensors is overestimated for the other seasons.

In Figure 4.12, the evolution of the INH index for low spatial resolution sensors and SEVIRI pixel is shown. For sensor with low resolution, Doñana and especially Cabo de Gata show the lowest values. Homogeneity in Balsa Blanca is always lower than 2.6 K while in Fuente Duque and Juncabalejo it depends of the marshland flooding. If marshland is completely flooded or dry, the homogeneity is high while when the marshland is partially flooded (usually in spring), the INH index around 2 K. In general, it is possible to consider that in Doñana the INH is below 2 K in summer, autumn and winter. For Barrax, only in autumn and winter, the homogeneity is high, coinciding with the period when the majority of fields are without crops. In Figure 4.12, SEVIRI variability was also retrieved showing the same pattern as low resolution sensor pixel although with higher values of INH.

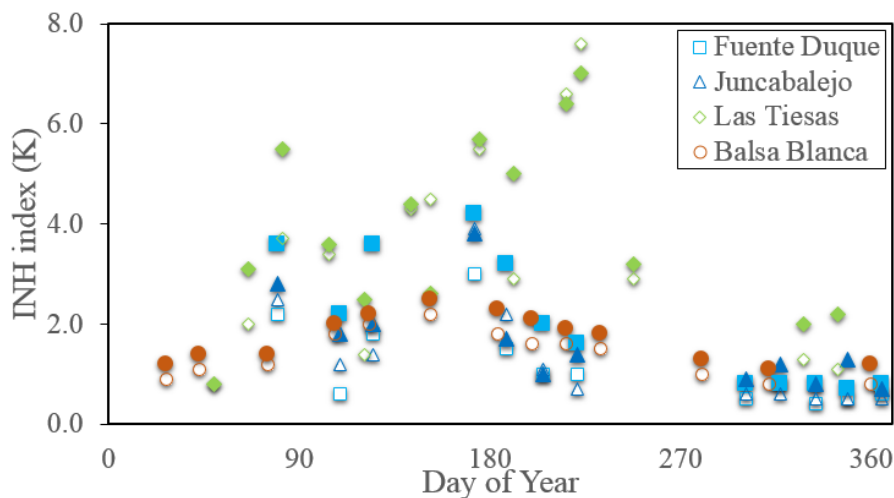


Figure 4.12. Temporal evolution of the INH index in four fixed locations: Fuente Duque, Juncabalejo, Balsa Blanca and Las Tiesas. Open symbols represents an area of 2×2 km while filled symbols represents approximately a SEVIRI pixel.

Finally, it can be concluded that the ideal periods to perform cal/val activities are the late summer, autumn and winter. In these periods the INH index is below 2 K. Table 4.10 summarizes the results for our fixed stations.

Table 4.10. Summary of the INH results obtained at four fixed stations for three spatial resolutions: 100 m (high-medium EOS), 2 km (low EOS) and 4 km (approximately SEVIRI spatial resolution). Mean and min – max values have been retrieved as the average and minimal-maximal INH value of our study.

Zone (Name)	100 m	2 km (MODIS)		SEVIRI	
	Sample (K)	Mean (K)	min – max (K)	Mean (K)	min – max (K)
Las Tiasas	1.0	3.2	1.0 – 7.5	3.4	1.0 – 7.0
Fuente Duque	0.7	1.1	0.5 – 3.5	1.7	0.5 – 4.0
Juncabalejo	1.2	1.2	0.5 – 4.0	1.5	0.5 – 4.0
Balsa Blanca	1.4*	1.2	0.5 – 2.2	1.6	1.0 – 3.0

* Obtained in a similar area to Balsa Blanca

4.6.4. INH with transects

Complementary to high-moderate spatial resolution pixels, as there was not possible to analyze the temporal evolution because of the not high spatial resolution data availability, transects were performed to complement the seasonal INH index. Because it was not always possible the access to the test sites – e.g. when the marshland is flooded – transects do not cover all the season of the year for some fixed stations. In these cases, sporadic measurements were performed in these test sites – especially Fuente Duque and Balsa Blanca – for INH estimation.

The transect measurements were performed as quickly as possible, typically in a lapse of 3 minutes, in which 10-15 values were taken around the fixed radiometer location and on the radiometer location itself. Eq. 4.2, 4.3 and 4.4 were used to obtain the INH index. Because in 3 min it is not possible to cover an area of 100 m, the process was repeated 3-4 times and the average value was selected as INH index. Table 4.11 shows transects performed for INH estimation, and includes the date and number of measurements performed. The sporadic measurements are not shown, although they were taken in account for the seasonal evolution, shown in the next section.

CHAPTER 4: UNCERTAINTY OF IN-SITU MEASUREMENTS

Table 4.11. Transects performed for inhomogeneity (INH) retrievals. The number of measurements (n) and date is also shown.

Location	Date	n	INH (K)	Location	Date	n	INH (K)
Balsa Blanca	15/12/2015	50	0.6	Fuente Duque	05/09/2014	27	1.0
	24/02/2017	47	0.5		31/10/2016	35	0.8
Juncabalejo	05/09/2014	38	1.1	Cortes	05/09/2014	29	1.4
	31/10/2016	27	0.8		31/10/2016	32	0.8
Las Tiasas	20/07/2015	59	1.1	El Cruce	20/07/2015	46	1.0
	10/11/2016	83	0.4		10/11/2016	47	0.5
	23/02/2017	48	0.6		23/02/2017	50	0.8

4.7. TOTAL IN-SITU UNCERTAINTY

To summarize the uncertainties contribution, Table 4.12 shows the main characteristics of fixed stations and the expected total LST uncertainty for low and moderate spatial resolution sensors. Following the classic error theory, the final LST uncertainty can be retrieved as the root mean square of all the contributions involved in the LST estimation, as long as uncertainties are independent one from another – radiometer filter function effect (δ_{FILTER}) was also included as ± 0.1 K.

Some difficultness have been found in INH index uncertainties assumption and in confection of the summary table:

- For INH index estimation of moderate spatial resolution, it was not possible to establish seasonal evolution because of lack of airborne sensor data. Only real available data was retrieved with transects although the values are only representative of conditions prevailing at that time. For this reason, despite of the data showed in Table 4.12, these values are not extracted from real values (because it was not possible) but have been estimated using the real transect data and complementary material as station pictures, differences between radiometer measurements or even with VNIR data of Landsat sensors.
- For INH index estimated for low spatial resolution, temporal evolution is available although the analysis performed in this work encompasses only one year. Due to probably undergo changes of test sites cover and keeping in mind that satellite data was extracted for punctual days, the INH index can change year after year, not always meeting the expected uncertainties.

CHAPTER 4: UNCERTAINTY OF IN-SITU MEASUREMENTS

Table 4.12. Summary of main fixed stations characteristics managed in Doñana, Barrax and Cabo de Gata test sites. Type field cover was defined as: PN is pine forest, W is water, BS is bare soil, GV is green vegetation, SV is senescent vegetation, CR is crop and GG is green grass. Moderate and low are moderate and low spatial resolution sensors, respectively. The inhomogeneity was divided in seasons: Wi, Sp, Su and Au are Winter, Spring, Summer and Autumn seasons respectively. LST uncertainty was calculated as the root sum square of errors due to: LSE ($\delta\epsilon$), downward radiance (δL_d), radiometer calibration (δT_{CAL}) and surface inhomogeneity (INH).

Test sites	Doñana			Barrax		Cabo de Gata
	Names	Cortes	Fuente Duque	Juncabalejo	Las Tiasas	El Cruce
Location	36.996 N 6.513 W	36.998 N 6.434 W	36.946 N 6.389 W	39.059 N 2.099 W	39.061 N 2.099 W	36.939 N 2.034 W
Field cover	PN	W or BS/SV	W or BS/SV	BS or CR	GG	BS/SV or BS/GV
Field extension (km × km)	2.5 × 3	> 10 × 10	2 × 5	1 × 1	0.12 × 0.20	4 × 4
Measured area	5 m ²	5 m ²	2 m ²	3 m ²	1 m ²	2 m ²
ϵ range	0.97-0.99	0.95-0.99	0.95-0.99	0.95-0.99	0.97-0.99	0.96-0.98
$\delta\epsilon$ (K)	0.3	0.4	0.4	0.4	0.3	0.4
δL_d (K)	0.2	0.2	0.2	> 0.1	> 0.1	0.1
δT_{CAL} (K)	0.3	0.3	0.3	0.2	0.2	0.2
INH INDEX (10 ⁻¹ K)	MODERATE 7-21-11-5	MODERATE 4-10-7-4	MODERATE 5-12-9-4	MODERATE 5-8-11-4	MODERATE 5-8-10-5	MODERATE 5-14-9-6
Wi-Sp-Su-Au	/-/ /-/ LOW	8-20-9-5 LOW	8-25-11-6 LOW	10-/ /-8 * LOW	/-/ /-/ LOW	7-22-11-7 LOW
LST Uncertainty (10 ⁻¹ K) **	MODERATE 8-22-12-7	MODERATE 6-11-9-6	MODERATE 7-13-10-6	MODERATE 7-9-12-6	MODERATE 7-9-11-7	MODERATE 7-15-12-8
Wi-Sp-Su-Au	/-/ /-/ LOW	9-21-11-7 LOW	9-26-13-8 LOW	12-/ /-10 * LOW	/-/ /-/ LOW	9-23-13-9 LOW

* Only computed for autumn/winter season.

$$** \delta LST = \sqrt{\delta_{FILTER}^2 + \delta\epsilon^2 + \delta L_d^2 + \delta T_{CAL}^2 + \delta INH^2}$$

CHAPTER 4: UNCERTAINTY OF IN-SITU MEASUREMENTS

Keeping in mind the INH index estimation, in general, the final LST uncertainty for moderate and low resolution sensors was retrieved to be below 1.5 K, excluding the spring season for low spatial resolution sensors. Spring is the season where the uncertainty is higher – following the INH index estimated in the section above – and autumn-winter period is the ideal for cal/val activities. The main contribution of uncertainty is due to inhomogeneity which varies for each station and season. LSE can contribute with a 50% of indetermination in some periods. The other components have less influence, especially in seasons where the inhomogeneity is high. As the uncertainty in spring is above 2 K, this period was excluded for the direct validation and Vicarious Calibration performed for MODIS sensor, but not for Landsat sensors.

Finally, to summarize which fixed station fit with what sensor, Table 4.13 shows the test site and the time period in which the cal/val activities can be performed with uncertainties below 2 K, for ETM+, TIRS – moderate resolution sensor – and for MODIS and SEVIRI – low resolution sensor. Spring was excluded in all the stations for MODIS/SEVIRI because of the high inhomogeneity while for Cortes station ETM+ and TIRS cal/val is possible only in autumn and winter.

Because of the short field dimensions of El Cruce station and because of the available data of Balsa Blanca from beginning of year 2016, El Cruce and Balsa Blanca only allowed cal/val activities for ETM+ and MODIS, respectively.

Table 4.13. Summary of suitable periods for cal/val activities for ETM+, TIRS (moderate spatial resolution) and MODIS, SEVIRI (low spatial resolution). Period validity is shown in colors: green for valid periods (uncertainty below 2 K) and red for not allowed seasons.

Test site	ETM+/TIRS				MODIS/SEVIRI			
	Winter	Spring	Sumer	Autumn	Winter	Spring	Sumer	Autumn
Las Tiasas	Yes	Yes	Yes	Yes	Yes	No	No	Yes
El Cruce *	Yes	Yes	Yes	Yes	No	No	No	No
Cortes	Yes	No	No	Yes	No	No	No	No
Juncabalejo	Yes	Yes	Yes	Yes	Yes	No	Yes	Yes
Fuente Duque	Yes	Yes	Yes	Yes	Yes	No	Yes	Yes
Balsa Blanca **	Yes	Yes	Yes	Yes	Yes	No	Yes	Yes

* Only available for ETM+ cal/val activities

** Only used for MODIS cal/val activities

CHAPTER 5: VICARIOUS CALIBRATION AND LST/SST VALIDATION

This chapter presents the results of cal/val activities developed in the framework of CEOS-SPAIN project. The chapter is divided in five sections that include the atmospheric analysis uncertainty, the TIR VC, the LST and SST algorithms validation and the test of the sharpening methods described in this work. Additionally, presentation of possible down-scaled LST products and a MODIS SST product were presented for future inclusion on the group processing scheme.

5.1. ATMOSPHERIC INFLUENCE ON CAL/VAL ACTIVITIES

Before showing cal/val results, the expected uncertainty of VC and LST validation was calculated in order to assess its validity. The in-situ LST measurements uncertainty was retrieved in the previous chapter for each station although the atmospheric influence – the radiance disturbance through the path to the sensor – due to the inaccurate knowledge of the atmospheric profile was not estimated. In order to retrieve this influence, a comparison of a real atmospheric profile – sounding measurements – and the MOD07 version 6 atmospheric product was performed for years 2013, 2014 and 2015. MOD07 product was selected because it was used in all the cal/val activities and because of its easy access and data extraction. Because each sensor has different filter function in TIR spectrum, the MOD07 inaccuracy should be retrieved for each sensor band, algorithm and test site. TIRS and MODIS bands – MODIS band 31 with TIRS band 10 and MODIS band 32 with TIRS band 11 – were put together in the study due to the similitude of the retrieved results.

Only two locations of real sounding are available near our test sites: Madrid (inland atmosphere) and Murcia (coastal atmosphere), which were selected as representative of Barrax (inland atmospheric profile) and Doñana - Cabo de Gata (coastal atmospheric profiles) test sites. Retrieving the atmospheric parameters (τ , L_d , L_u and w) for sounding and MOD07 product and introducing them as input of LST retrievals, the difference in radiance or temperature between the profiles can be obtained and then, the uncertainty (respect to sounding, which is considered our profile-true) of the MOD07 product. The uncertainty is conditioned by the time difference between the sounding and the MODIS measurement, which ranges from plus 0:30 hours to 2:30 hours. In order to minimize time error, the maximal gap accepted in this study was about plus 1:30 hours – shorter gap could be accepted although number of data available would have been small for study requirement. Furthermore, despite of the time of sounding launch, the complete analysis of the profile require more than 30 min, which reduces time gap between MODIS measurement and sounding data.

Two LST retrievals were analyzed: RTE and SC_w algorithm. SW algorithm was excluded because of its low atmospheric dependence (around 0.1 K as was indicated in the Chapter 1). Figure 5.1 and 5.2 show the results retrieved for Single-Channel water vapor approximation (SC_w) and RTE respectively in function of the atmospheric water vapor content (w), while in Table 5.1 and 5.2 a summary of the figures results is shown. As is expected, the gap between the atmospheric results increases when the w grows, especially for SC_w algorithm. If we divide the w in two groups, e.g. below 1.6 g/cm²

and above 1.6 g/cm^2 (Qin et al. 2002), it is appreciated that the RMSE of SC_w rises above 1 K or more with high atmospheric w content, while the RTE increases 0.2-0.5 K, depending on the band selected. In terms of bias, no significant changes have been observed (less than 0.2 K) as the standard deviation – especially on SC_w – is four or five times higher.

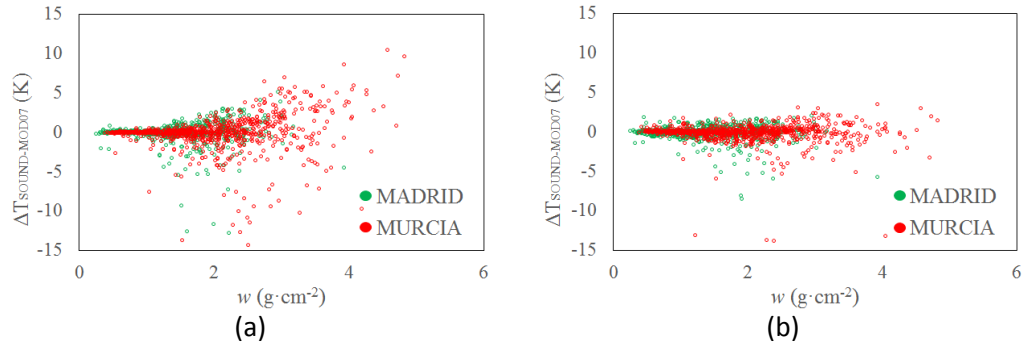


Figure 5.1. SC_w differences (in Kelvin) between real sounding and MOD07 atmospheric product (ΔT), in function of the sounding atmospheric water vapor content. The analysis was performed for (a) ETM+ band 6 and (b) TIRS band 10.

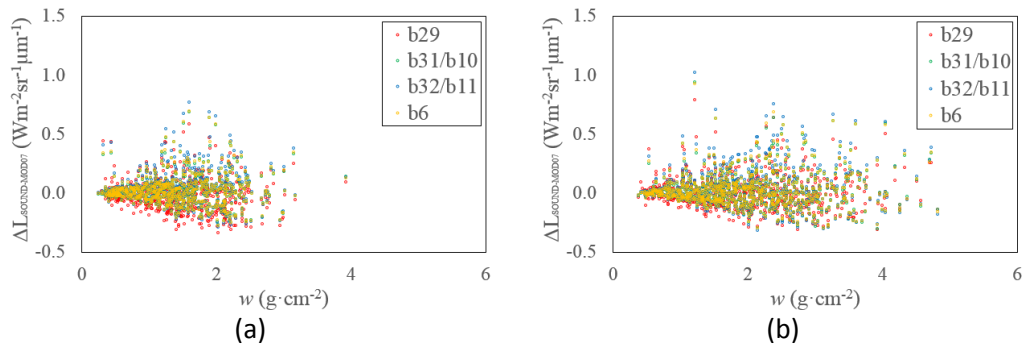


Figure 5.2. RTE differences (ΔL) – sounding minus MOD07 product – (in $\text{W}\cdot\text{m}^{-2}\cdot\text{sr}^{-1}\cdot\mu\text{m}^{-1}$) versus the sounding atmospheric water vapor content (w) for: MODIS (b29, b31 and b32), TIRS (b10 and b11) and ETM+ (b6) into two locations: (a) Madrid and (b) Murcia.

CHAPTER 5: VC AND LST/SST VALIDATION

Comparing the inland (Madrid) and coastal (Murcia) profiles retrieved with MOD07, there is not location influence on the RTE results while in SC_w these are more pronounced, especially for the ETM+ sensor. ETM+ has a coarser band filter function than TIRS which is more located in the w absorption spectrum. For this reason, ETM+ band is more affected by the w inaccuracy than TIRS band 10. One factor that explains the location differences is the mean w obtained in the analysis which is higher in Murcia than in Madrid (2.48 g/cm² versus 2.08 g/cm²). Another factor is the extreme differences retrieved between sounding and MOD07 profiles at Murcia (see Figure 5.3a) which in some cases reach values above 2-4 g/cm². This, sometimes, implies over-underestimations of more than 10 K on the LST (see Figure 5.1a). The high inaccuracies in w estimation can drive to dramatically bias changes into the SC_w algorithm (see Table 5.2) while the RTE is more stable and little changes in LST estimation between high-low atmospheric w content – below 0.5 K – are. Excluding the values with high w differences (sounding minus MOD07) of the Figure 5.3 (above-below two standard deviations $\pm 2\sigma$ g/cm²), MOD07 uncertainty decreases – especially at Murcia test site – between 0.2-0.4 K (depending on the band) for the RTE and above 1 K for the SC_w algorithm. These values – shown in brackets into Table 5.1 and 5.2 – were used for the algorithm uncertainty analysis.

Table 5.1. RTE uncertainty due to MOD07 version 6 inaccuracy in comparison to sounding values at Murcia and Madrid test sites (in brackets is included the number of data analyzed). Results summary of the Figure 5.2 is given in Kelvin for each thermal MODIS, ETM+ and TIRS band. Finally, in brackets, RMSE is also given for the w difference values (sounding minus MOD07) that are between above-below 2 standard deviations (exclusion of extreme Δw that can be found in Figure 5.3).

RTE $\Delta L_{\text{SOUNDING-MOD07}}$ ($W \cdot m^{-2} \cdot sr^{-1} \cdot \mu m^{-1}$)									
		Murcia (808)				Madrid (681)			
w (g·cm ²)		b29	b31/b10	b32/b11	b6	b29	b31/b10	b32/b11	b6
< 1.6	Bias	0.0	0.1	0.2	0.1	0.0	0.1	0.2	0.1
	σ	0.7	0.7	0.9	0.8	0.7	0.7	0.9	0.8
	RMSE	0.7	0.7	0.9	0.8	0.7	0.7	0.9	0.8
		(0.5)	(0.5)	(0.6)	(0.5)	(0.6)	(0.5)	(0.7)	(0.6)
> 1.6	Bias	0.0	0.1	0.2	0.2	-0.2	0.1	0.2	0.1
	σ	0.8	1.1	1.5	1.3	0.9	1.1	1.4	1.3
	RMSE	0.8	1.2	1.5	1.4	0.9	1.1	1.4	1.3
		(0.7)	(0.9)	(1.1)	(1.0)	(0.8)	(0.9)	(1.0)	(0.9)

Table 5.2. SC_w uncertainty results (Figure 5.2b) given for ETM+ band 6 (b6) and TIRS bands 10 and 11 (b10, b11). Bias (sounding minus MOD07), σ and RMSE results are given in K. In brackets, results without high w differences (excluding $\geq 2\sigma$ g/cm^2 Δw values) are also given.

w ($g \cdot cm^{-2}$)	Mean w ($g \cdot cm^{-2}$)		Madrid		Murcia		
	Madrid	Murcia	b6	b10	b6	b10	
< 1.6	1.01	1.09	Bias	-0.07	-0.04	-0.29	-0.10
			σ	0.79 (0.70)	0.59 (0.52)	1.98 (0.76)	0.95 (0.50)
			RMSE	0.80 (0.72)	0.59 (0.53)	2.00 (0.79)	0.96 (0.51)
> 1.6	2.08	2.48	Bias	-0.06	-0.22	-0.06	-0.22
			σ	2.37 (1.49)	1.43 (1.05)	3.10 (1.78)	1.52 (0.79)
			RMSE	2.37 (1.50)	1.45 (1.05)	3.10 (1.79)	1.53 (0.79)

Finally, total uncertainty associated to VC can be computed as the root sum square of the uncertainties due to in-situ LST measurements plus the atmospheric inaccuracy. The inhomogeneity contribution was averaged for each sensor band considering the homogeneity for each measurement, test site and season. In order to obtain the highest atmospheric precision and, in addition, the smallest uncertainty in the VC, the total amount of water vapor in the atmosphere was taken as small as possible. For this reason only the atmospheric w values below $1.6 g/cm^2$ were used for the VC. In Table 5.3 the uncertainty for each station and sensor band is shown. In the case of ETM+ and TIRS VC, the use of NCPD atmospheric data can lower the LST uncertainty as the reanalysis profiles have obtained more accurate results than the MOD07 product, as is described in Jimenez-Muñoz et al. (2010).

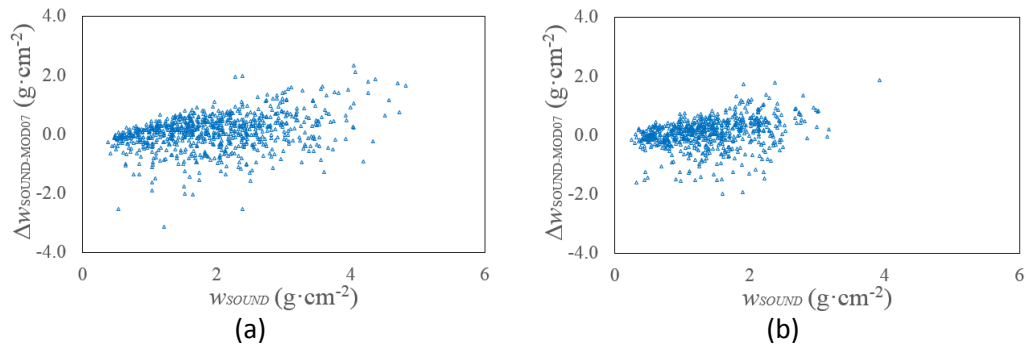


Figure 5.3. Diagrams of the water vapor difference – Sounding minus MOD07 product – versus the atmospheric water vapor registered by the soundings. (a) refer to Murcia test site and (b) to Madrid test site.

CHAPTER 5: VC AND LST/SST VALIDATION

Table 5.3. Expected uncertainty associated to TIR bands and fixed stations. The values are given in Kelvin.

	Band	El Cruce	Las Tiasas	Fuente Duque	Cortes	Juncabalejo	Balsa Blanca
δVC_{MODIS} (K)	29	-	1.2	1.1	-	1.2	1.1
	31	-	1.1	1.0	-	1.1	1.0
	32	-	1.2	1.1	-	1.2	1.1
δVC_{ETM+} (K)	6	0.7	0.7	0.8	0.8	0.8	-
δVC_{TIRS} (K)	10	-	0.8	0.8	0.9	0.8	-
	11	-	0.9	1.0	1.0	1.0	-

Values between 0.7-1.2 K are expected for the VC uncertainty. It should be noted that the brightness temperature inaccuracy in the EO sensors above that values can be detected in our test sites. If sensor band inaccuracy is below, the results must be accepted as valid and radiance correction should not be implemented at the sensor band. Results are a preliminary test of the VC suitability and should not be considered as a final VC uncertainty as it will be retrieved statistically in the VC process.

Validation expected uncertainties for our algorithms are also obtained with the root sum square of the algorithm uncertainty (extracted from Table 1.8), INH index (see Table 4.11) and atmospheric uncertainty (Table 5.1 and 5.2). Because TES algorithm does not have theoretical algorithm uncertainty – as it use the RTE for each sensor thermal band –, TES uncertainty was computed as a RTE uncertainty plus the emissivity MMD contrast uncertainty (0.3 K).

Table 5.4 shows validation expected uncertainties separated for two atmospheric w values (above and below 1.6 g/cm^2).

Table 5.4. Expected uncertainty associated to LST algorithms for atmospheric w below 1.6 g/cm^2 and, in brackets, for w above 1.6 g/cm^2 . The values are given in Kelvin.

	Band	El Cruce	Las Tiasas	Fuente Duque	Cortes	Junca balejo	Balsa Blanca
δVC_{MODIS} (K)	SW	-	2.1	2.1	-	2.1	2.1
	MOD11	-	1.4	1.2	-	1.3	1.3
	TES	-	1.2 (1.5)	1.1 (1.4)	-	1.2 (1.5)	1.1 (1.4)
δVC_{ETM+} (K)	SC _w	1.3 (3.0)	1.3 (3.0)	1.4 (3.2)	1.3 (3.2)	1.4 (3.2)	-
	RTE/SC	0.7 (1.1)	0.7 (1.1)	0.8 (1.2)	0.8 (1.2)	0.8 (1.2)	-
δVC_{TIRS} (K)	SC _w	-	1.5 (1.5)	1.6 (1.7)	1.5 (1.7)	1.6 (1.7)	-
	RTE	-	0.8 (1.1)	0.8 (1.1)	0.9 (1.2)	0.8 (1.1)	-
	SW	-	1.7	1.7	1.7	1.7	-

It is noticed that the lowest validation uncertainty is expected for RTE and for Landsat sensors (between 0.8-1.2 K, depending of atmospheric w) while for MODIS the lowest expected validation uncertainty is shared by MOD11 and TES product (1.1-1.5 K). As is expected, the highest values are retrieved for SC_w algorithms with expected uncertainties of 1.7 K (band 10 TIRS) and 3.2 K (band 6 ETM+). As the atmospheric w content has a minimal influence in SW algorithm, its uncertainty remains constant. These values are expected values which can meet (or not) with the statistical values of validation procedure.

5.2. VICARIOUS CALIBRATION

5.2.1. ETM+ and TIRS

Predicted at-sensor radiances through inverse RTE have been compared to the values registered with ETM+ and TIRS in order to retrieve the calibration assessment. ETM+ was evaluated with three different atmospheric profiles while TIRS atmospheric correction was performed with reanalysis NCEP data.

Thirty-five predicted radiances for three atmospheric profiles – MOD07 version 5 and 6 and reanalysis NCEP data – and forty-four TIRS values were used for the VC. Because of the high amount of in-situ and Landsat's data used in VC, Appendix A shows the registered values through the years 2013 to 2016. Specifically, Appendix A shows in Table A1 and A2 the ETM+ values and in Table A3 and A4 the TIRS registers. Data considered for VC is marked in bold type – w below 1.6 g/cm^2 .

The results for each station are presented in Figure 5.4 and 5.5 and in Tables 5.5 and 5.6. Details of bias, 1-sigma standard deviation (σ), slope, coefficient of determination (R^2) and RMSE are given in Table 5.7. Predicted and L7 derived radiances show a high linear correlation, with values for each profile within the 1:1 line. Results show an almost constant bias below $-0.03 \text{ W}\cdot\text{m}^{-2}\cdot\text{sr}^{-1}\cdot\mu\text{m}^{-1}$ or -0.2 K (see Figure 5.4 and Table 5.7) that underestimate radiance values (bias was calculated as ETM+ radiance minus predicted VC radiance). As Table 5.5 shows, there are no significant differences (less than 0.2 K) between the atmospheric profiles. Furthermore, differences of less than 0.5 K in bias and standard deviation were obtained comparing the VC for each station. Because the magnitude of retrieved bias is lower than the uncertainty of VC (σ), the bias was considered negligible for the algorithms validation.

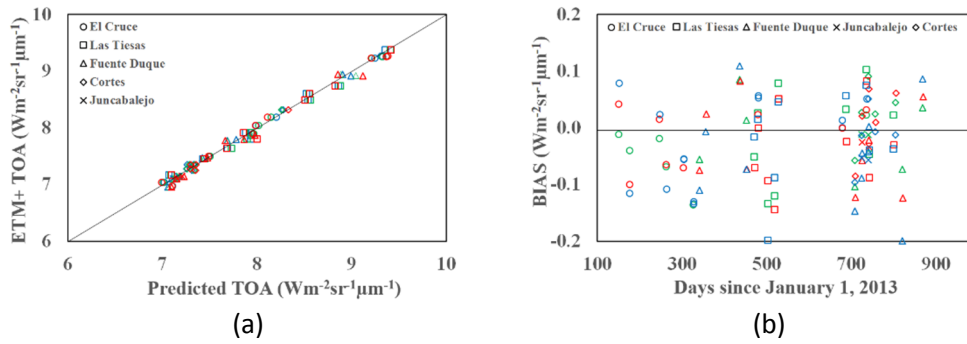


Figure 5.4. VC results for L7 ETM+ sensor: (a) is the sensor radiance versus the VC-based (TOA predicted) radiance, (b) is the plot of residual bias error through three years. Results present values for each test site and for three atmospheric profiles: In red: NCEP data, in blue: MOD07 version 6 data and in green: MOD07 version 5 data.

Table 5.5. Results of VC for three atmospheric profiles between L7 ETM+ versus TOA predicted radiance data. N is the number of data used in VC and, in brackets, the data considered in each fixed station. Bias and σ (1-sigma standard deviation) are given in W·m⁻²·sr⁻¹·μm⁻¹ and, in brackets, the temperature equivalency at 300 K is also included.

N=35	MOD07 v5		MOD07 v6		NCEP	
	Bias	σ	Bias	σ	Bias	σ
El Cruce (9)	-0.03 (-0.2)	0.06 (0.5)	-0.03 (-0.2)	0.06 (0.5)	-0.02 (-0.2)	0.08 (0.7)
Las Tiasas (9)	-0.01 (-0.1)	0.08 (0.7)	-0.04 (-0.3)	0.07 (0.6)	-0.02 (-0.2)	0.08 (0.7)
Fuente Duque (9)	-0.01 (-0.1)	0.06 (0.5)	-0.03 (-0.3)	0.08 (0.7)	-0.05 (-0.4)	0.10 (0.8)
Cortes (6)	0.03 (0.2)	0.05 (0.5)	0.01 (0.1)	0.06 (0.5)	-0.02 (-0.1)	0.05 (0.4)
Juncabalejo (2)	-0.01 (-0.1)	0.04 (0.4)	-0.03 (-0.3)	0.05 (0.4)	-0.06 (-0.5)	0.05 (0.4)

In the case of TIRS, RMSE variability (see Table 5.6) between stations show minimal differences (below 0.4 K) for both bands, and stray light effect is minimal and very equal for our stations, probably due to the surroundings of the considered image which are similar to our plots. Predicted and TIRS-derived radiances show also a high linear correlation, with values for band 11 showing more scatter than band 10. For this reason, grouping the station values, Table 5.8 shows bias values for two bands and for three reference brightness temperature. It can be appreciated that TIRS overestimates radiance values for brightness temperature above 300 K and underestimates below 295 K. These differences are clearer in the band 11, where the bias is more brightness temperature dependent.

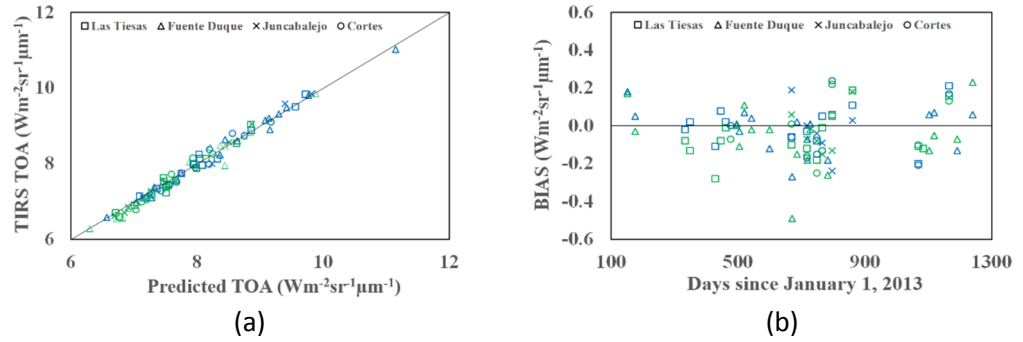


Figure 5.5. VC results for L8 TIRS sensor: (a) sensor radiance versus the VC-based (TOA predicted) radiance and (b) plot of residual bias error through three years. Results present plots for each test site and for the two thermal bands: band 10 in blue and band 11 in green color.

Table 5.6. Results of VC between L8 TIRS versus in situ predicted radiance data for four Spanish test sites. N is the number of data used in VC and, in brackets, the data considered in each fixed station. Bias, σ and RMSE are given in $W \cdot m^{-2} \cdot sr^{-1} \cdot \mu m^{-1}$ and, in brackets, the temperature equivalency at 300 K is included too.

N=44		Las Tiesas (14)	Fuente Duque (16)	Juncabalejo (5)	Cortes (8)
VC _{B10}	Bias	-0.01 (-0.1)	-0.01 (-0.1)	-0.07 (-0.5)	-0.04 (-0.3)
	σ	0.11 (0.8)	0.11 (0.8)	0.11 (0.8)	0.16 (1.1)
	RMSE	0.11 (0.8)	0.11 (0.8)	0.13 (1.0)	0.17 (1.2)
VC _{B11}	Bias	-0.06 (-0.5)	-0.06 (-0.5)	-0.05 (-0.4)	-0.04 (-0.3)
	σ	0.13 (1.1)	0.17 (1.4)	0.13 (1.1)	0.16 (1.3)
	RMSE	0.14 (1.2)	0.18 (1.5)	0.13 (1.1)	0.16 (1.3)

Table 5.7. VC summary of the L7 ETM+ sensor (see Table 5.5) and L8 TIRS (see Table 5.6). Bias, σ and RMSE are given in radiances ($W \cdot m^{-2} \cdot sr^{-1} \cdot \mu m^{-1}$) and, in brackets, the equivalency in temperatures at 300 K is also shown.

			Slope	R ²	bias	σ	RMSE
L8 TIRS	VC _{B10}	NCEP	1.018±0.016	0.985	-0.01 (-0.1)	0.11 (0.8)	0.12 (0.9)
		NCEP	1.073±0.028	0.973	-0.05 (-0.4)	0.14 (1.2)	0.15 (1.3)
	VC _{B11}	NCEP	1.003±0.019	0.991	-0.03 (-0.2)	0.08 (0.7)	0.09 (0.7)
L7 EMT+	VC _{B6}	MOD v6	1.006±0.016	0.990	-0.03 (-0.2)	0.07 (0.6)	0.07 (0.6)
		MOD v5	1.006±0.015	0.991	-0.01 (-0.1)	0.06 (0.5)	0.06 (0.5)

CHAPTER 5: VC AND LST/SST VALIDATION

Table 5.8. Bias (TIRS minus VC) values for three different brightness temperature measured in Kelvin. The results are given in radiances ($\text{W}\cdot\text{m}^{-2}\cdot\text{sr}^{-1}\cdot\mu\text{m}^{-1}$) and, in brackets, the equivalency in temperatures (K).

		Brightness Temperature (K)		
		Bands	280	295
Radiance (Temperature) Offset	B10	-0.04 (-0.2)	-0.01 (-0.1)	0.03 (0.2)
	B11	-0.11 (-0.9)	0.00 (0.0)	0.10 (0.8)

Finally, results presented in Table 5.7 show an almost average bias – calculated as TIRS radiance minus predicted (VC) radiance – for band 11 of $-0.05 \text{ W}\cdot\text{m}^{-2}\cdot\text{sr}^{-1}\cdot\mu\text{m}^{-1}$ or -0.6 K , whereas the bias for band 10 is close to zero. Because the magnitude of standard deviation is greater than the bias (σ of 0.8 K and 1.2 K for band 10 and 11 respectively), it can be considered negligible for both bands.

To end the analysis of Landsat's sensors, the statistical VC uncertainty agrees with the expected uncertainty retrieved in Section 1, with statistical values of $0.5\text{-}0.7 \text{ K}$ vs predicted values of 0.7 K for ETM+, 0.8 K (statistical) vs 0.9 K (predicted) for TIRS band 10 and a slightly underestimation in the case of TIRS band 11 (1.2 K , statistical vs 1.0 K , predicted) probably due to stray light influence.

5.2.2. MODIS

Predicted radiances (398 for Aqua and 381 for Terra platform) for the three MODIS TIR bands – with the respective in-situ measurements – were compared for the VC. Figure 5.6 and Table 5.9 show the results obtained for each band and station. Excluding Las Tiesas station, – which results differ in comparison to other stations – RMSE variability show minimal differences (below 0.3 K) for the considered bands, even between day and night values. Night performance, due to increase of homogeneity, is slightly better than the daytime result. Bias differences between stations are below 0.7 K while day-night gap shows values below 1.0 K in the same station. These biases gap are expected as the expected uncertainty retrieved in Section 5.1 (approximately 1.0 K) barely differs from these values. Fuente Duque shows the highest day-night range (1.0 K) while Balsa Blanca demonstrates to be the more stable (0.2 K).

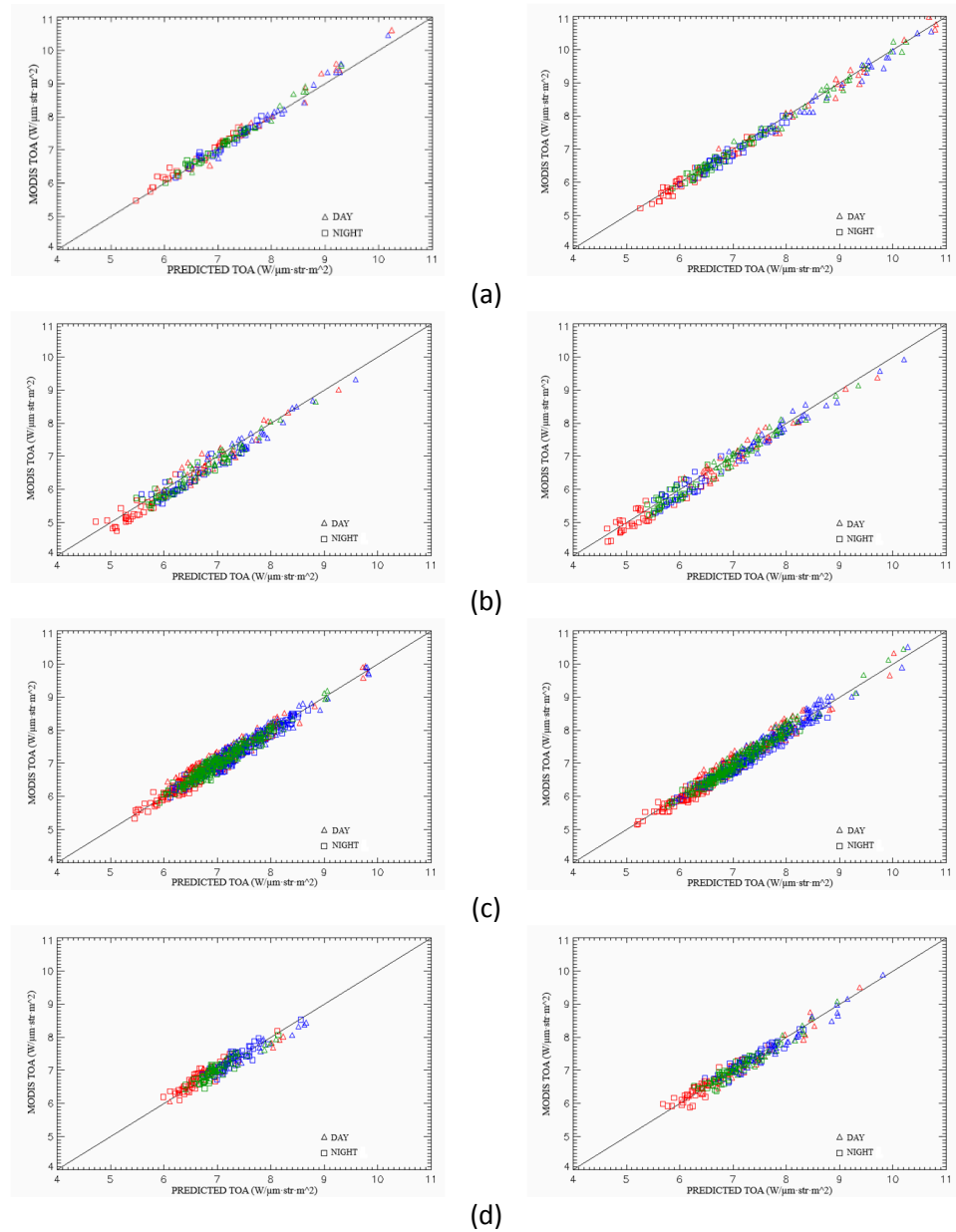


Figure 5.6. Comparison of MODIS Terra (left side) and Aqua (right side) radiances versus the VC-based (TOA predicted) radiances. Results are presented for each test site – (a) Balsa Blanca (b) Las Tiasas (c) Fuente Duque (d) Juncabalejo – and band, where colors symbolize the band 29 (in red), band 31 (in blue) and band 32 (in green). A say-night split was also differenced in the figures.

CHAPTER 5: VC AND LST/SST VALIDATION

Table 5.9. Results of the MODIS VC – Terra and Aqua platforms – at four Spanish test sites and for the three TIR bands (29, 31 and 32) considered in this work. Bias, σ and RMSE are given in $W \cdot m^{-2} \cdot sr^{-1} \cdot \mu m^{-1}$ and, in brackets, the equivalency in temperature at 300 K is also given. The values have been divided for day and night periods. At the bottom part of the table, the number of values (N) used in the VC is shown.

		Period	Balsa Blanca	Fuente Duque	Juncabalejo	Las Tiesas
Terra VC_{B29}	Bias	Day	0.08 (0.5)	0.08 (0.5)	0.06 (0.3)	-0.04 (-0.2)
		Night	0.08 (0.5)	0.00 (0.0)	0.10 (0.6)	-0.11 (-0.7)
	Sigma	Day	0.14 (0.8)	0.15 (0.9)	0.15 (0.9)	0.16 (0.9)
		Night	0.09 (0.6)	0.12 (0.7)	0.12 (0.7)	0.16 (0.9)
	RMSE	Day	0.16 (0.9)	0.17 (1.0)	0.16 (0.9)	0.17 (1.0)
		Night	0.12 (0.7)	0.12 (0.7)	0.16 (0.9)	0.19 (1.1)
Terra VC_{B31}	Bias	Day	0.04 (0.3)	0.04 (0.3)	-0.01 (-0.1)	-0.11 (-0.8)
		Night	0.03 (0.2)	-0.05 (-0.4)	0.02 (0.1)	-0.16 (-1.2)
	Sigma	Day	0.10 (0.7)	0.13 (1.0)	0.14 (1.0)	0.14 (1.0)
		Night	0.08 (0.6)	0.11 (0.8)	0.12 (0.9)	0.15 (1.1)
	RMSE	Day	0.11 (0.8)	0.14 (1.0)	0.14 (1.0)	0.18 (1.3)
		Night	0.09 (0.7)	0.12 (0.9)	0.12 (0.9)	0.22 (1.6)
Terra VC_{B32}	Bias	Day	0.07 (0.6)	0.06 (0.5)	0.01 (0.1)	-0.09 (-0.8)
		Night	0.05 (0.4)	-0.02 (-0.2)	0.04 (0.3)	-0.12 (-1.0)
	Sigma	Day	0.09 (0.8)	0.11 (0.9)	0.12 (1.0)	0.12 (1.0)
		Night	0.07 (0.6)	0.09 (0.8)	0.11 (0.9)	0.14 (1.2)
	RMSE	Day	0.11 (0.9)	0.13 (1.1)	0.12 (1.0)	0.15 (1.3)
		Night	0.09 (0.8)	0.09 (0.8)	0.12 (1.0)	0.19 (1.6)
Aqua VC_{B29}	Bias	Day	-0.04 (-0.2)	0.05 (0.3)	-0.04 (-0.2)	-0.02 (-0.1)
		Night	-0.05 (-0.3)	0.08 (0.5)	0.08 (0.5)	-0.04 (-0.2)
	Sigma	Day	0.12 (0.7)	0.16 (0.9)	0.13 (0.8)	0.16 (0.9)
		Night	0.11 (0.7)	0.11 (0.7)	0.12 (0.7)	0.20 (1.2)
	RMSE	Day	0.13 (0.8)	0.17 (1.0)	0.13 (0.8)	0.16 (0.9)
		Night	0.12 (0.7)	0.13 (0.8)	0.14 (0.8)	0.21 (1.2)
Aqua VC_{B31}	Bias	Day	-0.07 (-0.5)	0.01 (0.1)	-0.08 (-0.6)	-0.05 (-0.3)
		Night	-0.08 (-0.6)	-0.12 (-1.0)	0.01 (0.1)	-0.06 (-0.4)
	Sigma	Day	0.10 (0.7)	0.14 (1.0)	0.12 (1.0)	0.13 (1.0)
		Night	0.11 (0.8)	0.10 (0.7)	0.12 (0.9)	0.20 (1.4)
	RMSE	Day	0.13 (1.0)	0.14 (1.0)	0.15 (1.1)	0.14 (1.0)
		Night	0.14 (1.0)	0.15 (1.1)	0.12 (0.9)	0.21 (1.5)
Aqua VC_{B32}	Bias	Day	-0.02 (-0.2)	0.03 (0.3)	-0.05 (-0.4)	-0.02 (-0.2)
		Night	-0.05 (-0.4)	-0.08 (-0.7)	0.03 (0.3)	-0.04 (-0.3)
	Sigma	Day	0.08 (0.7)	0.12 (1.0)	0.12 (1.0)	0.12 (1.0)
		Night	0.09 (0.8)	0.09 (0.8)	0.10 (0.9)	0.17 (1.5)
	RMSE	Day	0.09 (0.8)	0.12 (1.0)	0.13 (1.1)	0.12 (1.0)
		Night	0.11 (0.9)	0.12 (1.0)	0.10 (0.9)	0.18 (1.6)
N_{TERRA}	(Day, Night)	(12, 30)	(67, 159)	(26, 41)	(22, 24)	
N_{AQUA}	(Day, Night)	(18, 44)	(77, 130)	(30, 42)	(30, 27)	

Precision value of Las Tiesas station – between 0.9-1.5 K (see Table 5.9) – was slightly higher than expected – 1.1-1.2 K (see Table 5.3) – which probably is due to the change on INH index year after year. Las Tiesas lays on an agricultural area, where the distribution of crops and fallows change yearly (even in autumn and winter). Because of this, the INH index at Barrax is not stable – for low resolution sensors – and should be controlled yearly for a precise prediction.

Finally, summarizing the results in Table 5.10, mean values for each band and platform were estimated. Biases of Aqua bands present values of -0.1 to 0.2 K while Terra shows values range of -0.4 to -0.1. As the case of Landsat’s sensors, the magnitude of standard deviation is greater than the bias (σ is approximately 0.8-1.0 K) and then the inaccuracy can be considered negligible for all the bands.

Table 5.10. VC summary of Table 5.9. Bias, standard deviation and RMSE are given in radiances ($W \cdot m^{-2} \cdot sr^{-1} \cdot \mu m^{-1}$) and, in brackets, the equivalency in temperatures at 300 K is also given.

Platform		n	slope	R ²	bias	σ	RMSE
Terra	B29		1.002±0.014	0.98	-0.02 (-0.1)	0.13 (0.8)	0.13 (0.8) / (0.7)*
	B31	381	0.998±0.016	0.98	-0.06 (-0.4)	0.12 (1.0)	0.14 (1.0) / (0.8)*
	B32		1.009±0.011	0.98	-0.03 (-0.3)	0.11 (0.9)	0.11 (0.9) / (0.8)*
Aqua	B29		1.012±0.019	0.97	0.03 (0.2)	0.14 (0.8)	0.15 (0.9) / (0.8)*
	B31	398	1.014±0.018	0.96	-0.02 (-0.1)	0.13 (1.0)	0.13 (1.0) / (0.7)*
	B32		1.018±0.016	0.97	0.00 (0.0)	0.12 (1.0)	0.12 (1.0) / (0.8)*

* Without Las Tiesas test site

5.3. DIRECT VALIDATION

The algorithms presented in Chapter 1 were tested with the in-situ data measured by our fixed stations or buoys. The results have been presented by sensors, indicating in each case the performance of the algorithms.

5.3.1. ETM+ LST algorithms

Table 5.11 shows the validation results with ground-based measurements of the RTE and SC algorithms. Detailed in-situ and ETM+ data can be found in Appendix A (Table A1 and A2). Because LST uncertainty increases with the amount of w (and also with

CHAPTER 5: VC AND LST/SST VALIDATION

the LST, see Figure 5.7), the validation was separated in three ranges as has been done for the VC.

All LST methods provide similar results when w content is low, with RMSE below 1.0 K and 1-sigma standard deviation around 0.7 K. Note that the bias changes with the algorithm: RTE and SC_{ψ} algorithm show positive values near 0.3 K while for SC_w algorithm it is negative or near zero. When the w content increases, the magnitude of the bias gets larger and turns negative, especially for SC_w datasets (see Figure 5.7). σ values increase for all the algorithms with greater or lesser extension depending on the atmospheric datasets considered.

Table 5.11. Comparison between Land Surface Temperatures measured in situ (LST_{SITU}) and LST obtained with different algorithms (LST_{ALG}) (RTE: inversion of the Radiative Transfer Equation; SC_{ψ} : Single-Channel general algorithm; SC_w : Single-Channel water vapor approximation algorithm, where the sub index indicates the atmospheric dataset used in the approximation). The algorithms were tested with MOD07 profiles and reanalysis data. Validation was performed for three total atmospheric water vapor content ranges: below 1.5 g/cm^2 (with $N=35$ values), above 1.5 g/cm^2 (with $N=29$ values) and all data.

Atmospheric Profile	Algorithm	$\Delta LST_{SITU-LST_{ALG}} \text{ (K)}$								
		$w < 1.5 \text{ g/cm}^2$			$w > 1.5 \text{ g/cm}^2$			w		
		bias	σ	RMSE	bias	σ	RMSE	bias	σ	RMSE
MOD v5	RTE	0.2	0.8	0.8	-0.1	1.6	1.7	0.0	1.3	1.3
	SC_{ψ}	0.1	0.8	0.8	-0.4	1.7	1.7	-0.1	1.3	1.3
	SC_w_{STD}	-0.3	1.0	1.0	-3.2	2.5	4.0	-1.5	2.3	2.8
	SC_w_{TIGR61}	-0.2	1.0	1.0	-2.7	2.2	3.5	-1.3	2.0	2.4
	$SC_w_{TIGR1761}$	-0.3	1.0	1.0	-3.7	2.5	4.5	-1.7	2.5	3.0
	$SC_w_{TIGR2311}$	0.0	1.0	1.0	-2.5	2.3	3.4	-1.0	2.1	2.4
MOD v6	RTE	0.1	0.8	0.8	-0.7	2.1	2.2	-0.2	1.6	1.6
	SC_{ψ}	0.1	0.8	0.8	-1.0	2.2	2.4	-0.4	1.7	1.7
	SC_w_{STD}	-0.5	0.8	1.0	-2.7	3.3	4.3	-1.4	2.5	2.9
	SC_w_{TIGR61}	-0.3	0.8	0.9	-2.2	2.9	3.7	-1.1	2.3	2.5
	$SC_w_{TIGR1761}$	-0.5	0.9	1.0	-3.2	3.4	4.6	-1.6	2.7	3.1
	$SC_w_{TIGR2311}$	-0.2	0.9	0.9	-2.0	3.1	3.7	-0.9	2.3	2.5
NCEP	RTE	0.3	0.7	0.8	0.3	1.4	1.5	0.3	1.2	1.2
	SC_{ψ}	0.3	0.7	0.8	0.1	1.5	1.5	0.2	1.2	1.2
	SC_w_{STD}	-0.5	0.7	0.8	-1.5	2.2	2.6	-1.0	1.7	2.0
	SC_w_{TIGR61}	-0.3	0.7	0.7	-1.3	2.0	2.4	-0.8	1.6	1.8
	$SC_w_{TIGR1761}$	-0.4	0.7	0.8	-2.0	2.3	3.0	-1.2	1.9	2.3
	$SC_w_{TIGR2311}$	-0.1	0.7	0.7	-1.0	2.1	2.3	-0.5	1.7	1.8

In order to show how the atmospheric differences in w values generate differences in the LST retrievals, Table 5.12 shows how LST change (for RTE and for SC_w algorithm) in comparison to w differences between atmospheres.

Table 5.12. LST differences obtained by applying different atmospheric profiles to RTE and SC_w algorithm. Δ_{ATM} is the difference between: MOD07 version 5 (M5) profile, MOD07 version 6 (M6) profile and reanalysis (NCEP) profile. Δ (difference), σ (1-sigma standard deviation) and RMSE (Root mean square error) are the statistics of atmospheric comparison for water vapor total column (w), inversion of the Radiative Transfer Equation (RTE) and Single-Channel water vapor approximation algorithm for a TIGR2311 dataset. Results are separated for three total atmospheric water vapor content ranges: below 1.5 g/cm^2 (N=34), above 1.5 g/cm^2 (N=29) and all data.

		$w < 1.5 \text{ g/cm}^2$			$w > 1.5 \text{ g/cm}^2$			All w		
		Δ	σ	RMSE	Δ	σ	RMSE	Δ	σ	RMSE
$\Delta_{ATM}_{M5-NCEP}$	$w \text{ (g/cm}^2\text{)}$	0.1	0.2	0.3	0.2	0.4	0.5	0.2	0.3	0.3
	RTE (K)	0.3	0.5	0.5	0.7	0.7	1.0	0.5	0.6	0.8
	SC_w TIGR (K)	-0.1	0.2	0.2	-1.1	1.4	1.8	-0.5	1.1	1.2
$\Delta_{ATM}_{M6-NCEP}$	$w \text{ (g/cm}^2\text{)}$	0.0	0.2	0.2	0.1	0.4	0.4	0.0	0.3	0.3
	RTE (K)	0.1	0.4	0.4	1.0	1.2	1.6	0.5	1.0	1.1
	SC_w TIGR (K)	0.0	0.1	0.1	-0.9	1.3	1.5	-0.4	1.0	1.1
Δ_{ATM}_{M5-M6}	$w \text{ (g/cm}^2\text{)}$	0.2	0.1	0.2	0.1	0.2	0.2	0.1	0.2	0.3
	RTE (K)	0.2	0.3	0.3	-0.7	0.9	1.1	-0.2	0.8	0.8
	SC_w TIGR (K)	-0.1	0.2	0.2	-0.2	1.1	1.1	-0.1	0.8	0.8

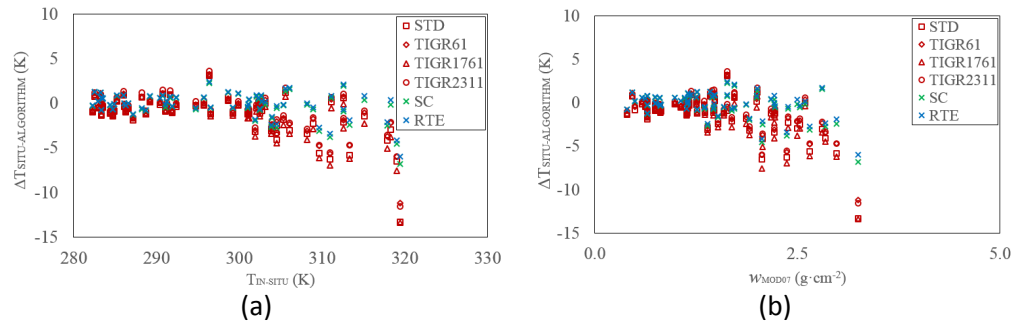


Figure 5.7. Plots of in-situ LST minus algorithm LST versus: (s) in-situ LST measurements and (b) MOD07 v6 atmospheric w content.

CHAPTER 5: VC AND LST/SST VALIDATION

For RTE, the divergence between w atmospheric profiles (see Table 5.12) generates differences three times greater between high and low atmospheric w content (RMSE change from 0.3-0.5 K for $w < 1.5 \text{ g/cm}^2$ to 1.0-1.6 K for $w > 1.5 \text{ g/cm}^2$). These differences between high and low w becomes more important for SC_w as the uncertainty in LST increases nearly 10 times from 0.1-0.2 K for $w < 1.5 \text{ g/cm}^2$ to 1.1-1.8 K for $w > 1.5 \text{ g/cm}^2$. This means that the atmospheric contribution between atmospheres to the SC_w validation RMSE of Table 5.11 represents approximately 15-20% for low w (0.1-0.2 K of 0.8-1.0 K) but increases dramatically for high w (1.1-1.8 K of 2.3-3.7 K) up to 50%, while the contribution to the RTE remains constant, around 50-60% (0.3-0.5 K of 0.8 K and 1.0-1.6 K of 1.5-2.2 K). RTE/ SC_ψ algorithms are more stable, independently of the atmospheric profile chosen.

In general, for low w content, all the atmospheric profiles retrieve similar results, but for high w content, NCEP has demonstrated the best performance, especially for the SC_w algorithm with RMSE differences of 1.0 K or more in contrast to MOD07 profiles. Two factors can be considered to explain these differences. The first one, which agrees with Jiménez-Muñoz et al. (2010), is the mean overestimation of the atmospheric w content of 0.1-0.2 g/cm^2 in comparison to the NCEP estimation (see Δw in Table 5.12 for high w). This implies an overestimation in the LST of 1.1 K for MOD07 v5 and 0.9 K for MOD07 v6 (see Table 5.12). The second one implies the atmospheric profiles obtained with the MOD07 product. High differences in comparison to the NCEP profiles were observed in the last atmospheric pressure levels (from 1000 hPa to 800 hPa) for the air temperature (approximately 5 K) and for the dew point temperature data. These differences, more pronounced in the MOD07 version 6 on August 4, 2014 in Cortes and on July 6 and 22, 2015 in Fuente Duque (see Table 5.13), are the cause of the underestimation and overestimation of the τ and w parameters respectively. Consequently, the LST is overestimated for the SC_w algorithm and inversion of the RTE. These extreme values have been observed in the Section 5.1 where a few high w values were detected in the coastal (Murcia) atmospheric profiles.

Additionally, in the values shown into Table 5.13, a lack of data was also observed for the first 4 pressure levels (from 5 hPa to 40 hPa) in the MOD07 v6 profiles which have influenced the results of LST retrievals. Because the MODIS sensor does not have the appropriate channels for information retrieval at the last atmospheric levels, performance of the MOD07 product in this region is poor (or lacking data as in our three cases) in comparison to NCEP or sounding data which implies in some cases large differences (25 K) in dew point data (Jiménez-Muñoz et al. 2010).

Table 5.13. Atmospheric parameters (transmissivity; up-welling radiance, given in $W \cdot \mu m^{-1} \cdot m^{-2} \cdot sr^{-1}$; total water vapor, given in g/cm^2) and LST validation of the RTE ($\Delta_{SITU-RTE}$) and the SC TIGR2311 dataset ($\Delta_{SITU-SC}$) for each Atmospheric profile (MOD07 v5, MOD07 v6 and NCEP) in Doñana test site.

Date	Profile	τ	Lu	w	$\Delta_{LST_{SITU-RTE}}$ (K)	$\Delta_{LST_{SITU-SC}}$ (K)
06 July, 2015 (Fuente Duque)	MOD5	0.72	2.27	2.86	-2.2	-8.2
	MOD6	0.61	3.29	3.25	-6.0	-11.6
	NCEP	0.70	2.64	2.74	-1.4	-7.3
22 July, 2015 (Fuente Duque)	MOD5	0.81	1.65	1.88	-2.5	-4.9
	MOD6	0.76	2.05	2.06	-4.2	-6.0
	NCEP	0.80	1.77	1.74	-1.8	-4.2
04 August, 2014 (Cortes)	MOD5	0.68	2.64	2.99	-1.6	-6.6
	MOD6	0.65	2.86	2.65	-2.8	-4.7
	NCEP	0.75	2.10	2.09	-0.3	-2.1

Excluding data showed in Table 5.13 from the validation, MOD07 v6 retrieve similar results to the MOD07 v5 product. For example, in high w values, the RMSE of inversion of the RTE, SC_ψ and SC_{wT2311} decrease from 2.2 K, 2.4 K and 3.7 to 1.5 K, 1.6 K and 2.4 K respectively, near to MOD07 v5 results (1.6 K, 1.6 K and 2.7 K for RTE, SC_ψ and SC_{wT2311} respectively).

Finally, a comparison of validation uncertainties (expected versus statistical) is shown in Table 5.14. While RTE and SC_ψ show good agreement (differences between 0.0 K to 0.4 K excluding the three extreme values of Table 5.13), SC_{wT2311} shows an overestimation of the expected uncertainty, probably due to the imprecisions in the computation of the algorithm's expected value. In the case of high w values, the agreement is more precise (3.1 K vs 3.1 K) without the exclusion of extreme values, which demonstrates the difficult of the uncertainty computation for SC_w algorithm as it needs a precise algorithm and atmospheric estimation, which is not possible attending to data range variation retrieved for the algorithm (set between 2.0-3.0 K as it is shown in Table 1.9) and the atmosphere (set between 1.5-3.1 K as it is shown in Table 5.2)

Table 5.14. Expected and statistical uncertainties for LST algorithms of ETM+ sensor for high and low atmospheric w content. In brackets, the statistical uncertainties without the three extreme values included in the Table 5.13 are also shown.

	$w < 1.5 g/cm^2$			$w > 1.5 g/cm^2$		
	RTE	SC_ψ	SC_{wT2311}	RTE	SC_ψ	SC_{wT2311}
Expected (K)	0.8	0.8	1.4	1.2	1.2	3.1
Statistical (K)	0.8	0.8	1.0	2.1 (1.5)	2.2 (1.6)	3.1 (2.4)

5.3.2. TIRS LST algorithms

Table 5.15 and Figure 5.8a show the validation for RTE and SC-SW algorithms for each fixed station. Detailed in-situ and TIRS data can be found in Appendix A (Table A3 and A4). Retrieved results show similar values of σ between stations – differences below 0.5 K – increasing for high atmospheric w content (see Figure 5.8b). SC_w contrast in σ can be observed in Juncabalejo and Fuente Duque – probably because of higher mean w in comparison to Las Tiasas (2.2-2.7 g/cm² versus 1.9 g/cm²) – while in Cortes the results are not significant because only two values are available. The high σ values in Juncabalejo are also explained because of the few data available (only four values) which is highly influenced by punctual values. Because not enough data is available for high w values, the stability of the stations was analyzed for all the w range (see Table 5.16) and for all the stations in the three w ranges proposed (see Table 5.17).

Table 5.15. Validation of TIRS LST algorithms for each station (in brackets the number of LST values analyzed for low, high atmospheric w content). Bias is the difference between in-situ LST values and estimated LST for all algorithms. All the values are given in Kelvin.

Algorithm	w (g/cm ²)	Las Tiasas (11, 4)		Fuente Duque (9, 20)		Juncabalejo (5, 4)		Cortes (7, 2)	
		< 1.6	> 1.6	< 1.6	> 1.6	< 1.6	> 1.6	< 1.6	> 1.6
	mean w	1.0	1.9	1.3	2.7	1.2	2.2	1.4	2.4
RTE	bias	0.0	0.8	0.4	-0.2	0.8	-0.6	0.1	-0.5
	σ	1.0	1.6	0.8	1.7	0.9	2.1	1.3	1.4
	RMSE	1.0	1.8	0.9	1.7	1.2	2.2	1.3	1.4
SC_w	bias	0.4	2.3	0.9	1.2	1.6	0.0	1.1	1.3
	σ	1.2	1.4	0.9	2.3	0.8	3.1	1.1	1.9
	RMSE	1.3	2.7	1.3	2.6	1.8	3.1	1.6	2.3
SW	bias	-0.7	1.0	-0.3	-0.6	0.1	-1.6	-0.2	-1.7
	σ	1.5	1.6	1.3	1.8	1.9	2.8	1.6	0.7
	RMSE	1.7	1.9	1.3	1.9	1.9	3.2	1.6	1.8

Comparing data altogether for each station, bias and σ show similar values (see Table 5.16) which demonstrates the uniformity of the station’s data. Differences below 0.5 K – except for SC_w standard deviation – were retrieved.

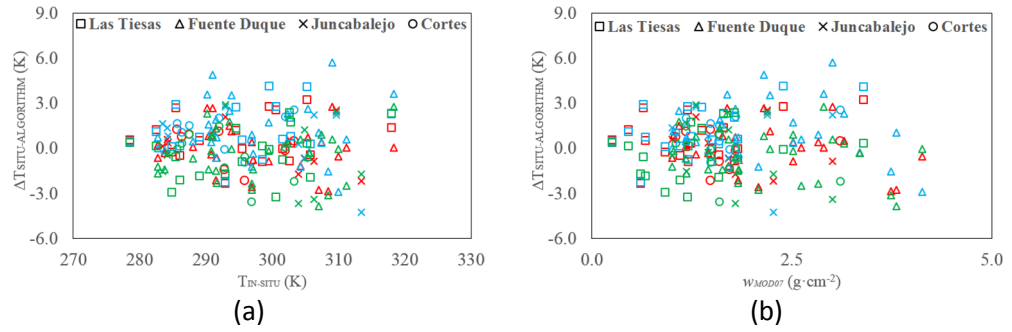


Figure 5.8. Diagrams of in-situ LST measurements minus LST retrieved by the algorithms – in blue, SC algorithm; in green SW algorithm; in red RTE – are shown in function of (a) in-situ LST and (b) atmospheric w content.

Table 5.16. Validation of TIRS LST algorithms in each station (in brackets the number of LST values analyzed). Bias is the difference between in-situ LST values minus estimated LST through the algorithms. All the values are given in Kelvin.

Algorithm		Las Tiesas (15)	Fuente Duque (29)	Juncabalejo (9)	Cortes (9)
RTE	bias	0.2	0.0	0.0	0.0
	σ	1.2	1.5	1.6	1.2
	RMSE	1.2	1.5	1.6	1.2
SC	bias	0.9	1.1	0.7	1.2
	σ	1.5	2.0	2.1	1.1
	RMSE	1.8	2.2	2.3	1.6
SW	bias	-0.2	-0.5	-0.5	-0.5
	σ	1.7	1.6	2.4	1.6
	RMSE	1.7	1.7	2.4	1.7

Taking into account the final results for each algorithm (see Table 5.17), RTE shows the lowest RMSE values while SW shows the major stability between high-low atmospheric w . In general, RMSE is below 2.0 K, with a pronounced bias for SC_w algorithm (1.0 K) which is not observed in the other algorithms. This inaccuracy is detected for all stations (0.7-1.2 K) which indicates no location or atmospheric dependence (see the bias of Table 5.17) and probably is due to algorithm sensitivity. These results are slightly higher than the validation performed over different atmospheric datasets presented in the Chapter 1 – 1.1 K vs 1.8 K for SW algorithm and 1.7 K vs 2.0 K for SC_w algorithm.

CHAPTER 5: VC AND LST/SST VALIDATION

Table 5.17. Validation of TIRS LST algorithms for three w ranges.

Algorithm	LST _{SITU} -LST _{ALG} (K)								
	$w < 1.5 \text{ g/cm}^2$			$w > 1.5 \text{ g/cm}^2$			w		
	bias	σ	RMSE	bias	σ	RMSE	bias	σ	RMSE
RTE	0.2	1.0	1.0	-0.1	1.7	1.7	0.1	1.4	1.4
SC _w	0.8	1.1	1.4	1.2	2.3	2.6	1.0	1.8	2.0
SW	-0.3	1.5	1.5	-0.6	1.9	2.0	-0.5	1.7	1.8

Note that the divergences between the VC and the validation of RTE for low w content – below 0.2 K in the standard deviation – are due to atmospheric profile (MOD07 version 6 for validation and NCEP profiles for VC). Note also that the SC_w algorithm retrieves opposite bias for ETM+ and TIRS data – negative and positive respectively – which show differences between them of more than 3.0 K for high w content. This is probably due to the atmospheric dataset used for the relationship, as is shown in the validation with simulated data in which biases higher than -1.0 K (referred to absolute values) have been obtained with other datasets used for ETM+ SC_w simulations (see Table 1.4). For TIRS, GAPRI dataset was used while for ETM+, TIGR atmospheres were fitted for w relation.

Finally, comparing the expected uncertainty results versus the σ values obtained in validation, similar results were retrieved for low w values in the RTE (0.8-0.9 K versus 0.8-1.3 K) and slightly higher prediction was obtained for SC_w (1.5 K vs 0.8-1.2 K) while for high w values, the expected values underestimate the validation uncertainty by 0.5 K in the RTE and 1.0 K in SC_w. If the expected uncertainty extreme values had been included, the gap would have been smaller (0.3 K in RTE and 0.5 K in SC_w). Finally, for the SW algorithm, little differences were observed and the expected forecast showed small differences with σ values (1.7 K vs 1.3-1.9 K).

5.3.3. MODIS LST algorithms

Figure 5.9 shows the validation results retrieved for the SW algorithms – MOD11 and Jimenez-Muñoz et al. (2011) – and the TES algorithm, which are summarized in Table 5.18. Because there is angle dependence in the validation uncertainty (see Figure 5.10) as reported by Wang et al. (2002), the data was divided in three conditions: For angles and atmospheric w content below 35° and 2 g/cm²; for angles below 35° and for all angles. The results were separated for each station and algorithm (see Appendix B, Table B1 and B2 for more detailed information).

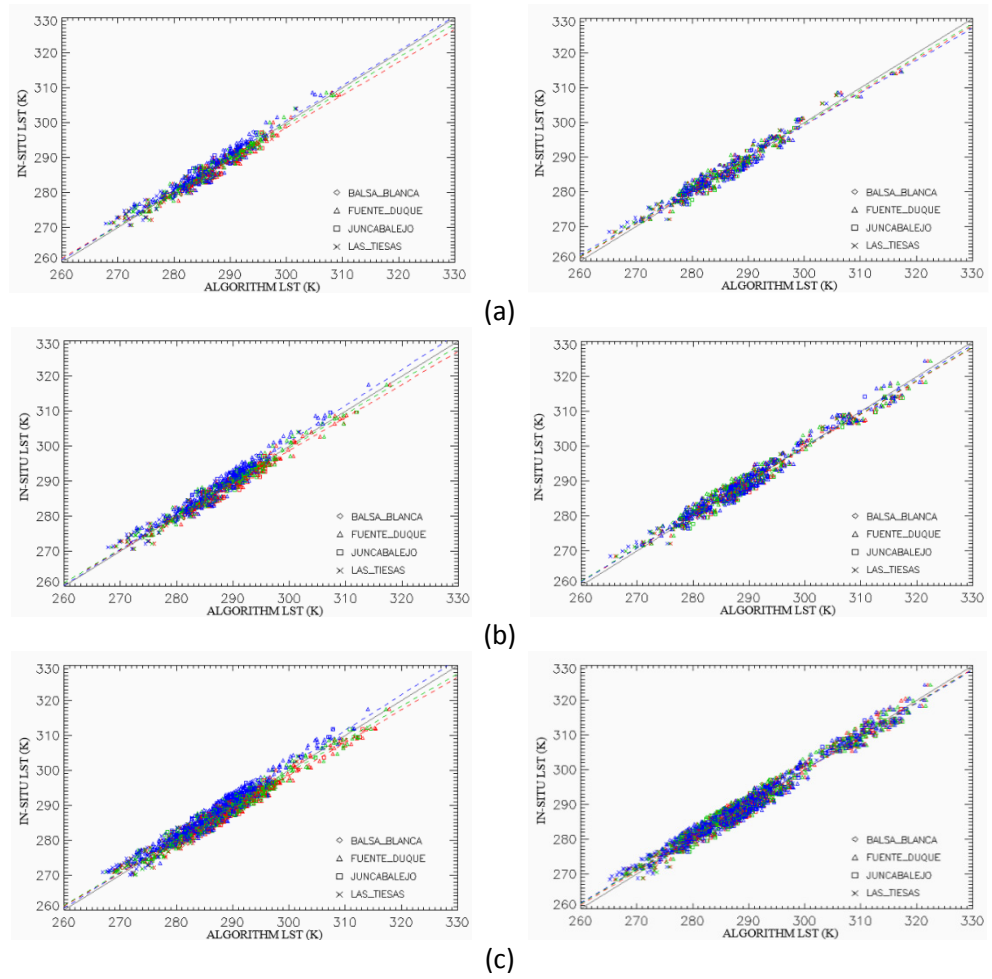


Figure 5.9. Comparison of MODIS Terra (left) and Aqua (right) LST retrievals – in blue, TES algorithm; in green MOD11 product; in red SW algorithm – versus the in-situ LST measurements. Results are presented for three different conditions: (a) $w < 2 \text{ g/cm}^2$ & $\theta < 35^\circ$ (b) $\theta < 35^\circ$ (c) $\theta < 65^\circ$.

CHAPTER 5: VC AND LST/SST VALIDATION

Table 5.18. MODIS LST algorithms versus in-situ values retrieved at our test sites. Validation was performed for three conditions and for both platforms. $\Delta_{\text{LST-ALG}}$ is the bias between in-situ LST values minus estimated LST through the algorithms.

Condition	Platform	Algorithm	n	m	r^2	$\Delta_{\text{LST-ALG}}$ (K)	σ (K)	RMSE (K)
$\theta < 35^\circ$ $w < 2 \text{ g/cm}^2$	Aqua	TES	398	0.974	0.972	0.2	1.3	1.3 (1.3)
		SW	398	0.962	0.959	0.2	1.4	1.4 (1.4)
		M11	398	0.916	0.947	0.1	1.6	1.6 (1.5)
	Terra	TES	378	0.948	0.966	-0.2	1.2	1.2 (1.2)
		SW	378	0.968	0.963	0.2	1.2	1.2 (1.2)
		M11	378	1.006	0.954	0.9	1.5	1.7 (1.7)
$\theta < 35^\circ$	Aqua	TES	559	0.974	0.976	0.2	1.4	1.4 (1.3)
		SW	559	0.973	0.970	0.3	1.5	1.6 (1.5)
		M11	559	0.976	0.968	0.2	1.6	1.6 (1.5)
	Terra	TES	499	0.979	0.984	-0.3	1.2	1.3 (1.2)
		SW	499	0.988	0.981	0.3	1.3	1.4 (1.4)
		M11	499	1.034	0.963	1.1	1.5	1.8 (1.8)
$\theta < 65^\circ$	Aqua	TES	1244	0.974	0.976	0.3	1.4	1.5 (1.4)
		SW	1244	0.968	0.974	0.5	1.5	1.6 (1.5)
		M11	1244	0.954	0.972	0.4	1.7	1.7 (1.6)
	Terra	TES	1109	0.971	0.980	-0.3	1.4	1.5 (1.4)
		SW	1109	0.989	0.976	0.2	1.5	1.5 (1.5)
		M11	1109	1.026	0.961	1.2	1.6	2.0 (2.0)

General results show a small increase in the precision value with the angle (see Figure 5.10), about 0.1-0.3 K, and minimal changes in the accuracy (0.1-0.3 K). Between algorithms, TES retrieved the highest precision but with no significant differences with the SW methods. It should be noted that MOD11 LST retrieved through Terra platform presents a noticeable bias of 1.0 K that underestimates the LST value – on Aqua platform accuracy of the algorithms is very similar. This bias increases with the LST as the slope values (1.00 to 1.03) and the left plots of the Figure 5.9 suggest and it is very similar for all of our test sites – differences of 0.5 K (see Appendix B). As for TES algorithm, bias differences reaches maximal values of 1.5 K. In comparison to SW algorithm, which shares similar mathematical structure and is based on similar physical principles, mean differences of 0.8 K are observed.

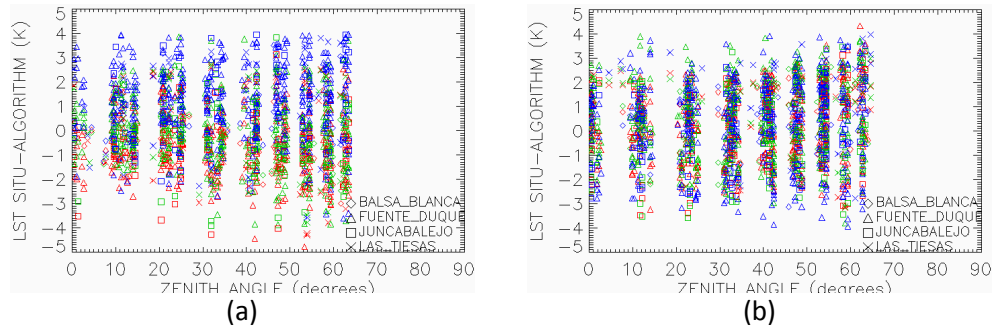


Figure 5.10. In-situ measurements minus MODIS Terra (a) and Aqua (b) LST algorithms – in blue, TES algorithm; in green MOD11 product; in red SW algorithm – versus MODIS zenith angle.

Between stations, bias differences are no higher than 0.9 K for TES algorithm, going in the worst case from -0.4 K in Juncabalejo to 0.5 K in Balsa Blanca on Aqua platform and for angle values below 35°. This bias is acceptable because it is below the precision of our validation (1.4 K). As it was mentioned in the VC section, Las Tiesas presents the highest σ values because of its higher inhomogeneity. As a validation complement (see Table 5.18) in brackets, the RMSE was also given without these data.

Precision obtained for the algorithms was in consensus with our predictions with a slightly better SW σ than expected (2.1 K versus 1.2-1.5 K) and higher σ than expected (0.2-0.3 K higher) in the MOD11 product.

5.3.4. MODIS SST algorithms

Figure 5.11 and Figure 5.12 show SST validation results for the Mediterranean Sea and Atlantic Ocean respectively. Validation was divided in two zones because of the particularity of the Mediterranean Sea – closed versus open waters – and because of NASA data, which were only extracted for the Mediterranean Sea. As is shown in the figures, the precision of the algorithms strongly depends on sensor zenith view angle and wind velocity, decreasing and increasing respectively the precision of the results. Table 5.19 shows the algorithms precision as a function of the zenith angle and Table 5.20 as a function of the wind velocity.

CHAPTER 5: VC AND LST/SST VALIDATION

On the one hand, a σ increase of 0.15-0.25 K can be observed if the measurements are taken at large zenith angles (above 55°), which is directly related with the fit uncertainty of the WPSST algorithm at large angles and with the atmospheric disturbance for both algorithms. On the other hand, for moderate wind velocities – between 4 m/s to 10 m/s – a σ decreases of 0.20-0.15 K is observed. Because of the waves movement increase at high wind velocities, the temperature layers that stratify the first meters of the sea depth break, reducing in this way the bulk-skin effect. The generated uniformity in the temperature is the cause of the precision lift. In ideal conditions – zenith angles below 45° and wind velocity between 3 m/s and 10 m/s – the precision of the algorithms reaches values for Aqua-Terra platforms of 0.522-0.558 K and 0.518-0.548 K for WPSST and NLSST algorithm respectively.

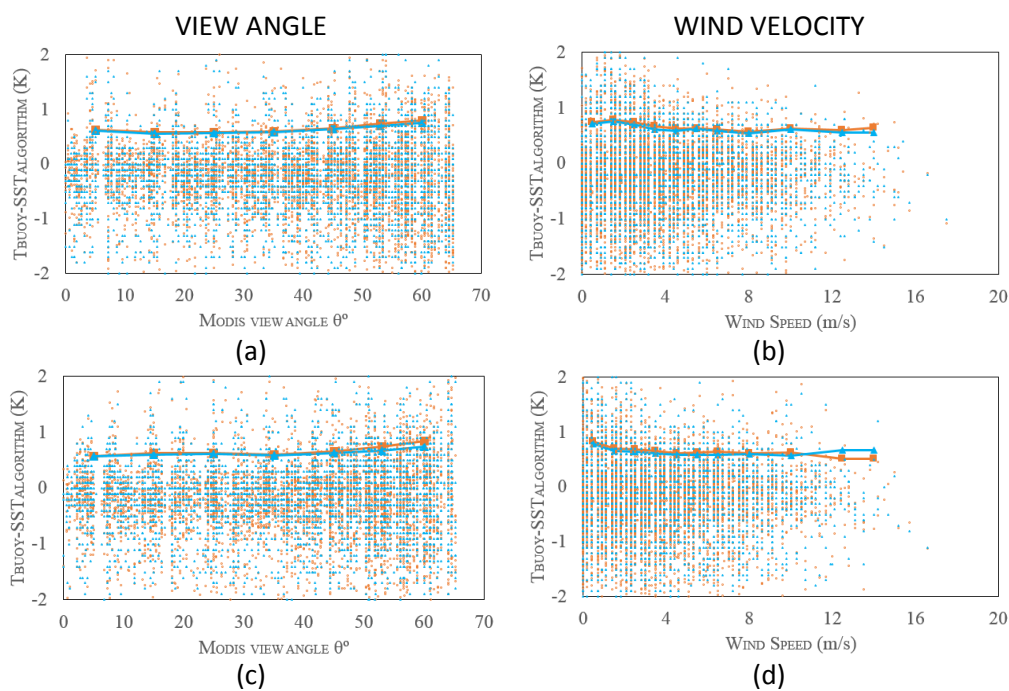


Figure 5.11. Buoy minus SST algorithm – in blue NLSST and in orange WPSST – in the Mediterranean Sea versus zenith angle (a)-(c) and wind velocity (b)-(d). Aqua is represented on (a), (b) while Terra is represented on (c)-(d).

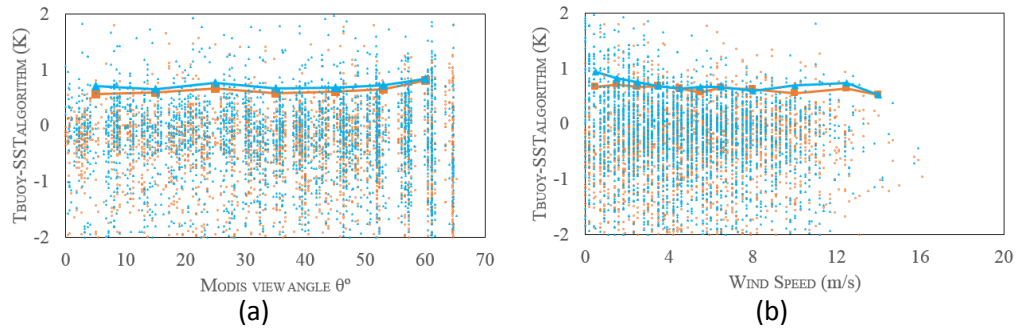


Figure 5.12. Buoy minus WPSST algorithm in the Atlantic Ocean versus (a) the zenith angle and (b) the wind velocity. Aqua is plotted in orange while Terra is plotted in blue.

Table 5.19. Results of SST validation versus MODIS zenith angle. Precision (σ) is given for each angle (in Kelvin).

	Platform	Algorithm	MODIS Zenith angle (°)						
			5	15	25	35	45	53	60
Mediterranean Sea	Aqua	WPSST	0.63	0.59	0.59	0.60	0.65	0.75	0.81
		NLSST	0.62	0.56	0.57	0.59	0.64	0.70	0.76
	Terra	WPSST	0.58	0.63	0.64	0.60	0.66	0.74	0.84
		NLSST	0.58	0.60	0.62	0.59	0.63	0.67	0.75
Atlantic Ocean	Aqua	WPSST	0.57	0.60	0.67	0.58	0.62	0.66	0.82
	Terra	WPSST	0.71	0.66	0.77	0.68	0.69	0.73	0.85

Table 5.20. Results of SST validation versus wind velocity. Precision (σ) is given for each speed (in Kelvin).

	Platform	Algorithm	Wind velocity (m/s)								
			0.5	1.5	2.5	3.5	4.5	5.5	6.5	8	>10
Mediterranean Sea	Aqua	WPSST	0.75	0.79	0.75	0.68	0.62	0.64	0.62	0.58	0.62
		NLSST	0.72	0.75	0.71	0.62	0.58	0.62	0.59	0.55	0.58
	Terra	WPSST	0.83	0.70	0.69	0.66	0.62	0.63	0.65	0.62	0.55
		NLSST	0.79	0.66	0.65	0.61	0.58	0.58	0.59	0.61	0.64
Atlantic Ocean	Aqua	WPSST	0.75	0.79	0.75	0.68	0.62	0.64	0.62	0.58	0.60
	Terra	WPSST	0.94	0.83	0.76	0.69	0.64	0.67	0.67	0.61	0.66

Results were also separated between day and night measurements avoiding in this way the influence of the solar radiation in the validation. Table 5.21 and 5.22 show the

CHAPTER 5: VC AND LST/SST VALIDATION

validation of the algorithms for daytime and nighttime data over Mediterranean Sea and Atlantic Ocean. A clear gap in the precision of day-night data of 0.06 K (Terra) and 0.12-0.15 K (Aqua) is observed in the Mediterranean Sea while in the Atlantic Ocean a difference of 0.10 K is evidenced. As solar radiation is one of the factors that induces the stratification of the sea as is reported e.g. in Gentemann et al. (2003), the precision of the algorithms is highly influenced by this factor and a decrease of the precision value is observed for nighttime measurements. With all the data, a precision of 0.67-0.68 K and 0.64 K is obtained for WPSST and NLSST algorithms respectively, which implies a better performance for NASA product of 0.03 K. This result may not be significant as the buoy temperature uncertainty measurement is ± 0.03 K.

Taking the ideal measurements conditions of zenith angle and wind velocity plus the nighttime data, σ values for Aqua-Terra platforms of 0.488-0.544 K and 0.470-0.541 K can be retrieved for WPSST and NLSST algorithm respectively. These are the maximal precision values that can be retrieved in the anchor buoys validation by both algorithms for the SST retrievals. In this case, the differences between algorithms are minimal (0.018 K for Aqua and 0.003 K for Terra).

Table 5.21. Results of SST algorithms validation with anchor buoys in the Mediterranean Sea. N is the number of data used for the validation which was splitted into day and night time values.

Platform		All		Day		Night	
		WPSST	NLSST	WPSST	NLSST	WPSST	NLSST
Aqua	Accuracy (K)	-0.226	-0.211	-0.085	-0.076	-0.406	-0.383
	Precision (K)	0.673	0.637	0.722	0.698	0.599	0.551
	N _{AQUA}	4492		2343		2148	
Terra	Accuracy (K)	-0.218	-0.141	-0.112	-0.031	-0.340	-0.268
	Precision (K)	0.683	0.641	0.714	0.668	0.642	0.605
	N _{TERRA}	4169		2123		2046	

Table 5.22. Results of Water vapor Path length SST algorithm validation with anchor buoys in the Atlantic Ocean. N is the number of data used for the validation.

Algorithm		All		Day		Night	
		Terra	Aqua	Terra	Aqua	Terra	Aqua
WPSST	Accuracy (K)	-0.189	-0.347	-0.132	-0.136	-0.434	-0.386
	Precision (K)	0.729	0.651	0.738	0.732	0.638	0.627
	N _{VALUES}	2574	2664	2084	412	489	2252

Finally, Figure 5.13 shows the biases (bulk-skin differences) obtained with the SST algorithms respect to the buoys measurements. Differences of 0.1 K to -0.2 K were observed for daytime data and values of -0.2 K to -0.5 K for nighttime. It is reported that the buoy temperature at 3 m is always lower than the skin temperature especially for nighttime periods with differences of -0.3 K (Schluessel et al. 1990). The pattern between algorithms is very similar, showing only higher differences for the lowest and highest temperatures.

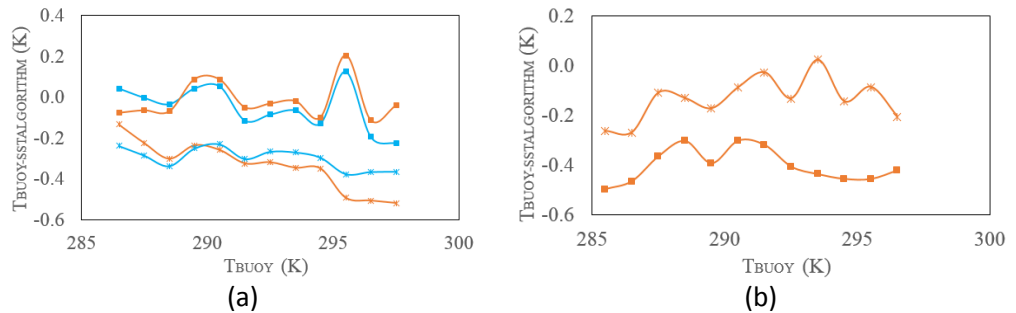


Figure 5.13. Buoy bulk temperature minus NLSST (in blue) and WPSST (in orange) SST algorithms as a function of buoy bulk temperature. Squares and crosses represent the daytime and nighttime values, respectively. Accuracy was extracted for (a) Mediterranean Sea and (b) Atlantic Ocean.

5.4. DOWN-SCALING RESULTS VALIDITY

As was commented in Chapter 3, statistical methods proposed for LST sharpening do not maintain the radiometry of the original image. Because of this, the distortion between the original (coarse resolution) and the sharpened image (thin resolution image, up-scaled to original resolution) should be retrieved over our test sites for MODIS and L8 imagery in order to quantify the uncertainty (and bias) introduced to the down-scaled images. For this reason, year 2014 data – for MODIS, 345 daytime images were computed – and all the data available between 2014 and 2016 – for L8, 69 Barrax and 54 Doñana images – were analyzed, computing for each image the accuracy and the precision (bias, σ) combined with the percentage of pixels (PPT) that show differences below 0.5 K (PPT_{0.5}) and 1.5 K (PPT_{1.5}) between original and sharpened images.

CHAPTER 5: VC AND LST/SST VALIDATION

Figure 5.14 shows σ and $PPT_{0.5}$ for MODIS and L8 images in Doñana and Barrax test site. Results show a clear seasonal pattern (for both algorithms), with high σ values and low $PPT_{0.5}$ pixels in spring and in summer images, and vice versa in autumn and winter seasons – following the LST homogeneity pattern described in the previous chapter. NNTS method presents lower σ values in all the cases, showing better $PPT_{0.5}$ especially for high solar radiation periods. Differences between methods present σ values of 0.2 K to 0.5 K (see Table 5.23) and $PPT_{0.5}$ of 10% or even 20% for L8 images (see Table 5.24). These percentages drop to 1-8% for $PPT_{1.5}$ values.

The peaks observed in Figure 5.14 are due to cloudy days, for which the uncertainty of the down-scaled images increases. Because of this, in the summary of the results shown in Table 5.23 and 5.24, a cloud percentage separation was performed. For cloudless images σ shows lowest values than for cloudy days which indicates a better performance of the algorithms for clear skies. For L8 images these difference (cloudly-cloudless) are below 0.1 K while for MODIS the reduction is more important, with decreases of 0.4 K in Doñana and 0.7 K in Barrax.

In Tables 5.23 and 5.24 and Figure 5.14 one can also observe that the down-scaled L8 images show better stability in the radiometry than the MODIS images. This means that the sharpening is more precise in middle resolution sensors than in low resolution sensors in spite of the pixel size reduction applied, which is greater in L8/TIRS (third part of the coarse LST pixel) than in MODIS (half of the coarse spatial resolution) – L8/TIRS images by a higher factor sharpened than the MODIS images.

Table 5.23. Minimal, maximal and average (σ) values obtained in the comparison of down-scaled and coarse L8/TIRS and MODIS images. Results are divided for each method, test site and two percentage range of image clouds.

Average (%) Clouds	Doñana						Barrax					
	NNTS (K)			TsHARP (K)			NNTS (K)			TsHARP (K)		
	min	max	σ	min	max	σ	min	max	σ	min	max	σ
MOD < 70%	0.35	5.40	1.29	0.43	6.24	1.84	0.41	7.72	1.69	0.45	9.48	2.13
MOD < 30%	0.35	1.47	0.87	0.43	2.68	1.30	0.41	1.50	1.00	0.45	3.03	1.27
L8 < 70%	0.12	1.39	0.35	0.17	1.64	0.57	0.13	1.40	0.59	0.20	1.95	0.99
L8 < 30%	0.12	0.77	0.33	0.17	1.10	0.55	0.13	1.09	0.50	0.20	1.65	0.89

Table 5.24. Average percentage of pixels that show radiometry changes below 0.5 K ($T_{0.5}$) and 1.5 K ($T_{1.5}$).

(% Average values)	Doñana				Barrax			
	NNTS		TsHARP		NNTS		TsHARP	
(% clouds)	$T_{0.5}$ (%)	$T_{1.5}$ (%)	$T_{0.5}$ (%)	$T_{1.5}$ (%)	$T_{0.5}$ (%)	$T_{1.5}$ (%)	$T_{0.5}$ (%)	$T_{1.5}$ (%)
MOD < 70%	56.42	97.23	44.24	91.41	55.06	96.84	46.11	88.74
MOD < 30%	61.82	98.39	50.57	94.55	58.57	97.97	51.39	94.84
L8 < 70%	93.37	99.13	80.52	98.02	88.11	98.59	67.39	92.38
L8 < 30%	93.59	99.15	80.85	98.08	89.26	98.63	68.92	92.46

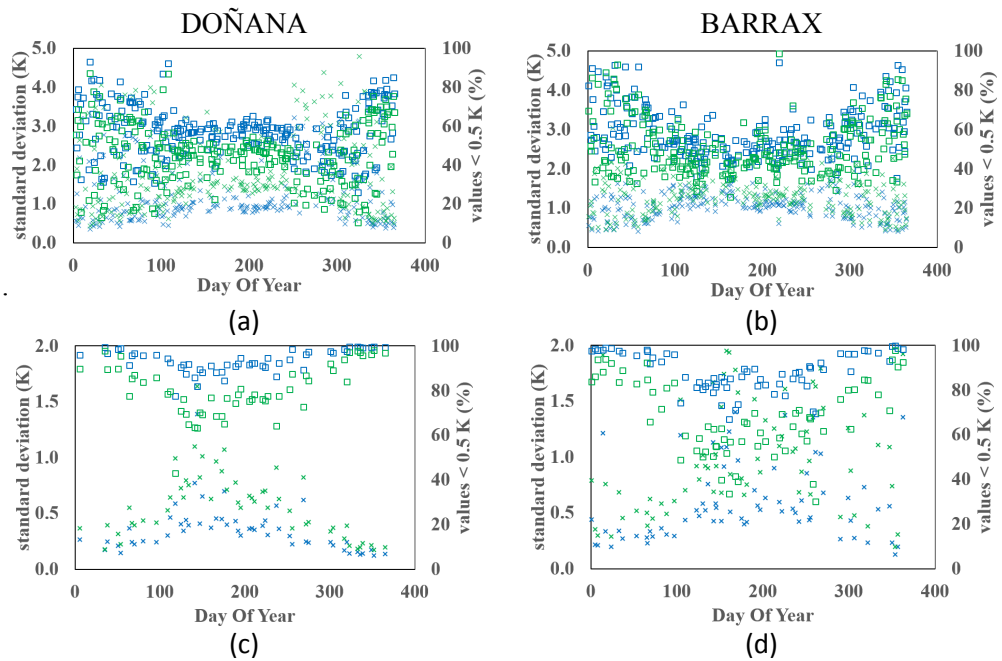


Figure 5.14. Plots of standard deviation (crosses) and percentage of values below 0.5 K (squares) between the coarse images versus the NNTS (in blue) and TsHARP (in green) sharpened images. Diagrams represent the radiometry changes on down-scaled images for Doñana and Barrax test sites. Data was extracted for year 2014 – MODIS imagery (a)-(b) – and from year 2013 to 2016 – L8 imagery (c)-(d).

Finally, it should be noted that the major part of the pixels (more than 97% in the NNTS method and above 90% in the TsHARP method) show radiometry changes

below 1.5 K and that the bias between coarse and down-scaled images is near zero. This is important because the pixel radiometry changes have, in general, less contribution to the final down-scaled LST uncertainty than the validation uncertainty obtained in the previous section – which was retrieved as 1.5-2.0 K. If radiometry changes had been greater than the validation uncertainty or bias had not been zero, those would have had high influence on the precision and accuracy of the down-scaled product.

5.5. INDIRECT VALIDATION

Direct validation has allowed us to test the performance of the algorithms over punctual landscapes and for several images in different time periods. With the indirect validation, the algorithms can be tested over a high number of pixels and, in our case, for a few air-borne images. This is another type of validation that can be considered complementary to the in-situ tests. Furthermore, the use of AHS images allows for the validation of the sharpened images, as AHS spatial resolution shows a high pixel variability which cannot be obtained with our fixed station measurements. The test of the SEVIRI SW algorithm is also included in this section.

5.5.1. TIRS

The TIRS validation was performed on May 11, 2015 over the Doñana test site. Figures 5.15 and 5.16 show the plots of the validation which are summarized in Table 5.25. Furthermore, in Appendix C (Figure C5b), the up-scaled AHS image versus the TIRS image can be found.

Bias validation results (-0.7/-0.8 K for RTE, -0.7/-0.4 for SC_w and 0.0/0.4 K for SW) at coarse spatial resolution of 90 m (close to the TIRS spatial resolution which is 100 m) are similar to the direct validation results of that day (see Appendix A, Table A3) with negative values of RTE (-0.7 K in Fuente Duque and -1.2 K in Juncabalejo) and SC_w (-0.6 K in Fuente Duque and -1.3 K in Juncabalejo) and a positive bias for SW (1.2 K in Fuente Duque and 0.6 K in Juncabalejo). Regarding the precision values, these are in agreement with the direct validation uncertainties retrieved above (see Table 5.17).

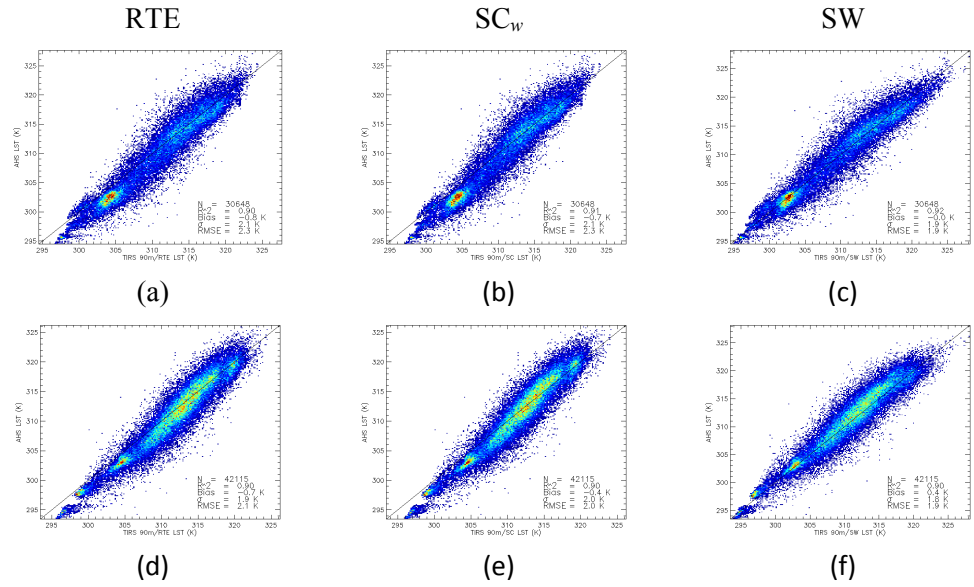


Figure 5.15. LST validation of TIRS algorithms versus AHS data. The top and bottom figures represents the AHS pass taken at 10:51 UTC and 11:09 UTC, respectively.

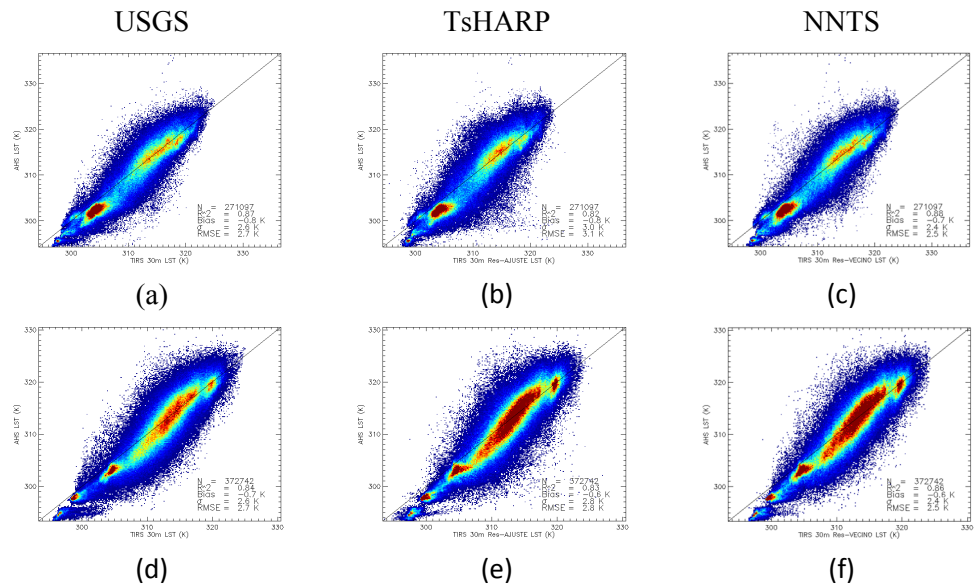


Figure 5.16. Validation of resampled LST obtained with inverse RTE versus AHS data. The top and bottom figures represents different AHS passes.

CHAPTER 5: VC AND LST/SST VALIDATION

Table 5.25. Main statistics of the up-scaling AHS process on TIRS coarse image and on sharpened images. N symbolizes the number of pixels used in the validation at 90 m and, in brackets, at 30 m. See also Figure 5.15 and 5.16.

	Statics	Δ_{sw}	Δ_{sc}	Δ_{RTE90}	Δ_{USGS}	Δ_{TsHARP}	Δ_{NNTS}
10:51 UTC	r^2	0.921	0.909	0.913	0.873	0.822	0.882
	Bias	0.0	-0.7	-0.8	-0.8	-0.8	-0.7
N=30,648	Sigma	1.9	2.1	2.1	2.6	3.0	2.4
(271,097)	RMSE	1.9	2.3	2.3	2.7	3.1	2.5
11:09 UTC	r^2	0.903	0.902	0.914	0.839	0.831	0.863
	Bias	0.4	-0.4	-0.7	-0.7	-0.6	-0.6
N=42,115	Sigma	1.8	2.0	1.9	2.6	2.8	2.4
(372,742)	RMSE	1.9	2.0	2.1	2.7	2.8	2.5

Regarding the down-scaled RTE images, in the validation it is appreciated that the bias values does not change and that the σ values are slightly higher than the coarse RTE image with increases of 0.3-1.0 K, which are expected as the up-scaling process generates uncertainties in the simulated pixel due to the imperfect combination of the high resolution pixels for the coarse pixel retrieval. Furthermore, the uncertainty of the radiometry changes must to be added in TsHARP and NNTS regression model, which in this particular image is approximately of 0.80 K and 0.44 K respectively.

Comparing the models, NNTS retrieves the lowest RMSE values (0.2 K and 0.6 K lower than the USGS and TsHARP respectively) and the highest correlation coefficient (0.88-0.86) probably because of the low radiometry changes in comparison to TsHARP method and because NNTS method represents better the LST at 30 m than the USGS interpolation method (see the r^2 in Table 5.25). This is also shown in the Figure 5.17 in which the LST of the roads in Doñana are neatly seen in comparison to the USGS image.

5.5.2. MODIS

Figure 5.18 and Tables 5.26 and 5.27 show the MODIS indirect validation during three field campaigns. The area of the simulated pixels obtained with the up-scaling method applied to the AHS pixels can be found in Appendix C (Figures C2, C3a and C4a).

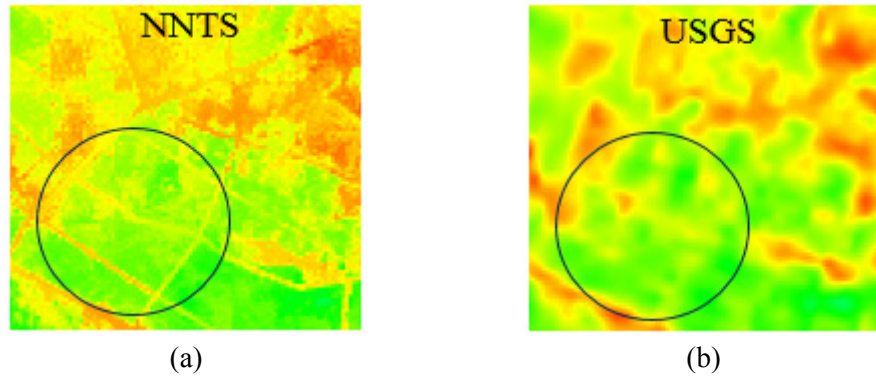


Figure 5.17. Down-scaled LST image obtained with the inverse RTE in Doñana test site: (a) is the LST obtained with NNTS method; (b) is the original USGS LST. Doñana’s roads are marked in the figures with a circle.

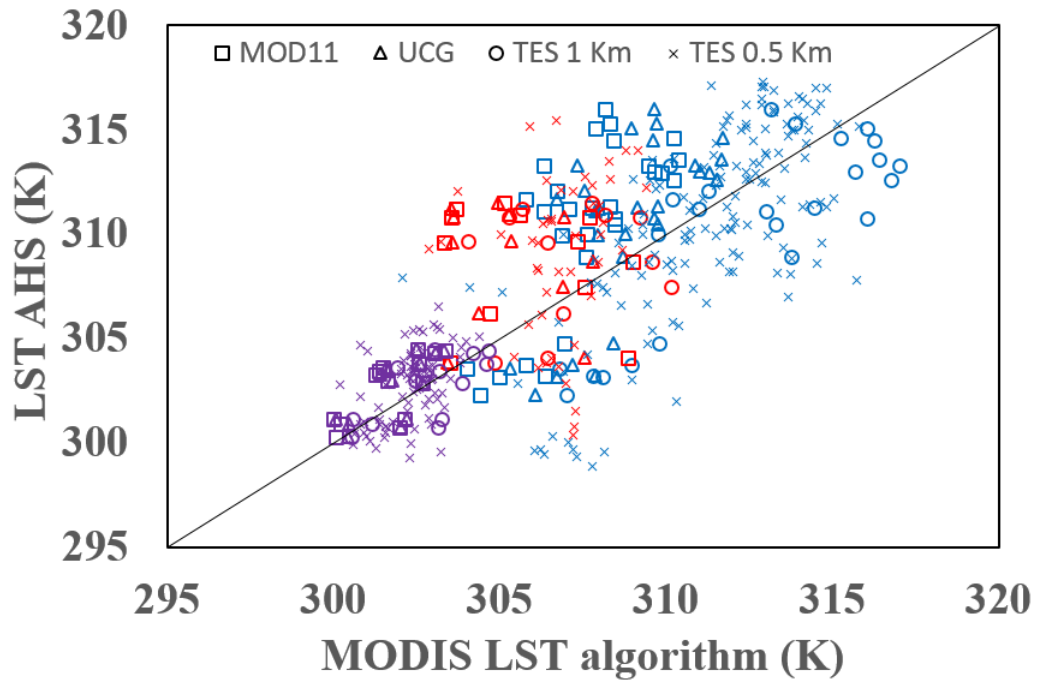


Figure 5.18. LST validation of MODIS algorithms versus AHS data. Colors represent field campaigns: Blue, Doñana 2015; Red, Doñana 2013 and purple Miajadas 2012.

CHAPTER 5: VC AND LST/SST VALIDATION

These tables show unequal RMSE due to the zenith angle at which the data was achieved. In Doñana, the MODIS overpass was carried out with zenith angles of more than 55°, while in Miajadas the view angle was about 40°. This large angle increases location pixel uncertainty in addition to algorithm precision. Miajadas validation matches with the direct validation results (Table 5.18), even for the bias estimation (0.9 K vs 0.8 K, 0.2 K vs 0.4 K and -0.2 K vs -0.2 K for MOD11, SW and TES respectively) while in Doñana the RMSE results overestimate the direct validation values. In spite of the larger angle in the Doñana 2015 field campaign, the RMSE obtained was lower than in the Doñana 2013 campaign. This is due to the cloud cover which in year 2013 was higher (25%) than in year 2015 (8%). Additionally to the factors mentioned above, the AHS thin pixels that simulate the up-scaled pixel show dramatic changes on the land cover (see the Appendix C images) as flooded lakes versus dry surfaces over the marshland area or a coast line that separates sand dunes (hot spot) and Ocean water (cold spot). This huge difference between pixels and the high Doñana's INH index in the spring season (higher than 1.5 K) adds even more uncertainty to the up-scaling process and then, to the validation results. If these pixels with high land cover variance are not taken into account, the RMSE values improve towards 0.5-1.0 K.

Table 5.26. Bias, standard deviation and RMSE (given in kelvin) between LST retrieved by MODIS algorithms and LST obtained with AHS. In brackets, these values are shown without the high land cover variance pixels. In the campaign column, the mean MODIS measurement angle (θ) and number of pixels (n) tested (in brackets n for 0.5 km product) were included.

Campaign	Estadística	SW _{M11}	SW _{UCG}	TES _{1 Km}	TES _{0.5 Km}
Doñana	Bias	2.9 (2.4)	1.6 (1.2)	-2.1 (-1.3)	-0.6 (-0.4)
11/05/2015 10:35	Sigma	3.1 (2.6)	3.2 (2.8)	2.6 (2.5)	3.3 (3.1)
$\theta = -63^\circ$ $n = 28$ (144)	RMSE	4.2 (3.6)	3.6 (3.0)	3.4 (2.8)	3.3 (3.1)
Doñana	Bias	3.5 (2.7)	2.9 (2.0)	1.7 (0.6)	2.3 (1.5)
07/05/2013 11:55	Sigma	3.4 (3.2)	3.8 (3.5)	3.1 (2.8)	4.0 (3.6)
$\theta = 55^\circ$ $n = 12$ (48)	RMSE	4.9 (4.1)	4.8 (4.0)	3.6 (3.0)	4.6 (3.9)
Miajadas	Bias	0.8	0.4	-0.2	0.4
04/10/2012 11:45	Sigma	1.1	1.1	1.2	1.5
$\theta = 41^\circ$ $n = 14$ (80)	RMSE	1.3	1.2	1.2	1.6

Applying the NNTS method to the TES algorithm, a LST product at 0.5 km was also validated. Table 5.27 shows that 95% of pixels in Miajadas have differences below 1 K respect to the original image, while in Doñana this percentage drops to 70-80%. This

generates an extra uncertainty to the σ values in the validation – as is shown in Table 5.26 and in Figure 5.18 – especially in Doñana. RMSE of sharpened images increases in all the cases except for Doñana 2015, where in spite of σ increase the RMSE does not change because of the bias diminution in terms of absolute values. This bias behavior is observed in all the cases with increases of 1.5 K in Doñana 2015 campaign and of 0.6 K in Miajadas 2012 and Doñana 2013 campaigns in spite of the bias result (see Table 5.27) obtained in the coarse-sharpened comparison. The bias change can be explained because of the fill of the gaps performed with the NNTS method. The TES original image shows striping effects and, when the NNTS method is applied, these gaps are filled as the sharpened LST is based on the visible-infrared relationship which does not show striping effects. This gap fill explains part of the bias modification. If we do not consider these values for the validation, the bias turns closer to its original values (-0.9 K to -0.4, 0.9 K to 0.6 K and 0.0 K to -0.2 K for Doñana 2015, 2013 and Miajadas 2012 respectively). Even so, there is a change in the bias, although it can be neglected in comparison to the σ values.

Table 5.27. Bias and standard deviation values (in Kelvin) in addition to the correlation coefficient and clouds percentage obtained in the comparison of down-scaled and coarse MODIS images for the three field campaigns. PPT is the percentage of pixels that show radiometry changes below certain LST value.

	r^2	Clouds (%)	bias (K)	sigma (K)	PPT (%)			
					< 0.5	0.5-1	1-2	> 2
Doñana	0.986	8 %	-0.04	0.92	48.6	34.5	12.1	4.8
Doñana	0.988	25 %	0.00	2.29	36.7	33.3	13.2	16.8
Miajadas	0.922	0 %	0.01	0.60	56.8	37.9	5.1	0.1

5.5.3. SEVIRI

Only an indirect validation was performed for the SEVIRI SW algorithm. Because there are several SEVIRI images during 1-2 hours (mean time of field campaigns), several AHS overpasses were selected for validation. For each overpass, only few pixels were obtained because of SEVIRI pixel size which, in some cases, were not totally filled with AHS pixels – in these cases, the pixels were simulated with 80% or more of valid AHS values. To ensure the SEVIRI SW validation with a high amount of filled pixels, the SEVIRI image was also cross-validated with the TIRS LST product. The simulated

CHAPTER 5: VC AND LST/SST VALIDATION

pixels for the AHS sensor and TIRS can be found in Appendix C (Figures C1, C3b, C4b and C5a).

Figure 5.19 and Table 5.28 show the validation with the TES AHS product and with all the algorithms tested for TIRS. In the case of AHS comparison, the highest RMSE values were obtained for Doñana 2013 campaign (6.8 K), as it occurred for the MODIS validation, and the lowest in Miajadas (2.5 K). As was explained in the MODIS case, the coast lines generate high uncertainties in the up-scaling process which explains in part these high values. For this reason, when the coastal pixels are not considered, the validation results improve, reducing the RMSE values in 2.5 K. Even so, Doñana 2013 retrieves higher results than the other two campaigns (2.0 K higher) which, as in the case of MODIS, is probably due to cloud presence.

Results between TIRS and SVIRI agree with the AHS validation. The bias is positive which indicates an overestimation of TIRS values (as it was reported from in-situ and indirect TIRS validations) and the σ values are close to root sum square of the TIRS-SEVIRI validation sigmas (3.2 K vs 2.9-3.1 K, depending on the TIRS algorithm and erasing the line coast effects). As was expected, SEVIRI and TIRS SW bias difference is near zero, in opposition with RTE and SC_w (RTE and SC_w overestimate the SW SEVIRI LST).

Table 5.28. Bias, standard deviation and RMSE (given in kelvin), of the cross-validation performed on SEVIRI SW algorithm with the AHS sensor and TIRS. The results were split with the inclusion or not (in brackets for Landsat) of the coastal pixels.

Up-scaled Campaign	AHS					Landsat		
	Doñana 2015		Doñana 2013		Miajadas	Doñana 2015		
	coast	no coast	coast	no coast	no coast	SC	SW	RTE
Bias (K)	-1.3	0.2	-4.6	-2.7	-1.6	0.3 (1.0)	-0.6 (0.2)	0.5 (1.2)
Sigma (K)	4.8	2.6	5.0	3.4	1.8	4.5 (2.7)	4.9 (3.1)	4.6 (2.8)
RMSE (K)	5.0	2.6	6.8	4.4	2.5	4.5 (2.9)	4.9 (3.1)	4.6 (3.1)
N	74	67	67	53	9	198 (168)		

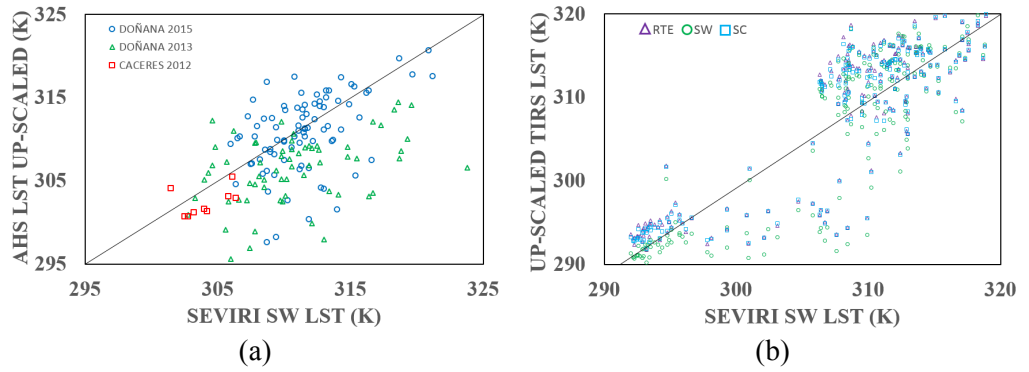


Figure 5.19. LST validation of SEVIRI SW algorithm versus (a) AHS TES product and (b) TIRS algorithms.

5.6. LST VALIDATION SUMMARY

Finally, a summary of the LST results – in-situ (direct) and cross-validation (indirect) – is shown in Table 5.29. The results were sorted by sensor and algorithm, in which the sharpening NNTS results were also included (sharpened RTE image for TIRS and sharpened TES algorithm for MODIS). In the table, the better and the worst RMSE cases are shown.

Table 5.29. Summary of direct (in-situ) and indirect (cross) validation results of ETM+, TIRS, MODIS and SEVIRI sensors given in Kelvin. The validation of the NNTS method was also included.

Algorithm	Type Val	RTE	SC _w	SW	M11	TES	NNTS
ETM+	In-situ	1.2-1.6	1.8-3.0	-	-	-	-
TIRS	In-situ	1.0-1.4	1.4-2.0	1.5-1.8	-	-	-
	Cross	2.1-2.3	2.0-2.3	1.9	-	-	2.5
MODIS	MYD	In-situ	-	1.4-1.6	1.6-1.7	1.3-1.5	-
	MOD	In-situ	-	1.2-1.5	1.7-2.0	1.2-1.5	-
		Cross	-	-	1.2-4.0	1.3-4.0	1.2-3.0
SEVIRI	Cross	-	-	2.5-4.0	-	-	-

CHAPTER 5: VC AND LST/SST VALIDATION

The results show that the algorithms, in general, retrieve LST with an uncertainty of 1.2-1.8 K (depending of the sensor) in the most favorable conditions – i.e with low atmospheric water vapor content (below 1.6 g/cm²) and minimal land cover inhomogeneity. Because it is not always possible to obtain the LST in these conditions, the algorithms allow the LST retrieval with an uncertainty below 2.0 K which strongly depends on the instantaneous atmospheric conditions and the adequate characterization of the surface. In general, RTE, TES and SW retrievals obtain the lowest RMSE values with little changes due to atmospheric conditions, while SC_w algorithm retrieve acceptable results only for low *w* conditions. These results have been confirmed by the cross-validation results which – avoiding the up-scaling difficulties – agree, in general, with the in-situ validations. In MODIS cases, with large angles, the RMSE differences are notable (1.5 K).

NNTS method has demonstrated to be useful for LST sharpening as it shows that the LST could be down-scaled with an increase of the uncertainty below 1.0 K – in respect to the coarse MODIS LST product – and below 0.5 K in respect to the coarse TIRS LST.

5.7. LST/SST PRODUCTS

As a last part of the chapter, three different temperature products – which have been validated in this chapter – have been proposed for implementation as a part of the MODIS chain process, which has been implemented in the installations of our group, the Global Change Unit (GCU) that is integrated in the Image Processing Laboratory. The process chain is part of the CEOS-SPAIN project, which supplies in near-real time MODIS products as fire detection, emissivity or NDVI, among others. For this purpose, the GCU team receives MODIS raw images with the group's antenna which are processed and transformed in the products previously mentioned. These products are available from the web page <http://ceosspain.lpi.uv.es/> and can be downloaded providing a previous registration. Additionally to MODIS data, SEVIRI data are also available from this web page.

The products proposed for their implementation are: MODIS TES algorithm with a spatial resolution of 500 m; MODIS SW algorithm for SST retrieval and Landsat-8 TIRS LST with the RTE at 30 m. Because the products are not yet implemented (but are expected its integration in the chain process in the near future), only an example is shown in this section.

5.7.1. MODIS

From radiance data of bands 29, 31 and 32 and the atmospheric product MOD07 version 6 up-scaled to 20×20 km (as mentioned in Chapter 2) – also generated by our team – the LST can be estimated. In order to show the striping problems in band 29 and how it is possible to reconstruct the gaps by the application of the NNTS method, – which it is not the primary objective of the method – Figure 5.20 shows a quicklook of the TES product over the Iberian Peninsula at 500 m and 1 km. The final product shows the image without gaps and sharpened LST.

Considering sea temperature, a yearly SST product was generated for years 2011 and 2012 (see Figure 5.21). The average was performed with all the valid data provided by Terra and Aqua platforms – excluding the cloud pixels, which are detected by cloud mask estimated in the GCU process chain. The image shows the expected SST distribution (colder in the north and hotter in the south part and in the Mediterranean Sea) and the changes between the analyzed years. Comparing the image values over the Mediterranean buoys, a little drop is observed in the SST of year 2012 (in comparison to year 2011) which agrees with the difference extracted directly from buoys values (see Table 5.30). Differences retrieved between buoys and satellite data can be attributed to algorithm uncertainty, to the averaging procedure – which include hourly data for the buoys in contrast to the 2-3 daily valid values obtained from satellite data – or to the cloud detection through satellite images. In spite of these uncertainty sources, data show the same pattern with minimal and maximal differences of -0.12 K and -0.40 K.

5.7.2. Landsat-8 TIRS

LST product at 30 m was estimated for Barrax and Doñana test sites (see Figure 5.22 and 5.23, respectively). USGS offers by default the product at 30 m (for agreement with the other Landsat bands) but, as was obtained with the indirect validation, with higher RMSE values and correlation coefficients than the NNTS method. Both products are shown in order to compare visually the differences.

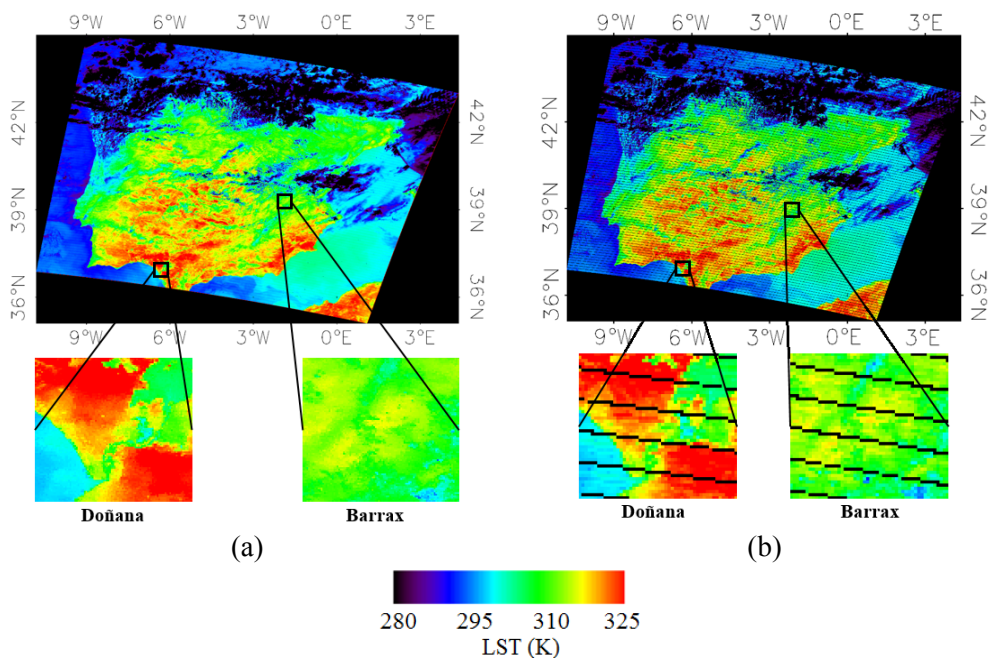


Figure 5.20. MODIS LST image of the Iberian Peninsula for August 13, 2014 at 11 o'clock provided by Terra platform with spatial resolution at (a) 500 m (b) 1000 m.

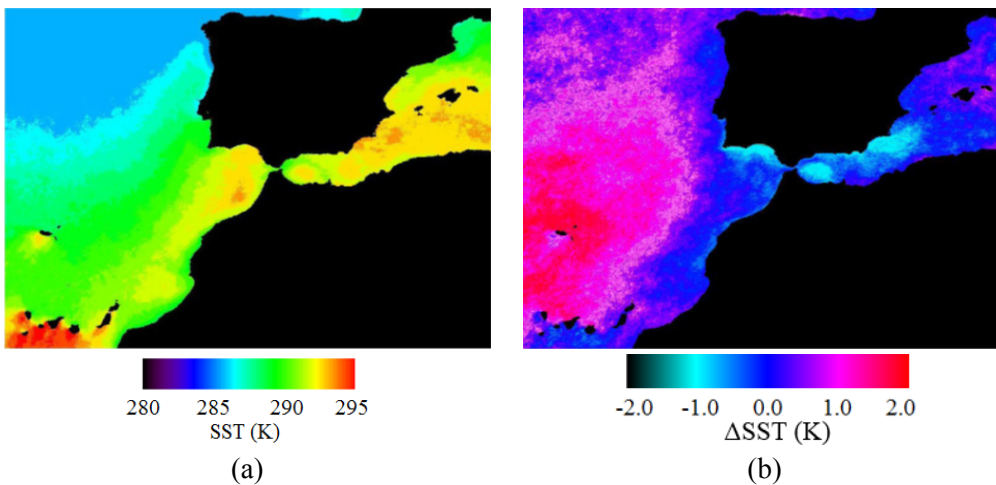


Figure 5.21. MODIS SST retrieved by the WPSST algorithm for Atlantic Ocean and Mediterranean Sea. Image (a) shows the average SST for year 2011 while (b) provides the difference between year 2012 and year 2011.

Table 5.30. SST and bulk temperature differences between years 2011 and 2012 (2012 minus 2011). ΔB symbolizes buoys difference while ΔSST symbolizes SST difference (given in K).

Cabo de Gata		Cabo de Palos		Valencia		Dragonera		Tarragona	
ΔB	ΔSST	ΔB	ΔSST	ΔB	ΔSST	ΔB	ΔSST	ΔB	ΔSST
-0.67	-0.79	-0.50	-0.78	-1.01	-0.65	-0.86	-0.46	-0.14	0.02

In Barrax and Doñana images, sharp land cover types can be appreciated with the NNTS method which present a more real contrast between LST. For example, in Barrax the contour of the crop-bare lands is clearer than in the USGS image as well as the roads and little pools that covers Doñana. The proposed LST product is operative and only needs the MOD07 atmospheric product as atmospheric input.

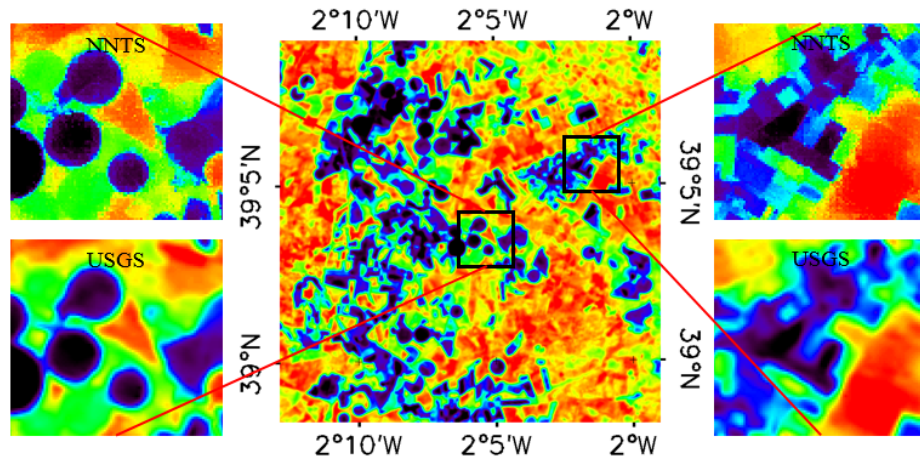


Figure 5.22. LST product estimated with RTE at 30 m over Barrax test site. The amplified images show the results of NNTS and USGS sharpening methods.

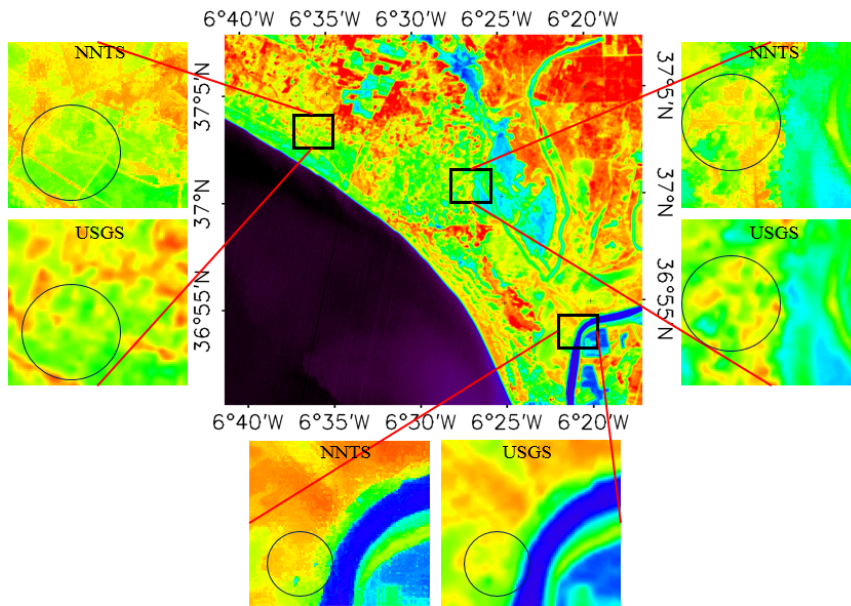


Figure 5.23. LST product estimated with RTE at 30 m over Doñana test site. The circles in the amplified images show the shapes of the roads and lakes with the NNTS and USGS down-scaling methods.

CONCLUSIONS

The importance of the high quality data is essential to ensure a consistent temporal study that require high precision and accuracy. In this thesis, a contribution to TIR data was added in the framework of the WGCV needs. In this work, three important activities were developed for the improvement of TIR cal/val data: The establishment of permanent and automatic station for the cal/val, the VC of the TIR data collected by EO sensors and the validation of the Land/Sea Surface Temperature through different algorithms. Additionally to these activities, three algorithms – two for TIRS LST estimation and one for MODIS SST estimation – and one method for LST sharpening

CONCLUSIONS

were developed in order to integrate three new LST/SST products in the process chain of our group.

The setup of the fixed stations was the first step for the beginning of the cal/val activities. As one station was not enough for covering all the land and atmospheric characteristics (different land emissivities and covers or dry and wet atmospheres), through time and depending on budget availability (high costs of the necessary instruments for the automatic station set up) the web of stations started to grow in order to obtain more in-situ data and to encompass as much EO sensors as possible – regarding the spatial resolution. Now, three automatic stations are operating in Doñana National Park, two more in Barrax and one in the National Park of Cabo de Gata. All the stations are managed by our team in collaboration with Doñana, Barrax and Almeria staff.

Because of the increase of available TIR in-situ data, a quality control – with specific programs created by our team – and a unified procedure for the in-situ LST retrieval was required. The first step was the control of the emissivity, with dedicated field campaigns that included direct emissivity measurements and the evolution of the land covers where the stations laid. This last was important, as the uncertainty had a strong land cover dependence. The second one was the establishment of the down-welling radiance estimation and the control of the direct measurements performed by the radiometers that included a calibration protocol and the conversion of the radiance to LST and vice versa – in order to avoid the pass band effect. The third and most important step was to quantify the INH index for each EO sensor type. This study was essential as it was demonstrated to be the major uncertainty source for cal/val activities. Finally, with each uncertainty source contribution it was possible to establish the precision of our in-situ measurements regarding the sensor's spatial resolution: 0.6 K and 0.7 K as a maximal precision for middle and low resolution sensors respectively in the best measurement conditions, and 1.0 K as an average values of our measurements.

Additionally to this uncertainty, the amount of atmosphere between in-situ data and satellite, plays a strong role in the sensor data collection. This uncertainty was also taken into account to establish a final expected uncertainty for our cal/val activities. The expected values obtained ranged between 0.6-1.2 K for the VC and between 0.7-3.0 K for algorithm validation. These values strongly depends on the sensor spatial resolution and the type of LST algorithm considered. As in other works, e.g. Coll et al. (2010) or Wang (2014), the validation uncertainty retrieved for the EO sensors was below 1.5-2.0 K. These values agreed with the expected precision obtained in this work, allowing us the realization of cal/val activities with the required precision to retrieve appropriate

results. If expected uncertainties had been above the validation requirements, the stations would not have obtained a high quality comparison.

VC was performed on Landsat (TIRS and ETM+) and Terra/Aqua (MODIS) TIR bands. According to the results obtained in the VC, a near zero bias was retrieved for all the analyzed bands except for band 11 of the TIRS sensor, which was found to be brightness temperature dependent with values for 280 K and 310 K of -0.9 K (temperature underestimation) and 0.8 K (temperature overestimation) respectively. Because the statistical uncertainty of VC (1.2 K for the TIRS 11 band) was above the bias absolute values, it was not possible to consider the results as definitive and additional measurements should be performed to obtain a significant conclusions.

In general, the direct validation of the LST algorithms for ETM+ and TIRS showed uncertainties below 2.0 K, always dependent of the atmospheric conditions and the algorithm used. The RTE shows the lowest RMSE values for both sensors and for the major part of atmospheric conditions (below 1.5 K) while the SC_w algorithm shows the poorest performance with values around 2.0 K or more (especially for atmospheric conditions of high w content in which the RMSE reaches values of 3.0 K).

Atmospheric profiles analyzed for L7, MOD07 and reanalysis profiles used in the VC and LST validation showed to be useful for low w atmospheric content (with slightly lower RMSE for NCEP) but, in general and especially for high w values, the use of NCEP data for Landsat-7 platform is recommended.

The TIRS SW algorithm shows a stable value – independently of the atmospheric w content – with average RMSE of 1.8 K. Although in our test sites deviations for band 11 were not as dramatic as expected, – because of stray light – band 11 is still providing worse accuracies than band 10. Even if band 11 is still affected by undesired noise, the SW approach provided a moderate uncertainty. This can be attributed to the SW technique itself, since the highest contribution to the LST retrieval is coming from band 10, and then the atmospheric correction is performed by using the difference between band 10 and band 11. Therefore, absolute values of band 11 are not used in the SW technique, which somehow minimizes the calibration problems in this band (at least when these calibration errors are not extremely huge). However, we emphasize that these results should be considered with caution, since the stray light problem could influence TIRS bands differently depending on the site and temporal period (Barsi et al. 2015).

MODIS algorithm validation showed similar values for the SW/TES algorithm and MOD11 product with uncertainties ranging between 1.2 K and 2.0 K. TES algorithm

CONCLUSIONS

retrieved a slightly higher precision than the SW methods but only 0.1-0.2 K better. MOD11 product on Terra platform shows the highest RMSE values due to its higher inaccuracy in comparison to the other two methods. This inaccuracy which presents values of 1 K, underestimates the LST and is the cause of the high RMSE retrieved (2.0 K in the worst case). Even so, the results obtained agree with other independent validations that shows values of 1.5 K for TES algorithm and 1.0-2.0 K for MOD11 product.

Taking into account these results and the spatial and temporal cover of current atmospheric products – with which it is possible to retrieve the atmospheric parameters of transmissivity, up-welling and down-welling radiance around the world – it is recommended, in stable atmospheric conditions, the use of RTE, TES and SC_{ψ} general equation for the LST estimation. SC_w algorithm can be also used, but only for low atmospheric water vapor contents. SW algorithm retrieved a little higher RMSE values than RTE or TES, but more stable results (less standard deviation variability) regarding the atmospheric conditions, which makes it more suitable for analysis of global data. Furthermore, SW and SC_w algorithm only require w input which implies a faster computational time as no atmospheric profile nor radiative transfer code execution are required. For these reasons, SW is more operative for global LST estimation although, in general, the precision values is little higher than TES or RTE.

The cross-validation has been performed over a high amount of pixels at the same time and with an air-borne sensor (in our case the AHS) differing with the direct validation in the retrieval of the ground-true measurements (in the direct validation it comes from in-situ radiometers while in the indirect validation the truth is the air-borne data which is up-scaled to a desired sensor resolution). Products with their original spatial resolution have been validated, retrieving similar results as the direct validation – differences below 0.3 K – which demonstrates by other way the validity of our results. The major discrepancies come from the MODIS data obtained at very large angles $> 55^{\circ}$ in which case the validation results show uncertainties of 3.0 K.

Because of the pixels heterogeneity in the AHS image and its high pixel resolution – between 3-5 m – it was possible to test the down-scaled MODIS TES algorithm and TIRS RTE product at 500 m and 30 m respectively. The comparison between the two sharpening models and the USGS 30 m TIRS LST product showed highest imprecisions (0.5-0.8 K) in comparison to the coarse image (90 m) probably due to the uncertainties involved in the up-scaling process. The comparison between products show that the NNTS method retrieves lower RMSE values than the USGS and TsHARP method. Although NNTS down-scaling method does not maintain the radiometry of the

original image, the precision is higher than for the USGS image because of the low uncertainty due to radiometric changes (0.5 K) which have a minimal contribution in the final LST estimation in comparison to the algorithm uncertainty (2.1 K).

Results similar to TIRS down-scaling were retrieved for MODIS. Comparing the results of the sharpened versus the coarse image, a slightly higher imprecisions of 0.4-1.0 K was obtained, but with the difference that the bias is not maintained, which is not detected in TIRS down-scaling process. The bias increase is not dramatic (around 0.4 K) and can be considered acceptable as the mean radiometry change between the sharpened and coarse image is approximately 0.9 K.

To conclude the algorithm analysis, the WPSST and the NASA SST product have been validated over the Mediterranean and Atlantic Sea. Validation has been performed over the anchor buoys and has shown similar results between the algorithms, with precision values of 0.67-0.68 K and 0.64 K for WPSST and NASA algorithms respectively. In spite of the minimal gap between the algorithms, the WPSST algorithm is more operative than the other one as it does not need external information for the SST estimation unlike the NASA algorithm, which needs the OISST data as input. Differences decreased when the best conditions for SST were selected: Moderate wind speed, view zenith angle below 45° and no solar or minimal radiation. In these conditions, the precision of the algorithms is near 0.48 K and 0.54 K for Aqua and Terra platforms respectively, with differences between them of 0.01 K. This means that the SST retrieval through satellite data applying the SW methods cannot obtain lower uncertainties (through buoys validation) than 0.5 K instead of the 0.2-0.3 K that can be retrieved with the M-AERI (robust, accurate, self-calibrating, seagoing Fourier-transform infrared spectro-radiometer) skin SST. This has important consequences as the SST validation through buoys cannot guarantee the climate studies requirement – a precision below 0.3 K (Emery et al. 2001) – as SST skin measurements do. Anyway, buoys validation is necessary as it provides a very long sea temperature series data which cannot be retrieved with ship transects, and are necessary for a continuous long-time SST validation.

With the results of the VC and the algorithms validation, it is possible to estimate whereas the fixed stations are in agreement between them. Regarding the bias results of the cal/val activities, it is appreciated that the bias differences are minimal between the stations – comparing the same EO sensor – in comparison to the standard deviation obtained in the cal/val process. In the worst case, the bias gap reaches a value of 1.0 K but usually this difference is lower and closer to 0.6-0.3 K, especially for Landsat sensors. This demonstrates that station data are consistent, and that the procedure

CONCLUSIONS

followed for the in-situ LST estimation is the appropriated. Furthermore, the expected uncertainty analysis is consistent with the statistical uncertainties retrieved from the cal/val activities which indicate good computation performance – except for Las Tiesas station, in which the inhomogeneity for low spatial resolution sensors should be controlled every year. This analysis between biases is important as it is one of the better ways in which it is possible to retrieve the malfunction of the radiometers or of the punctual steps in the LST retrieval procedure.

In order to try to improve the precision of our cal/val activities, some upgrades can be performed on our fixed stations. These encompass the improvement of the emissivity control (as it is the main contribution to LST uncertainty) through time periods with dramatic land cover changes and the installation of various sensors in the same fixed station in order to guarantee maximal accuracy of TIR measurements. With these improvements, uncertainty of LST estimation can be reduced in 0.1-0.2 K for the periods of low INH index value, which is the main contribution of cal/val uncertainties and cannot be lowered as it is environment dependent.

Results of VC and LST algorithms validation retrieved in this work are referred to our test sites, but the results can be extrapolated to other regions with similar surfaces and atmospheric conditions. In spite of test sites representing different land covers (bare soil, vegetation and water) with a moderate emissivity range (0.95-0.99) and with variable w values (0.5 g/cm² to 3.5 g/cm²), validation over additional test sites is recommended in order to test LST algorithms over extreme atmospheric conditions like dry atmospheres in desert, Artic zones with glaciers or permanents snow covers as well as in humid tropic atmospheres such as Amazonia.

As part of possible future actions, the installation of additional fixed stations should be accomplished in order to test satellite raw data and LST algorithms over an extended emissivity land surface range and in order to enlarge the amount of valid data with more independent points, which can contribute to the land quality control data between stations and to reinforce the validity of the VC and validation activities. Moreover, the implementation of the LST and SST new products on the processing chain of the GCU group will allow improved bio-physical studies that involve the LST or temporal studies that require precise SST.

APPENDIX A

In the next tables, it is detailed in-situ and sensor values taken in account for VC and validation process for L7 ETM+ and L8 TIRS. Table A1, A2, A3 and A4 show a comparison between sensor radiances and brightness temperatures versus predicted TOA values through inverse RTE. All the values were used for algorithm validation while the data used for VC purposes is shown in bold type. LST_s symbolizes the land surface temperature measured in situ; ETM+ and TIRS represents radiances (temperatures) measured by sensors; ϵ is the ETM+ and TIRS Land Surface Emissivity; $\Delta_{L7-MODv5}$, $\Delta_{L7-MODv6}$ and $\Delta_{L7-NCEP}$ in Table A1 and A2 are the differences between predicted TOA radiance for three atmospheric profiles (MOD07 version 5, MOD07 version 6 and reanalysis data provided by NCEP respectively) and radiance obtained from band 6. Δ_{RT} , Δ_{SC} and Δ_{SW} in Table A3 and A4 are the differences between in-situ LST values minus estimated LST through RTE, SC and SW algorithm, respectively. Finally, S-CT is the Station-Cover Type of four fixed stations.

APPENDIX A

Table A1. Band 6 ETM+ and in-situ values obtained in Doñana test site: FUENTE DUQUE (F) and JUNCABALEJO (J), covered by Water (WA), senescent vegetation (SV) or green vegetation (GV); CORTES (C), situated in a pine forest (PF) area.

Date ddmmyy	S-CT	ETM+	ϵ	LSTs (K)	$\Delta_{L7-MODv5}$	$\Delta_{L7-MODv6}$	$\Delta_{L7-NCEP}$
		$W \cdot \mu m^{-1} \cdot m^{-2} \cdot sr^{-1}$ (K)	(band 6)		$W \cdot \mu m^{-1} \cdot m^{-2} \cdot sr^{-1}$ (K)	$W \cdot \mu m^{-1} \cdot m^{-2} \cdot sr^{-1}$ (K)	$W \cdot \mu m^{-1} \cdot m^{-2} \cdot sr^{-1}$ (K)
14.06.13	F-SV	9.39 (299.7)	0.970	306.1	-0.14 (-1.0)	-0.16 (-1.2)	-0.22 (-1.6)
30.06.13	F-SV	9.88 (303.3)	0.970	308.2	-0.07 (-0.5)	0.00 (0.0)	-0.09 (-0.6)
02.09.13	F-SV	10.25 (305.9)	0.950	311.0	0.22 (1.6)	0.34 (2.4)	0.24 (1.7)
04.10.13	F-SV	9.06 (297.3)	0.950	305.6	-0.41 (-3.0)	-0.16 (-1.2)	-0.08 (-0.6)
07.12.13	F-SV	7.87 (287.9)	0.950	292.4	-0.06 (-0.5)	-0.07 (-0.6)	-0.11 (-0.9)
23.12.13	F-GV	7.47 (284.6)	0.980	286.3	0.05 (0.4)	0.02 (0.2)	-0.01 (-0.1)
13.03.14	F-GV	7.77 (287.1)	0.980	288.8	0.08 (0.7)	0.08 (0.7)	0.11 (0.9)
29.03.14	F-SV	7.79 (287.3)	0.970	291.7	0.01 (0.1)	-0.07 (-0.6)	-0.07 (-0.6)
30.04.14	F-WA	9.18 (298.2)	0.985	302.1	-0.08 (-0.6)	-0.09 (-0.7)	-0.10 (-0.7)
16.05.14	F-GV	9.35 (299.4)	0.980	301.9	0.16 (1.2)	0.19 (1.4)	0.19 (1.4)
04.08.14	F-SV	10.59 (308.3)	0.950	318.3	-0.20 (-1.4)	-0.03 (-0.2)	-0.21 (-1.4)
20.08.14	F-SV	10.27 (306.1)	0.950	315.1	-0.20 (-1.4)	-0.08 (-0.6)	-0.26 (-1.8)
05.09.14	F-SV	10.09 (304.8)	0.950	313.3	0.07 (0.5)	0.17 (1.2)	0.00 (0.0)
07.10.14	F-SV	9.24 (298.6)	0.950	304.6	0.20 (1.5)	0.20 (1.5)	0.03 (0.2)
23.10.14	F-SV	9.48 (300.4)	0.950	303.9	0.29 (2.1)	0.27 (2.0)	0.16 (1.2)
10.12.14	F-WA	6.95 (280.2)	0.985	282.5	-0.10 (-0.9)	-0.12 (-1.1)	-0.15 (-1.3)
26.12.14	F-WA	7.14 (281.8)	0.985	283.5	-0.05 (-0.4)	-0.06 (-0.5)	-0.09 (-0.8)
11.01.15	F-WA	7.10 (281.5)	0.985	283.0	0.00 (0.0)	-0.02 (-0.2)	-0.04 (-0.4)
12.02.15	F-WA	7.27 (282.9)	0.985	286.0	-0.07 (-0.6)	-0.09 (-0.8)	-0.07 (-0.6)
28.02.15	F-SV	7.43 (284.3)	0.960	288.3	0.00 (0.0)	0.05 (0.4)	-0.11 (-0.9)
01.04.15	F-GV	8.92 (296.2)	0.980	299.9	-0.07 (-0.6)	-0.12 (-0.9)	-0.20 (-1.5)
19.05.15	F-GV	8.94 (296.3)	0.980	299.2	0.04 (0.3)	0.06 (0.4)	0.09 (0.7)
20.06.15	F-SV	11.05 (311.4)	0.970	317.9	-0.03 (-0.2)	0.17 (1.2)	-0.03 (-0.2)
06.07.15	F-SV	11.14 (312.0)	0.970	319.4	0.18 (1.2)	0.51 (3.5)	0.09 (0.6)
22.07.15	F-SV	11.56 (314.8)	0.970	319.1	0.31 (2.1)	0.49 (3.3)	0.22 (1.4)
07.10.14	J-SV	9.24 (298.6)	0.970	304.5	-0.02 (-0.2)	-0.02 (-0.1)	-0.08 (-0.6)
23.10.14	J-SV	9.46 (300.2)	0.970	304.0	0.09 (0.6)	0.10 (0.8)	0.00 (0.0)
26.12.14	J-GV	7.15 (281.9)	0.980	283.5	-0.01 (-0.1)	-0.03 (-0.2)	-0.05 (-0.5)
11.01.15	J-GV	7.10 (281.5)	0.980	283.4	-0.01 (-0.1)	-0.03 (-0.3)	-0.06 (-0.5)
04.06.15	J-SV	10.39 (306.9)	0.970	312.6	-0.04 (-0.3)	0.00 (0.0)	-0.07 (-0.5)
30.04.14	C-PF	10.25 (305.9)	0.985	312.6	-0.29 (-2.0)	-0.24 (-1.7)	-0.23 (-1.6)
16.05.14	C-PF	10.01 (304.2)	0.985	311.1	-0.18 (-1.3)	-0.09 (-0.7)	-0.18 (-1.2)
04.08.14	C-PF	10.11 (304.9)	0.985	309.6	0.16 (1.2)	0.26 (1.9)	0.03 (0.2)
20.08.14	C-PF	9.85 (303.1)	0.985	308.9	-0.06 (-0.4)	0.05 (0.3)	-0.21 (-1.5)
07.10.14	C-PF	8.99 (296.7)	0.985	303.2	-0.03 (-0.2)	-0.01 (-0.1)	-0.24 (-1.8)
23.10.14	C-PF	9.33 (299.3)	0.985	302.5	0.13 (1.0)	0.07 (0.6)	-0.05 (-0.4)
10.12.14	C-PF	7.25 (282.8)	0.980	285.2	-0.06 (-0.5)	-0.08 (-0.7)	-0.10 (-0.8)
26.12.14	C-PF	7.28 (283.0)	0.980	284.4	0.03 (0.2)	0.02 (0.2)	-0.01 (-0.1)
11.01.15	C-PF	7.35 (283.6)	0.980	284.7	0.09 (0.8)	0.07 (0.6)	0.05 (0.4)
27.01.15	C-PF	7.35 (283.6)	0.985	284.9	0.02 (0.2)	0.01 (0.1)	-0.01 (-0.1)
28.02.15	C-PF	8.14 (290.1)	0.985	296.4	-0.29 (-2.3)	-0.24 (-1.9)	-0.37 (-2.9)
16.03.15	C-PF	8.32 (291.5)	0.980	294.8	0.04 (0.3)	0.06 (0.5)	-0.01 (-0.1)

Table A2. Band 6 ETM+ and in-situ values obtained in Barrax test site. EL CRUCE (EC) covered by Green Grass (GG) area; LAS TIESAS (LT) covered by Wheat (WH) or Bare Soil (BS) area.

Date ddmmyy	S-CT	ETM+ $W \cdot \mu\text{m}^{-1} \cdot \text{m}^{-2} \cdot \text{sr}^{-1}$ (K)	ϵ (band 6)	LST_s (K)	$\Delta_{\text{ETM-MODv5}}$ $W \cdot \mu\text{m}^{-1} \cdot \text{m}^{-2} \cdot \text{sr}^{-1}$ (K)	$\Delta_{\text{ETM-MODv6}}$ $W \cdot \mu\text{m}^{-1} \cdot \text{m}^{-2} \cdot \text{sr}^{-1}$ (K)	$\Delta_{\text{ETM-NCEP}}$ $W \cdot \mu\text{m}^{-1} \cdot \text{m}^{-2} \cdot \text{sr}^{-1}$ (K)
31.05.13	EC-GG	8.19 (290.5)	0.990	291.9	-0.01 (-0.1)	0.04 (0.3)	0.08 (0.6)
16.06.13	EC-GG	9.05 (297.2)	0.990	301.2	-0.22 (-1.7)	-0.04 (-0.3)	-0.11 (-0.8)
25.06.13	EC-GG	9.27 (298.8)	0.980	302.7	-0.04 (-0.3)	-0.10 (-0.7)	-0.12 (-0.9)
11.07.13	EC-GG	9.63 (301.5)	0.985	305.3	0.00 (0.0)	0.02 (0.1)	0.00 (0.0)
04.09.13	EC-GG	9.23 (298.5)	0.985	301.1	-0.02 (-0.1)	0.01 (0.1)	0.02 (0.2)
20.09.13	EC-GG	9.26 (298.7)	0.985	302.3	-0.07 (-0.5)	-0.07 (-0.5)	-0.11 (-0.8)
31.10.13	EC-GG	7.90 (288.2)	0.985	290.5	-0.05 (-0.4)	-0.07 (-0.6)	-0.06 (-0.5)
23.11.13	EC-GG	6.97 (280.3)	0.980	283.2	-0.14 (-1.2)	-0.13 (-1.2)	-0.13 (-1.1)
25.04.14	EC-GG	8.04 (289.3)	0.990	291.1	0.05 (0.4)	0.02 (0.2)	0.06 (0.5)
10.11.14	EC-GG	7.50 (284.9)	0.985	286.6	0.00 (0.0)	0.00 (0.0)	0.01 (0.1)
06.01.15	EC-GG	7.04 (281.0)	0.980	282.3	0.02 (0.2)	0.03 (0.3)	0.05 (0.4)
16.04.14	LT-WH	8.49 (292.9)	0.990	295.7	-0.05 (-0.4)	-0.07 (-0.6)	-0.02 (-0.1)
25.04.14	LT-WH	7.45 (284.5)	0.990	286.1	0.03 (0.2)	0.00 (0.0)	0.01 (0.1)
18.05.14	LT-WH	7.80 (287.4)	0.990	290.8	-0.13 (-1.1)	-0.09 (-0.8)	-0.20 (-1.6)
03.06.14	LT-WH	8.74 (294.8)	0.985	298.7	-0.12 (-0.9)	-0.14 (-1.1)	-0.09 (-0.7)
12.06.14	LT-WH	8.60 (293.7)	0.980	296.5	0.08 (0.6)	0.05 (0.4)	0.05 (0.4)
19.06.14	LT-BS	8.94 (296.3)	0.975	301.0	0.07 (0.6)	0.04 (0.3)	0.16 (1.2)
10.11.14	LT-BS	7.59 (285.6)	0.975	287.2	0.10 (0.9)	0.09 (0.8)	0.09 (0.7)
19.11.14	LT-BS	7.91 (288.3)	0.975	291.2	0.03 (0.3)	-0.02 (-0.2)	0.06 (0.5)
06.01.15	LT-BS	7.17 (282.1)	0.975	283.3	0.10 (0.9)	0.08 (0.7)	0.07 (0.6)
13.01.15	LT-BS	7.64 (286.0)	0.975	289.2	-0.05 (-0.4)	-0.09 (-0.7)	-0.04 (-0.3)
11.03.15	LT-BS	9.38 (299.6)	0.975	302.7	0.02 (0.2)	-0.03 (-0.2)	-0.04 (-0.3)

APPENDIX A

Table A3. Band 10 and 11 TIRS and in-situ values obtained in Barrax test site: FUENTE DUQUE (F), covered by Water (WA), senescent vegetation (SV), green vegetation (GV) or senescent-green vegetation (SG).

Date ddmmyy	S-CT	TIRS _{B10} W·μm ⁻¹ ·m ⁻² ·sr ⁻¹ (K)	TIRS _{B11} W·μm ⁻¹ ·m ⁻² ·sr ⁻¹ (K)	LST _s (K)	ε (×10 ⁻³) b10/b11	Δ _{RT} (K)	Δ _{SC} (K)	Δ _{SW} (K)	w
19.04.13	F-WA	8.71 (293.4)	7.89 (290.8)	297.0	990/985	0.4	0.9	-2.4	2.8
05.05.13	F-WA	8.96 (295.3)	8.17 (293.3)	296.9	985/985	-2.6	-1.2	-2.8	2.1
22.06.13	F-GV	9.69 (300.6)	8.74 (298.2)	305.6	970/975	-0.3	-0.3	-0.3	3.4
25.08.13	F-SV	10.01 (302.9)	8.87 (299.3)	308.5	960/970	-2.9	-1.6	-3.1	3.7
10.09.13	F-SV	10.33 (305.1)	9.13 (301.5)	311.2	960/970	0.1	0.6	-2.5	2.6
26.09.13	F-SV	9.67 (300.5)	8.53 (296.4)	307.0	960/970	-2.8	1.0	-3.9	3.8
29.11.13	F-SG	7.73 (285.7)	7.20 (284.5)	288.1	975/980	0.1	0.5	-0.7	1.2
15.12.13	F-SG	7.97 (287.6)	7.37 (286.1)	290.8	970/975	0.9	1.1	-0.2	1.0
05.03.14	F-GV	7.88 (286.9)	7.23 (284.8)	290.4	980/980	0.8	1.6	-1.4	1.5
21.03.14	F-GV	8.13 (288.9)	7.44 (286.7)	291.7	980/980	-0.6	0.7	-2.3	1.6
06.04.14	F-WA	8.88 (294.7)	8.13 (292.9)	297.2	990/985	-0.8	-0.4	-1.4	1.6
22.04.14	F-WA	8.12 (288.8)	7.43 (286.6)	293.9	990/985	1.1	3.6	-0.1	2.2
08.05.14	F-GV	9.11 (296.4)	8.25 (294.0)	302.3	980/980	0.5	2.3	0.3	3.2
11.07.14	F-SV	10.82 (308.4)	9.59 (305.2)	318.4	960/970	0.0	3.6	2.7	2.9
29.09.14	F-SV	9.47 (299.0)	8.40 (295.3)	309.1	960/670	2.8	5.7	0.6	3.0
31.10.14	F-SV	9.50 (299.2)	8.53 (296.4)	305.4	970/975	0.7	2.6	-0.6	1.6
02.12.14	F-SG	7.64 (285.0)	7.14 (283.9)	290.2	975/980	2.7	3.6	2.3	2.0
18.12.14	F-SG	7.33 (282.5)	6.89 (281.6)	283.8	980/980	-0.3	-0.2	-1.4	1.5
19.01.15	F-WA	7.08 (280.4)	6.59 (278.7)	282.7	990/985	0.2	0.7	-1.7	1.2
04.02.15	F-WA	7.14 (280.9)	6.70 (279.8)	282.7	990/985	-0.7	0.0	-1.2	1.0
08.03.15	F-SG	8.00 (287.9)	7.53 (287.5)	290.8	970/975	-0.4	0.4	0.8	1.3
11.05.15	F-GV	9.83 (301.6)	9.04 (300.7)	304.3	980/980	-1.2	-1.3	0.6	1.6
27.05.15	F-GV	9.90 (302.1)	8.98 (300.2)	307.4	980/980	0.4	0.3	0.9	2.5
05.12.15	F-SV	8.12 (288.8)	7.55 (287.7)	293.6	970/975	1.5	2.5	1.8	1.1
21.12.15	F-SV	7.96 (287.5)	7.42 (286.5)	291.5	970/975	1.3	1.9	1.3	1.5
06.01.16	F-SV	7.67 (285.2)	7.04 (283.0)	291.0	970/975	2.7	4.9	0.8	2.2
10.03.16	F-GV	8.24 (289.8)	7.63 (288.4)	291.6	985/985	-2.1	-0.6	-1.5	1.6
29.05.16	F-SG	8.87 (294.6)	8.10 (292.6)	299.5	970/975	-0.9	1.7	-0.2	2.5
14.06.16	F-GV	10.24 (304.5)	9.22 (302.2)	310.0	980/980	-0.5	-2.9	0.0	4.1

Table A4. Band 10 and 11 TIRS and in-situ values obtained in Barrax and Doñana test sites. LAS TIESAS (LT) covered by Crop (CR) or Bare Soil (BS) area; JUNCABALEJO (J), covered by Water (WA), senescent vegetation (SV), green vegetation (GV) or senescent-green vegetation (SG); CORTES (C), situated in a pine forest (PF) area.

Date ddmmyy	S-CT	TIRS _{B10} W·μm ⁻¹ ·m ⁻² ·sr ⁻¹ (K)	TIRS _{B11} W·μm ⁻¹ ·m ⁻² ·sr ⁻¹ (K)	TST (K)	ε (×10 ⁻³) b10/b11	Δ _{RT} (K)	Δ _{sc} (K)	Δ _{sw} (K)	w
01.06.13	LT-CR	8.63 (292.8)	8.05 (292.2)	292.9	990/990	-2.3	-2.2	-1.7	0.6
24.06.13	LT-CR	9.47 (299.0)	8.72 (298.0)	302.7	990/990	0.3	0.8	1.8	1.2
10.05.14	LT-CR	9.31 (297.8)	8.45 (295.7)	301.5	990/990	0.0	0.7	-0.7	1.6
19.05.14	LT-CR	8.61 (292.6)	7.89 (290.8)	295.4	990/990	0.0	0.6	-0.9	1.5
04.06.14	LT-CR	9.15 (296.7)	8.48 (296.0)	298.4	985/985	-0.9	-0.8	0.2	1.2
11.06.14	LT-CR	8.67 (293.1)	7.82 (290.2)	299.5	980/980	2.8	4.2	0.0	2.4
27.06.14	LT-BS	9.81 (301.5)	8.83 (298.9)	305.7	960/970	-0.4	0.3	-1.9	1.6
23.08.14	LT-BS	11.03 (309.8)	9.86 (307.4)	317.9	960/970	1.4	2.3	2.3	1.5
18.11.14	LT-BS	7.76 (286.0)	7.15 (284.0)	289.0	960/970	0.6	0.8	-1.8	0.7
20.12.14	LT-BS	6.97 (279.5)	6.54 (278.2)	282.5	960/970	1.3	1.1	0.2	0.5
29.12.14	LT-BS	6.58 (276.2)	6.28 (275.7)	278.5	960/970	0.6	0.5	0.4	0.3
08.01.16	LT-BS	7.38 (282.9)	6.81 (280.8)	284.8	960/970	-0.2	0.1	-2.9	0.9
24.01.16	LT-BS	7.53 (284.1)	6.97 (282.3)	286.1	960/970	-0.5	0.2	-2.1	1.1
07.04.16	LT-CR	8.23 (289.7)	7.60 (288.2)	294.5	980/980	1.2	2.8	1.4	1.4
25.05.16	LT-CR	9.20 (297.0)	8.44 (295.6)	302.6	985/985	-0.8	2.1	2.4	1.6
29.09.14	J-SV	9.52 (299.4)	8.41 (295.4)	306.3	965/970	-0.9	2.2	-3.4	3.0
31.10.14	J-SV	9.59 (299.9)	8.57 (296.7)	304.0	965/970	-1.7	0.3	-3.7	1.8
18.12.14	J-SG	7.27 (282.0)	6.84 (281.1)	284.3	970/975	0.4	0.8	-0.3	1.5
19.01.15	J-WA	7.11 (280.6)	6.61 (278.9)	283.4	990/985	0.1	1.6	-1.6	1.2
04.02.15	J-WA	7.16 (281.0)	6.70 (279.8)	284.2	990/985	0.6	1.3	-0.4	1.0
08.03.15	J-SG	8.00 (287.9)	7.53 (287.5)	293.0	970/975	2.1	2.7	2.9	1.3
11.05.15	J-GV	9.85 (301.7)	9.05 (300.8)	304.9	985/980	-0.7	-0.6	1.2	1.6
27.05.15	J-GV	10.04 (303.1)	9.09 (301.1)	309.7	980/980	2.6	2.2	2.4	2.2
14.07.15	J-SV	11.22 (311.0)	10.10 (309.2)	313.5	965/970	-2.2	-4.3	-1.8	2.3
22.04.14	C-PF	8.75 (293.7)	7.90 (290.9)	296.9	985/985	-0.9	0.5	-3.5	1.6
29.09.14	C-PF	9.21 (297.1)	8.23 (293.8)	303.2	980/980	0.5	2.6	-2.2	3.1
31.10.14	C-PF	9.11 (296.4)	8.26 (294.0)	301.9	980/980	-0.1	2.1	0.1	1.6
18.12.14	C-PF	7.51 (283.9)	7.04 (283.0)	287.4	980/980	0.9	1.5	1.0	1.5
19.01.15	C-PF	7.28 (282.0)	6.78 (280.5)	285.6	980/980	1.3	1.7	-0.1	1.5
04.02.15	C-PF	7.44 (283.4)	6.99 (282.5)	286.4	980/980	0.8	1.1	0.4	1.1
08.03.15	C-PF	8.80 (294.1)	8.15 (293.1)	295.8	985/985	-2.2	-0.9	-0.6	1.5
05.12.15	C-PF	7.98 (287.7)	7.44 (286.7)	291.9	980/980	1.1	2.0	1.5	1.2
10.03.16	C-PF	8.37 (290.8)	7.72 (289.2)	292.8	985/985	-1.4	0.0	-1.3	1.6

APPENDIX B

In next tables, it is detailed in-situ and MODIS measurements taken in account for validation process of the SW methods and TES algorithm. In Table B1 and B2 results of validation are shown for different atmospheric conditions related to atmospheric water vapor content and the radiance path length. SW algorithm (Jimenez-Muñoz et al. 2011), MOD 11 product and TES algorithm were validated in four test sites. $\Delta_{LST-ALG}$ is the bias between in-situ LST values minus estimated LST through the algorithms, σ is the 1-sigma standard deviation, n is the number of values used in each station, m and r^2 are the slope and correlation coefficient of the fit. The values are separated for Terra and Aqua platforms.

APPENDIX B

Table B1. MODIS LST algorithms and in-situ values retrieved at Cabo de Gata and Barrax test site: Balsa Blanca and Las Tiasas.

Test Site	Condition	Platform	Algorithm	n	m	r ²	$\Delta_{LST-ALG}$ (K)	σ (K)	RMSE (K)
BALSA BLANCA	$\theta < 35$ $w < 2$	Aqua	TES	62	0.990	0.992	0.4	1.0	1.1
			SW	62	0.982	0.988	0.3	1.3	1.3
			M11	62	0.979	0.955	0.0	1.3	1.3
		Terra	TES	41	0.965	0.990	-0.6	0.7	1.0
			SW	41	0.971	0.981	-0.1	1.0	1.0
			M11	41	1.121	0.990	0.7	1.2	1.4
	$\theta < 35$	Aqua	TES	72	0.988	0.992	0.5	1.0	1.1
			SW	72	0.975	0.988	0.3	1.3	1.3
			M11	72	1.049	0.972	0.4	1.3	1.4
		Terra	TES	44	0.982	0.990	-0.7	0.8	1.0
			SW	44	0.986	0.983	-0.1	1.0	1.0
			M11	44	1.121	0.990	0.7	1.2	1.4
	$\theta < 65$	Aqua	TES	152	0.999	0.99	0.6	1.1	1.2
			SW	152	0.984	0.986	0.4	1.3	1.3
			M11	152	0.972	0.975	0.2	1.2	1.2
		Terra	TES	96	0.987	0.981	-0.7	1.1	1.3
			SW	96	1.006	0.975	-0.1	1.3	1.3
			M11	96	1.133	0.990	0.7	1.3	1.4
LAS TIASAS	$\theta < 35$ $w < 2$	Aqua	TES	57	0.972	0.969	0.1	1.6	1.6
			SW	57	0.965	0.964	0.0	1.8	1.8
			M11	57	0.856	0.961	0.8	1.6	1.8
		Terra	TES	46	0.918	0.962	0.3	1.7	1.7
			SW	46	0.939	0.965	0.4	1.5	1.6
			M11	46	0.922	0.957	1.0	1.8	2.0
	$\theta < 35$	Aqua	TES	63	0.969	0.968	0.0	1.6	1.6
			SW	63	0.969	0.962	0.1	1.8	1.8
			M11	63	0.917	0.98	1.1	1.7	2.1
		Terra	TES	46	0.918	0.962	0.3	1.7	1.7
			SW	46	0.939	0.965	0.4	1.5	1.6
			M11	46	0.922	0.957	1.0	1.8	2.0
	$\theta < 65$	Aqua	TES	144	0.965	0.962	0.3	1.7	1.8
			SW	144	0.970	0.959	0.4	1.8	1.8
			M11	144	0.899	0.968	1.5	1.9	2.4
		Terra	TES	106	0.928	0.938	0.1	1.9	1.9
			SW	106	0.953	0.941	0.3	1.8	1.9
			M11	106	0.921	0.944	1.1	1.9	2.2

Table B2. MODIS LST algorithms and in-situ values retrieved at Doñana test site: Fuente Duque and Juncabalejo.

Test Site	Condition	Platform	Algorithm	n	m	r ²	$\Delta_{LST-ALG}$ (K)	σ (K)	RMSE (K)
FUENTE DUQUE	$\theta < 35$ $w < 2$	Aqua	TES	207	0.944	0.962	0.3	1.2	1.3
			SW	207	0.967	0.963	0.3	1.3	1.3
			M11	207	0.934	0.946	0.2	1.6	1.6
		Terra	TES	224	0.954	0.965	-0.2	1.1	1.2
			SW	224	0.972	0.962	0.3	1.2	1.2
			M11	224	1.027	0.950	1.0	1.4	1.7
	$\theta < 35$	Aqua	TES	319	0.959	0.977	0.3	1.3	1.3
			SW	319	0.964	0.970	0.6	1.4	1.5
			M11	319	0.980	0.971	0.3	1.5	1.5
		Terra	TES	326	0.987	0.988	-0.2	1.1	1.2
			SW	326	0.991	0.984	0.4	1.3	1.3
			M11	326	1.051	0.959	1.2	1.4	1.8
	$\theta < 65$	Aqua	TES	716	0.961	0.976	0.5	1.4	1.5
			SW	716	0.958	0.973	0.6	1.5	1.6
			M11	716	0.955	0.970	0.4	1.7	1.7
		Terra	TES	732	0.975	0.984	-0.2	1.3	1.4
			SW	732	0.990	0.979	0.2	1.5	1.5
			M11	732	1.033	0.960	1.4	1.5	2.0
JUNCA BALEJO	$\theta < 35$ $w < 2$	Aqua	TES	72	1.022	0.931	-0.2	1.3	1.3
			SW	72	0.999	0.916	0.0	1.4	1.4
			M11	72	0.993	0.929	-0.6	1.3	1.5
		Terra	TES	67	1.037	0.914	-0.6	1.1	1.3
			SW	67	1.030	0.904	0.0	1.2	1.2
			M11	67	1.054	0.869	0.4	1.4	1.5
	$\theta < 35$	Aqua	TES	105	0.997	0.939	-0.4	1.5	1.5
			SW	105	0.972	0.927	0.0	1.6	1.6
			M11	105	1.050	0.947	-0.6	1.5	1.6
		Terra	TES	83	0.951	0.951	-0.7	1.4	1.6
			SW	83	0.964	0.943	-0.1	1.5	1.5
			M11	83	1.099	0.962	0.6	1.5	1.6
	$\theta < 65$	Aqua	TES	232	0.986	0.967	-0.1	1.4	1.4
			SW	232	0.965	0.961	0.1	1.6	1.6
			M11	232	1.007	0.976	-0.2	1.5	1.5
		Terra	TES	175	0.947	0.956	-0.7	1.4	1.6
			SW	175	0.979	0.947	-0.1	1.5	1.5
			M11	175	1.093	0.949	0.7	1.6	1.8

APPENDIX C

Simulated pixels obtained through the up-scaling process are shown in this section. Composite of AHS images retrieved in field campaigns performed in Doñana – May 2013 and 2015 – and Miajadas – October 2012 – test sites were used to simulate TIRS, MODIS and SEVIRI pixels. In the images, squares were set in order to mark the edges of the simulated pixels. As general condition, if up-scaled pixels is not composed by 80% or more of valid data, it is not taken in account for validation process and it is not marked in the below figures. Figures are sorted by campaign and sensor, showing in each case LST scale.

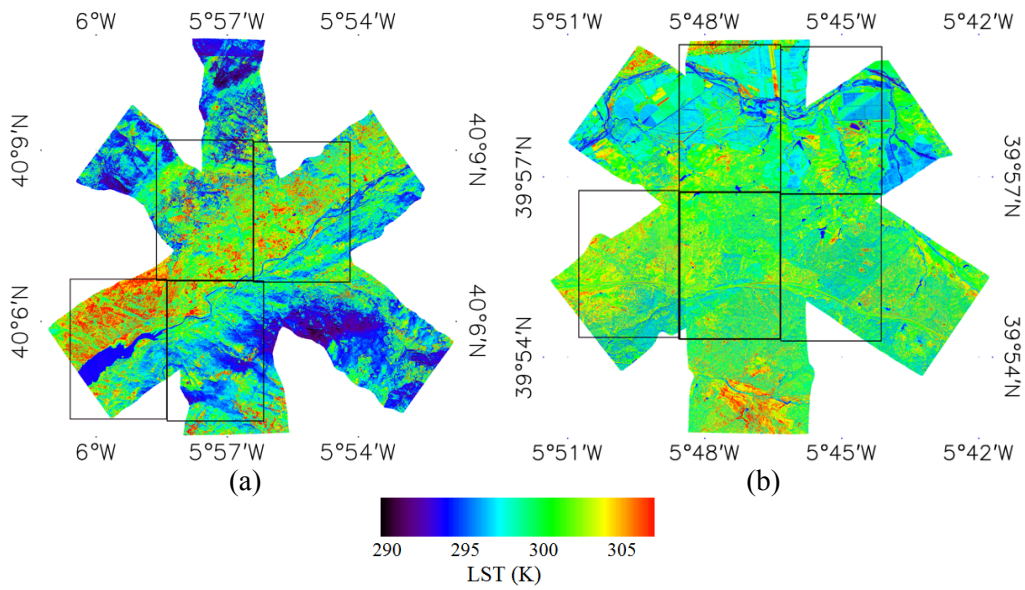


Figure C1. Borders of SEVIRI simulated pixels in (a) northern and (b) southern Miajadas area.

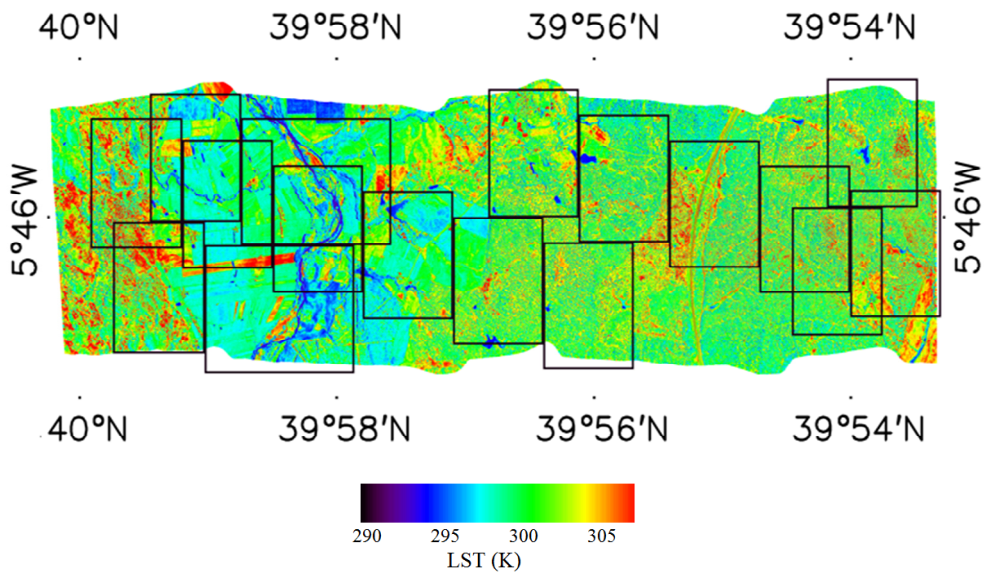


Figure C2. Borders of MODIS simulated pixels in southern Miajadas area.

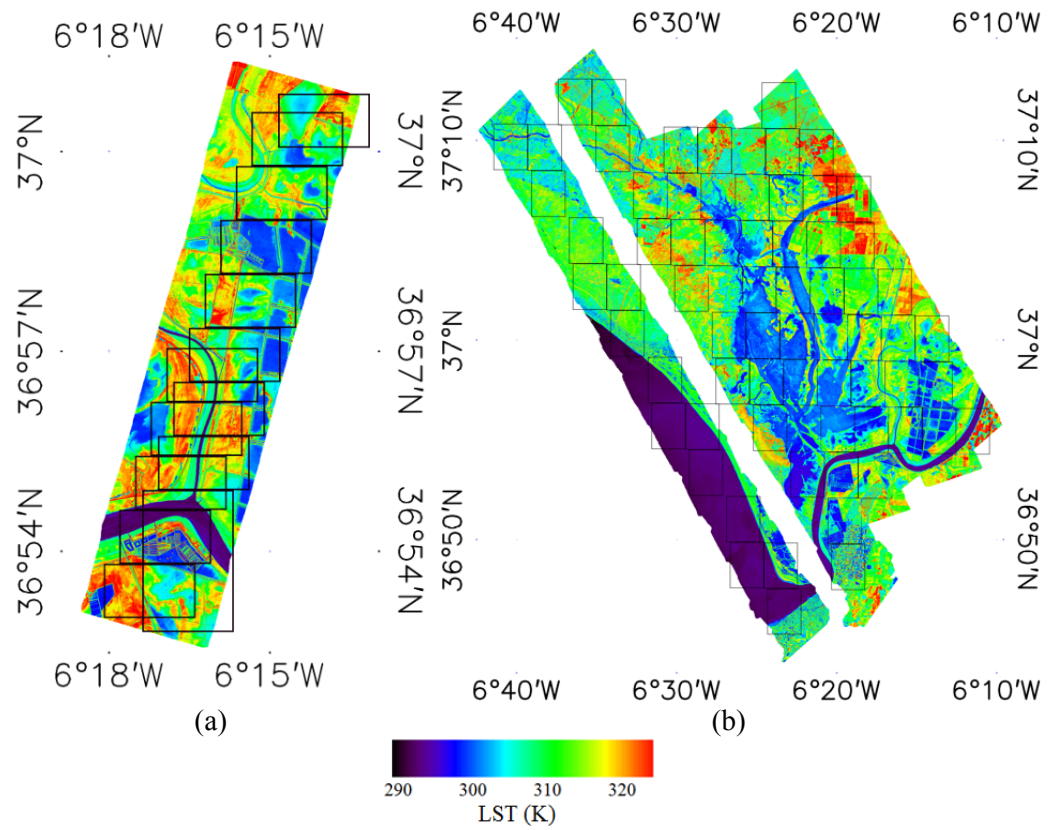


Figure C3. Borders of: (a) MODIS simulated pixels and (b) SEVIRI simulated pixels in Doñana field campaign of year 2013.

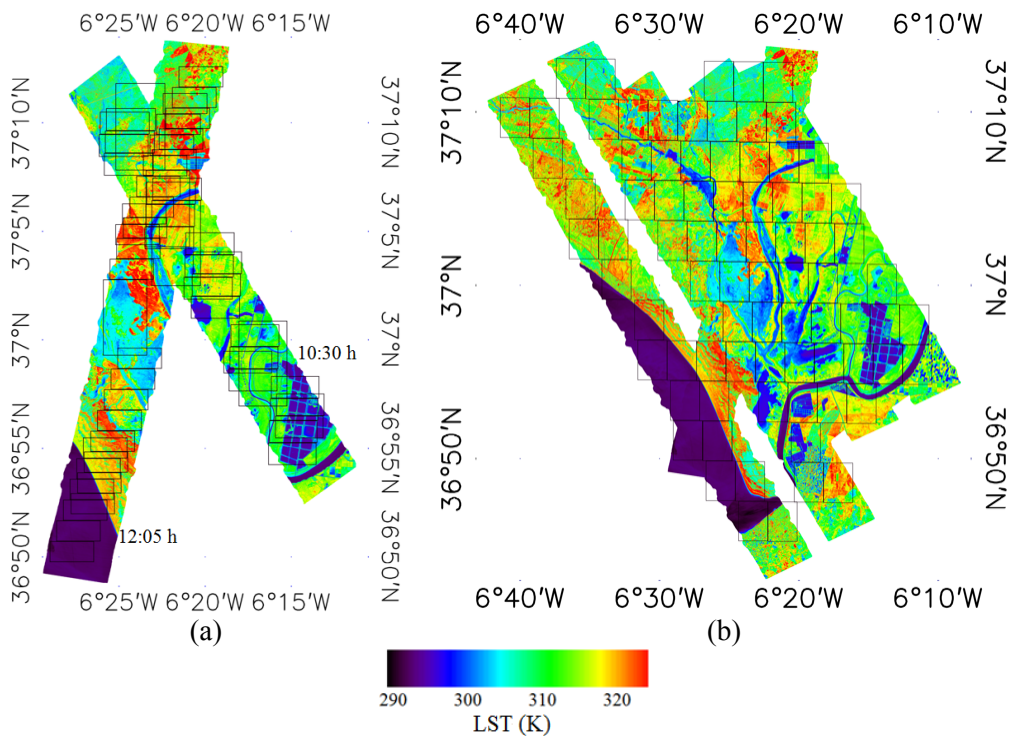


Figure C4. Borders of: (a) simulated pixels for two MODIS images and (b) SEVIRI simulated pixels in Doñana field campaign of year 2015.

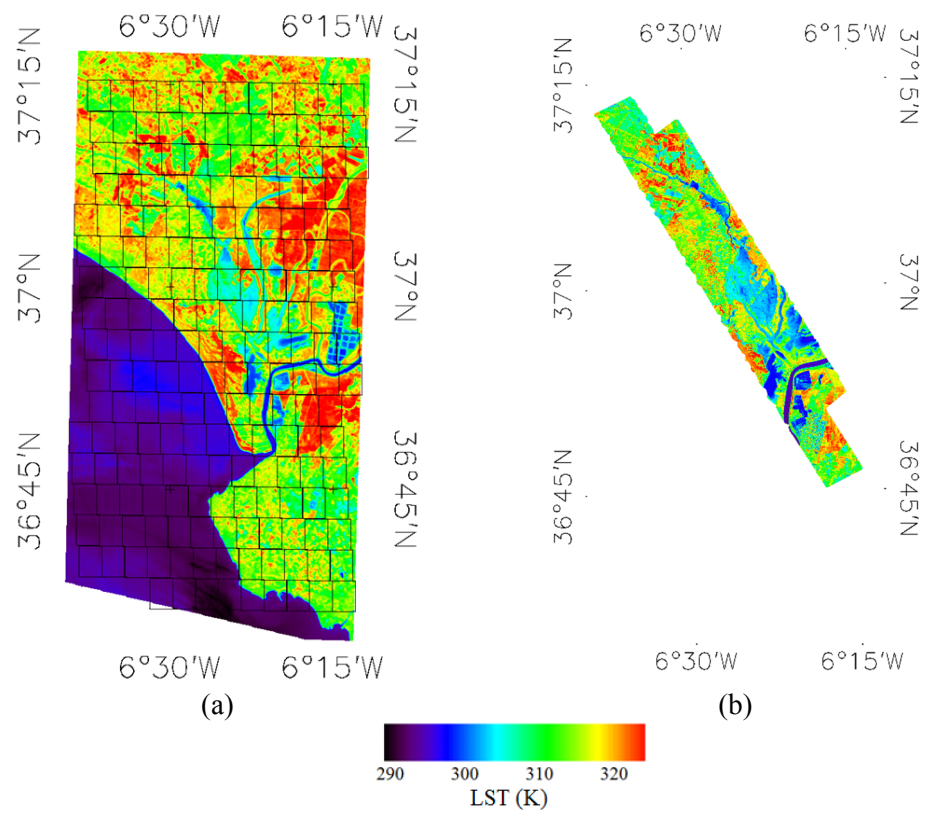


Figure C5. (a) Borders of SEVIRI pixels over TIRS LST image and (b) TIRS simulated image by up-scaled AHS data.

APPENDIX D: LIST OF RELATED PUBLICATIONS

- Skokovic, D., Sobrino, J.A., Jimenez-Munoz, J.C., Thermal infra-red band calibration and LST algorithm validation of Landsat 7 ETM+ instrument using three global atmospheric profiles, IEEE Geoscience and Remote Sensing Letters 55(3), pp. 1804-1811, 2016.
- Sobrino, J.A., Skokovic, D, Permanent stations for calibration/validation of thermal sensors over Spain, Data, 1(2), 10, 2016.

- Sobrino, J.A., Skokovic, D., Jimenez-Munoz, J.C., Spatial analysis of the homogeneity of the Land Surface Temperature in three Spanish test sites. *International Journal of Remote Sensing*, 36 (19-20), pp. 4793-4807, 2015.
- Jimenez-Munoz, J.C., Sobrino, J.A., Skokovic, D., Mattar, C., Cristobal, J. Land surface temperature retrieval methods from landsat-8 thermal infrared sensor data, *IEEE Geoscience and Remote Sensing Letters* 11 (10), 6784508, pp. 1840-1843, 2014.
- Skokovic, D., Sobrino, J.A., Jimenez-Munoz, J.C, Soria, G. & Julien, Y. Estudio de la homogeneidad de la temperatura de la superficie terrestre mediante imágenes MODIS de la zona de Doñana *Revista de Teledetección*, Vol. 40, pp. 71-77, 2013

REFERENCES

- Agam, N., Kustas, W.P., Anderson, M.C., Li, F. and Neale, C.M.U.** (2007) “A vegetation index based technique for spatial sharpening of thermal imagery” *Remote Sens. Environ.*, vol. 107, pp. 545–558.
- Atitar, M. and Sobrino, J.A.** (2009) “Split-Window Algorithm for Estimating LST From Meteosat 9 Data: Test and Comparison With In Situ Data and MODIS LSTs” *IEEE Geoscience and Remote Sens. Letters*, vol. 6, no. 1.
- Baldrige, A. M., Hook, S. J., Grove, C. I., and Rivera, G.** (2009) “The ASTER spectral library version 2.0” *Remote Sensing of Environment*, vol. 113, pp. 711-715.

REFERENCES

- Barsi, J.A., Schott, J.R., Palluconi, D.L., Helder, F.D., Hook, S.J., Markham, B.L., Chander, G. and O'Donnell, E.M.** (2003) "Landsat TM and ETM+ thermal band calibration" *Canadian Journal of Remote Sensing*, vol. 29, no. 2, pp. 141–153.
- Barsi, J.A., Schott, J.R., Palluconi, F.D. and Hook, S.J.** (2005) "Validation of a Web-Based Atmospheric Correction Tool for Single Thermal Band" *Instruments. Earth Observing Systems X, Proc. SPIE Vol. 5882*, San Diego, CA.
- Barsi, J.A., Schott, J.R., Hook, S.J., Raqueno, N.G., Markham, B.L. and Radocinski, R.G.** (2015) "Landsat-8 Thermal Infrared Sensor (TIRS) Vicarious Radiometric Calibration" *Remote Sensing*, vol. 6, 11607-11626.
- Beck, A., Anderson, G. P., Acharya, P. K., Chetwynd, J. H., Bernstein, L. S., Shettle, E. P., Matthew, M. W. and Adler-Golden, S. M.** (1999) "MODTRAN4 User's Manual" Air Force Research Laboratory, Hanscom AFB, MA.
- Belward, A.S., Skøien, J.O.** (2015) "Who launched what, when and why; trends in global land-cover observation capacity from civilian earth observation satellites". *ISPRS Journal of Photogrammetry and Remote Sensing*, vol. 103, pp. 115–128.
- Borbás, E.E, Seemann, S.W, Kern, Moy, Li, J, Gumley, L.E. and Menzel, W.P.** (2011) "MODIS Atmospheric Profile Retrieval Algorithm Theoretical Basis Document (version 7)." Available at http://modis-atmos.gsfc.nasa.gov/reference_atbd.html.
- Brutsaert, W.** (1975) "On a derivable formula for long-wave radiation from clear skies" *Water Resour Res*, no. 11, pp.742–744.
- Carmona, F., Rivas, R. and Caselles, V.** (2014) "Estimation of daytime downward longwave radiation under clear and cloudy skies conditions over a sub-humid region" *Theor Appl Climatol*, no. 115, pp. 281–295.
- Chavez, P. S.** (1996) "Image-based atmospheric correction – revisited and improved" *Photogrammetric Engineering and Remote Sensing*, vol. 62, no. 9, pp. 1025-1036.
- Chéruiy, F., Scott, N. A. and Chéidin, A.** (1998). "A neural network approach for a fast and accurate computation of a longwave radiative budget," *J. Appl. Meteorol.*, vol. 37, no. 11, pp. 1385–197.
- Clinton, N., Yu, L., Fu, H., He, C. and Gong, P.** (2014) "Global-Scale Associations of Vegetation Phenology with Rainfall and Temperature at a High Spatio-Temporal Resolution" *Remote Sens.*, vol. 6, pp. 7320–7338.
- Coll, C., Galve, J. M., Sánchez, J. M. and Caselles, V.** (2010) "Validation of Landsat-7/ETM+ Thermal-Band Calibration and Atmospheric Correction With Ground-Based Measurements", *IEEE Transactions on Geoscience and Remote Sensing*, vol. 48, no. 1, pp. 547–555.
- Davis, G.,** (2007) History of the NOAA satellite program. *J. Appl. Remote Sens.*, vol. 1, pp. 012504–012504.

- Dee, D. P., Uppala, S. M., Simmons, A. J., Berrisford, P., Poli, P., Kobayashi, S., et al.** (2011). "The ERA interim reanalysis: Configuration and performance of the data assimilation system" *Quarterly Journal of the Royal Meteorological Society*, vol. 137, pp. 553-597
- Donlon, C. J., Minnett, P. J., Gentemann, C., Nightingale, T. J., Barton, I. J., Ward, B. and Murray, M. J.** (2002) "Toward improved validation of satellite sea surface skin temperature measurements for climate research". *J. Climate*, vol. 15, pp. 353-369.
- Embury, O., Merchant, C. J. and Corlett, G. K.** (2012b) "A reprocessing for climate of sea surface temperature from the along-track scanning radiometers: Initial validation, accounting for skin and diurnal variability" *Remote Sens. Environ.*, vol. 116, pp. 62-78.
- Emery, W. J., Yu, Y., Wick, G. A., Schluessel, P. and Reynolds, R. W.** (1994) "Correcting infrared satellite estimates of sea surface temperature for atmospheric water vapor attenuation" *J. Geophys. Res.*, vol. 99, pp. 5219-5236.
- Emery, W. J., Castro, S., Wick, G. A., Schluessel, P. and Donlon, C. J.** (2001) "Estimating sea surface temperature from infrared satellite and in situ temperature data" *Bull. Amer. Meteor. Soc.*, vol. 82, pp. 2773-2784.
- Escobar, J.** (1993). "Base de Données Pour la Restitution de Paramètres Atmosphériques À L'échelle Globale; Étude Sur L'Inversion par Réseaux de Neurones des Données des Sondeurs Verticaux Atmosphériques Satellitaires Présents et à Venir," Ph.D. dissertation, Université Denis Diderot, Paris, France.
- Galve, J. M., Coll, C., Caselles, V. and Valor, E.** (2008) "An atmospheric radiosounding database for generating land surface temperature algorithms," *IEEE Trans. Geosci. Remote Sens.*, vol. 46, no. 5, pp. 1547-1557.
- Gentemann, C. L., Donlon, C. J., Stuart-Menteth, A. and Wentz, F. J.** (2003) "Diurnal signals in satellite sea surface temperature measurements". *Geophys. Res. Lett.* vol. 30, Issue 3.
- Ghanea, M., Moradia, M., Kabiria, K. and Mehdiab, A.** (2016) "Investigation and validation of MODIS SST in the northern Persian Gulf". *Advances in Space Research*, vol. 57, no. 1, pp. 127-136.
- Gillespie, A. R., Rokugawa, S., Hook, S., Matsunaga, T., and Kahle, A. B.** (1998) "A temperature and emissivity separation algorithm for Advanced Spaceborne Thermal Emission and Reflection Radiometer (ASTER) images" *IEEE Transactions on Geoscience and Remote Sensing*, vol. 36, pp. 1113-1126.
- Gutman, G., and Ignatov, A.** (1998) "The derivation of the green vegetation fraction from NOAA/AVHRR data for use in numerical weather prediction models" *International Journal of Remote Sensing*, vol. 19, no. 8, pp. 1533-1543.
- Hook, S. J., Prata, A. J., Alley, R. E., Abtahi, A., Richards, R. C., Schladow, S. G. and Pálmarsson, S. Ó.** (2003) "Retrieval of lake bulk and skin temperatures using Along-Track Scanning Radiometer (ATSR-2) data: A case study using Lake Tahoe, California", *J. Atmos. Oceanic Technol.*, vol. 20, pp. 534-548.

REFERENCES

- Jeganathan, C., Hamm, N.A.S., Mukherjee, S., Atkinson, P.M., Raju, P.L.N. and Dadhwal, V.K.** (2011) "Evaluating a thermal image sharpening model over a mixed agricultural landscape in India" *International Journal of Applied Earth Observation and Geoinformation*, vol. 13, pp. 178–191.
- Jiménez-Muñoz, J. C. and Sobrino, J. A.** (2003) "A generalized single-channel method for retrieving land surface temperature from remote sensing data". *Journal of Geophysical Research*, vol. 108, no. d22, pp. 4688.
- Jiménez-Muñoz, J.C. and Sobrino, J.A.** (2006) "Error sources on the land surface temperature retrieved from thermal infrared single channel remote sensing data" *International Journal of Remote Sensing*, vol. 27, pp. 999–1014.
- Jiménez-Muñoz, J. C., and Sobrino, J. A.** (2008). "Split-Window Coefficients for Land Surface Temperature Retrieval From Low-Resolution Thermal Infrared Sensors" *IEEE Geoscience and Remote Sensing Letters*, vol. 5(4), pp. 806-809.
- Jiménez-Muñoz, J. C., Cristóbal, J., Sobrino, J.A., Sòria, G., Ninyerola, M. & Pons, X.** (2009a). "Revision of the Single-Channel Algorithm for Land Surface Temperature Retrieval From Landsat Thermal-Infrared Data" *IEEE Transactions on Geoscience and Remote Sensing*, vol. 47, no 1, pp. 339-349.
- Jiménez-Muñoz, J. C., Sobrino, J. A., Plaza, A., Guanter, L., Moreno, J., and Martínez, P.** (2009b). "Comparison between fractional vegetation cover retrievals from vegetation indices and spectral mixture analysis: case study of PROBA/CHRIS data over an agricultural area" *Sensors*, vol. 9, pp. 768-793.
- Jiménez-Muñoz, J. C., Sobrino, J. A., Mattar, C., Hulley, G. and Göttsche, F-M.** (2014) "Temperature and Emissivity Separation from MSG/SEVIRI Data". *IEEE Transactions on Geoscience and Remote Sensing*, vol. 52, no. 9.
- Julien, Y., Sobrino, J.A. and Verhoef, W.** (1999) "Changes in land surface temperatures and NDVI values over Europe between 1982 and 1999" *Remote Sens. Environ.*, vol. 103, pp. 43–55.
- Justice, C., Belward, A., Morisette, J., Lewis, P., Privette, J. and Baret, F.** (2000), "Developments in the validation of satellite products for the study of the land surface", *Int. J. Remote Sensing*, vol. 21, no. 17, pp. 3383-3390.
- Kallel, A., Otlé, C., Le Hegarat-Masclé, S., Maignan, F. and Courault, D.** (2013) "Surface Temperature Downscaling from Multiresolution Instruments Based on Markov Models" *IEEE Trans. Geosci. Remote Sens.*, vol. 51, pp. 1588–1612.
- Kalma, J.D., McVicar, T.R. and McCabe, M.F.** (2008) "Estimating land surface evaporation: A review of methods using remotely sensed surface temperature data" *Surv. Geophys.*, vol. 29, pp. 421–469.
- Karnieli, A., Agam, N., Pinker, R.T., Anderson, M., Imhoff, M.L. and Gutman, G.G.** (2010) "Use of NDVI and land surface temperature for drought assessment: Merits and limitations." *J. Clim.*, vol. 23, pp. 618–633.
- Kilpatrick, K.A., Podestá, G., Walsh, S., Williams, E., Halliwell, V., Szczodrak, M., Brown, O.B., Minnett, P.J. and Evans, R.** (2015) "A decade of sea surface temperature from MODIS". *Remote Sensing of Environment*, vol. 165, pp. 27–41.

- Kustas, W. and Anderson, M.** (2009) “Advances in thermal infrared remote sensing for land surface modeling.” *Agric. For. Meteorol.*, vol. 149, pp. 2071–2081.
- Kustas, W.P., Norman, J.M., Anderson, M.C. and French, A.N.** (2003) “Estimating subpixel surface temperatures and energy fluxes from the vegetation index-radiometric temperature relationship” *Remote Sens. Environ.*, vol. 85, pp. 429–440.
- Lehoczky, A., Sobrino, J.A., Skoković, D. and Aguilar, E.** (2017) “The Urban Heat Island Effect in the City of Valencia: A Case Study for Hot Summer Days” *Urban Sci.*, vol. 1, Issue 9.
- Li, Z-L., Tang, B-H. Wu, H., Ren, H., Yan, G., Wan, Z., Trigo I.F. and Sobrino, J.A.** (2013) “Satellite-derived land surface temperature: Current status and perspectives”. *Remote Sensing of Environment*, vol. 131, pp. 14–37
- Liang, X. and Ignatov, A.** (2013) “AVHRR, MODIS, and VIIRS radiometric stability and consistency in SST bands” *J. Geophys. Res. Oceans*, vol. 118(6), pp. 3161–3171.
- Maa, Y., Wub, H., Wanga, L., Huangc, B., Ranjand, R., Zomayae, A. and Jief, W.** (2015) “Remote sensing big data computing: Challenges and opportunities”. Vol. 51, pp. 47–60.
- Mattar, C., Durán-Alarcón, C., Jiménez-Muñoz, J. C., Santamaría-Artigas, A., Olivera-Guerra, L., and Sobrino, J. A.** (2013) “Global Atmospheric Profiles derived from Reanalysis Information (GAPRI)” *IEEE Transactions on Geoscience and Remote Sensing*, Vol. 36, Nos. 19–20, pp. 5045–5060.
- McClain, E. P., Pichel, W. P. and Walton, C. C.** (1985) “Comparative performance of AVHRR-based multichannel sea surface temperatures” *J. Geophys. Res.*, vol. 90, pp. 11587–11601.
- Mechri, R., Otlé, C., Pannekoucke, O., Kallel, A., Maignan, F., Courault, D. and Trigo, I. F.** (2016) “Downscaling Meteosat Land Surface Temperature over a Heterogeneous Landscape Using a Data Assimilation Approach” *Remote Sens.*, vol. 8, pp. 586-604.
- Merchant, C.J., Embury, O., Rayner, N.A., Berry, D.I., Corlett, G.K., Lean, K., Veal, K.L., Kent, E.C., Llewellyn-Jones, D.T., Remedios, J.J. and Saunders, R.** (2012) “A 20 year independent record of sea surface temperature for climate from Along-Track Scanning Radiometers”, *Journal of Geophysical Research*, vol. 117, Issue C12.
- Minnett, P.J.** (1990b). “The regional optimization of infrared measurements of sea-surface temperature from space” *J. Geophys. Res.*, vol. 95(13), pp. 497-13.
- Minnett, P. J., Brown, O. B., Evans, R. H., Key, E. L., Kearns, E. J., Kilpatrick, K. and Szczodrak, G.** (2004) “Sea-surface temperature measurements from the moderate-resolution imaging spectroradiometer (MODIS) on aqua and terra” *IEEE International Geoscience and Remote Sensing Symposium, 2004. IGARSS '04. Proceedings.*

REFERENCES

- Morillas, L., García, M., Nieto, H., Villagarcia, L., Sandholt, I., Gonzalez-Dugo, M.P., Zarco-Tejada, P.J. and Domingo, F.** (2013) "Using radiometric surface temperature for surface energy flux estimation in Mediterranean drylands from a two-source perspective" *Remote Sensing of Environment*, vol.136, pp. 234–246.
- Mukherjee, S., Joshi, P.K. and Garg, R.D.** (2014) "comparison of different regression models for downscaling Landsat and MODIS land surface temperature images over heterogeneous landscape" *Advances in Space Research*, no. 54, pp. 655–669.
- Nichol J.E. and Wong M.S.** (2009) "High resolution remote sensing of densely urbanised regions: A case study of Hong Kong" *Sensors*, vol. 9, pp. 4695–4708.
- North, G. R., Pyle, J. A. and Zhang, F.** (2002) "Encyclopedia of Atmospheric Sciences". vol. 1-6.
- Perry, E. M. and Moran, M. S.** (1994) "An evaluation of atmospheric corrections of radiometric surface temperatures for a semiarid rangeland watershed" *Water Resources Research*, vol. 30, pp. 1261–1269.
- Prata, A.J.** (1996) "A new long-wave formula for estimating downward clear-sky radiation at the surface" *Quart J Roy Meteorol Soc*, no. 122, pp. 1127–1151.
- Qin, H., Chen, G., Wang, W., Wang, D. and Zeng, L.** (2014). "Validation and application of MODIS-derived SST in the South China Sea". *Int. J. Remote Sens.*, vol. 35 (11–12), pp. 4315–4328
- Qin, Z., Karnieli, A. and Berliner, P.** (2001) "A mono-window algorithm for retrieving land surface temperature from Landsat TM data and its application to the Israel-Egypt border region." *Int. J. Remote Sens.*, vol. 22, pp. 3719–3746.
- Rayner, N.A., Parker, D.E., Horton, E.B., Folland, C.K., Alexander, L.V., Rowell, D.P., and Kent, E.C.** (2003) "A. Kaplan Global analyses of sea surface temperature, sea ice, and night marine air temperature since the late nineteenth century" *Journal of Geophysical Research*, vol. 108, Issue D14.
- Ren, H., Du, C., Liu, R., Qin, Q., Meng, J., Li, Z.-L., and Yan, G.** (2014) "Evaluation of Radiometric Performance for Thermal InfraRed 8 Sensor onboard Landsat 8" *Remote Sens*, vol. 6, pp. 12776-12788.
- Reynolds, R. W., Rayner, N. A., Smith, T. M., Stokes, D. C. and Wang, W.** (2002). "An Improved In Situ and Satellite SST Analysis for Climate." *Journal of climate*, vol. 15, pp. 1609-1625.
- Reynolds, R.W., Zhang, H.-M., Smith, T.M., Gentemann, C.L. and Wentz, F.** (2005) "Impacts of in situ and additional satellite data on the accuracy of a sea-surface temperature analysis for climate", *International Journal of Climatology*, vol. 25, pp. 857–864.
- Richter, R. and Coll, C.** (2002) "Band-pass resampling effects for the retrieval of surface emissivity," *Appl. Opt.*, vol. 41, no. 18, pp. 3523–3529.
- Rodriguez-Galiano, V., Pardo-Iguzquiza, E., Sanchez-Castillo, M., Chica-Olmo, M. and Chica-Rivas, M.** (2012) "Downscaling Landsat 7 ETM+ thermal imagery using land surface temperature and NDVI images" *International Journal of Applied Earth Observation and Geoinformation*, vol. 18, pp. 515–527.

- Sánchez, J.M., Kustas, W.P., Caselles, V. and Anderson, M.C.** (2008) “Modelling surface energy fluxes over maize using a two-source patch model and radiometric soil and canopy temperature observations” *Remote Sens. Environ.*, vol. 112, pp. 1130–1143.
- Schluessel, P., Emery, W.J., Grassl, H. and Mammen, T.** (1990) “On the bulk-skin temperature difference and its impact on satellite remote sensing of sea surface temperature” *Journal of Geophysical Research*, vol. 95, no. C8, pp. 13341–13356.
- Schott, R., Hook, S. J., Barsi, J. A., Markham, B. L., Miller, J., Padula, F. P. and Raqueno, N. G.** (2012) “Thermal Infrared Radiometric Calibration of the Entire Landsat 4, 5, and 7 Archive (1982-2010)”, *Remote Sensing of Environment.*, vol. 122, pp. 41–49.
- Seemann, S.W., Borbas, E.E., Li, J., Menzel, W.P. and Gumley, L.E.** (2006) “MODIS atmospheric profile retrieval Algorithm Theoretical Basis Document (version 6).” Available at http://modis-atmos.gsfc.nasa.gov/reference_atbd.html.
- Seidel, F. C., Kokhanovsky, A. A. and Schaepman, M. E.** (2010) “Fast and simple model for atmospheric radiative transfer” *Atmos. Meas. Tech.*, vol. 3, pp. 1129–1141.
- Sobrino, J.A., Li, Z.-L. and Stoll, M. P.** (1993). “Impact of the atmospheric transmittance and total water vapor content in the algorithms for estimating satellite sea surface temperatures” *IEEE Trans. Geosci. Remote Sens.*, vol. 31, no. 5, pp. 946–952.
- Sobrino, J.A., Raissouni, N. and Li, Z.-L.** (2001) “A comparative study of land surface emissivity retrieval from NOAA data” *Remote Sens Environ.* vol. 75, Issue 2, pp. 256-266.
- Sobrino, J. A., Jiménez-Muñoz, J. C., Sòria, G., Gómez, M., Ortiz, A. Barella, Romaguera, M., Zaragoza, M., Julien, Y., Cuenca, J., Atitar, M., Hidalgo, V., Franch, B., Mattar, C., Ruescas, A., Morales, L., Gillespie, A., Balick, L., Su, Z., Nerry, F., Peres, L. and Libonati, R.** (2008) “Thermal remote sensing in the framework of the SEN2FLEX project: field measurements, airborne data and applications”, *International Journal of Remote Sensing*, vol. 29, Issue 17, pp. 4961-4991.
- Sobrino, J. A., Jiménez-Muñoz, J. C., Sòria, G., Romaguera, M., Guanter, L., Moreno, J., Plaza, A. and Martínez, P.** (2008) “Land surface emissivity retrieval from different VNIR and TIR sensors,” *IEEE Trans. Geosci. Remote Sens.*, vol. 48, no. 2, pp. 316–327.
- Stathopoulou, M. and Cartalis, C.** (2009) “Downscaling AVHRR land surface temperatures for improved surface urban heat island intensity estimation” *Remote Sensing of Environment*, vol. 113, no. 12, pp. 2592–2605.
- Storey, J., Choate, M., Falls, S., and Dakota, S.** (2014) “Geometric and spatial performance of Landsat 8” *ASPRS Annual Conference & co-located JACIE Workshop*.
- Sun, J. and Wang, M.** (2016a) “Electronic Crosstalk in Aqua MODIS Long-Wave Infrared Photovoltaic Bands” *Remote Sensing*, vol. 8, pp. 806.

REFERENCES

- Sun, J., Madhavan, S. and Wang, M.** (2016b) "Investigation and Mitigation of the Crosstalk Effect in Terra MODIS Band 30" *Remote Sensing*, vol. 8, pp. 249.
- Tatem, A. J., Goetz, S. J., and Hay, S. I.** (2008). Fifty Years of Earth Observation Satellites: Views from above have lead to countless advances on the ground in both scientific knowledge and daily life. *American Scientist*, vol. 96(5), pp. 390–398.
- Thome, K. J., Schiller, S., Conel, J. E., Arai, K. and Tsuchida, S.** (1998) "Results of the 1996 Earth Observing System vicarious calibration joint campaign at Lunar Lake Playa, Nevada (USA)" *Metrologia*, vol. 35, pp. 631-638.
- Tonooka, H.** (2005) "Inflight straylight analysis for ASTER thermal infrared bands" *IEEE Transactions on Geoscience and Remote Sensing*. vol.43, pp. 2752–2762.
- Vaughan, R.G., Calvin, W.M. and Taranik, J.V.** (2003) "SEBASS hyperspectral thermal infrared data: Surface emissivity measurement and mineral mapping" *Remote Sens. Environ.*, no. 85, pp. 48–63.
- Walton, C. C.** (1988): Nonlinear multichannel algorithms for estimating sea surface temperature with AVHRR satellite data. *J. Appl. Meteorol.*, vol. 27, pp. 115–124.
- Walton, C. C., W. G. Pichel and J. F. Sapper** (1998) "The development and operational application of nonlinear algorithms for the measurements of sea surface temperatures with the NOAA polar-orbiting environmental satellites" *J. Geophys. Res.*, vol. 103, pp. 27999–28012.
- Wan, Z., and Dozier, J.** (1996) "A generalized split-window algorithm for retrieving land surface temperature from space" *IEEE Transactions on Geoscience and Remote Sensing*, vol. 34, pp. 892–905.
- Wang, F., Qin, Z., Li, W., Song, C., Karnieli, A. and Zhao, S.** (2015) "An Efficient Approach for Pixel Decomposition to Increase the Spatial Resolution of Land Surface Temperature Images from MODIS Thermal Infrared Band Data" *Sensors*, vol. 15, no. 1, pp. 304–330.
- Wang, W.** (2014). "New refinements and validation of the collection-6 MODIS land-surface." *Remote Sens. Environ.*, vol. 140, pp. 36-45
- Wolfe, R. E., Nishihama, M., Fleiga, A. J., Kuypers, J. A. and Roy, D. P.** (2002) "Achieving sub-pixel geolocation accuracy in support of MODIS land science" *Remote Sensing of Environment*, Vol. 83, no. 1–2, pp. 31–49.
- Xiong, X., Wu, A., Wenny, B. N., Madhavan, S., Wang, Z., Li, Y., Chen, N., Barnes, W. L. and Salomonson, V. V.** (2015) "Terra and Aqua MODIS Thermal Emissive Bands On-Orbit Calibration and Performance" *IEEE Transactions on Geoscience and Remote Sensing*. vol. 53, no. 10, pp. 5709–5721.
- Zhu X., Chen J., Gao F., Chen X. and Masek J.G.** (2010) "An enhanced spatial and temporal adaptive reflectance fusion model for complex heterogeneous regions" *Remote Sens. Environ.*, vol. 114, pp. 2610–2623.